Alma Mater Studiorum – Università di Bologna

DOTTORATO DI RICERCA IN

Scienze Chimiche

Ciclo XXVI

Settore Concorsuale di afferenza: 03/A2

Settore Scientifico disciplinare: CHIM/02

ELEMENTARY PROCESSES OF RADIATION DAMAGE IN ORGANIC MOLECULES OF BIOLOGICAL INTEREST

Presentata da: **Mattea Carmen Castrovilli**

Coordinatore Dottorato

Prof. Aldo Roda

Relatore

Prof. Walther Caminati

Co-relatore

Dr.ssa Paola Bolognesi

Esame finale anno 2014

Alla mia famiglia

1 Introduction

1.1 The DNA and the origin of life

A discussion on the origin of life necessarily presupposes the knowledge of the basic characteristics of living organisms and in particular the functioning of a living cell. As the historian of biology Harmke Kamminga has observed, "At the heart of the problem of the origin of life lies a fundamental question: What is it exactly that we are trying to explain the origin of?" [1], or as the pioneering chemical evolutionary theorist Alexander Oparin said, 'the problem of the nature of life and the problem of its origin have become inseparable' [2]. The starting point for an answer to this fundamental question lies in understanding the functioning of the first and presumably simplest (or, at least, minimally complex) living cells. As a result, developments in fields that explicate the nature of unicellular life have historically defined the questions to which the origin-of-life study must answer.

Since 1950s the researchers have increasingly recognized the complex and specific nature of unicellular life and the biomacromolecules upon which such systems depend. Molecular biologists identified the DNA, RNA and proteins as carriers or repositories of 'information' [3,4,5,6]. Further, many others regarded the origin of the information in these biomacromolecules as the central question facing origin-of-life research. As Bernd-Olaf Kuppers has stated, "the problem of the origin of life is clearly basically equivalent to the problem of the origin of biological information" [7].

Yet evolutionary biologists in the 1870s and 1880s such as Ernst Haeckel and Thomas Huxley assumed life was, in its essence, a chemically simple substance called 'protoplasm'. Both thought that protoplasm could be easily constructed by combining and recombining simple chemical species such as carbon dioxide, oxygen and nitrogen. Over the next sixty years biologists and biochemists gradually revised the Haeckel and Huxley's theory describing the cell as a complex metabolic system. Alexander Oparin's theory of *evolutionary* abiogenesis envisioned a multi-billion year process of transformation from simple chemicals to a complex metabolic system[8,9]. Most of these scientists underestimated the complexity of the

cellular system that became clear with the development of molecular biology.

Many scientists in principle mistakenly believed that proteins also contained the source of heredity information. At the beginning of the 1950s, however, the biologists made a series of discoveries that caused this simplistic view of proteins to change.

The biochemists recognized that whereas proteins are built from chemically rather simple amino acid ‘building blocks,’ their function (whether as enzymes, signal transducers or structural components in the cell) depends crucially upon the complex but specific arrangement of these building blocks. For a functioning protein, its three-dimensional shape gives it a 'hand-in-glove' fit with other molecules in the cell, enabling it to catalyze specific chemical reactions or to build specific structures within the cell. During the early part on the twentieth century, researchers also vastly underestimated the complexity (and significance) of nucleic acids such as DNA and RNA. By the early part of the twentieth century, biologists knew the chemical composition of DNA. Chemists knew that in addition to sugars (and later phosphates), DNA was composed of four different nucleotide bases, called adenine, thymine, cytosine and guanine.

To account for the heritable differences between species, biologists needed to discover some source of variable or irregular specificity within the germlines of different organisms. As long as DNA was seen as an uninterestingly repetitive molecule most biologists assumed that DNA could play a little role in the transmission of heredity.

This view began to be accepted in the mid-1940s thanks to the Chargaff’s studies. He showed that the sequences of nucleotide in the DNA chain are different between the species even if they often are the same within the same species or within the same organs or tissues of a single organism. He recognized also that even for nucleic acids of exactly “the same analytical composition” (meaning those with precisely the same relative proportions of A, T, C, and G) “enormous” numbers of variations in sequencing were possible. We had to wait for the study by Watson and Crick in 1953 to recognize that the DNA could function as a carrier of hereditary information [3]. The model that Watson and Crick proposed envisioned a double-helix structure to explain the cross pattern derived from X-Ray crystallographic studies of DNA by Franklin, Wilkins and Bragg in the

early 1950s. According to the now well-known Watson and Crick model, the two strands of the helix were made of sugar and phosphate molecules linked by phosphodiester bonds.

Let's look more in detail the structure of the DNA (deoxyribonucleic acid) and the RNA (ribonucleic acid) which are the chemical carriers of the genetic information of the cell. All the information about the nature, the growth and the division of the cell are located in the DNA as well as the biosynthesis of the enzymes and proteins. These nucleic acids are biopolymers made of nucleotides joined together to make a long chain. Each nucleotide consists of a nucleoside linked to a phosphate group and each nucleoside is composed of a sugar linked to a purine or pyrimidine heterocyclic base (Fig 1.1—1).

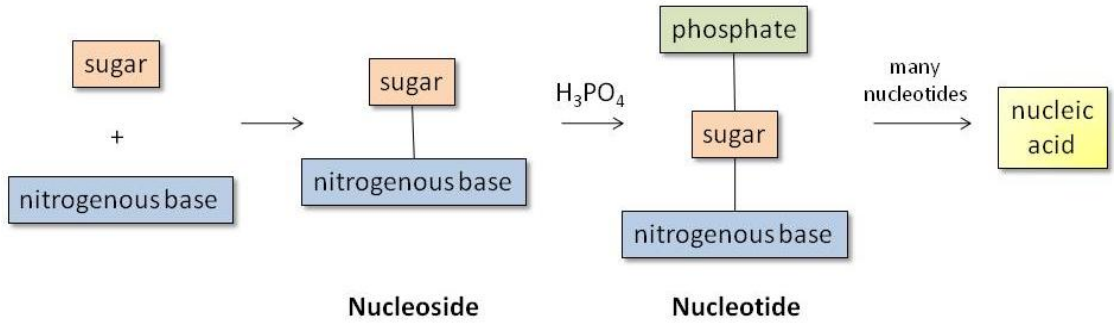

Fig 1.1—1 Schematic of the building blocks of a generic nucleic acid (DNA or RNA).

The sugar in the RNA is the ribose while in the DNA is 2-deoxyribose, which means that there isn't the OH group in position 2 of the ring (see Fig 1.1—2).

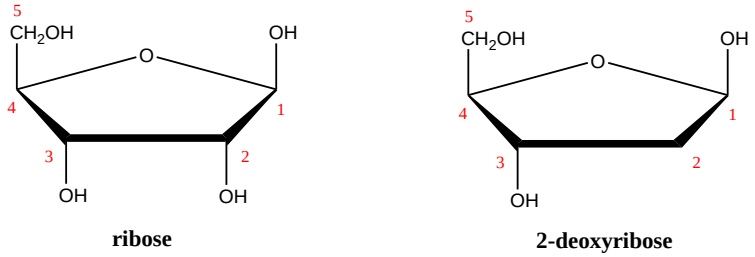

Fig 1.1—2 Difference between the ribose (in RNA) and 2-deoxyribose (in DNA)sugar.

In the DNA there are four different nitrogenous bases two of which are purinic bases (adenine and guanine) and the other two are pyrimidinic bases (cytosine and thymine). In the RNA there are the same bases except for thymine which is substituted by uracil (Fig 1.1—3).

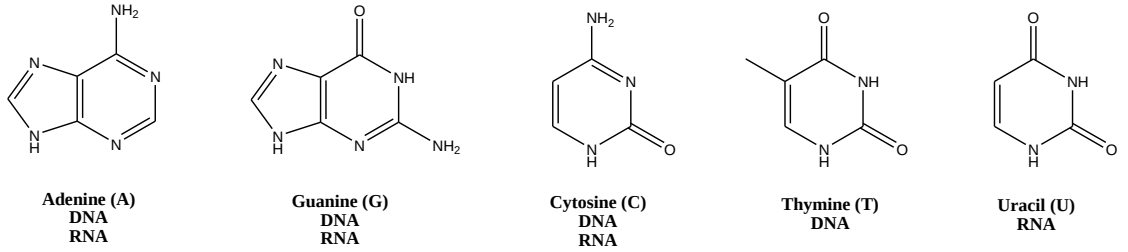

Fig 1.1—3 Different nucleosidic bases present in the DNA and RNA.

Both in DNA and RNA a nucleosidic base is joined to the carbon 1 (C1) on the sugar ring and the phosphoric group is joined in position 5 on the ring (C5) as shown in Fig 1.1—4.

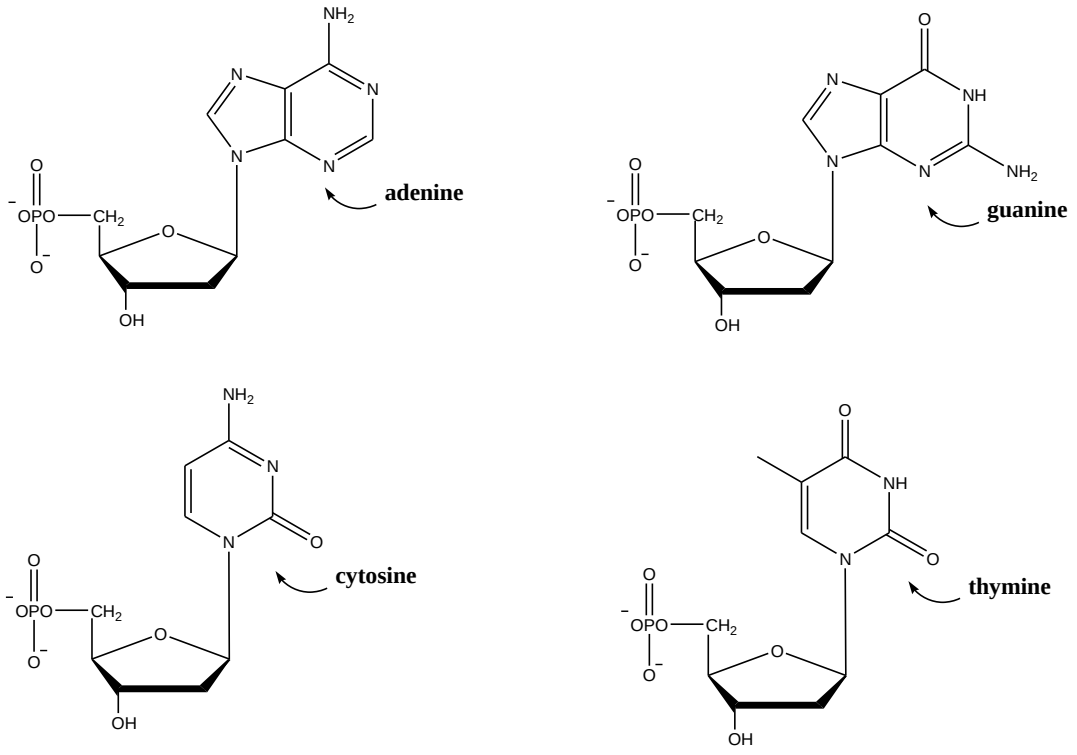

Fig 1.1—4 The four different nucleotides present in the DNA chain.

The nucleotides are joined together in the DNA strand through a bond between the phosphoric group in position 5 of a nucleotide and a OH group in position 3 of the neighbouring nucleotide (Fig 1.1—5).

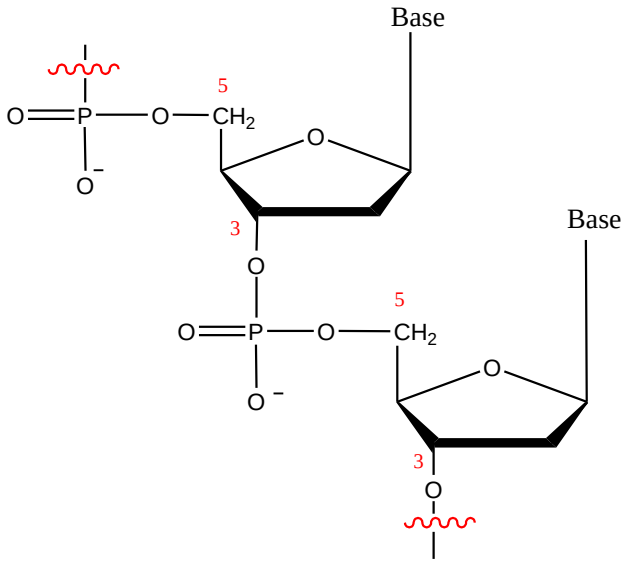

Fig 1.1—5 Description of the DNA chain structure.

Nucleotide bases are linked horizontally to the sugars on each strand of the helix and to a complementary base on the other strand through hydrogen bonds to form an internal ‘rung’ on the twisting ‘ladder.’ For geometric reasons, Watson and Crick’s model required the pairing (across the helix) of adenine with thymine and cytosine with guanine, respectively. This complementary pairing helped to explain a significant regularity in composition ratios that already Chargaff had discovered. Though Chargaff had shown that none of the four nucleotide bases appear with the same frequency as all the other three, he had not discovered that the molar proportions of adenine and thymine, on the one hand, and cytosine and guanine, on the other, do consistently equal each other [10]. Watson and Crick’s model explained this regularity as Chargaff had expressed it in his famous “ratios.”

The two strands of the double helix are wound in such a manner as to form two grooves: the major groove 1.2 nm large (12 Å) and the minor groove 600 pm large (6 Å). The major groove is slightly deeper than that minor one and both are coated of groups that could in principle create hydrogen bonds with other species. As a result it is possible for a variety of

polycyclic aromatic planar molecules to introduce laterally or intercalate between the stacked bases (Fig 1.1—6). Many carcinogens and anticancer agents carry out their function by interacting with DNA in this way.

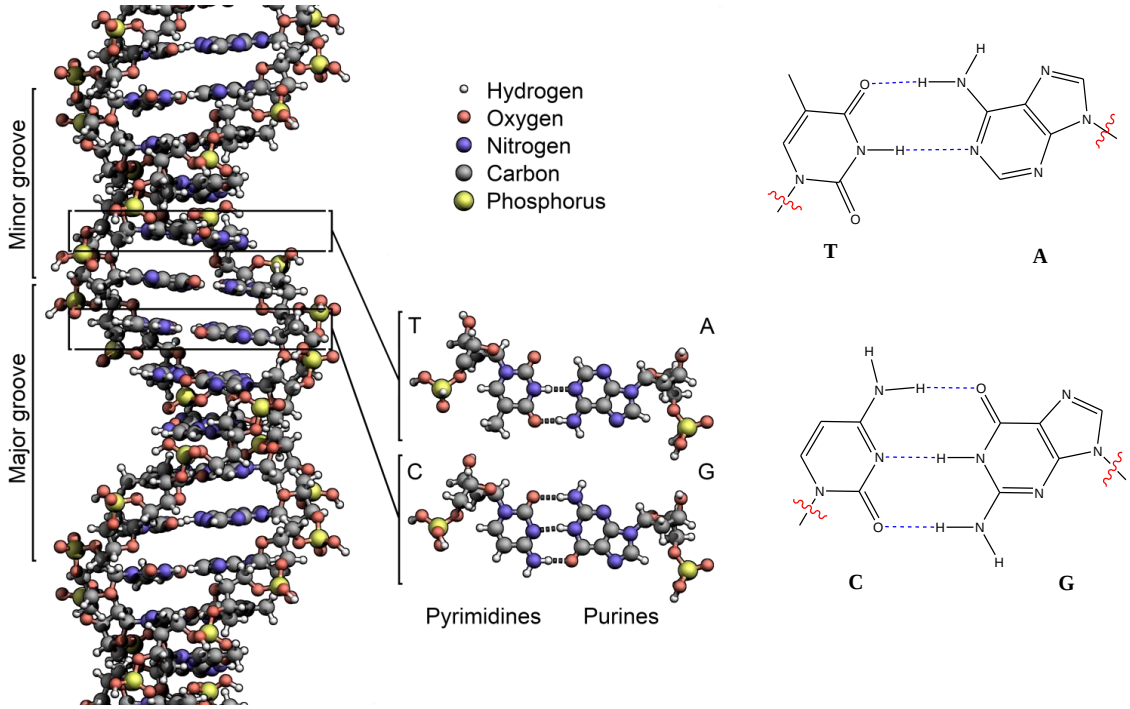

Fig 1.1—6 A twist (360°) of the DNA double helix. The skeleton (made of sugar and phosphoric group) runs along the outer wall of the helix; the nitrogenous bases are joined together in the inner part. The major and minor groove are also visible.

Our experiments provide insights into the structure and mechanisms of fragmentation of these elementary constituents and consequences in living organisms exposed to the irradiation. The assumption of an exogenous origin of life suggests that the prebiotic molecules, which are considered the building blocks that make up the living, may have formed in the interstellar medium.

This model is supported by the discovery of biologically relevant molecules (nucleic base, amino acids...) in meteorites and in the tails of comets (study of spectroscopy). Studies were also made on the possible formation of these species directly in the interstellar medium. It is necessary to understand this phenomenon to consider how these complex molecules are formed via irradiation in the interstellar medium starting by

an environment which contains the components.
In particular the work of this thesis is focused on the study of radiation damage induced on the halo-substituted nitrogenous bases of DNA by different kind of radiation. This type of molecules constitutes an important class of radiosensitizers used in radiotherapy for the treatment of cancer. A radiosensitizer is a drug that makes tumor cells more sensitive to radiation therapy enhancing tumour cell killing while having much less effect on normal tissues.
Two different kind of target molecules, the halo-pyrimidine and halo-uracil molecules have been studied in order to understand the different fragmentation induced by the absorption of two different kind of radiation: a low energy charged ion beam and the synchrotron radiation in the VUV and soft X-ray range. As we said above, the first kind of target molecule (the pyrimidine) is the building block of three important nucleobases into the DNA and RNA which are C, T and U, and its halogenated derivatives are considered prototype radiosensitizer molecules. The study of the valence shell fragmentation induced by the absorption of VUV radiation is an important starting point to understand the dynamic of dissociation of these molecules. This allows to reveal the role of a halogen atom on different sites on the aromatic ring as well as the role of the different halogen atoms in the same position of the ring. The fragmentation studies have highlighted that the site of halogenation and the type of halogen atom play a crucial role in the mechanisms of molecular fragmentation, leading, on one hand, to the preferential cleavage of a bond of the pyrimidinc ring or, on the other, to the release of halogen/hydrogen radical in the surrounding environment. The two different processes consequently trigger different mechanisms of biological damage. This has allowed to explain some of the very fundamental mechanisms in the case of isolated ‘single’ molecules that may lead to the increased effectiveness of halopyrimidines as radiosensitisers. This first part of the study has provided new insight on the fragmentation of these prototype molecules, useful to understand their behaviour as radiosensitizers in the gaseous phase, where the molecule is not affected by the interactions with water molecules or other particles as would be in a cellular environment. To understand how the molecular environment may affect the fragmentation dynamic of a radiosensitizer the second part of the work has been devoted to the study of more specific and

realistic molecules, like the 5Br-uracil molecule, which is the basic component of the 5Br-deoxyuridine used in radiotherapy. Firstly the entire series of 5-halouracile molecules has been characterized through XPS, NEXAFS and FT-IR spectroscopies then, the ion-induced fragmentation of homogenous and hydrated clusters of 5Br-uracil has been studied and compared to similar studies performed on the isolated molecule., in order to understand the role played by the environment on the properties of the single molecule.
But what is exactly the radiation damage and why these molecules are so important as radisensitizers?

1.2 Goal of the thesis and radiation damage

It has long been known that the passage of energetic photons, electrons and ions in living organisms produces a track of ionized and excited atoms and molecules within the irradiated matter, which leads to alterations, malfunctioning as well as mutations and even cellular death. Nowadays, there is substantial evidence that macroscopic damage is initiated at the microscopic scale of the DNA chain contained in living cells, which is the most sensitive part of the cell. These DNA alterations are due to significant energy deposition either in the DNA constituents or in its neighboring molecules, causing direct and indirect damage effects, respectively. The study of molecules of biological interest as isolated systems in gas phase can help determining the intrinsic properties of the single molecule and therefore disentangle these two effects. These studies in gas phase provide information about the dynamic of ionization/fragmentation at the microscopic scale that is where everything starts. On the other hand, the same pathogenic effects of radiation can be efficiently used in radiotherapy for cancer treatment. In this respect, the harmful action of the ionising radiation on tumour cells can be further enhanced via the use of properly designed radiosensitisers in order to produce a selective and amplified damage of the tumour rather than healthy cells.
Previous experiments, performed by Watanabe et al. [11] were focused on incorporating pyrimidine analogues into fast reproducing RNA/DNA of cancerous cells, radiating the sample and counting the damage as the number of single (SSB) and double (DSB) strand breaks. They studied the

strand break induced by the absorption of X-ray photons with and without the incorporated Br/I deoxyuridine in cell-mimetic conditions. The increase of DNA strand breaks induction was modelled by taking into account both the direct energy deposition and the effect of the radicals. The calculation of the yield and the spectrum of strand breaks at various degrees of Br/IdU incorporation lead to the observation that the excess strand breaks due to Br/IdU incorporation was assumed to be induced by highly reactive uracilyl radicals. Four mechanisms were considered for the production of uracilyl radicals generated by hydrated electrons, by direct energy deposition, and by both hydrated electrons and direct energy depositions. However this is not the only mechanism to increase the radiation damage in modified cancerous cells.

Electromagnetic radiation below 10 keV creates more complex and clustered molecular damage in cellular DNA because it produces denser low-energy electron tracks per absorbed dose relative to hard X-rays or γ rays [12]. These electrons become thermalized by loosing their energy during inelastic collisions in the medium. It has been shown that they induce strand breaks in plasmids [13] as well as ionic and neutral fragment formation in oligonucleotides by dissociative electron attachment (DEA) and dipolar dissociation [14]. Studies of DNA damage upon core ionization at the carbon, nitrogen, oxygen, [15] and phosphorous [16] 1s edges have focused on both direct decomposition of DNA due to the core hole created and the effect of the fast Auger electrons ejected in secondary processes. While a large body of results has been produced in the study of the DEA process in DNA/RNA bases [17] and their halogenated analogues [18--20], much less effort has been devoted to the investigation of the ‘direct’ effects due to the absorption of VUV, soft and hard X-ray radiation by the DNA constituents and to collisions with a multiple charged ion beam. Nevertheless, in the case of halogenated analogues of DNA bases, the formation and no-radiative decay of core vacancies has long been pointed out as a leading channel in the selective tumor damage induced by these radiosensitizers [21,22]. A selective and enhanced molecular fragmentation of the halogenated species has also been proposed and investigated by Bolognesi et al. [23]. Fluoro- (FdU) and bromo-deoxyuridine (BrdU) and Gemcitabine, a fluorine substitute of deoxycytidine, are just some of the most common analogues of pyrimidines used in radioteraphy. A broad

investigation of their building block, the pyrimidine molecule, and the halogenated pyrimidine molecules, has provided useful insights into the relevant mechanisms that, acting at the single molecule level, may explain their radiosensitizing effects.

The therapy, based on radiation damage, uses both X-ray and γ-ray beams but also beams of charged particles (protons and heavy ions like C^{4+}). In the latter case the therapy is known as hadrontherapy. The strength of hadrontherapy lies in the unique physical and radiobiological properties of these particles. They can penetrate the tissues with little diffusion and deposit the maximum energy just before stopping. This allows a precise definition of the specific region to be irradiated. The peak at the end of the hadron energy deposition curve is called the Bragg peak. With the use of hadrons the tumour, situated deeply inside the body, can be irradiated while keeping the damage to more superficial healthy tissues lower than with X-rays irradiation.

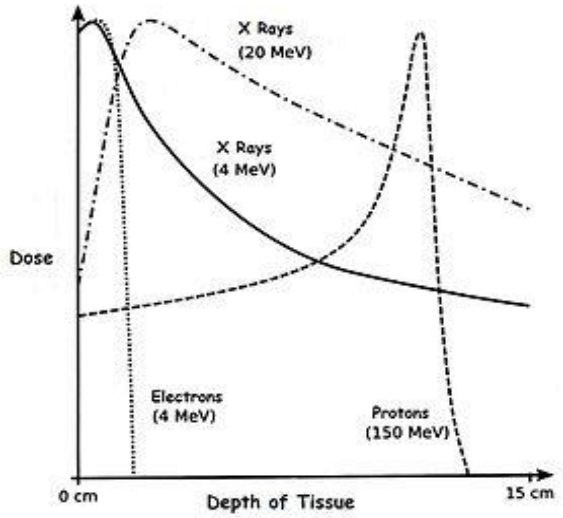

1.2—1 The Bragg peak shows that the dose transferred from the protons to the tissue is maximum in a region of a few millimetres at the end of the proton path, unlike the case of electrons or X-rays.

Nowadays the most common ion beam used for treating cancer is a C^{4+} ion beam and in our experiments this beam has been used to study the fragmentation of halogenated uracil molecules. In order to mimic a more realistic environment, experiments on homogeneous cluster and hydrated clusters of halogenated uracil molecules have also been performed. Interesting results regarding the ‘protective’ effect of the environment with

respect to the isolated molecule, the selective fragmentation and the probable tautomerization induced by water molecules have been obtained A detailed description of the characteristics of the target molecules used for the two kind of experiments: the photofragmentation of halogenated pyrimidine molecules induced by the absorption of VUV radiation and the fragmentation of halogenated uracil molecules by ion impact are described in section 1.3.

1.3 The target molecules

It is possible to divide the work presented in this thesis in two parts. The first one involves the study of photofragmentation of halogenated pyrimidine molecules in the VUV range, in particular 5Br-pyrimidine, 2Br-pyrimidine and 2Cl-pyrimidine, and the second one the ion-impact fragmentation of the halogenated uracil molecule, 5Br-uracil.

1.3.1 Halogenated pyrimidine molecules

From the experimental point of view, the pyrimidine molecule presents the advantages that i) having the fundamental structure of the cytosine, thymine and uracil DNA/RNA bases it shares with the bases many of its properties and ii) can be easily produced in the gas phase, due to its relatively high vapor pressure at room temperature that does not require heating of the sample, therefore removing the risk of thermal decomposition. Previous fragmentation [23, 24, , , 27] and ionization studies of pyrimidine and halogenated pyrimidines in the valence [28, , 30] and inner shell regions [31, , , 34] have provided a comprehensive spectroscopic characterization of these molecules. In the pyrimidine case, taking advantage of the non-equivalent binding energies of the localized C and N core electrons, time-of-flight mass spectrometric measurements have been performed at several photon energies across the excitation/ionization thresholds of the C and N K edges using tunable synchrotron radiation in the soft X-ray range. These experiments revealed both the photon energy dependence and the site-selectivity of the molecular fragmentation of pyrimidine. The more selective resonant Auger electron-ion coincidence measurements [23], which focus on the electron decay to the lowest

electronic states of the pyrimidine cation, proved that the fragmentation pattern is determined by the final rather than the intermediate, site-selected, state. The so-called ‘molecular knife’ effect [35, , 37], where a localized core excitation is proposed to control selective molecular bond breaking was found to be, in the pyrimidine case, an indirect effect. The fast de-excitation of the intermediate states via spectator/participator resonant Auger decay affects the branching ratio of the populated valence electronic states with respect to direct ionization. Together with the selective fragmentation of these valence shell electronic states already observed by Plekan et al. [38], the resonant Auger electron – ion experiments in pyrimidine showed the crucial role played by the valence shell in the fragmentation dynamics also when soft X-rays are absorbed. In the investigated ionization energy range, 9–15 eV, of the photoelectron-ion [38] and resonant Auger electron-ion coincidence experiments [23] the dominant fragmentation patterns of the energy selected electronic states appear to correlate to the nearest appearance potential. Stimulated by these results in pyrimidine, a joint experimental and computational study of the photofragmentation of the 2Br-, 2Cl- and 5Br- pyrimidine molecules (Fig 1.3—1) has been undertaken in the VUV range.

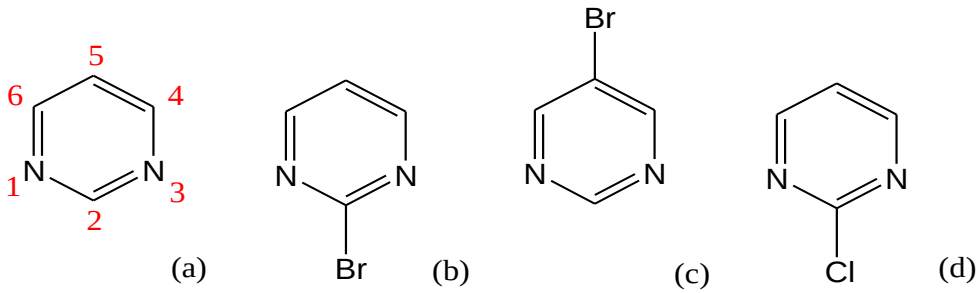

Fig 1.3—1 The target molecules under investigation in the VUV photofragmentation study: 2Br-pyrimidine (b), 5Br-pyrimidne (c) and 2Cl-pyrimidine (d). In the pyrimidine molecule (a) the positions of the atoms are indicated (red).

Although halogen substituted pyrimidines have similar structure to the pyrimidine molecule and share many of its photophysical and photochemical properties, their photodissociation dynamics may be quite

different. These targets have been chosen with the purpose of investigating the effect of the specific halogen atom and the site of halogenation on the fragmentation dynamics. As it will be discussed in chapter 4 the most relevant effects are due to the inductive and resonant effects that may have a different weight depending on the type of halogen atom and on the site of halogenation on the aromatic ring. All the experiments were performed at the CiPo beamline of the ELETTRA synchrotron radiation source in Trieste.

1.3.2 Halogenated uracil molecules

The replacement of uracil with 5-X Uracil (X=F, Cl, Br, I) significantly changes its chemical and spectroscopic properties, as well as its in vivo activity. The biological activity of 5-XU (X=F, Cl, Br, I) is not fully understood and requires continuous studies. 5F-uracil (5FU) is a drug that is used in the treatment of cancer. It belongs to the family of drugs called Antimetabolite. 5Cl-uracil (5ClU) has also antitumor activity and forms complexes with some metal (II) ions. It has been suggested that peroxidase secreted by human phagocytes facilitate the formation of 5-ClU and 5Br-uracil (5BrU) in the human inflammatory tissue. The essential biological importance of 5BrU is that it is one of the well known uncommon nucleotide bases and has the ability to coordinate with metals or to bind to tissue via metals which interface with the growth of cancer cells [39]. 5I-uracil (5IU) is an important antimetabolite like other halogenated uracils, being in the case of 4-aminobutyrate aminotransferase the most effective inhibitor [40]. Some of the 5IU derivatives also posses antitumor activity [41] and have been used in the treatment of the hepatitis B infections [42]. Some 5IU based nucleoside analogues were found to be selective inhibitors of herpes simplex viruses.

Before starting with the study of the fragmentation of halo-uracil molecules by ion-impact, an extensive FT-IR characterization of these molecules at different temperatures has been performed in order to choose the suitable one for the sublimation in the gas phase, preventing a thermal decomposition of the target molecules (Fig 1.3—2) during the sublimation. The experimental set-up used is described in chapter 2 and the FT-IR spectra collected are shown in chapter 5. All these preliminary tests were

necessary to perform the gas phase experiments at the GasPhase beamline of the ELETTRA synchrotron radiation source in Trieste. In this occasion XPS and NEXAFS experiments have been performed in order to characterize these molecules and analyse the different resonant and inductive effects (already noted for the pyrimidine case) due to the presence of different halogen atoms on the same position of the ring. These results provide the spectroscopic characterization of the targets necessary for the interpretation of the electronic decay and fragmentation studies that will be performed in the future.

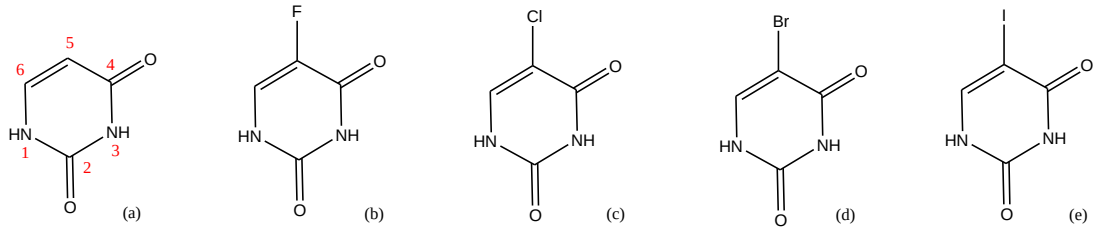

Fig 1.3—2 The target molecules under investigation in the FT-IR, XPS, NEXAFS and ion-induced fragmentation study: 5F-uracil (b), 5Cl-uracil (c), 5Br-uracil (d) and 5I-uracil (e). In the uracil molecule (a) the positions of the atoms are indicated (red).

Then the study of these important radiosensitising molecules fragmentation by ion-impact experiment has been followed. In such collisions, the relative yield of multiply charged species is enhanced compared to X-rays leading to the production of numerous secondary particles. Moreover, using the gas aggregation source of the ARIBE beamline in GANIL (National Large Heavy Ion Accelerator) in Caen, France, it is possible to mimic a simple chemical environment by embedding the molecule in both pure (i.e. of the molecule of interest Mm) and hydrated (MmWw) clusters (Fig 1.3—3). This latter study will allow to consider the role of the environment on the fragmentation dynamics.

The collision of the neutral target molecules with multiply charged ions at low collision energy is an efficient method to create multiply charged ions in the target molecule. The low-energy C^{4+} (36 keV) ions are used to simulate conditions in hadrontherapy below the Bragg peak energy. Indeed, in a recent theoretical work, the calculated charge transfer cross section of

the C^{4+} halogenated uracil reaction [43] is compared to the C^{4+} uracil one [44], revealing a strong lowering of the charge transfer cross section (by at least a factor 100) for collisions involving halouracil targets.

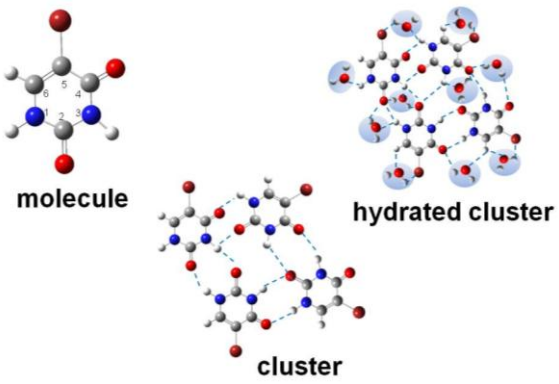

Fig 1.3—3 Target species used in ion-beam fragmentation experiments performed at the ARIBE beamline in Ganil.

Considering that charge transfer and fragmentation have been shown to be complementary processes [45], this may lead to the enhanced fragmentation of halouracil, in complete agreement with their observed radiosensitising properties. Moreover, these experiments have allowed to explore a fragmentation regime not easily accessible by photoionisation experiments, where the formation of multiply charged ions is barely observed. The measure and the comparison of the fragmentation patterns of the isolated molecules and their homogeneous and hydrated cluster compounds will allow to investigate the role of the environment on the molecular fragmentation and possibly lead to the understanding of whether the environment will emphasise or reduce their 'radiosensitising' effect. The 5Br-uracil, has been selected with the purpose of investigating the effect of the halogenation on the uracil and the probable keto-eno tautomerization induced by the water molecules as already proposed by van Mourik et al. [46, 129]. The ion-beam fragmentation spectra of the single molecules, the homogeneous clusters and the hydrated clusters of 5BrU have been studied, underlining the different fragmentation patterns induced by the modified environment (clusters/hydrated clusters). These results will be compared and discussed in chapter 5. All the instrumental techniques employed in this work of thesis will be described in chapter 2. The

theoretical analysis and the experimental results about the photofragmentation of halogenated pyrimidine molecules in the VUV range will be described in chapter 3 and 4 respectively.

2 Instrumental techniques

In this chapter all the instrumental techniques employed in the work of thesis will be described. The first experiment performed and discussed in chapter 4 regards the measurement of the mass spectra and the appearance energy values of the halogenated pyrimidine molecules and their relative fragments. These experiments have been performed at the CiPo beamline of the Elettra synchrotron radiation source in Trieste. For this reason the main properties of Synchrotron radiation and the CiPo beamline characteristics will be described in section 2.1 and 2.2.1 respectively. The second part regards the study of the halogenated uracil molecules. An extensive characterization of these molecules has been performed through FT-IR spectroscopy, described section 2.4, in order to find a good sublimation temperature avoiding thermal decomposition. These preliminary tests were necessary to find the better working condition for the NEXAFS and XPS experiments performed at the GasPhase beamline (sections 2.2.4, 2.2.5 and 2.2.3 respectively). These experiments provide the spectroscopic characterization of the targets necessary for the interpretation of the electronic decay and fragmentations studies that will be performed in the future. The last experimental part regards the measurement of the ion impact fragmentation mass spectra of the 5Br-uracil molecule and its homogeneous and hydrated clusters. These experiments were performed at the Aribe beamline of Ganil in Basse Normandie, France. The experimental set-up of the beamline is described in section 2.3.

2.1 The main properties of Synchrotron radiation

The main characteristics of a synchrotron particle accelerator will be described below with particular attention to the radiation properties, the spectral brilliance and the insertion devices.

2.1.1 What's the Synchrotron radiation

When the electrons or other charged particles are forced to move with relativistic speeds by means of the application of an electric or magnetic

field, following curved trajectories, they radiate electromagnetic radiation in a narrow cone in the direction of their motion. This highly collimated radiation is called synchrotron radiation. Synchrotron radiation emitted by electrons in particle accelerators is extremely intense and extends over a broad energy range from the infrared through the visible and ultraviolet, to the soft and hard x-ray regions of the electromagnetic spectrum.
Nowadays synchrotron radiation is used to study many aspects of the structure of matter at the atomic and molecular level, from surface properties of solids to the structure of protein molecules.
Synchrotron radiation was observed for the first time in 1947 from the General Electric synchrotron in the USA and announced in a letter entitled "Radiation from Electrons in a Synchrotron"[47]. In the last sixties the scientists have realized the great importance of the use of synchrotron radiation for condensed matter research. Since then, an explosive growth in the building of dedicated synchrotron radiation facilities made this radiation a unique tool in many research fields.

2.1.2 Storage rings and synchrotron radiation sources

Electrons travelling at relativistic speed and forced to change the direction of their motion under the effect of magnetic fields emit light with peculiar characteristics, called synchrotron radiation. The man-made sources of this radiation [48] are high energy electron or positron circular accelerators, like storage rings. They consist of evacuated pipes where the electrons are forced to follow approximately circular paths under the action of magnets placed along the circumference (bending magnets). The electrons enter the storage ring after they have been accelerated in a linear accelerator or 'linac', until their energy reaches several millions of electronvolts (MeV); in the Elettra synchrotron radiation source in Trieste, the injection chain consists of a 100 MeV linear accelerator and a 2.0 or 2.5 GeV booster that injects the electron beam bunches into the storage ring at a rate of up to 3 Hz. This new building accommodating a small linac injector and a booster has been built in the central empty space of the storage ring building. The electrons are generated in a small linac. They start off from a ceramic disc that is heated to very high temperature. An electric field of up to 100 kV draws out the electrons that are then accelerated through two radio-

frequency structures that make up the linac. The linac is composed of the Gun (that houses the ceramic disc), a low energy bunching section and two high-energy sections. The overall length of the linac is 12 m and contains two high-energy sections each 5 m long. Between accelerating sections quadrupole magnets keep the electron beam focused. The linac operates at 3 GHz and generates a pulse of electron bunches that are accelerated to the final energy of 100 MeV. The electrons exiting the linac are then transported to the booster by a transfer line (a series of deflection and focussing magnets). The booster is a 'simple' synchrotron of 118 m of circumference that can accelerate a maximum of 6 mA current from 100 MeV up to 2.0 or 2.5 GeV. The storage ring is filled by a multi-turn injection process whereby pulses of electrons from the booster are gradually fed into the ring three times a second until the desired current is achieved. Usually Elettra is filled with 310 mA when at 2 GeV and 150 mA when at 2.4 GeV. More than 500 mA have been stored at 1.5 GeV and more than 700 mA at 1 GeV. The maximum intensity is limited by the radiofrequency power and the thermal load in the vacuum chambers due to synchrotron radiation. The electrons circulating in the ring do so in metal vacuum chambers. The vacuum that is maintained in the storage ring, as well as in the linac and booster, must be of very high quality, in the order of 10^{-10} mbar, in order to maintain a long beam lifetime reducing the chance of electrons colliding with gas molecules. The situation is further complicated by the copious emission of synchrotron radiation, around 90 kW of power just from the bending magnets. The unused radiation must be absorbed in special places otherwise chamber deformation and photo-electron release of surface gasses will occur.

In the circular accelerator the electrons may be further accelerated to higher energies by the radio frequency (RF) electric fields. When the electrons reach the expected energy they are in a quasi-stationary situation; forced to follow circular paths by the magnetic field of the bending magnets, they lose, during each turn, part of their energy, emitting, synchrotron radiation. The energy lost in this way is fully regained in passing through the RF cavities.

In more details, storage rings consist of an array of magnets for focusing and bending the beam connected by straight linear sections (Fig 2.1—1). In one or more of these linear sections, RF cavities are installed in order to

accelerate the particles.

After its discovery in 1947, during the 1960's and early 70's pioneering use of the light was made in the so called *first generation synchrotron radiation facilities*; these machines were not dedicated to synchrotron radiation studies, but were used in a parasitic way, during high energy physics experiments (the synchrotrons were primarily designed for high-energy or nuclear physics experiments). A pilot experimental programme exploiting synchrotron radiation began when the National Bureau of Standards modified its 180-MeV electron synchrotron in Washington D. C. to allow access to the radiation via a tangent section into the machine's vacuum system. Thus was born the Synchrotron Ultraviolet Radiation Facility (SURF I), the first facility catering for regular users of synchrotron radiation. In addition to SURF I, facilities in Frascati and in Japan soon after began to attract a regular stream of physicists keen to explore the possibilities of synchrotron radiation. More would soon follow suit. Because most of these early facilities had storage-ring energies around or below 1 GeV, experiments were concentrated in the ultraviolet and soft x-ray regimes. The year 1964 saw the first users of synchrotron radiation from the 6 GeV Deutsches Elektronen-Synchrotron (DESY) in Hamburg and suddenly the range of synchrotron radiation was extended to the hard x-ray region down to 0.1 Å (about 125 keV). Many further facilities began to accommodate synchrotron-radiation users. One of the first of these was the 240 MeV machine 'Tantalus' in Wisconsin. Although not originally designed to provide synchrotron radiation, it became the first facility to be exclusively used for synchrotron experiments, providing radiation in the ultraviolet up to a few tens of eV.

In the mid-70's facilities totally dedicated to synchrotron light, were constructed. These facilities, where most of the synchrotron light was produced by bending magnets, were called *second generation sources*. The 2 GeV Synchrotron Radiation Source (SRS) at Daresbury, England, was the first of these so-called 'second-generation' synchrotron sources. Experiments began in 1981. Several more new facilities were soon built and commissioned, while some first-generation sources were upgraded to second-generation status.

In the last ten years, the use of high field magnetic structures, like wigglers and undulators, placed in straight sections has made possible the realization

of new synchrotron radiation sources the so called *third generation sources* like the European Synchrotron Radiation Facility (E.S.R.F. 6 GeV storage ring, in Grenoble, France) and Elettra (2 and 2.4 GeV storage ring, in Trieste, Italy), for example.

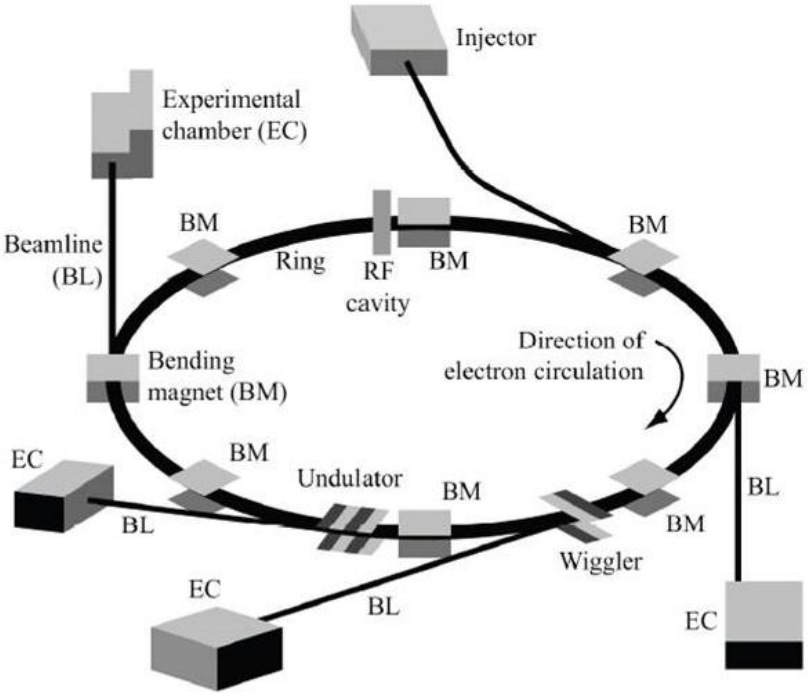

Fig 2.1—1 Schematic view of a storage ring where some of the main elements like bending magnets (main dipoles), insertion devices (undulators, wigglers) and the RF cavities are visible.

Since May 2010 Elettra has become a third-generation synchrotron that operates in full top-up mode and at multiple energies too. In top-up mode, the storage ring intensity is kept constant by frequent beam injections, in contrast with the decay mode where the stored beam is allowed to decay to some level before refilling occurs. In these facilities an incredible gain in the quality of the synchrotron light was achieved. Fig 2.1—2 shows the gain in the brilliance achieved in the last decades by synchrotron radiation sources. A high brilliance means thus high intensity combined with tight focusing and spectral purity. The brilliance of X-FELs, sometimes considered as “the fourth generation” synchrotrons, will surpass that of the most advanced synchrotron light sources by 12 orders of magnitude. This gives an idea of the spectacular progress obtained in the quality of the sources.

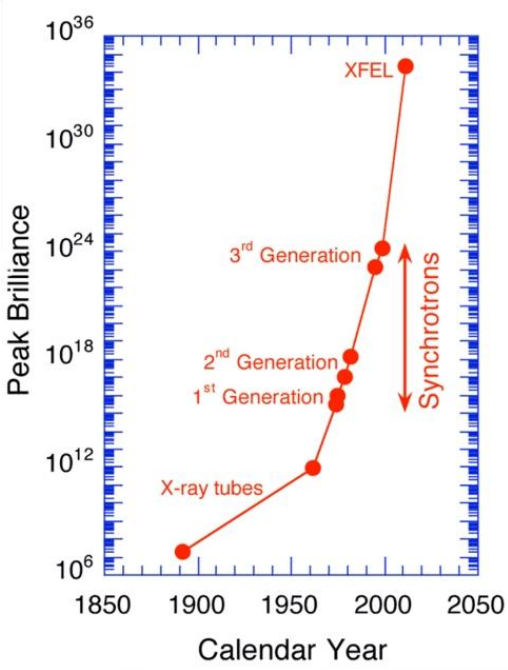

Fig 2.1—2 Comparison between the average brilliance of storage rings of different generations. As a comparison also the average brilliance of x-ray tubes and of x-ray FEL (Free Electron Laser) are reported.

2.1.3 Synchrotron radiation properties

The main properties of the emitted radiation depend on the characteristics of the storage ring and can be summarized as follows:

1. high intensity
2. very broad and continuous spectral range from infrared up to the hard x-ray region
3. natural narrow angular collimation
4. high degree of polarization
5. pulsed time structure
6. high brilliance of the source due to the small cross section of the electron beam and high degree of collimation of the radiation
7. high beam stability
8. all properties quantitatively evaluable.

All the properties of synchrotron radiation can be calculated by applying the methods of classical electrodynamics to the motion of relativistic charged particles.

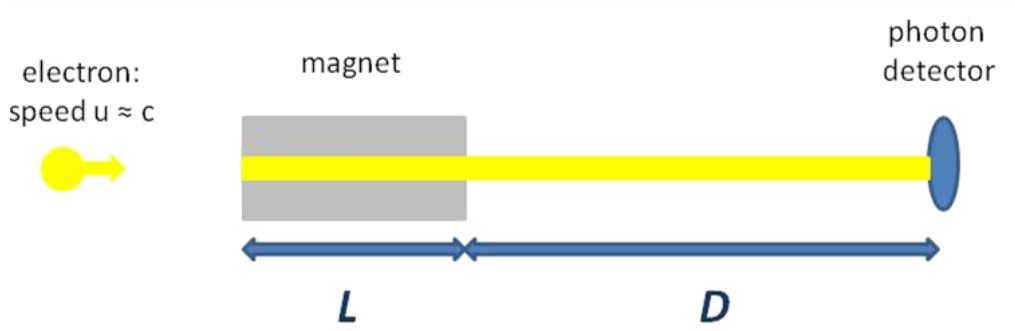

Fig 2.1—3 Schematic of the variables used to derive the frequency of the photon emitted by a relativistic electron inside the magnet.

Lets consider an electron moving at speed approaching that of light, when it enters in a magnet (at time zero) it is accelerated by the Lorentz force and emits a photon. The electron leaves the magnet at time *L/u* where *L* is the length of the magnet and u is the velocity of the electron. So the first photon will arrive at the detector at the time *(L+D)/c* (where *D* is the distance between the magnet and the detector and *c* is the speed of light) and the last one will arrive at the time *(L/u+D/c)*. Changing the length of the magnet and the relativistic speed of the electron it is possible to obtain different radiation frequency. For example the photon pulse duration is:

$$\Delta t = \frac{L}{u} - \frac{L}{c} = \left(\frac{L}{u}\right)\left(1 - \frac{u}{c}\right) \tag{2.1-1}$$

from eq (2.1-1) it is possible to derive the characteristic frequency:

$$\omega = \frac{1}{\Delta t} = \frac{u}{\left[L\left(1 - \frac{u}{c}\right)\right]} = u\sigma^2 \frac{\left(1 + \frac{u}{c}\right)}{L} \tag{2.1-2}$$

Where σ^2 is $\frac{1}{\left(1-\frac{u^2}{c^2}\right)}$ so for $u \approx c$,$\left(1 + \frac{u}{c}\right) \approx 2$ and the frequency is

$$\omega \approx \frac{2c\sigma^2}{L} \tag{2.1-3}$$

In this case if L = 0.1 m and σ= 4000 then the frequency becomes: $\omega \approx 10^{17}$ s^{-1} in the x-ray spectrum region.

The total power emitted by a relativistic electron along a circular orbit in CGS units is given by the Schwinger's formula [49]:

$$P_{Tot} = \iint P(\lambda,\psi)d\lambda d\psi = \frac{2}{3}\frac{e^2 c}{R^2}\left[\frac{E}{mc^2}\right]^4 \tag{2.1-4}$$

where λ is the wavelength of the emitted radiation, ψ is the azimuthal or vertical half-opening angle perpendicular to the orbital plane. $P(\lambda,\psi)$, the power radiated by an electron in an unit wavelength interval centered at λ and in a unit vertical angular aperture centered at ψ is given by:

$$P(\lambda,\psi) = \frac{27}{32\pi^3}\frac{e^2 c}{R^3}\left(\frac{\lambda_c}{\lambda}\right)^4 \gamma^8[1+(\gamma\psi)^2]^2\left[K^2_{2/3}(\xi) + \frac{(\gamma\psi)^2}{1+(\gamma\psi)^2}K^2_{1/3}(\xi)\right] \tag{2.1-5}$$

In this equation R is the bending radius of the electron orbit and $K_{1/3}$ and $K_{2/3}$ are the modified Bessel functions of the second kind.
γ is the relativistic quantity $E/(mc^2)$, where mc^2 is the electron rest mass energy. λ_c is the so called critical wavelength given by:

$$\lambda_c = \left(4/3\right)\pi R\gamma^{-3} \tag{2.1-6}$$

Finally ξ is equal to :

$$\xi = \left(\lambda_c/2\lambda\right)[1+(\gamma\psi)^2]^{3/2} \tag{2.1-7}$$

In eq.(2.1-4), the dependence of the radiated power on E^4 implies that, in order to keep the radiated power at reasonable values to increase the energy of the storage rings it is necessary to increase also the radius of the storage ring. In the same equation it is also easy to see that, due to the dependence on m^{-1} the radiation produced by accelerators is negligible.
In eq.(2.1-5) it is easy to note how the irradiated power per unit wavelength interval and unit vertical aperture depends only on the machine parameters

γ and R and on the ratio λ_c/λ.

In order to understand the angular and spectral distribution of the emitted radiation let us first remind the emission from a classical electron moving at a speed, v, much lower than the speed of light, c ($v << c$) [50]. In this case, as shown in Fig 2.1—4, the emitted pattern is similar to the one of an oscillating dipole with its maximum of intensity in the direction perpendicular to the acceleration and do not depend on the electron speed.

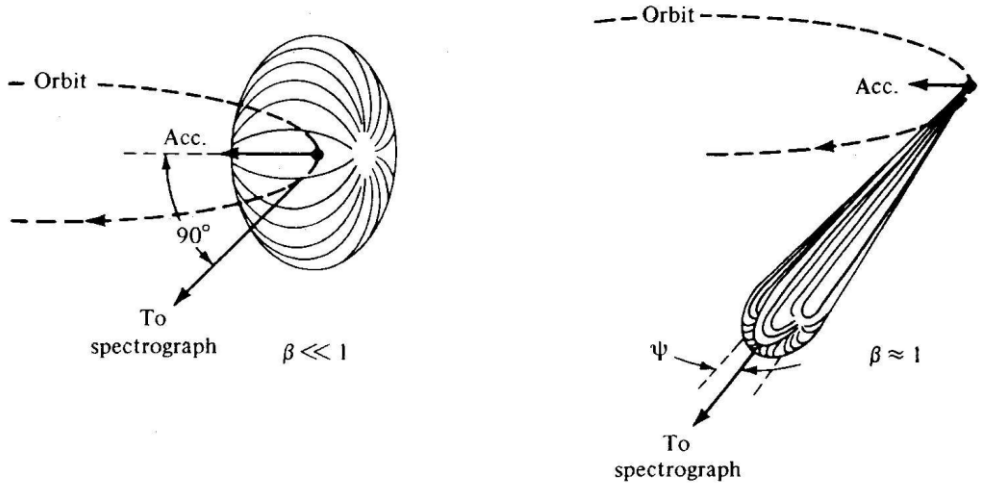

Fig 2.1—4 Qualitative radiation patterns related to charged particles moving in a circular orbit. The dipole pattern achieved for slow particles (left) ($\beta = v/c << 1$) is distorted into a narrow cone when $\beta \approx 1$ (right).

Thanks to a relativistic effect, when the speed of the emitting electrons increases to reach relativistic values (v ≈ c) the radiation pattern is compressed into a narrow cone in the direction of motion, resulting into an emission tangential to the particle orbit. The vertical half-opening angle, ψ, is given by:

$$\psi \approx {mc^2}/{E} \approx \gamma^{-1} \tag{2.1-8}$$

For electrons and positrons, γ = 1957 E (GeV), so for a storage ring of energy E = 1 GeV it follows that $\psi \approx 0.5$ mrad. In this way it follows that the synchrotron radiation is highly collimated. This characteristic provides extremely high fluxes on very small areas also at distances of about 40 m,

from the storage ring.
In a bending magnet the orbit of the electrons is circular and the radiation is emitted tangentially. It is collected, for experiments, through a horizontal slit (S) of width, *w*, at a distance, *D*, from the electron orbit (see Fig 2.1—**5**); this corresponds to an angular aperture, $\Delta\theta = w/D >> \psi$.

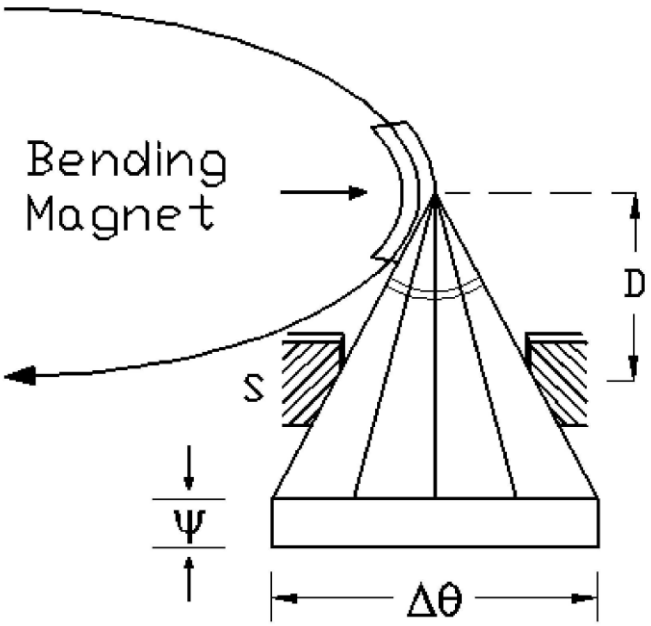

Fig 2.1—5 Synchrotron radiation emitted by a relativistic electron tavelling along a curved trajectory. The magnetic field is perpendicular to the electron orbit plane, ψ is the natural opening angle in the vertical plane while $\Delta\theta$ is the horizontal angular distribution, much bigger than ψ.

This imply that all the radiation emitted along an orbital arc, $\Delta\theta$, is summed incoherently. For this reason the natural narrow collimation, ψ, is preserved only in the vertical direction, the direction perpendicular to the plane of the orbit as also shown in Fig 2.1—5. Nevertheless using special insertion devices the collimation can be kept in both directions.
The spectral distribution of synchrotron radiation is shown in Fig 2.1—6: it has a very specific shape, it is continuous and it extends from the x-ray to the infrared region.
The physical origin can be understood considering to have a single electron in the storage ring and to record the emitted radiation using a point detector which looks tangentially at a specific point of the orbit (see Fig 2.1—7). The detector will receive a short pulse of radiation every time the electron

passes through that point of the orbit, i.e. at a frequency equal to the frequency of the period of motion $\omega = v/2\pi R$.

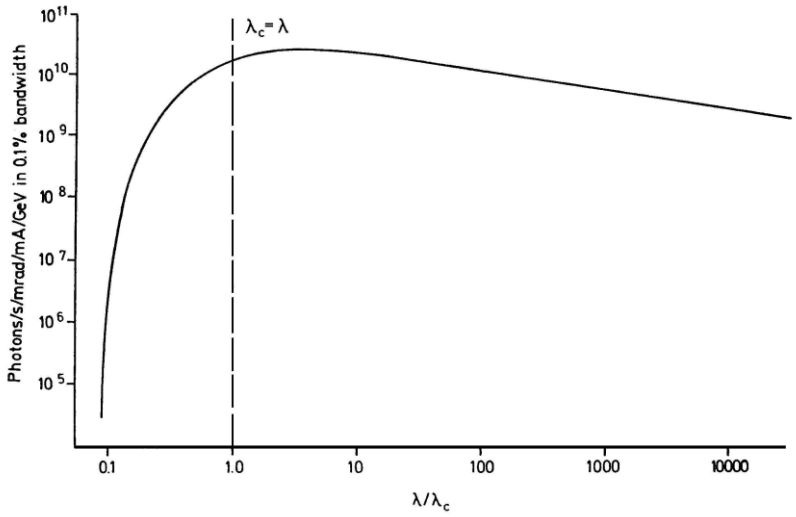

Fig 2.1—6 Universal curve function of the spectral distribution of synchrotron radiation.

In the frequency domain the spectral distribution will be composed of the fundamental frequency and of its harmonics. At high frequency a cutoff will be present because the detector will receive the radiation emitted by the electron along the arc $2/\gamma$ (Fig 2.1—7). This originates a pulse of non zero duration, τ, given by the difference between the time for the electron to travel along the arc and the time for the light to travel along the chord subtended by this arc (see Fig 2.1—7):

$$\tau = \frac{R}{c}\left[\frac{1}{\gamma\beta} - 2sin\left(\frac{1}{2\gamma}\right)\right] \cong \frac{R}{c\gamma^3} \tag{2.1-9}$$

A light pulse of this duration has frequency components up to about:

$$\omega_{cutoff} \approx \tau^{-1} = c\gamma^3/R \tag{2.1-10}$$

which correspond to cutoff wavelengths of $\lambda_{cutoff} = 2\pi R/\gamma^3$. Therefore, in principle, synchrotron radiation from one electron consists of a discrete spectrum of closely spaced lines up to $\omega_{cutoff.}$

In practice, the spectral distribution coming from many electrons is continuous due to the statistical oscillations of the electrons around the main orbit, to the fluctuations in their kinetic energy and to the statistical nature of the emission itself, all effects that lead to a line broadening of each harmonic. This results in the continuous broad spectrum of fig. 6, with the cutoff at $\lambda<\lambda_c$, which depends on the size of the ring (R) and the energy of the electron beam.

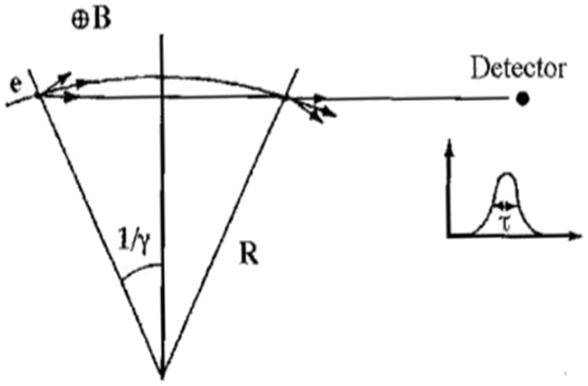

Fig 2.1—7 Graphical view of the origin of the duration of the light pulse emitted by a bending magnet (the figure was redrawn.

In the storage ring the radiation emitted by a bending magnet is mostly linearly polarized. When observed on the horizontal plane, the electric field is parallel to the plane of the electron orbit (horizontal). Above and below this plane, at finite vertical angles, a polarization component perpendicular to the orbit plane is present. The two terms reported, in square brackets, in eq.(2.1-5), describe the two components of the polarization [51]. The term, $K^2_{2/3}$, describes the one with the electric field parallel to the orbital plane while the term, $K^2_{1/3}$, the one with the electric field perpendicular to the orbital plane, i.e.

$$I_{\parallel}(\lambda,\psi) \approx [1+(\gamma\psi)^2]^2 K^2_{2/3}(\xi) \tag{2.1-11}$$

$$I_{\perp}(\lambda,\psi) \approx (\gamma\psi)^2[1+(\gamma\psi)^2]^2 K_{1/3}^2(\xi)$$

(2.1-12)

In Fig 2.1—8 the behavior of these two components as a function of $\gamma\psi$, is shown: it is clearly visible that the vertical opening angle, $\Delta\psi$, is approximately given by γ^{-1} ($\gamma\psi = 1$) when $\lambda \approx \lambda_c$. For $\lambda < \lambda_c$ the radiation is more collimated, while for $\lambda > \lambda_c$ it becomes wider.

The overall polarization is elliptic because the horizontal and vertical components are out of phase by a factor $\pi/2$. Therefore it is useful to define the degree of linear polarization, P_{Linear}, as [2]:

$$P_{Linear} = \frac{I_{\parallel} - I_{\perp}}{I_{\parallel} + I_{\perp}}$$

(2.1-13)

that gives:

$$P_{Linear}\,(\lambda,\psi) = \frac{K_{2/3}^2(\xi) - \left[(\gamma\psi)^2/(1+(\gamma\psi)^2)K_{1/3}^2(\xi)\right]}{K_{2/3}^2(\xi) + \left[(\gamma\psi)^2/(1+(\gamma\psi)^2)K_{1/3}^2(\xi)\right]}$$

(2.1-14)

In the orbital plane, ($\psi=0$), P is equal to 1, i.e. the light is 100% linearly polarized. When the observation is off axis the linear polarization decreases as a function of $\gamma\psi$.

Above and below the plane there is a constant phase difference of $+\pi/2$ and $-\pi/2$ between the parallel and perpendicular components of the electric field.

Therefore the radiation is respectively elliptically right and left polarized.

The degree of circular polarization, P_c, defined as:

$$P_C = \frac{I_R - I_L}{I_R + I_L} = \frac{\pm 2\sqrt{(I_{\parallel} I_{\perp})}}{I_{\parallel} + I_{\perp}}$$

(2.1-15)

Where I_R and I_L are the intensities of the right and left polarized light and the sign, ±, corresponds to positive or negative values of ψ, and compared with the degree of linear polarization.

A quantity very useful for experiments which does not use focusing optics, is the *brightness* or photon flux per solid angle.

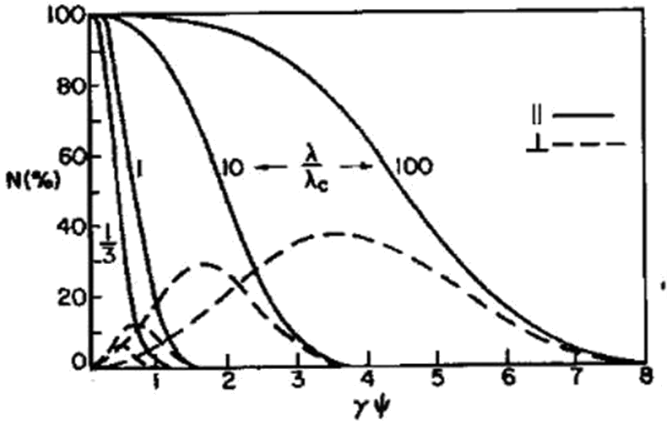

Fig 2.1—8 Intensity of the parallel and perpendicular components of the photon flux as a function of γψ. The curves are reported for λ/λc=1/3, 1, 10 and 100 and are normalized to the intensity at ψ=0.

From the brightness, the photon flux impinging on a sample may be easily evaluated using simple geometrical considerations.

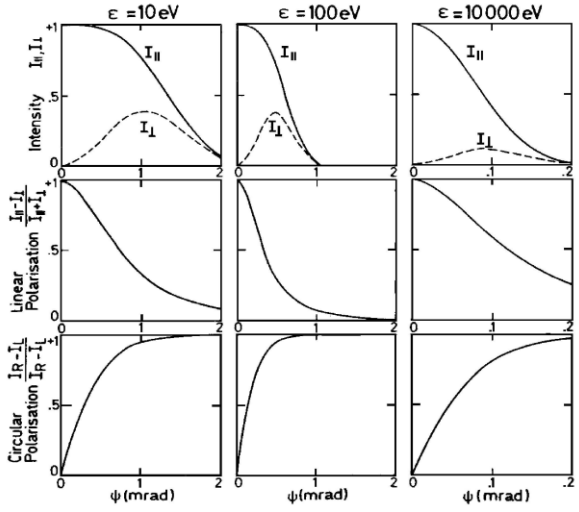

Fig 2.1—9 Intensity distribution of the parallel and perpendicular components of the radiation as a function of ψ at three different photon energies, for a storage ring with E = 3.5 GeV, R = 12.12 m; the critical energy is 7.8 keV and 1/γ is 0.146. The behavior of the linear and circular degrees of polarization are also shown.

Brightness or brilliance is defined as the number of photons per second passing through a given cross section area and within a given narrow solid

angle and spectral bandwidth. A high brightness means thus high intensity combined with tight focusing and spectral purity.
When focusing optics are used, the relevant quantity is the photon intensity that can be focused into a specific area; for this reason the brilliance of the source must be calculated.
As well known due to the Liouville's theorem, focusing preserves the brilliance, i.e. the brilliance of the source is equal to the brilliance of the beam when focused on the sample. The brilliance is determined by the size of the source, that in this case is given by the electron beam and by the angular spread of the radiation, obtained by the convolution of the angular distribution of synchrotron radiation, $\Delta\psi$ with the angular divergence of the electron beam. Therefore the quality of the electron beam source is essential in order to determine the brilliance of the photon beam. In a storage ring the product of the electron beam dimension and of the electron beam divergence is constant along the ring and is called the *emittance* of the ring. There is a horizontal and vertical emittance of the ring. In order to get high brilliance, small emittance machines must be used.
Brilliance is the main figure of merit of synchrotron radiation source. The huge increase in the value of the brilliance achieved during the last 10 years (see Fig 2.1—2) was obtained by designing low emittance machines minimizing the size beam and divergence.
In a storage ring the electrons must be kept at constant energy. Therefore the energy they loose emitting synchrotron radiation must be restored by the same amount. This action is performed by the radio frequency cavities (RF).
The stability condition to perform this actin is effectively more strict, and only 5% - 10% of the RF period is effective in restoring the electron energy. All the electrons, passing through the RF, not in phase with this 5%-10% effective time, do not follow the ideal circular orbit of the ring and therefore are lost. As a consequence the electrons in the storage ring are grouped in bunches with a time length that are typically 5% - 10% of the RF period.
Along the storage ring more bunches can be distributed. The time interval between them is an integer multiple of the RF period (called harmonic number of the ring).
The insertion devices (ID) are periodic magnetic structures installed in the

straight sections of a storage ring. Passing through such structures, electrons are accelerated and therefore emit synchrotron radiation at each bending of their trajectory. The primary role of the ID is to increase the spectral brilliance with respect to that achievable with bending magnets. The insertion devices are of two kinds, wigglers and undulators. Inside both these devices the electron beam periodically deflected but outside no deflection or displacement of the electron beam occurs (Fig 2.1—10).

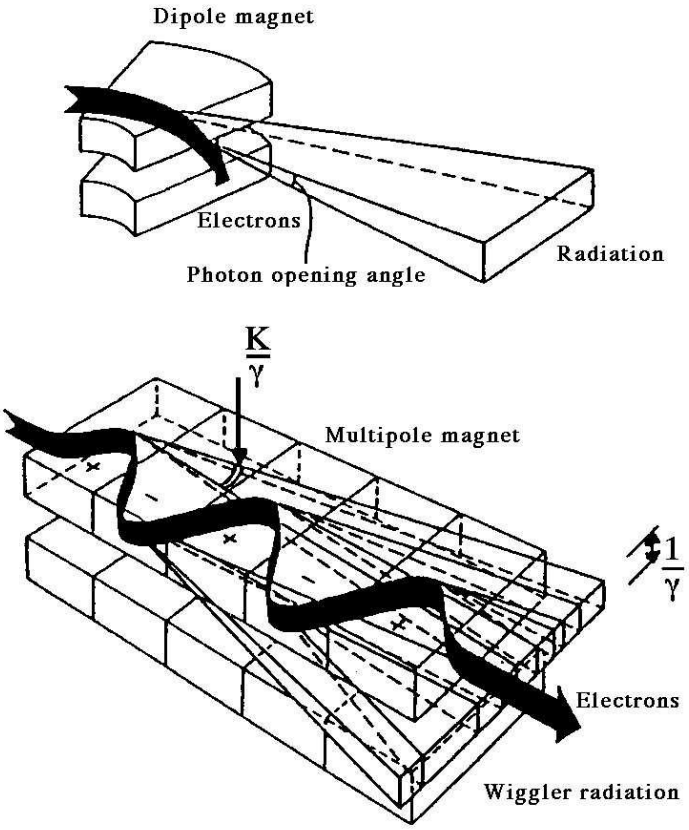

Fig 2.1—10 Schematic view of the radiation beams from a bending magnet and from a multipole magnetic structure

A wiggler is a multipole magnet made up of a periodic series of magnets (N periods of length λ_u, the overall length being $L = N\lambda_u$), whose magnetic field forces the electrons to wiggle around the straight path. The alternating magnetic field is normally applied in the vertical direction so the sinusoidal trajectory of the electron beam lies in the horizontal plane. The electrons follow in this way curved trajectories with a smaller local radius of curvature with respect to the one of the dipole-bending magnet, because the

magnetic fields is higher in a wiggler rather than in a bending magnet.
The radiation observed is the incoherent sum of the radiation emitted by each individual pole. Therefore the overall characteristics of the photon beam are the same as those of a bending magnet with the same magnetic field but with an intensity enhanced by the factor N, the number of poles.
To characterize the emission of an insertion device, it is useful to introduce the dimensionless parameter K. It is given by the ratio between the wiggling angle of the trajectory, α, and the natural angular aperture of synchrotron radiation, 1/γ, (Fig 2.1—11) i.e.

$$K = \alpha\gamma \tag{2.1-16}$$

In a wiggler the transverse oscillations of the electrons are very large and the angular deviations, α, (Fig 2.1—11) much wider than the natural opening angle $\psi=\gamma^{-1}$, therefore K>>1. In these large K devices, the interference effects between the emission from the different poles can be neglected and the overall intensity is obtained by summing the contribution of the individual poles.

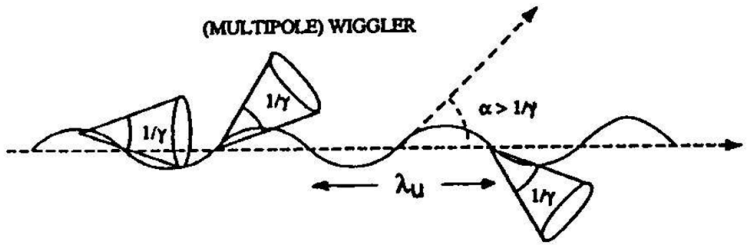

Fig 2.1—11 Schematic view of the 'wiggler' regime, where λu represents the period of the oscillations

An undulator is very similar to a wiggler, but its K value is less than 1, that means, that the wiggling angle α is smaller than, or close to, the photon natural emission angle γ^{-1} (Fig 2.1—12).

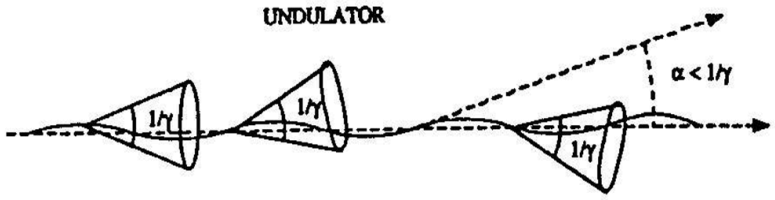

Fig 2.1—12 Schematic view of the 'undulator' regime

In this case interference occurs between the radition emitted by the same electron at different points along the trajectory. Considering the phase differences between the photons emitted at different points along the sinusoidal orbit, it is possible to show that observing the radiation in a direction forming an angle θ with the axis of the undulator, consecutive interferences occur for the wavelength:

$$\lambda = \frac{\lambda_u}{2\gamma^2}\left(1 + \frac{K^2}{2} + \gamma^2\theta^2\right)$$

(2.1-17)

In addition to this fundamental wavelength, also higher harmonics of shorter wavelength, $\lambda_n = \lambda/n$, are emitted. Their number and intensity increases with K; on the axis (θ=0) only odd harmonics are emitted.

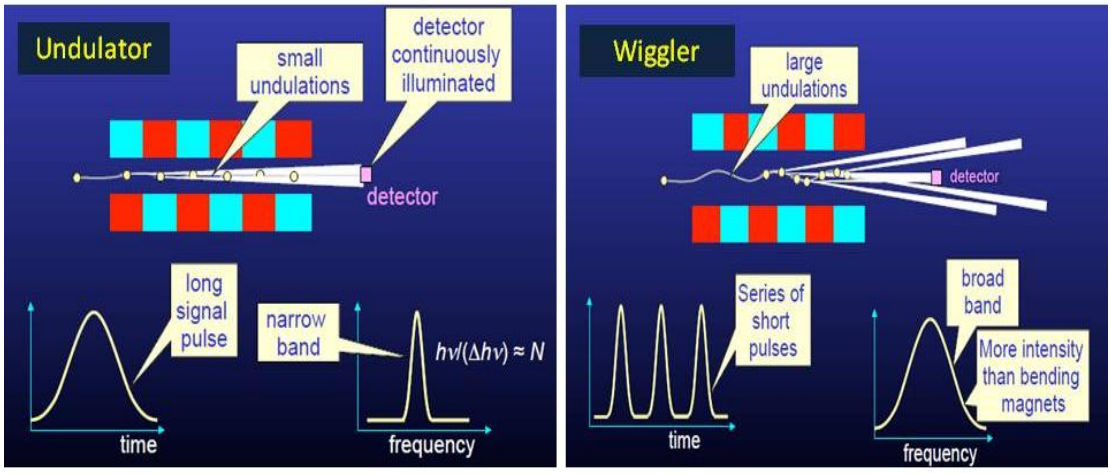

Fig 2.1—13 schematic view of the radiation emitted by an undulator and a wiggler.

In an undulator, the amplitudes of the fields radiated by each individual period of the undulator add up coherently, so the intensity increase with N^2 while it increases only as 2N in the wiggler.
Each harmonic has a limited wavelength bandwidth approximately given by:

$$\Delta\lambda/\lambda = 1/nN$$

(2.1-18)

Values of 10^{-2} can be easily achieved on the fundamental. Note that the bandwidth decrease with the number, *N*, of periods of the undulator and with the harmonic number, *n*.
The angular distribution, of the n-th harmonic is concentrated in a narrow cone in both the horizontal and vertical directions so it is always lower than the natural emission cone, $1/\gamma$ of a bending magnet and decreases as the square root of the number of poles and of the harmonic number.
This very narrow angular distribution together with the N^2 dependence of the intensity radiated in the 'undulator' regime explain why the spectral brilliance achievable with undulators exceeds by several order of magnitude that of bending magnets and wigglers (Fig 2.1—13). This is the main effect that has made it possible to achieve the incredible brilliance of the third generation synchrotron radiation facilities. The development of insertion devices to produce circularly polarized radiation is one of the major improvements in the third generation sources of synchrotron radiation. A source of circularly polarized radiation in the vacuum ultraviolet and soft x-ray regions allows a wide range of experiments, since both the absorption and the photoemission spectra can depend on the polarization state of light. This is obviously true for the magnetic materials and it happens also for nonmagnetic and nonchiral ones. Some of the possible experiments that can be done with circularly polarized radiation are: magnetic and natural dichroism, magnetic extended x-ray absorption fine structure, spin-resolved photoemission, two-photon absorption experiments, and vacuum ultraviolet (VUV) ellipsometry [52].

2.2 Synchrotron Beamline

The beamline refers to the path and instrumentation leading from the storage ring to the experimental endstation, which uses the radiation produced by the bending magnets and insertion devices in the storage ring of a synchrotron radiation facility. The differences between beamlines depend on the type of insertion device which, in turn, determines the intensity and spectral distribution of the radiation, the beam conditioning equipment and the experimental end station. Some of the beamline elements are located in radiation shielding enclosures, called hutches, or behind radiation shield wall.

Elements that are used in VUV to soft X-ray gas phase beamlines for conditioning the radiation beam between the storage ring and the end station include the following:

- windows: thin sheets of metal, often beryllium, which transmit almost all of the beam, but protect the vacuum within the storage ring from contamination
- slits: which control the physical width of the photon beam and its angular spread
- focusing mirrors: one or more mirrors, which may be flat, bent-flat, or toroidal, which help to collimate (focus) the beam
- monochromators: devices based on diffraction that select particular wavelength bands
- diagnostic tools: for measuring the photon beam properties, like intensity, shape and position.

The combination of beam conditioning devices controls the thermal load (heating caused by the beam) at the end station; the spectrum of radiation incident at the end station; and the focus or collimation of the beam. Devices along the beamline which absorb significant power from the beam may need to be actively cooled by water, or liquid nitrogen. The entire length of a beamline is normally kept under ultra high vacuum conditions.
Currently 26 beamlines utilize the radiation generated by the Elettra source. Beamtime usually refers to the period of time spent in carrying out the experiment at the synchrotron. In general the access to the facility to perform an experiment is subject to approval of the experimental plan by an international panel of experts. For successful experimental applications the beamtime generally covers a period of one week or so depending on the experiment. For this reason an organization among the users, in day and night shifts is often required. In the following the characteristics of the two beamlines involved in the experiments, presented in this thesis, are described.

2.2.1 Circular Polarized beamline

The experiments involving the fragmentation of halogenated pyrimidine molecules and the measurement of the appearance energies of the

respective generated fragments were carried out at the Circular Polarized (CiPo) beamline of the ELETTRA synchrotron radiation source in Trieste [52]. This beamline is primarely characterized by its capability of providing a synchrotron radiation beam of variable polarization (circular to linear) in a very broad range of photon energies, 8 to 900 eV. The photon beam is produced by an Electromagnetic Elliptical Wiggler (EEW) and is dispersed by means of two collinear monochromators, a Normal Incidence Monochromator (NIM) and a Spherical Grating Monochromator (SGM), that alternatively provide two beams in the UV-VUV (5 - 40 eV) and soft X-rays (40 - 900 eV) respectively. The availability of such a wide photon energy spectrum, together with the polarization selection makes the CiPo beamline extremely flexible for the experimental activity. In this work the characteristic of adjustable polarizability has not been exploited using a linear polarised photon beam. A schematic layout of the beamline is shown in Fig 2.2—1.

The first mirror of the beamline (M_0) is a flat mirror with 2.5º grazing incidence, which diverts vertically the radiation. This mirror protects the following optical elements from the hard portion of the radiation spectrum. The second mirror M_1, has a toroidal shape and returns the radiation parallel to the orbit plane with 2.5º grazing incidence.

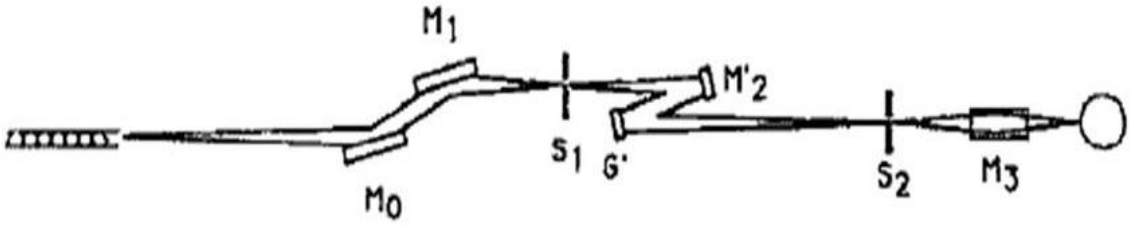

Fig 2.2—1 Schematic of the CiPo beamline (vertical view): flat (M_0), toroidal (M_1, M_3) and cylindrical ($\boldsymbol{M_2'}$) mirror, grating monochromator (G´), the entrance slit (S_1) and exit slit (S_2).

It has been designed to focalize the radiation onto the entrance slit along the tangential direction (magnification= l/3) and onto the exit slit along the sagittal one (magnification=2/3).

After the entrance slit (S_1) the radiation is deflected vertically and made backstigmatic by means of a normal incidence convex cylindrical mirror (M_2') whose coating could be either Au or Al+MgF_2. The radiation is then

diffracted and focalized onto the exit slit by a spherical grating, G´, working at normal incidence with a constant 2º included angle. The radiation, passing through the exit slit (S_2), is then refocused onto the sample by means of the toroidal mirror M_3, with a magnification equal to one. The mirror M_3 diverts the radiation of 5º in the horizontal plane.

A broad photon energy range (8-1200 eV) was chosen for the beamline. Two independent monochromators, one working at normal incidence, from 8 to 35 eV, and the other at grazing incidence, from 30 to 1200 eV, have been designed to cover efficiently the entire spectral range.

In the present VUV fragmentation measurements the radiation of the electromagnetic elliptical undulator was monochromatized by an alluminum normal incidence monochromator that covers the photon energy range 8-17 eV (resolving power, E/ΔE, of about 1000). The entire beamline is kept under UHV conditions to guarantee the purity of the optical elements and to match the UHV in the storage ring. A safety system of computer controllers and fast valves guarantee preservation of the vacuum between the different sections of the beamline and with respect to the storage ring. At the end of the beamline, a 'custom' set-up, which depends on the experiment to be performed can be connect. A precise aligning procedure, which guarantees the energy selected photon beam reaching the internal region of the set-up, is essential for the success of the experiment.

In this experiments the end-station consists of a five-element electrostatic lens which focuses and accelerates the charged ionic species from the region of interaction to the quadrupole mass spectrometer (QMS). This is a commercial QMS (10-4000 u, Extrel 150-QC 0.88 MHz) with a mass resolution M/ΔM of about 500. It is mounted perpendicular to the photon beam and to the gas source, which is an effusive beam located at 5 cm from the entrance of the QMS and about 2 mm below the photon beam. The typical flight time of the charged systems is in the order of 5 to 100 μs depending on the fragment. An overview of the experimental set-up is reported in Fig 2.2—2.

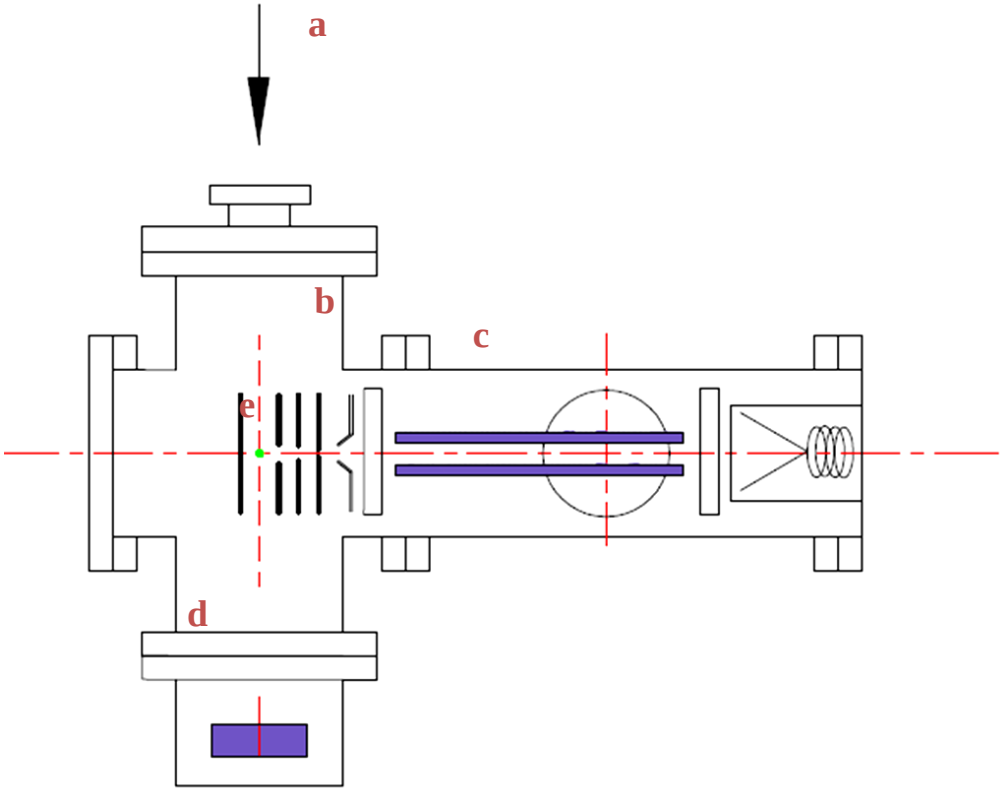

Fig 2.2—2 Schematic of the experimental apparatus: (a) direction of propagation of the photon beam, (b) electrostatic lens and (c) quadrupole mass spectrometer (QMS), (d) photodiode. The effusive gas beam is perpendicular to the plane of the drawing and crosses the synchrotron beam at (e).

The quadrupole mass analyzer is one type of mass analyzer used in mass spectrometry. It consists of four cylindrical rods, set parallel to each other where adjacent rods have opposite voltage polarity applied to them. The voltage applied to each rod is the summation of a constant DC voltage (U) and a varying radio frequency ($V_{RF}cos(wt)$), where w is the angular frequency of the radio frequency field (RF). The electric force causes the ions to oscillate/orbit in the area between the 4 rods. For each given voltage/RF setting, only ions of a certain mass-to-charge ratio will be maintained on orbit of a constant radio and will be able to reach the detector. Other ions have unstable trajectories and will collide with the rods. This permits selection of an ion with a particular m/z or allows the operator to scan for a range of m/z-values by continuously varying the applied voltage.

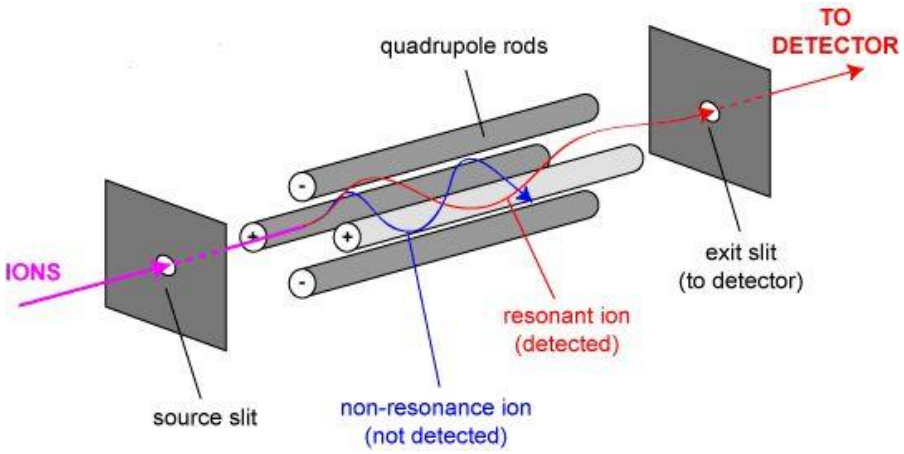

Fig 2.2—3 Schematic of a four rods quadrupole mass spectrometer. These rods generate an electric field by applying a direct current field to two rods and a radio frequency (RF) field to the other two rods.

2.2.2 Experimental procedures at the CiPo beamline

The pyrimidine molecule is liquid and its halosubstituted compounds are powders at standard ambient temperature (298K) and pressure, with vapor pressures varying between 0.04 and 22 mbar [53]. In the present set-up the powder of the target under investigation was maintained in a test tube outside the vacuum chamber, and admitted into the interaction region through a gas line producing an effusive beam, with a residual gas pressure in the experimental chamber in the order of few 10^{-6} mbar (base pressure $5x10^{-7}$ mbar), sufficient to perform the experiments.
For each target molecule the experiments consist of the acquisition of the mass spectra at fixed photon energy and the measurement of the photoionization efficiency curves (PECs) of the selected ions.
The mass spectrum of each target has been measured at 14 eV, providing an overview of the most relevant fragments at this photon energy as it will be shown in chapter 4. The data reported were not corrected for the transmission of the QMS, preventing a reliable measure of the absolute branching ratio of the different fragments. However, according to the nominal transmission of the instrument and by comparing the mass spectrum of the pyrimidine molecule measured at 17 eV with the spectra reported in the literature [25, 26] we inferred that the transmission of the spectrometer should not introduce major distortions in the range of masses

above 40 u. In the second part of the experiment, the experimental appearance energy (AE) values have been obtained by measuring the PECs of the parent ion and of selected fragments as a function of the photon energy (9-15 eV) with an energy step of 20 meV and an acquisition time of about 3 to 10 sec/point, depending on the intensity of the measured mass peak. The PECs were normalized to the photon intensity, which was measured simultaneously by a photodiode located at the end of the beamline. The photon energy was calibrated against the autoionization features observed in the Ar total photoionization efficiency spectra between the 3p spin orbit components. In the photon energy scans up to 11.7 eV, a Lithium Fluoride filter has been used to remove the second order radiation. Above this energy the contribution of the second order radiation has been evaluated by comparing the Ar^+ ion yield measured as function of the photon energy to its ionization cross section [54]. This second order contribution has been taken into account in the extraction of the PECs. All the PECs, presented in chapter 4, are shown on a linear scale. However, the experimental AE values are determined from their semilog plots by fitting straight lines to the background and to the ion signal in the threshold region. The photon energy at the intersection of these two lines is the measured AE value at 298K ($AE_T(exp)$) which is the temperature of the experiment [55]. The uncertainty is estimated to be on the order of 0.05-0.10 eV and depends on the sharpness of the photoionization efficiency curve. Even though the use of the semilog rather than the linear scale has the advantage of increasing the sensitivity of the data analysis procedure [56], it is important to remember that the measured values of AE also depend on the sensitivity of the experimental set-up (time of acquisition, number of counts, statistics, efficiency and sensitivity of the instrumental set-up), so that the measured AE have to be considered as the upper limits of the effective AE.

2.2.3 Gas Phase Beamline

The experiments involving the NEXAFS and XPS characterization of five different halogenated uracil molecules have been performed at the Gas Phase beamline of the Elettra synchrotron radiation source in Trieste [57]. A schematic layout of the beamline is shown in Fig 2.2—4.

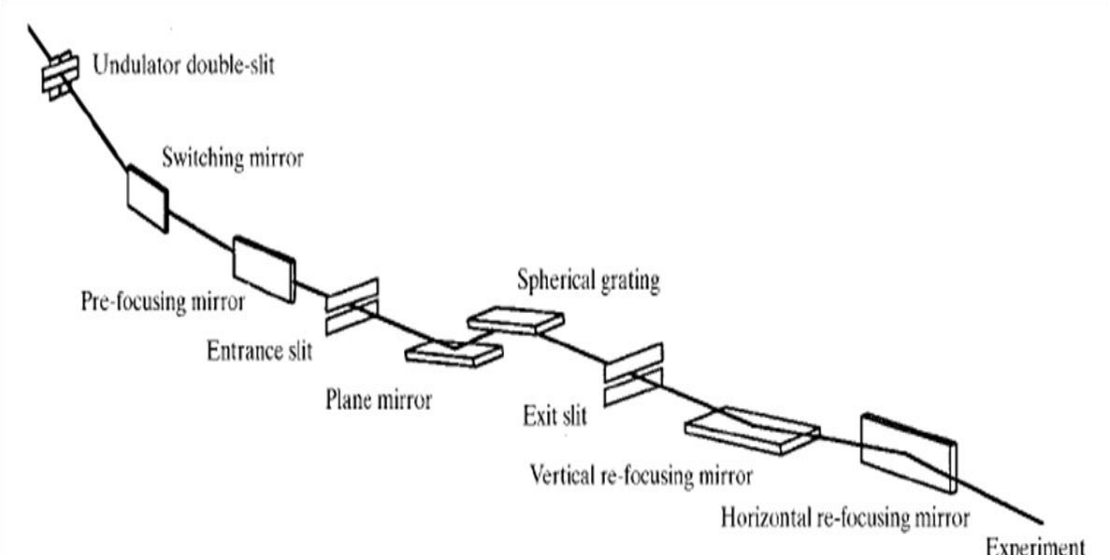

Fig 2.2—4 Schematic diagram of the optical layout of the gas-phase beamline

The Gas Phase Beamline is a high resolution/high photon flux beamline, comprised of an undulator source, a spherical grating monochromator equipped of a movable planar prefocusing-mirror and two refocusing mirrors, and a set of entrance and exit slits and baffles to define the beam shape. A differential pumping stage allows to decrease the local pressure from the end station, usually dedicated to gas phase studies, to the optics of the beamline and then the storage ring.

The undulator light source is of period 12.5 cm, 4.5 m long. The 100% linearly polarized radiation from the undulator is deflected to the variable-angle spherical grating monochromator by a prefocusing mirror. The monochromator, placed between entrance and exit slits for photon beam resolution, consists of two optical elements: a plane mirror and a spherical grating. Five interchangeable gratings cover the energy region 13-1000 eV, with a typical resolving power of about 10000. Two refocusing mirrors after the exit slit provide a roughly circular focus (radius about 300 μm) at the interaction region in the experimental chamber.

The XPS spectra were measured using a commercial 6-channel, 150 mm hemispherical electron energy VG analyzer [58].

The analyzer uses a multi-element electrostatic lens with well-defined electron optical properties. The lens is crucial for the transmission and the focusing of electrons from the interaction region to the entrance slit of the

hemispherical deflector analyzer, (HDA), which determines the energy resolution of the electron spectrometer. The resolving power, *RP*, of a hemispherical analyzer is approximated by:

$$RP = \frac{E_P}{\Delta E} \cong \frac{2R}{s} \tag{2.2-1}$$

where R is the analyzer mean radius, s the slit width, E_P the pass energy, and ΔE the energy resolution of the spectrometer. As can b seen from the equation, a larger radius gives a higher resolving power.

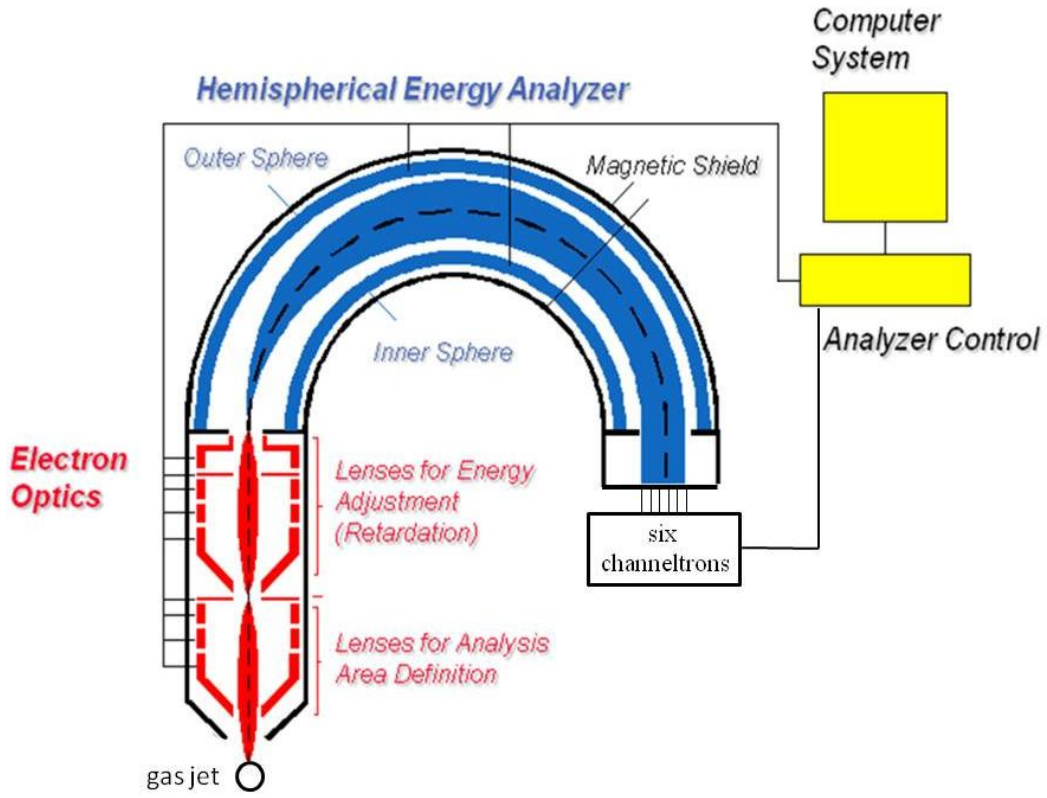

Fig 2.2—5 Schematic of a commercial hemispherical energy analyzer

For example, the HDA analyzer, used in the present experiments has a mean radius of 165 mm. A larger radius means of the analyzer provides a also higher transmission at the same energy resolution. As a rule of thumb, the transmission efficiency is linear with the radius at a given energy resolution.

The energy resolution and peak intensity are modified by varying the analyzer entrance slit size and shape, and the pass energy. The pass energy (10 eV in these experiments) is the kinetic energy of the electrons that are

able to pass through the analyzer. It is determined by the electrostatic field between the inner and outer spheres. The presence of six channeltrons at the exit of the analyzer in this set-up makes it possible the collection of all the electrons having a kinetic energy greater or less than that for which it is set the pass energy. Each channeltron is an electron multiplier which consists of a cone and a spiral-tube structure that multiplies incident charges, in this case electrons. In a process called secondary emission, a single electron can, when bombarded on secondary emissive material, induce emission of many more electrons. The application of about 2 to 3 keV electric potential between the core and the other end of the spiral accelerates the emitted electrons through the spiral inducing further secondary emission of more electrons. This can be repeated a number of times, resulting in a large shower of electrons all having been triggered by just one. The output signal from the channeltron is amplified passing through a pre-amplifier (PA), which increases the signal to noise ratio before coming to a constant fraction discriminator (CFD). The discriminated output signals of the six channeltrons are acquired by counters which are computer controlled: A LabView software controls the photon beam energy as well as the analyser settings and reports the channeltrons counting as function of the electron kinetic energy, which allows for a complete control over the experimental conditions and easy adjustments of the set-up.

The axis of the electron analyzer is set at the "magic angle" in the parallel plane, i.e. in the plane defined by the electric vector of the light and the photon propagation direction, at an angle of 54.7° with respect to the electric vector of the light. In this geometry the measurements are insensitive to the variation of the photoelectron asymmetry parameter, β.

To understand the importance of the β parameter, let's consider that within the dipole approximation, i.e. when the wavelength of the light is much larger than the dimension of the atoms (and therefore the electric field does not change within the atom), the photoelectron angular distribution can be expressed by the equation:

$$I(\theta) = \frac{\sigma}{4\pi}\left[1 + \frac{\beta}{2}(3Pcos^2\theta - 1)\right] \tag{2.2-1}$$

where θ is the angle between the polarization axis of the radiation and the direction of emission of photoelectron, σ is the total cross section integrated over all angles and β is called 'anisotropy parameter'. The angular distribution of a 1s photoelectron should be described by a pure p-wave and a parameter $\beta = 2$, Fig 2.2—6 orange curve. In this case, the electrons are emitted preferentially along the polarization vector, $\hat{\varepsilon}$. If $\beta = 0$, the angular distribution is completely isotropic. At the other extreme, if $\beta = -1$, the maximum of the distribution is perpendicular to the polarization vector. For $3Pcos^2\theta = 1$, i.e. $\theta = 54.7°$, the β dependency of the measured angular distribution is cancelled and only the proportionality to the total cross section, σ, remains.

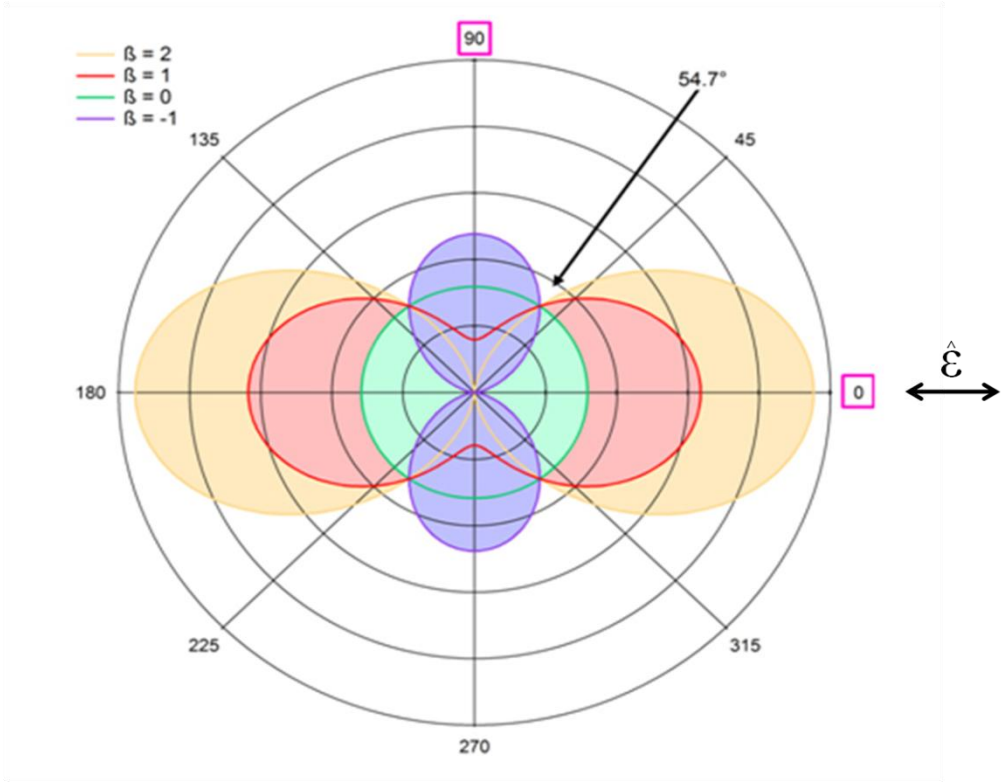

Fig 2.2—6 Polar representation of the differential cross section of the photoelectrons with four different values of β. The angle θ is the polar angle between the polarization vector of the light and the velocity vector of the electron (axis of the electron detector.) The arrow points in the direction of the magic angle, that for fully polarized light is at 54.7°, in which the measured cross section is just proportional to the total cross section σ, regardless of the specific β-value.

In the experimental staion, opposite to the electron analyser, a channeltron multiplier was placed at the same “magic angle,” 54.7° with respect to the photon beam polarization axis, in order to detect the ions produced by the decay of the core excited molecular states, measuring the near-edge-x-ray fine-absorption (NEXAFS) spectra.

The spectra at the carbon, nitrogen and oxygen K edges were normalized to the photon flux measured by a photodiode. The energy scale of the NEXAFS and XPS spectra were calibrated by taking simultaneous spectra of the sample and a calibrant gas introduced into the experimental chamber. The base pressure in the chamber is about $4 \cdot 10^{-8}$ mbar.

The GasPhase beamline was used to study the halogenated uracil molecules that need to be evaporated to be studied as isolated molecules in the gas phase (temperature about 170°C, it is below their thermal decomposition temperature).

In this experimental set-up the powder of the target molecule is heated in a stainless steel cylindrical crucible with a collimated nose 30 mm long (the internal diameter is 1 mm and the external diameter is 3 mm thick). The crucible is heated using a thermocoax, twin-core cable [59], rolled more closely at the top. In this way the distance between the coils is smaller in the upper part of the crucible in order to obtain a higher temperature and a gradient between the top and the bottom of the oven. This is crucial in order to avoid the blocking of the nose during the sublimation of the sample. The entrance of the crucible in the area of interaction is made possible without breaking the high vacuum condition thanks to a fast-entry setting. In this set-up, the crucible is screwed onto a metal rod and through a series of pre-vacuum pumping is possible to: introduce the rod fitted with the crucible in the interaction zone, insert the crucible in the oven (equipped with the rolled thermocoaxial wire), remove the rod and pull it out leaving the crucible in the chamber. In order to avoid that the evaporated molecules contaminate the set-up, stiking on the wall of the chamber and on the analyzer themselves, a cold trap, made of a copper cylinder surrounding the interaction region and cooled down via the thermal connection to a reservoir of liquid nitrogen, was used to condense the vapour beam..

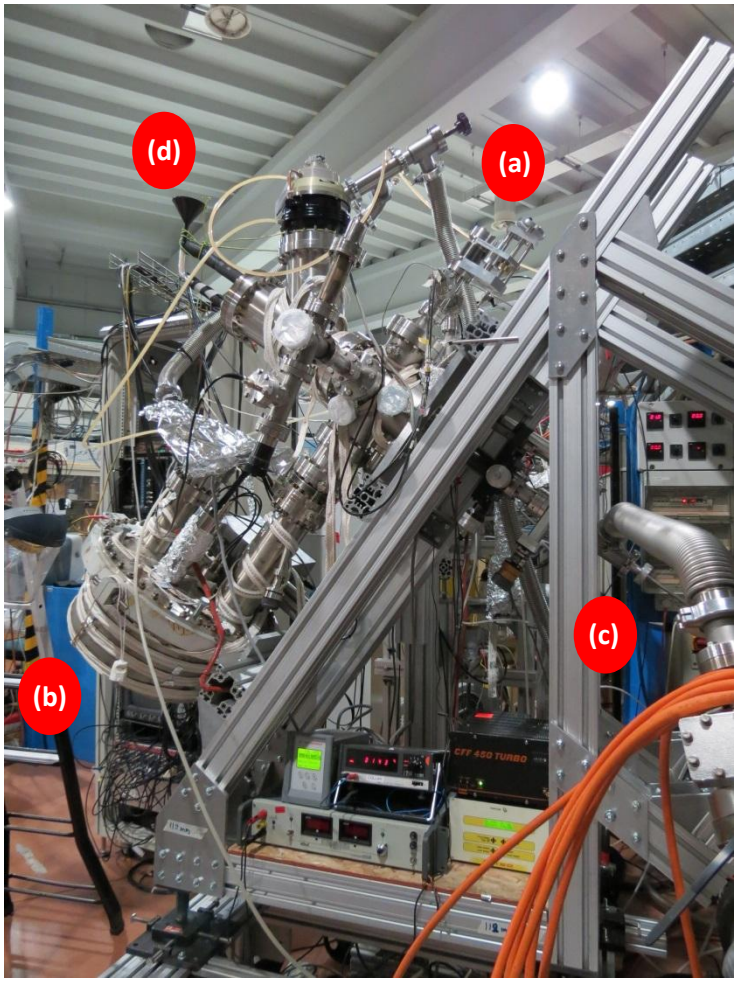

Fig 2.2—7 A picture of the experimental endstation located at the GasPhase beamline of the Elettra synchrotron radiation source in Trieste, (a) a channeltron multiplier to collect the NEXAFS spectra, (b) commercial 6 channel, hemispherical electron energy (VG) analyzer to collect the XPS spectra, (c) entrance of the crucible through the fast-entry setting and (d) the liquid nitrogen trap.

2.2.4 Near edge x-ray absorption fine structure spectroscopy

In the ultraviolet and X-ray range, the interaction between radiation and matter mainly consists of two processes, absorption and scattering. The experimental work will be focused only on the absorption process. Absorption allows the study of the distribution of the energy levels of a sample, providing a picture mainly on its electronic properties. After the absorption of an X-ray photon, an isolated atom can be either *excited*, if the

photon energy corresponds to the energy difference between an electronic core level and an unoccupied level, or *ionized*, if the photon energy is larger than the binding energy, so that the electron (photoelectron) is ejected from the atom. The NEXAFS spectroscopy relies on the absorption of a photon that leads the system under study into an excited state; after the excitation the system undergoes decay processes with emission of a fluorescence photon or one/more Auger electrons, when the excited state is above the ionization threshold. The fragmentation of the matter into ionized and neutral fragments is another effect that can follow the absorption. The absorption edges are originated when the photon energy becomes high enough to extract an electron from a deeper level. The highest-energy absorption edge, the K edge, corresponds to the extraction of an electron from the deepest level (1s level, see Table 2.2-1).

Edge:	...	M_1	L_3	L_2	L_1	K
Core level:	...	3s	$2p_{3/2}$	$2p_{1/2}$	2s	1s

Table 2.2-1 The relation between high energy edges and core electronic levels.

The edge energy depends on the binding energy of the corresponding core level. Since the binding energies grow monotonically with the atomic number, each edge energy corresponds to a well defined atomic species.
In correspondence of an edge, the absorption coefficient exhibits the *X-ray Absorption Fine Structure (XAFS)* [60, 61]. For isolated atoms (noble gases, metallic vapors) the XAFS is limited to a few eV around the edge, and reflects the transitions of the core electron to Rydberg levels: in molecular gases and condensed systems the XAFS, strongly influenced by the presence of the atoms surrounding the absorber one, can extend up to one thousand eV above the edge.
The XAFS spectrum is customarily divided into two regions.

a) The structure within 30-50 eV below the edge is called *NEXAFS* [62]. From NEXAFS, information can be obtained on the local electronic as well as geometric structure (in solid sample). Sometimes, the structure within a few eV around the edge is distinguished as *edge structure.*

b) The fine structure extending from the NEXAFS region up to typically one thousand eV is called (Extended X-ray Absorption Fine Structure). EXAFS carries information on the local geometric structure surrounding a given atomic species (in solid sample).

In this study, the NEXAFS spectroscopy, performed measuring the total ion-yield produced by the decay of the intermediate excited states, was used to study the core excited states of halogenated uracils. The photon energy scale was calibrated using a mixture of the molecule under study and a calibration gas with well known absorption peaks in the same energy range, i.e., the (C 1s→ π*) transition of CO_2 at 290.77 eV[63], the (N 1s→π*) of N_2 at 400.868 eV [64] and the (O 1s→π*) of CO_2 at 535.4 eV [65]. The energy resolution was approximately 60, 70 and 100 meV for the C, N and O 1s spectra, respectively. The uncertainty in the energy scale is estimated to be about 100 meV. The NEXAFS spectra have been obtained by scanning the photon energy over the range of interest, i.e., 283–320, 395–414 and 525-550 eV for the C, N and O spectra, respectively, and acquiring the ion signal through the channeltron. The spectra were then normalized to the simultaneously recorded photon beam intensity. In section 5 the NEXAFS spectra of four different halogenated uracil molecules will be analysed in order to understand the differences in the spectra of these molecules with respect to the unsubstitued one

2.2.5 X-ray photoemission spectroscopy

X-ray photoelectron spectroscopy (XPS) is a quantitative spectroscopic technique that measures the elemental composition, empirical formula, chemical state and electronic state of the elements that compose the sample. XPS spectra are obtained by irradiating the sample with a X-ray beam while simultaneously measuring the kinetic energy of the electrons that are released. If the photon energy (*hv*) is known and the emitted electrons kinetic energies (*KE*) are measured, the binding energy (*BE*) of each of the emitted electrons can be determined using the following equation:

$$\boldsymbol{BE = h\nu - KE} \tag{2.2-2}$$

A typical XPS spectrum reports the number of electrons detected versus their binding energy. Each element produces a specific set of XPS peaks at characteristic binding energy values that directly identify each element that exists in the sample.

An important property of the XPS spectroscopy is that the measured BE mainly depends on the type of atom, but it is also affected by the chemical environment surrounding the atom itself. So, for example, the C 1s BE of CO and CO_2 are 296.229 eV [66] and 297.69 eV [66] respectively, i.e. close but different enough to be distinguished. For this reason the XPS is accredited as a powerful analytical technique.

Similarly as for the calibration of the NEXAFS spectra it is advisable to perform the calibration using a mixture of two molecules, i.e. the molecule under investigation and the calibrant. This is due to the fact that the kinetic energy of the detected electrons is affected by the local field created in the interaction region by the positive and negative charges produced by the ionisation/fragmentation of the target molecules. This 'unquantified' kinetic energy shift can be considered as a sort of 'instrumental' effect, of the order of several hundreds of meV and is related to the composition of the target molecules, gas density, photon beam intensity, ionisation/dissociation cross sections of the target and any parameter that affects the probability of formation of positive/negative charges in the interaction region. Therefore, if the target molecule and the calibrant XPS spectra were measured in different time/experimental conditions it is likely that the calibration would be affected by a different kinetic energy shift, spoiling the kinetic energy calibration. If on the other hand the two XPS spectra were measured simultaneously, starting for a mixture of the two gases, this guarantees that the two photoelectrons are generated in the same local field and are therefore affected in the same way by this 'unknown' kinetic energy shift, which cancels out measuring the difference between the kinetic energy of the calibrant and of that of the target molecule to be calibrated.

In the present experiments the C(1s), N(1s) and O(1s) core level spectra were measured at about 100 eV above their respective ionization thresholds, using an energy resolution of the analyzer that varies between 100 and 200 meV, depending on the measured state and its natural width. The kinetic energy of about 100 eV in the photoelectron spectra guarantees that the Post Collision Interaction (PCI) effects [67] can be neglected in the

data analysis. Briefly, the PCI effect consists in the exchange of energy and momentum between the two (or more) free electrons in the continuum, i.e. the photoelectron and the Auger electrons. The result is an energy shift and line shape distorsion in both electrons. From a classical point of view, this can be explained as due to the different electric field experienced by the two escaping electrons when the Auger electron 'overtakes' the photoelectron. As a consequence, the photoelectron which was originally moving in the field generated by a singly charged ion suddenly finds itself in the field generated by a doubly charged ion, while the opposite happens for the Auger electron. As a consequence, the photoelectron will 'decelerate' while the Auger electron will 'accelerate'. As such they could lead to an erroneous evolution of the BE according to the formula (2.2-2). It is easy to predict that the faster the photoelectron the less interaction time there will be between the photoelectron and Auger electrons, so that PCI effects will be minimised and eventually disappear when the photoelectron is faster than the Auger electron. In the present work, the choice of 100 eV kinetic energy was dictated by a compromise among the requirements to have a photoelectron fast enough to make PCI negligible while remaining at sufficiently low photon energy in order to have more convenient experimental conditions, i.e. good photon flux for the Gas Phase beamline and good transmission of the electron spectrometer.

The energy spectra were calibrated using a mixture of the molecule under study and a calibration gas with well-known XPS peaks in the same binding energy range, that is, CH_4 (C1s) at 290.689 eV [66] in the case of 5FU and CO_2 (C1s, ν=0) at 297.69 eV [66] for all the other molecules, N_2 (N1s) at 409.9 eV [68], and CO_2 (O1s) at 541.254 eV [69] for C(1s), N(1s), and O(1s) respectively.

The XPS spectra of four different halogenated uracil molecules are presented and discussed in section 5 where they are also compared to the XPS spectrum of the unsubstitued uracil molecule.

2.3 The ion impact experiments at GANIL

The fragmentation experiments of 5Br-uracil isolated molecule, its clusters and hydrated clusters, obtained by ion-impact have been performed at the

ARIBE beamline of Ganil in Caen, Basse Normandie (France) [70].
The instrumentation used in these experiments is a crossed beam apparatus in which an ion beam of selected charged state intersects a neutral beam of gas phase isolated molecules, clusters or hydrated clusters. The molecules chosen are the 5Br-Uracil. The aggregates are created by a gas aggregation source [71] and the multiply charged ions are created by an Electron Cyclotron Resonance source. The charged fragments generated by the collision of the ion beam with the target are analysed using a time of flight (TOF) mass spectrometer. In this chapter the elements that constitute the instrument will be described in detail while in section 5 the different stages of data analysis will be discussed.

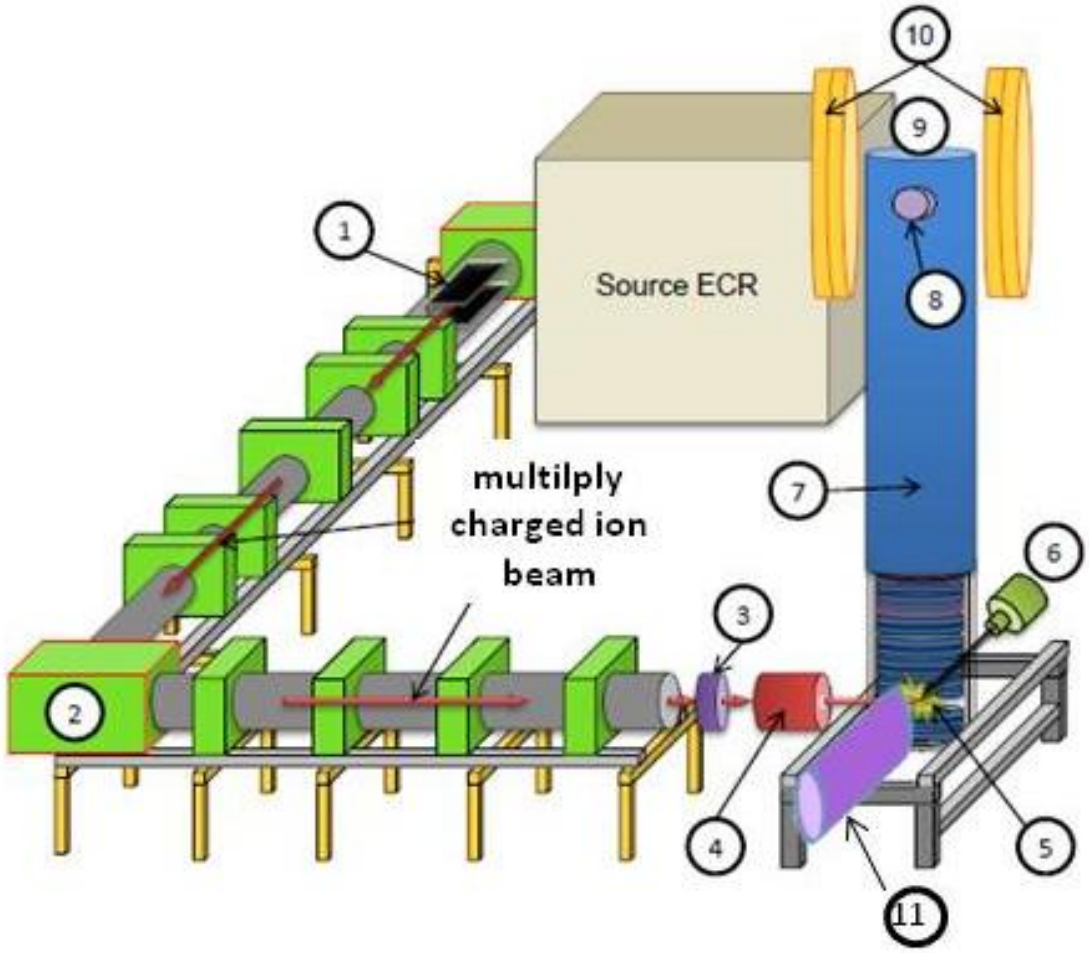

Fig 2.3—1 Schematic of the ARIBE beamline. 1) deflection plates, 2) diverter dipole, 3) diaphragm, 4) electrostatic lenses, 5) collision zone and extraction, 6) oven, 7) TOF spectrometer, 8) micro channel plates, 9) conversion plate, 10) Helmholtz coils and 11) aggregation source.

2.3.1 Principle of operation of an Electron Cyclotron Resonance source at ARIBE

The multiply charged ions are produced by an ECR source. They are extracted from a hot and dense plasma which is magnetically confined.
In this kind of source, suitable neutral atoms that will generate the plasma for the formation, extraction and acceleration of specific multiply charged ion, are introduced in gas phase into a vacuum chamber (10^{-7} mbar).
The interaction with an electromagnetic wave ionizes the gas atoms with the expulsion of energetic electrons. The fast electrons thus created can then ionize more neutral atoms or the weakly charged ions in the plasma. In this way the state of charge of the plasma is then increased with the formation of multiply charged ions and ionization of more electrons.
These electrons move in a charged B field, guided by the Lorentz force to rotate around the field lines. Their rotation frequency is called cyclotron frequency (ω_{cyc}). This containment of electron density facilitates the further ionization of the neutral/charged atoms.
The plasma naturally charged will be confined inside the source by the application of a magnetic field. Note that the production of multiply charged ions is obtained after several successive ionizations and only if the electrons are energetic enough. The magnetic field that ensures the confinement is inhomogeneous and results by the contribution of two permanent magnets and two solenoids which provide the confinement along the axis of extraction.
The radial component of the magnetic field is in turn induced by a hexapole.
In other words, the principle of this source is to apply a high frequency electromagnetic field in addition to a static magnetic field in a low pressure gas creating an ionized plasma. The electrons are then confined by the magnetic field and accelerated by electron cyclotron resonance. After many successive ionizations, multiply charged ions are produced in large quantities and extracted toward the beamline (a large distribution of charge states). At the exit of the source a magnetic dipole allows to select specific ions, at a well defined m/z ratio. The extracted and selected ions are then accelerated, focused and transported through the ARIBE beamline towards the experimental set-up.

The ions formed are then attracted by the first electrode then accelerated through the extraction system to the ARIBE beamline.
At the GANIL *(Grand Accélérateur National d'Ions Lourds)* facility there are 3 different beamlines, SME, IRRSUD and ARIBE whose ion beams differ in term of velocity: 10 au (SME), 1 au (IRRSUD) and 0.1 au (ARIBE). The experiments presented in this work where performed at ARIBE, which is the low energy beamline, and more precisely the characteristics of ARIBE are:

- energy of ions: 5 - 400 keV
- velocity of the ions: 0.1 - 0.7 au
- intensity at the exit of the source: 0.5 - 15 μA
- transmission (up to the set-up): 20 - 80 %
- intensity of the pulsed beam at the end of the set-up: 0.1 - 10 nA
- density of the ion bunch: 0.1 ions/mm3

More details about the ARIBE beamline are reported in the next section.

2.3.2 The ARIBE beamline

The ions generated by the ECR source are first extracted towards a magnetic diverter dipole. This locally creates a uniform magnetic field orthogonal to the beam path so that the ions, subjected to the Lorentz force, will proceed along the axis of the beamline. At this stage the beam can be deflected, by means of a set of deflectors, away from the axial path in order to create a pulsed ion beam of suitable time length and frequency. A series of dipoles and quadrupoles with defined apertures focus and transport the ion beam along the beamline. A large bending magnet directs the beam towards the designated experimental station, one among the three branches available at the ARIBE, low energy beam facility. A set of variable apertures can be used to control the intensity and velocity resolution on the ion beam pulses. The focused (≈ 1cm), energy and charge selected ion beam eventually enters the experimental end-station where, under UHV conditions interacts with an effusive, partially supersonic beam of the target molecule under study producing its fragmentation.
The 'formatting' of the pulsed ion beam by means of the two deflection plates, suitably polarized, is an essential part in our experiments, which are

based on the use of time of flight mass spectrometry. An HT brand Behlke controlled by a controller pulse Quantum Composur allows synchronization of the pulsed deflection plates with other pulsed voltages of the device. Indeed the pulse on the deflection plates, suitably delayed to take into account the travelling time of the ions along the beamline, is used to trigger the extraction of the fragments from the interaction region to the TOF spectrometer, which is in turn the origin of the time scale for the measurement of the flight time of the fragments produced during each ion pulse. The 'short' duration of the ion pulse is meant to guarantee that the fragments produced by the dissociation process with internal kinetic energy up to several tens of eV (depending of the mass) will not have enough time to travel outside the field of view of the TOF, and therefore they will still be collected by the extraction field applied just after the ion beam has left the interaction zone. This is important in order to have good detection efficiency for spectroscopic studies. The relatively 'low frequency' of the ion bunches allows for the long flight time of heavy particles like clusters along the full length of the TOF spectrometer, from the interaction region to the detector, and for the typical acquisition and processing time of the electronic units.

The ion beam transmission along the beamline is about 80%, depending on the type of beam. The intensity is controlled by three Faraday cups (2 removable mounted behind the magnetic dipole and 1 after the collision area) which provide an absolute reading of current collected (related to the number of ions).

2.3.3 Processes induced by ion-impact (excitation, ionization, charge transfer, fragmentation)

The interaction between a projectile A^{q+} and a neutral biological system *SB* can lead to an excitation of the target as described below:

$$A^{q+} + SB \rightarrow A^{q+*} + SB^{*} \tag{2.3-1}$$

This electronic excitation will lead to the emission of a photon or to a vibrational excitation of the target that can eventually fragment. This

process can also lead to a delayed electron emission from the target.
When the projectile approaches the target an ionization could happen with the releasing of a number (r) of electrons by the target.

$$A^{q+} + SB \rightarrow A^{q+*} + SB^{r+*} + re^{-} \tag{2.3-2}$$

The projectile passing near the target can also extract one or more electrons from the sample. This is called electron capture, or charge transfer. The following equation illustrates this mechanism:

$$A^{q+} + SB \rightarrow A^{(q-s)+*} + SB^{s+*} \tag{2.3-3}$$

This phenomenon of capture (or multiple catches) has been extensively studied between ions and atoms or between ions and aggregates.
The classical *over the barrier model* is one of the possible approaches [72]. The criterion states that when the maximum height of the potential energy barrier between two objects equals the stark-shifted ionization energy, an electron will be transferred. Note that this criterion relies on the assumption that there is always a resonant state on the projectile (quasi-continuum approximation), which is well-justified at least for highly charged projectiles.
However, for biomolecular systems, involving a large number of electrons, it is difficult to apply such simple model since the potential is unknown. This theory in fact considers the distance between the projectile and the target, which is a variable very difficult to estimate in the case of a biological system in which the conformation and the orientation of the molecule can change.
Most often in collision experiments with multiply charged ions, excitation, ionization and charge transfer can occur all together simultaneously:

$$A^{q+} + SB \rightarrow A^{(q-s)+*} + SB^{(s+r)+*} + re^{-} \tag{2.3-4}$$

where *s* is the number of electrons captured by the projectile and *r* is the number of electrons emitted by the target into the continuum.
Following the collision, the biological system is excited and may loose one

or more electrons. In this case, the system is charged. If the energy transferred during the collision is low and the electronic state of the biological system is stable, it then forms an intact parent ion. In other cases, there is fragmentation (either immediate or delayed if the system is in a metastable state). The time scale of this process varies over a range from fs to pico and microsecond. Thanks to the time and the mobility of the charge on the biological system, it is possible to observe the formation of several multiple charged fragments starting from the neutral systems. Part of the internal energy of the system can then be converted into kinetic energy in a process called KER (Kinetic Energy Release). Reaction (2.3-5) shows how the biological system produced in reaction (2.3-4) can fragment:

$$SB^{(s+r)+*} = X_1^{q_1+*} + X_2^{q_2+*} + X_3^{q_3+*} + \cdots + X_n^{q_n+*} + Y_1^* + \cdots + Y_m^* + KER \tag{2.3-5}$$

with X_i and Y_i the charged and neutral fragments of SB, respectively. The total mass and charge conservation equations (where m_{SB} is the mass of the biological system of interest) can be written:

$$m_{SB} = \sum_{i=1}^{n} m_{X_i} + \sum_{j=1}^{k} k_{Y_j} \tag{2.3-6}$$

and

$$r + s = \sum_{i=1}^{n} q_i \tag{2.3-7}$$

The distribution of the kinetic energy is given by the conservation of momentum. Considering a more simple case of the fragmentation of a system in two charged species (with q_1 and q_2 their respective charge and e the elementary charge), Coulomb repulsion then leads to significant KER values that can be estimated in the approximation of point charges. The energy is calculated as being equal to the Coulomb repulsion of these two charges that are at a distance R_0 (the equilibrium internuclear distance of

the molecule in its ground state). As a first approximation, this potential energy is converted into kinetic energy:

$$KER = \frac{q_1 q_2 e^2}{4\pi\varepsilon_0 R_0} \tag{2.3-8}$$

with permittivity of vacuum $\varepsilon_{0.}$ KER measurements provide additional information on the fragments and therefore the interaction. However, normally these measurements require consideration of possible neutral fragments resulting from the interaction and a careful evaluation of the kinetic energy of the charged fragments, which is beyond the purposes of the present experiments.

2.3.4 The target source

In this part of experiments the isolated 5BrU biomolecules and its homogeneous and hydrated clusters have been considered. These can be produced by two devices placed at the opposite sides of the interaction region. One of them, a simple inductively heated oven, produces a beam of isolated molecules while the other one produces clusters through a gas aggregation source.

A beam of single molecules is obtained by using an oven filled with the powder of the biomolecule. The proper operating temperatures for the oven were characterized during the off-line tests performed via FT-IR spectroscopy in Rome (see 2.4.4). The gas density can be controlled by adjusting the temperature of the oven, always taking care not to decompose the target biomolecules. Fig 2.3—2 shows the schematic of the single molecule beam. The oven consists of a tube surrounded by heating elements and covered with a thermal screen screwed to the base. The obtained effusive beam diameter depends on the diameter of a diaphragm, φ, through which the beam passes and the distances involved. This limits the size of the target beam for better resolution (see section 2.3.5). This also has the advantage of limiting the contamination of the set-up in the collision area, which is screened and cooled by a constant flow of liquid nitrogen.

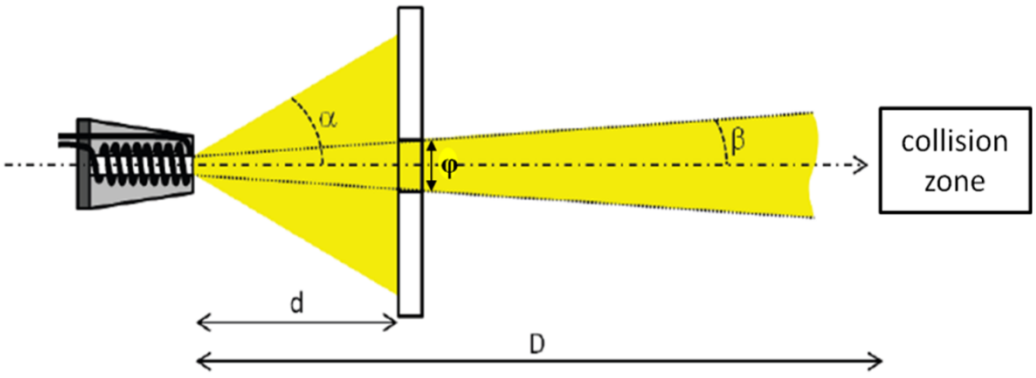

Fig 2.3—2 Schematic of the position of the oven with respect to the collision zone, where φ=0.53 cm, β = 2°, d =7·cm and D = 17 cm.

In first approximation, the diameter (cm) of the target beam in the interaction area is given by the formula:

$$\Phi \approx 2\tan(\beta)\cdot D \approx \frac{\varphi \cdot D}{d} \tag{2.3-9}$$

that in the present case gives $\Phi = 1.3$ cm.
This is greater than the size of projectile beam, which is 5 mm. This explains why the focus of the ion beam is very important for the time (i.e. m/z) resolution of the TOF spectrometer.
In front of the oven, on the opposite side of the interaction zone, is placed the cluster source. This allows to create a gas phase distribution of atomic or molecular clusters and hydrated clusters. An oven containing a powder of the sample is placed inside a bell at a few mbars of primary vacuum. The bell is equipped with a nose cooled with liquid nitrogen (see Fig 2.3—3) and is crossed by a carrier gas (typically He) at $1.5\cdot10^{-3}$ mbar pressure. With the increasing temperature of the oven the molecules inside the powder starts to evaporate, as in the case of the single molecule oven, and to collide with the carrier gas (helium) injected through the bottom of the bell. The carrier gas cools down passing through the nose and guides the molecules through the condensation channel. The molecules will then aggregate to each other forming a neutral distribution of clusters of various sizes and shapes. Indeed even if the system is relatively cool (-180°C) it is

not in the fundamental roto-vibrational level thereby it could vibrate and rotate to form more complex interactions. The clusters then reach the interaction zone, which is also the extraction zone of a time of flight spectrometer, where they interact with the multicharged ion beam coming from the ECR source. Several parameters have to be controlled which could affect the aggregation process. For example the temperature of the condensation channel is very important. If it is too high the aggregation doesn't happen. However it is usually not possible to affect this parameter experimentally since the condensation channel is directly in contact with the liquid nitrogen flow and it is therefore at about the same temperature. The quantity of helium gas injected is also an important parameter. If the flux is too weak there will be less collisions with the molecules, making the thermalization ineffective. This parameter may be controlled using a flow controller which can change the carrier gas flow rate from 0 to 600 mL/min (typically used around 120 mL/min). This corresponds to a pressure in the aggregation chamber of the order of the tens of millibars. And finally also the amount of the target molecules has to be controlled. The amount of evaporated molecules varies with the oven temperature which has to be over a threshold value in order to obtain a good aggregation. The quantity of molecules evaporated increases exponentially with temperature and could cause saturation of the vapor pressure. In addition, too high temperatures (for a given system) could decompose the molecule, or produce too much density, blocking the oven itself and requiring the user to open the device. All of these parameters have to be adjusted empirically during the experiment, in order to find the good working conditions of the source.

In order to produce a molecular beam of hydrated clusters, a high purity water flask was mounted just after the source of helium injection (see Fig 2.3—3). The entire line is heated to 50° C to minimize condensation of water on the walls. In this way the water vapor enters into the chamber carried by the helium. The proportions of helium and water can be changed by varying the temperature of the balloon, opening the leak valve or changing the helium pressure. The target molecules evaporated by the oven will then be able to aggregate among themselves and with the water molecules inside the condensation channel. In this way a distribution of homogeneous as well as hydrated clusters of different size and shape is

obtained. Unfortunately there is no precise information about the real nature of the clusters. It is in principle possible to form clusters of molecules surrounded by water molecules or cluster of molecules bound with clusters of water molecules. The nature of the target cluster will be discussed in section 5.3.

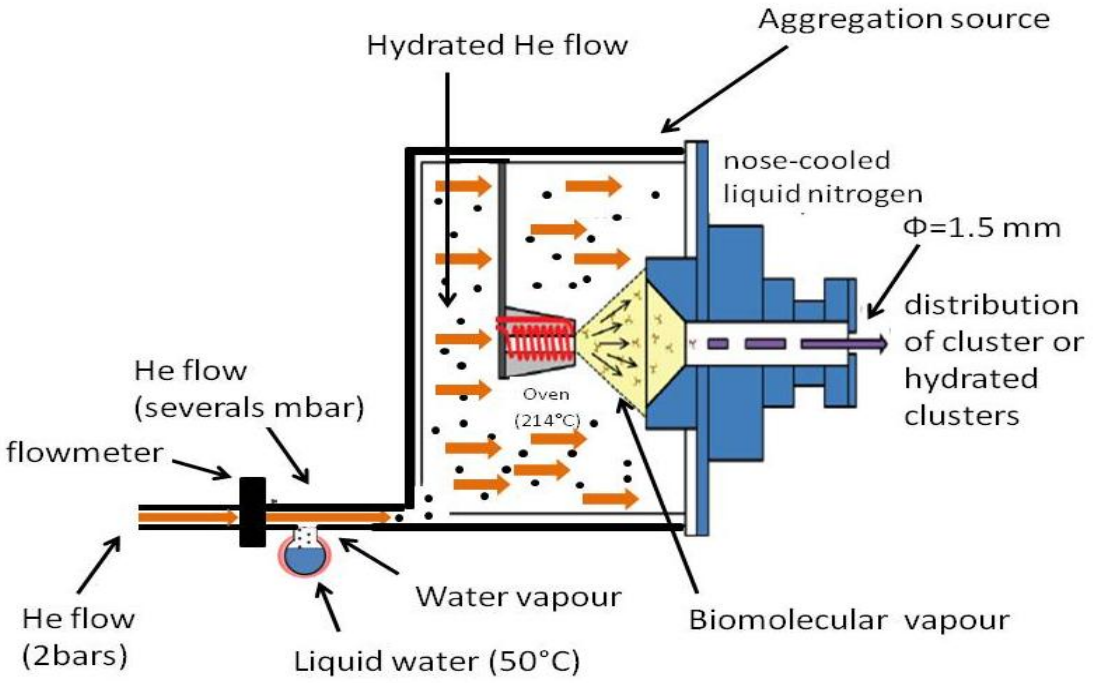

Fig 2.3—3 Schematic of the aggregation source. The balloon with water is inserted along the He line only for the formation of clusters hydrated.

2.3.5 Time of flight mass spectrometry

The mass spectrometry is a technique which allows to identify a set of charged fragments. Its principle is based on the separation of charged species according to their mass to charge ratio (m/z). Consider some charged particles situated between two electrodes mounted at a distance equal to L. If an electric field $\vec{E}$ is applied these particles with mass m and charge z are accelerated by the electric field and at the end of the acceleration zone they reach a velocity *v* equal to:

$$v = \sqrt{\frac{2zE}{m}}$$

(2.3-10)

So it is possible to derive the time employed by a particle (with velocity equal to *v*) to travel along a zone of length equal to *L*

$$T = \frac{L}{v} = \frac{L}{\sqrt{2E}}\sqrt{\frac{m}{z}}$$

(2.3-11)

This basic principle that the time of flight is directly proportional to the *m/z* square root is used to separate ions with different m/z ratio based on their time of flight in the spectrometer. One of the most common TOF spectrometers is the Wiley-Mclaren [73], where, with a careful design of the geometry and suitable choices of the applied voltages it is possible to compensate the time of flight uncertainty of the charged particles due to the finite space distribution of the source. This is particularly relevant in the experiments with the ion beam source, where the ion bunch extends over more than 1cm along the TOF axis.

In the TOF spectrometer used on the ARIBE beamline (see Fig 2.3—***4***), the target molecules enter in the spectrometer in the region 1 where they interact with the multicharged ion beam. The ionic fragments produced are extracted by the application of an electrostatic field $\vec{E}_1$ then accelerated through the region 2 by the field $\vec{E}_2$. After that, they enter in the free flight zone of the flight tube. In this zone they can be subjected to a field $\vec{E}_3$ perpendicular to the axis of spectrometer, which compensate for the effect of initial velocity in order to direct the ions towards the detector. This additional deflection turns out to be useful in the case of studies of heavy clusters hardly deflected by the extracting and accelerating fields. The fragment ions with different m/z ratio are separated in this region.

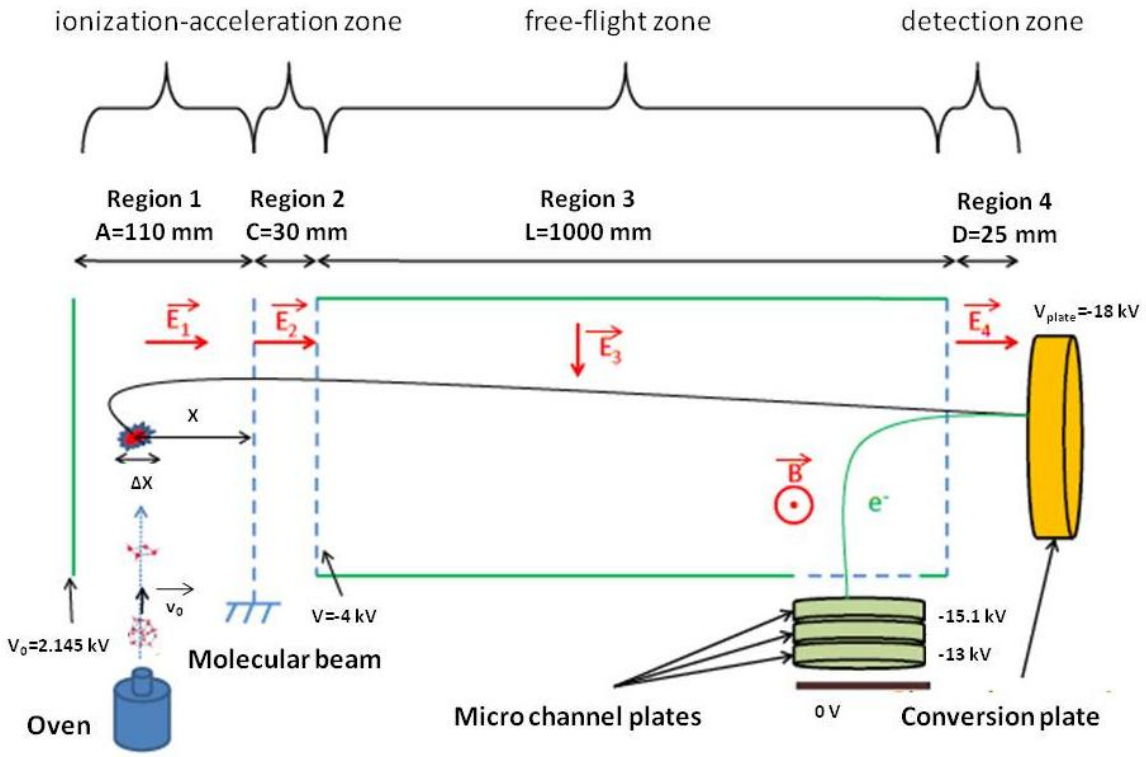

Fig 2.3—4 Schematic of the time of flight mass analyzer spectrometer available at the ARIBE beamline.

Finally, the ions are accelerated by the field $\vec{E}_4$ in the detection zone (region 4). By applying the fundamental principles of dynamics, it is possible to calculate the time of flight in each region *i* ($T_i(x,v)$) and the total time of flight $T = \sum_{i=1}^{4} T_i(x,v)$ with the following equation:

$$T_1(x,v) = \frac{m}{qE_1}\left(\sqrt{v^2 + \frac{2q}{m}V_a} - v\right) \tag{2.3-12}$$

$$T_2(x,v) = \frac{m}{qE_2}\left(\sqrt{v^2 + \frac{2q}{m}\left(V_a\frac{x}{A} + V\right)} - \sqrt{v^2 + \frac{2q}{m}V_a\frac{x}{A}}\right) \tag{2.3-13}$$

$$T_3(x,v) = \frac{L}{\sqrt{v^2 + \frac{2q}{m}(V_a \frac{x}{A} + V)}}$$

(2.3-14)

$$T_4(x,v) = \frac{m}{qE_4}\left(\sqrt{v^2 + \frac{2q}{m}(V_a \frac{x}{A} + V + (V_{plate} - V))} - \sqrt{v^2 + \frac{2q}{m}(V_a \frac{x}{A} + V)}\right)$$

(2.3-15)

The ionization-acceleration zone consists of regions 1 and 2. The region 1 is 11 cm long and consists of a circular stainless steel plate of 130 mm diameter followed by ten electrodes (outer diameter 130 mm and inner diameter 90 mm) separated by insulating ceramic and it ends with a nickel grid (transmission 90%). The rings located near the interaction regions have a particular geometry in order to allow the passage of the multicharged ion beam and the molecular beam.

The electric field $\vec{E}_1$ extracts the positive charged fragments created after the collision. This field is produced by applying a difference of potential between the first electrode the repeller and the last one, the extractor, which is grounded. The pulse V_a is obtained by a high voltage switch sincronised with the deflectors of the ion beam. Region 2, is 3 cm long, it has two equidistant rings and ends with a grid similar to the previous one, which is at potential V=-4 kV. The electrostatic field $\vec{E}_2$ is due to the difference between the last grid of region 2 and the entrance one, which is grounded. A stainless shield wherein liquid nitrogen flows is mounted around the extraction area to trap the residual gas and the vapour beam during the experiments, improving the background pressure of the vacuum chamber and limiting the contamination of the set-up due to the vapour beam, which will most likely stick on the coldest surfaces. In this way a vacuum of 10^{-10} mbar is reached

In the free flight zone, the separation of the fragments according to their

m/z ratio happens (region 3, Fig 2.3—4). This zone is 1 m long and consists of two stainless steel plates of 98x10 cm^2, separated by 10 cm. One of the two main plates is connected to the same voltage as the last grid of region 2 while the other can be independently polarised. This setting provides an electric field $\vec{E}_3$ to the axis of the spectrometer, which is used to compensate for the drift of ions due to their initial velocity orthogonal to the axis of the spectrometer. Typically the difference of potential is of about tens of volts. In order to ensure a homogeneous field, nine pairs of electrodes in the form of blades (97 cm long) are placed between these two large plates.

The last and most original part of the spectrometer is in the detection zone, which provides a detection efficiency almost constant up to 4600 u. In a conventional linear spectrometer the ions are detected when they collide directly with the detector which usually consists of a channeltron or multichannel plates. In this case the detection efficiency varies a lot according to the speed of the particles and the heavy fragments will be detected less efficiently. In order to avoid this problem the detection of the fragments will be done indirectly in this kind of spectrometer. A 'conversion plate' is located at the end of the region 4, polarised at potential V=-18 kV. The collision between the fragments and the surface of the plate causes the ejection of one or more electrons. The backscattered electrons are then deflected by a weak magnetic field $\vec{B}$ towards a microchannel plate placed at 90° with respect to the deflection plate. The time of flights of all particles will be increased by the same amount so that the mass spectrum reconstruction is not modified. At the final stage, a cone-shape anode collects the electrons emitted by the microchannel plates. The resulting signal is then processed by an electronic system. The analysis of the time of flight of the fragments requires a reference time called 'start'. This constraint imposes operating the ionisation/extraction in pulsed mode. As already described, this is achieved by directing the ion beam along or away from the beamline axis using two plates. The upper plate is connected to a power supply that delivers 500 V, the second one is connected to a pulse generator which works in association with a high-voltage switch. The lower plate is brought to a potential of 500 V during the time required (in these experiments 0.5 μs) to form an ion bunch. The packet of ions must travel a distance of 8.6 m before reaching the collision zone. The bunch speed and

this distance determines the time between the end of the formation of the ions bunch and the triggering of the extraction of the fragments products. The activation of the extraction in the TOF defines the time t = 0 of the time of flight of the fragments inside the spectrometer.

The signal obtained at the output of the detector passes through a preamplifier followed by an amplifier. The time signals are converted into NIM pulses by discriminator (-0.7 V amplitude and half-height width of approximately 20 ns). These pulses are sent to a computer equipped with a multiple-event time digitizers (FAST ComTec P7888) that stores the pulse arrival time (the 'stop') measured with respect to the trigger signal (the 'start'). For each 'start', the number of 'stops' defines the multiplicity of the event so physically corresponds to the number of charged fragments of specific m/z detected during the event.

Two important characteristics of a TOF mass spectrometer are the spatial and the energy resolutions.

The spatial resolution is defined as the capability to minimize the dispersion of the time of flight due to the dispersion of the initial position, *x*, along the spectrometer axis:

$$\frac{\partial T}{\partial x} = 0 \tag{2.3-16}$$

A Wiley-Maclaren type TOFMS is designed in such a way to compensate for this effect up to a certain extension of the source region, Δx. This is a particularly critical point in our set-up, where the ion beam has an extension of ≈ 1cm. The desing of the present set-up permits to minimize this disadvantage, analyzing the fragments produced by these very broad ions bunches with a mass resolution (R=$\frac{m}{\delta m}$) of 1500.

The energy resolving power of the spectrometer is its ability to compensate the dispersion in time of flight of the ions due to their initial velocity dispersion. Consider to have two identical ions of the same mass, charge, energy and initial position but opposite initial velocities (see Fig 2.3—***5***): ion 1 moves towards the detector at speed $\vec{v}$ while ion 2 goes in the opposite direction at speed $-\vec{v}$. In this case the application of the field $\vec{E}_1$ will force the ion 2 to turn around in order to reach the detector and the

time spent to change direction is equal to:

$$\delta T_v = T(x,-v) - T(x,v) \tag{2.3-17}$$

but substituting $T = \sum_{i=1}^{4} T_i(x,v)$ it follows that:

$$\delta T_v = \frac{2mv}{qE_1} \tag{2.3-18}$$

So the higher the speed (v) the greater the time (δT_v) and the lower is the resolution. In this way the time spent by the ion to change direction will be exploited in the analysis part of the results to assess the speed v of the fragments in the fragmentation, which combined with the m/z ratio, allows to deduce the kinetic energy of the fragment.

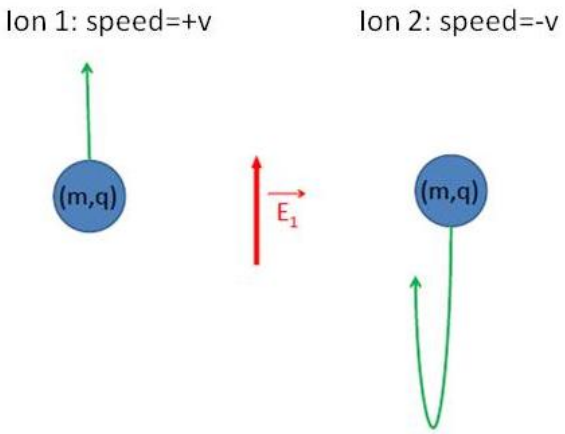

Fig 2.3—5 Schematic illustration of the time to "return" in the ionization zone.

2.4 Infrared spectroscopy

Infrared (IR) spectroscopy is a photoabsorption technique that exploits the interaction between radiation and matter, in the region of the electromagnetic spectrum between 13,000 and 10 cm^{-1}. This technique has been used to study and characterise the thermal decomposition analysis of five different halo-subsituted uracil molecules as will be described in section 2.4.4. Usually the IR spectrum is divided in three regions:

- near IR (NIR) → 13,000 – 4,000 cm^{-1}
- medium IR (MIR) → 4,000 – 200 cm^{-1}
- far IR (FIR) → 200 – 10 cm^{-1}

This technique is used mainly in analytical chemistry for the characterization of materials, as well as in physical chemistry for the study of the chemical bonds.

After the absorption of an infrared photon, the molecule will undergo a transition from its fundamental to an excited vibrational state. This process is based on the theoretical model of the harmonic oscillator, corrected for different levels of anharmonicity, which can be solved exactly for the simplest diatomic molecule. Complex quantum treatments describe that the condition for an infrared radiation to cause a vibrational transition consists in a change of the molecular dipole as a result of the change in the position of the atoms. For this reason molecules such as N_2 or O_2 are not active in the IR, while non-polar molecules such as CO_2 can be resonant with the IR radiation thanks to the asymmetric vibrations that produce a dipole moment. The infrared spectrum represents a fingerprint of a sample, with absorption peaks corresponding to the frequencies of vibration between the bonds of the atoms in the material. Because each different material is a unique combination of atoms, no two compounds produce the exact same IR spectrum. In order to have absorption or emission of radiation the selection rule $\Delta v = \pm 1$ must be satisfied. It is also possible to observe the so-called *overtone bands* in apparent violation of this selection rule. These particular bands are due to the anharmonicity of the chemical bond. In the case of molecules in the gas phase, where the free rotation is possible, the typical IR spectrum includes also the contributions of the rotational transitions and becomes a vibro-rotational spectrum more complex but also richer in information. According to the change of the quantum number J due to the transition, it is possible to distinguish, spectral branches P ($\Delta J = -1$), Q (in the molecules in which the transition $\Delta J = 0$ is possible) and R ($\Delta J = +1$). 3N-5 different vibrational modes are possible in a linear molecule formed by N atoms; in the case of a nonlinear molecule such vibrational modes are 3N-6.

The vibrations can be simply summarized into two types: the chemical bond stretching (stretching) and bond angle deformation (bending).

Stretching can be symmetrical, if the two atoms are moving towards each other or away simultaneously, or asymmetrical, in the opposite case, as for example in the CO_2 linear molecule, if the two oxygen atoms are moving in the same direction at the same time. The bending is called rocking when it is asymmetric and scissoring when it is symmetric and in both cases the movement of the atoms occurs along the same plane of the bond angle or it is called wagging (symmetric) and twisting (asymmetric) when the movement occurs outside that plane.

2.4.1 Instrumentation

Schematically a classic IR spectrophotometer is essentially constituted by a light source directed towards the sample, a monochromator used for reducing the scattered light, a *chopper*, which is a half-disk optical system and a detector. Infrared spectrometers can be dual-beam or single-beam. In dual beam instruments the chopper is also placed after the source in order to split the beam of light.

The most common IR sources are the incandescent lamps: the *Nernst* filaments made of sintered oxides, the *Globar* rods made of silicon carbide that work at a temperature (1300°C) lower than the Nernst filament in order to avoid the silicon carbide oxidation, and common resistors made of nickel-chromium.

One of the greatest challenges for the IR spectroscopist is the sample preparation.

In order to analyze the solid samples it is necessary to perform one of the following treatments:

• reduce the sample in thin layers;
• bring the samples in suspension by grinding with nujol in a mortar;
• ground finely the sample with KBr, CsI or KCl or in order to obtain a homogeneous disk using a special pellet-press.

The classic IR sampling technique is the alkali halide pellets preparation. In our case the pellets of potassium bromide were prepared using 0.7 mg of sample mixed with 200 mg of anhydrous potassium bromide, placing the mixture into a die (typically stainless steel), and subjecting it to

approximately 10,000 psi of pressure for an appropriate period of time (usually 5-10 minutes) to produce a glass pellet.
The detectors are constituted by devices able to convert the heat of the infrared radiation into signal. For this purpose thermocouples and thermistors are commonly used: thermocouples generate a difference of potential due to the difference of temperature that is established between two sensitive joints, while the thermistors are resistive components which form one of the four branches of a Wheatstone bridge that is unbalanced when their resistance varies as a function of temperature. The Golay detector is a very sensitive device and it exploits the increase of pressure of a gas within a micro-cell, caused by a temperature increase. This increased pressure deforms an elastic specular wall and the light produced by an auxiliary source that hits this wall is reflected on a photocell, which generates an electrical current that varies in function of the deformation.
In a typical infrared spectrum chart, the abscissa axis is a scale of frequencies expressed in wave number and the ordinate one is expressed in arbitrary units of absorbance. If a material is not completely transparent to the infrared radiation, a series of absorption peaks which represent transitions between vibrational energy levels appear.

2.4.2 Fourier transform IR spectroscopy

Nowadays all the spectrophotometers used for IR analysis are based on the principle of Fourier transform which has been widely applied to spectroscopies in order to overcome the limitations encountered with dispersive instruments. In fact, previously, the main difficulty was the slow scanning process. A method for measuring all of the infrared frequencies simultaneously, rather than individually, was needed.
The Fourier transform IR spectroscopy (FT-IR) is realized using an interferometer which scans all frequencies present in the IR radiation generated by the source.
The scan is possible by moving a movable mirror that introduces a difference of optical path, which originates a constructive or destructive interference with the reflected beam from a fixed mirror. In this way an interferogram is recorded that shows the intensity (arbitrary units) as function of the time (δ optical delay). By applying the Fourier transform, it

is possible to obtain the infrared spectrum, which gives the intensity in the frequency domain. A He-Ne laser that emits red light (632.8 nm) is used to measure the exact position of the mirror.

Among the main advantages of the FT-IR with respect to the classical infrared spectroscopy, there are: the improved signal/noise ratio, the significantly reduced analysis time, the negligible presence of scattered light and the high resolving power that remains constant throughout the IR spectrum.

In the equipment, used in this work, the Michelson interferometer is used, which produces the interferogram of the test substance during a scanning. After the radiation has crossed the sample, the acquired interferogram is processed by the computer connected to the instrument in a traditional infrared spectrum by a mathematical operation, the so-called Fourier transform. In this way, it is possible to switch from an interferogram (a graph of intensity in the time domain) to a common spectrum, which represents the variation of signal intensity as a function of the wave number (or wavelength) of the radiation.

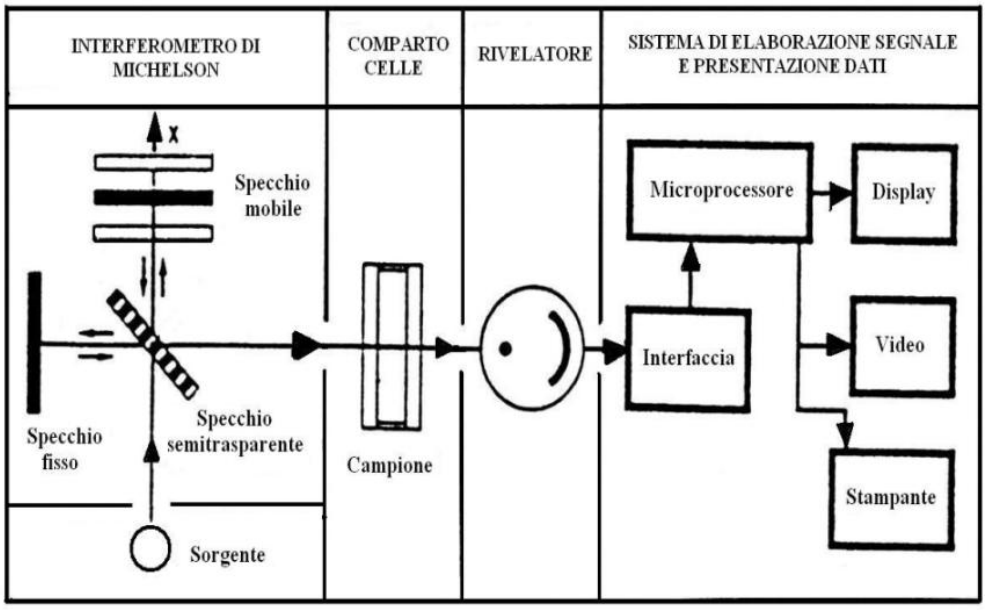

Fig 2.4—1 Diagram of the operation of a Fourier transform IR spectrophotometer.

In our case, the IR spectra were recorded in a range of 4,000-400 cm^{-1} (mid-infrared) with a resolution of 2 cm^{-1}, using a Perkin Elmer Paragon 1000 spectrophotometer.

Fig 2.4—2 Paragon 1000 spectrophotometer from Perkin Elmer Corporation, in use at the CNR-IMIP Area della Ricerca di Roma 1.

2.4.3 The IR spectrum

The IR spectrum can be divided into three different zones:

1) *area of the functional groups*, which extends from 3,800 to 1,300 cm^{-1} and includes bands due to stretching and deformation of the functional groups for example NH bonds, OH, CH, C=C, C=O, N=O, etc.., that show bands of stretching between 1,600 and 1,300 cm^{-1}. It should be noted that the bonds with the hydrogen are at very high frequencies because of the very low mass of these atoms;
2) *area of fingerprints*, which extends from 1,300 to 650 cm^{-1}. This region owes its name to the presence of typical bands characteristic of each individual molecule that are originated from the vibrations of the entire molecular skeleton;
3) *area of far IR*, which extends from 650 to 200 cm^{-1}. This region shows bands due to the stretching of heavy atoms, the deformation of groups without hydrogen and the vibration of the skeleton.

From the infrared spectrum, it is possible to draw useful information for the analysis of an unknown molecule.
Because the fingerprints of many compounds are unique, FT-IR is most commonly used to provide qualitative compound identification

2.4.4 Instrumentation for thermal decomposition analysis

The FT-IR spectroscopy has been used for the thermal decomposition analysis of four different halogenated uracil molecules. In the laboratories of the CNR- IMIP, Area della Ricerca di Roma 1, a test facility reproducing the evaporation system available at the GasPhase beamline (see section 2.2.3) was set up in order to identify a suitable range of working temperatures for the sublimation of the four molecules under analysis, before proceeding with the experiments at the GasPhase beamline of the Elettra synchrotron.

Crucibles made of different materials, in particular stainless steel and copper, have been tested. The thickness of the wall of the collimated nose has also been changed and the best compromise has been found using a copper crucible (which has the best thermal conduction) with a collimated nose 30 mm long, inner and outer diameters of 1 and 3 mm respectively.

Just above the oven an aluminum plate was mounted in order to recondense and collect the vapour beam of the sample after sublimation. The powder collected on this plate has been then analysed through FT-IR spectroscopy to check whether it was decomposed or not. The oven, the crucible and the plate were mounted as shown in Fig 2.4—3 in a vacuum chamber and all the experimental tests were performed at a pressure of $5 \cdot 10^{-6}$ mbar. No ionization source or detector is present in this set up.

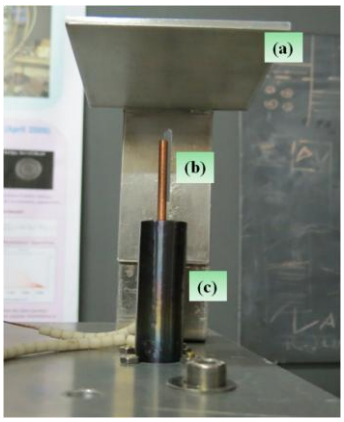

Fig 2.4—3 Experimental set-up employed for the thermal decomposition analysis in the laboratories of the CNR-IMIP, Area della Ricerca di Roma 1: (a) the aluminium plate, (b) the collimated copper crucible (58.5 mm long with a nose 30 mm long having inner and outer diameters of 1and 3 mm respectively) and (c) the cylindrical oven.

3 Theoretical calculations

In this chapter the theoretical methods employed to calculate the value of the appearance energy (AE_T) and enthalpy of formation (ΔH°_{fT}) of a particular molecule or a fragment are described. These theoretical values will be compared with the experimental ones in chapter 4 in order to associate a specific geometry to a particular fragment ion. In this way the global fragmentation pattern of the molecule will be revealed. The procedure used to calculate AE_T and ΔH°_{fT} will be now described with a particular attention to the correspondence of these quantities with the output values of a G3B3 calculation. A list of the optimized geometries of each fragment is shown in appendix.

3.1 The Appearance Energy

The AE is the minimum energy required to produce a particular fragment ion from the neutral parent molecule in its ground state. Theoretically the AE is defined as the difference between the energy of the ground state of the fragment and that of the neutral molecule, i.e. the adiabatic energy of the fragmentation process (Fig 3.1—1). In this work, ab initio calculations of the parent ion and some ionic fragments of 2Cl-, 2Br- and 5Br-pyrimidine using theoretical methods embedded in the Gaussian09 package of programs[74] have been performed.

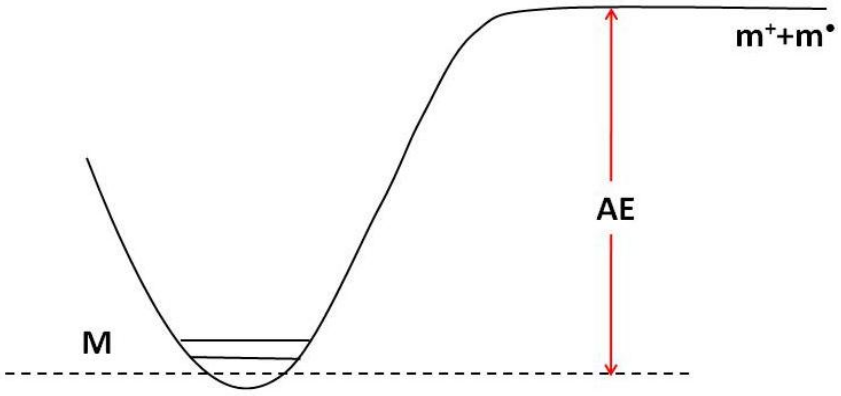

Fig 3.1—1 The appearance energy (AE) for the general dissociation of a molecule M into a charged fragment m^+ and a radical fragment $m^{\bullet}$.

It is important to notice that the AE is the energy directly correlated to the formation of a fragment. Before the breaking, the molecule M passes through the formation of the ionized parent molecule that subsequently breaks. In this case also the ionization energy (IE), which is defined as the minimum energy required to remove an electron from the molecule in the gaseous state is involved.

3.1.1 The parent ion

The adiabatic ionization energy, corresponds to the energy difference between the ground vibrational and rotational level of the lowest electronic state of the ion and the ground vibrational and rotational level of the lowest electronic state of the molecule.
This is rigorously equal to the difference in the heats of formation, ΔH°_{fT} of the ion (M^{+}) and the molecule (M) at 0 K [75] (3.1-1):

$$IE_{(ad)} = \Delta H^{\circ}_{f0}(M^{+}) - \Delta H^{\circ}_{f0}(M) \tag{3.1-1}$$

The experiments in this study were conducted at a temperature of 298, i.e. room temperature for experimental set-up.
The "enthalpy of ionization" is the difference between the heats of formation of the ion and of the corresponding molecule at a temperature T, above 0 K eq. (3.1-2).

$$\begin{aligned} \Delta H_{T(ioniz)} &= \Delta H^{\circ}_{fT}(M^{+}) - \Delta H^{\circ}_{fT}(M) \\ &= \left[\Delta H^{\circ}_{f0}(M^{+}) + \int_0^T C_P(M^{+})dT\right] - \left[\Delta H^{\circ}_{f0}(M) + \int_0^T C_P(M)dT\right] \\ &= IE_{(ad)} + \int_0^T C_P(M^{+})dT - \int_0^T C_P(M)dT \end{aligned} \tag{3.1-2}$$

where $C_P(M/M^{+})$ is the heat capacity of the neutral/ionised molecole.
It is clear, from eq(3.1-2), that $\Delta H_{T(ioniz)}$ is equal to the adiabatic ionization energy only in the case that the integrated heat capacities

$\left(\int_0^T C_P dT\right)$ of the ion and the molecule are identical. In order to verify that this assumption can be applicable in our calculation, it is necessary to examine the factors which influence the heat capacities of the ion and neutral molecule, and to evaluate the magnitude of possible difference.

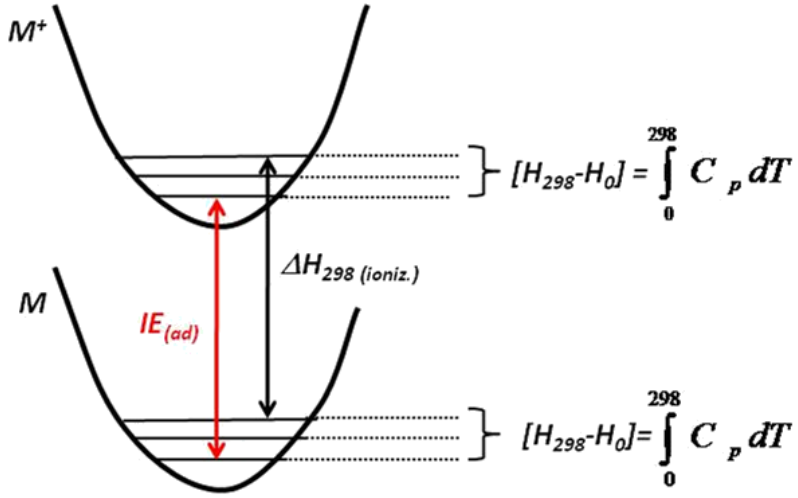

Fig 3.1—2 Ionization process of a molecule M. The adiabatic $IE_{(ad)}$ in red and $\boldsymbol{\Delta H_{T(ioniz)}}$ at 298K in black are described. The heat capacities are equal to $[H_{298}\text{-}H_0]$. The values obtained in output by a G3B3 calculation as described in the section 3.2.

The heat capacity at constant pressure results from the sum of the traslational, rotational and vibrational components:

$$C_P = C_{P(tr)} + C_{P(vib)} + C_{P(rot)} \tag{3.1-3}$$

The translational and rotational contributions to C_P, for a given three-dimensional species are given by [75]:

$$C_{P(tr+rot)} = \frac{7}{2}R + 0.0914\left(\frac{B}{T}\right)^2 \approx \frac{7}{2}R \tag{3.1-4}$$

Where $R = 8{,}314772\ J/(mol \cdot K)$ is the gas constant, $B = h/(8\pi^2 I)$ is the rotational constant, $h = 6{,}626 \cdot 10^{-34}\ J \cdot s$ is the Plank constant, I is the moment of inertia in $g \cdot cm^2$ and T is the temperature in K. The second term

in eq(3.1-4), the only one to contain the properties of the considered M/M^+ molecules, does not contribute significantly for values of I in the usual range of orders of magnitude. Therefore the translational and rotational contribution to ΔC_P can be neglected:

$$\Delta C_{P(tr+rot)}(M^+ - M) \approx 0 \tag{3.1-5}$$

For a given mode of vibration of a molecule at temperature T (in our case 298 K), there is a contribution to C_p of [75]:

$$C_{P(vib)} = R\frac{x_i^2 e^{x_i}}{(e^{x_i}-1)^2} \tag{3.1-6}$$

where $x_i = h\nu_i c/kT$, ν_i is the i^{th} vibrational level, c is the speed of light and $k = 3.181 \cdot 10^{-23}$ *J/K* is the Boltzmann constant.

At high temperatures different vibrational levels will be occupied for the molecule and the ion. This means that during the ionization at high temperatures, the heat of formation of the ion will be different from the one at 0 K. In other words because the $C_{P(vib)}$ depends on the particular vibrational frequency, $h\nu_i$, of the considered molecule it follows that the x_i term and therefore the heats of formation of M and M^+ will be different between themselves as well as from those at 0K. Therefore $C_{P(vib)}(\text{ion}) \neq C_{P(vib)}(\text{molecule})$.

A rough generalization on the effect of ionization upon molecular vibrations is that 1) the bond or bonds whose vibrations are most affected are those from which the electron was removed, and 2) removal of a bonding electron reduces the vibrational frequency of the bond, removal of an antibonding electron increases the vibrational frequency, and removal of a nonbonding electron has little effect.

All the compounds involved in this study are halogen substituted pyrimidines. The ionization to the lowest electronic state of the ion, in these compounds, has little effect on the modes and frequencies of vibration because the electron is removed from the nonbonding orbital of the nitrogen atom.

The differences between the heat capacity of the molecules and the

corresponding ions has been calculated of the order of 0.008 eV, so the adiabatic ionization potential is expected to be the same as the 298K enthalpy of ionization within the experimental error. Therefore it is possible to conclude that:

$$\int_0^T C_P\,(M^+)dT \approx \int_0^T C_P\,(M)\mathrm{dT} \tag{3.1-7}$$

and

$$\Delta H_{298(ioniz)} = IE_{(ad)} + \int_0^{298} C_P\,(M^+)dT - \int_0^{298} C_P\,(M)dT \tag{3.1-8}$$

becomes:

$$\Delta H_{298(ioniz)} = IE_{(ad)} \tag{3.1-9}$$

3.1.2 The fragment ions

In the photoionization and subsequent fragmentation of a molecule *M* by monochromatic radiation of energy *hv*, the ionic fragment m_1^+ and several neutral fragments m_i are produced

$$M + hv \rightarrow M^+ + e^- \rightarrow m_1^+ + \Sigma m_i + e^- \tag{3.1-10}$$

Equation (3.1-10) assumes that the energy of *hv* is below of the double ionization potential, so that only single charged ions can be formed.
Let us consider the general process (3.1-10) and assume that the potential barrier to the reverse reaction is zero. As already shown by Treager and McLoughlin [76], in this reaction (unimolecular decomposition) the initial translational momentum of the center of mass (CM) and the angular momentum about the CM of the precursor molecule plus that one of the photon is conserved during the reaction. In addition, the total energy of the photon and the precursor molecule must be conserved. From these

fundamental laws of energy and momentum conservation it is possible to construct a thermochemical cycle relevant to the dissociation of ions following photoionization [76] (Fig 3.1—3).

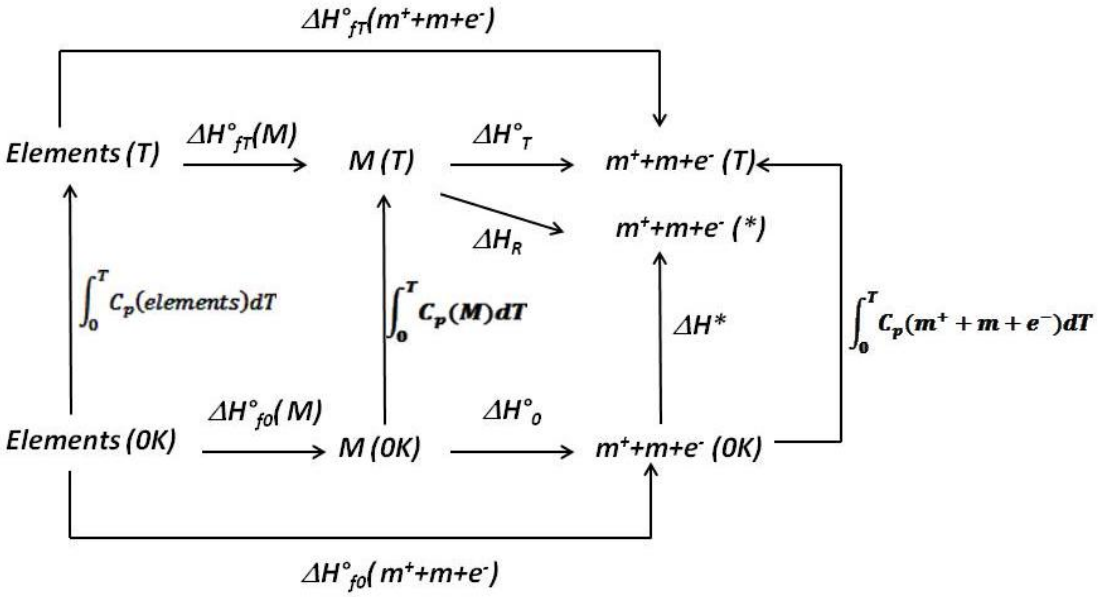

Fig 3.1—3 Thermochemical cycle relevant to the unimolecular decomposition of ions. The sign of each contribution is positive in the direction of the arrow or negative in the opposite [76].

If the unimolecular decomposition is sufficiently rapid, the observed appearance energy ($AE_{T(exp)}$) corresponds to the adiabatic appearance energy ($AE_{T(ad)}$), which represents the minimum energy to form $m_1^+ + \Sigma m_i + e^-$ from *M* at temperature *T*.

The products of this process ($m_1^+ + \Sigma m_i + e^-$) are not formed at any well-defined equilibrium thermodynamic temperature because the reaction occurs in isolation (unimolecular decomposition). Indeed, they are formed with 0 K translational energy with respect to the CM, with essentially 0 K internal energy (apart from the small residual rotational energy associated with the conservation of angular momentum about the CM), and with a CM translational energy equivalent to that of the precursor molecule (*M*) at the temperature *(T).* For this reason the products of reaction can be considered as formed at a "quasi-temperature" ("*" in Fig 3.1—3), an unknown temperature different from T.

Thus the measured experimental AE value at temperature T is:

$$AE_{T(exp)} = \Delta H_R$$

(3.1-11)

If any of the equilibrium thermodynamic quantities in Fig 3.1—***3*** have to be calculated from AE measurements recorded at T≠0 K, then ΔH^* (the enthalpy difference between $m^+ + m + e^-$ *(*)* and $m^+ + m + e^-$ *(0K)*) must be estimated with reasonable accuracy. Chupka [77] has shown that if an extrapolation of a linear post-threshold region can be used to determine $AE_{T(exp)}$, then

$$AE_{0(exp)} = AE_{T(exp)} + E_i$$

(3.1-12)

where E_i is the *M* internal thermal energy of effective in dissociation. From Fig 3.1—***3***, the enthalpy of the fragmentation process in eq.(3.1-10**)** at 0 K is:

$$\Delta H_0^\circ = \int_0^T C_P(M)dT + \Delta H_R - \Delta H^*$$

(3.1-13)

and for fragmentation at the ionization threshold, where $\Delta H_0 = AE_{0(exp)}$ and $\Delta H_R = AE_{T(exp)}$, according the cycle in Fig 3.1—***3***:

$$AE_{0(exp)} = \int_0^T C_P(M)dT + AE_{T(exp)} - \Delta H^*$$

(3.1-14)

Then by substitution of eq.(3.1-12) in eq.(3.1-14) it follows that:

$$\Delta H^* = \int_0^T C_P(M)dT - E_i$$

(3.1-15)

Experimental evidence [78] indicates that, to a good approximation, all the initial internal thermal energy of rotation and vibration of the precursor molecule *M(T)* is effective in dissociation. On this basis:

$$E_i = \int_0^T C_{P(rot)}(M)dT + \int_0^T C_{P(vib)}(M)dT \tag{3.1-16}$$

by substitution of eq.(3.1-16) in eq.(3.1-15) and considering eq. (3.1-3):

$$\Delta H^* = \int_0^T C_{P(tr)}(M)dT \approx \frac{5}{2}RT \tag{3.1-17}$$

From the cycle in Fig 3.1—3 and eq.(3.1-11) it follows that:

$$AE_{T(exp)} = \Delta H_{fT}^{\circ}(m^+) + \Delta H_{fT}^{\circ}(m) + \Delta H_{fT}^{\circ}(e^-) - \Delta H_{fT}^{\circ}(M) - \int_0^T C_P(m^+)dT - \int_0^T C_P(m)dT - \int_0^T C_P(e^-)dT + \Delta H^* \tag{3.1-18}$$

Adopting the stationary electron convention (i.e. $\int_0^T C_P(e^-)dT = 0$ and $\Delta H_{fT}(e^-) = 0$) it follows that:

$$AE_{T(exp)} = \Delta H_{fT}^{\circ}(m^+) + \Delta H_{fT}^{\circ}(m) - \Delta H_{fT}^{\circ}(M) - \int_0^T C_P(m^+)dT - \int_0^T C_P(m)dT + \Delta H^* \tag{3.1-19}$$

Where the $AE_T(exp)$ is the quantity derived by the AEs curves of the fragment ions obtained by the dissociation process at the quasi temperature (*) described by the thermochemical cycle in Fig 3.1—3. These same AE values will be calculated by the Gaussian package of programm and compared with the experimental ones.
The quantities $\Delta H_{fT}^{\circ}(m^+), \Delta H_{fT}^{\circ}(m)$ and $\Delta H_{fT}^{\circ}(M)$ will be calculated at the temperature T = 298 K which is the temperature of the experiment.
As already shown in eq.(3.1-2) for each single molecule it possible to say that:

$$\Delta H^{\circ}_{fT}(m^{+}) = \Delta H_{f0}(m^{+}) + \int_{0}^{T} C_P(m^{+})dT \tag{3.1-20}$$

$$\Delta H^{\circ}_{fT}(m) = \Delta H_{f0}(m) + \int_{0}^{T} C_P(m)dT \tag{3.1-21}$$

$$\Delta H^{\circ}_{fT}(M) = \Delta H_{f0}(M) + \int_{0}^{T} C_P(M)dT \tag{3.1-22}$$

Substituting these equations in eq.(3.1-19):

$$AE_{T(\exp)} = \Delta H^{\circ}_{f0}(m^{+}) + \Delta H^{\circ}_{f0}(m) - \Delta H^{\circ}_{f0}(M) - \int_{0}^{T} C_P(M)dT + \Delta H^{*} \tag{3.1-23}$$

knowing that

$$AE_0 = \Delta H^{\circ}_{f0}(m^{+}) + \Delta H^{\circ}_{f0}(m) - \Delta H^{\circ}_{f0}(M) \tag{3.1-24}$$

and $\Delta H^{*} = \frac{5}{2}RT$ as shown in eq.(3.1-17), it follows that:

$$AE_{T(exp)} = AE_0 - \int_{0}^{T} C_P(M)dT + \frac{5}{2}RT \tag{3.1-25}$$

where the first term is the appearance energy calculated at 0K, while the remaining terms represent the thermal energy correction, because the experiment has been performed at a temperature T.

The eq.(3.1-25) was used for the calculation of the theoretical values of AEs using Gaussian 09 program that gives as output $\{H^{\circ}_{298} - H^{\circ}_{0}\}(M) = \int_{0}^{298} C_P(M)dT$ as well as the AE_0 term. The details of this calculations will be described in the next session.

3.2 Thermochemistry in Gaussian

This chapter describes the methods applied to calculate the theoretical values of AEs of the fragments and their enthalpies of formation.
The relative energies and heat capacity for the reactants and products have been calculated using the G3B3 [79] method. The mean absolute deviation between the G3B3 computed and literature standard state enthalpies of formation is about 2.6 kJ/mol (0.027 eV) [80]. As it will be discussed in chapter 4, some of the final geometries of the studied fragments, even though representing the lowest, i.e. adiabatic, energy configuration would involve significant rearrangements of the molecular structure with respect to the neutral molecule. Such rearrangements consist of bond breakings and atom migrations, which can only be obtained by overcoming energy barriers in the potential energy surfaces. The last contribution is clearly not included in the adiabatic calculation, but has to be estimated separately. For this reason, the experimental determination of the AE of a fragmentation pattern can only be higher or equal to the corresponding, adiabatic, theoretical value. To investigate such mechanisms and to obtain the transition state between selected initial and final configurations, in some cases, a Synchronous Transit Guided uasi-Newton Method (qst3) calculation at B3LYP 6-31G(*d*) level of theory [81, 82] has been performed. The qst3 calculation needs an initial guess for reactants, transition states and products. The energy barrier is then calculated at B3LYP level of theory, as difference between the energy of the initial and intermediate states (see chapeter 4).
In the case of 2Cl-pyrimidine molecules, the values of the enthalpies of formation of the species using G3B3 and G2 [83] calculations have also been calculated. The comparison between the two methods will be described in section 4.2.1

3.2.1 Output from a G3B3 calculation

Gaussian-3 theory consists of a sequence of well-defined *ab initio* molecular orbital calculations performed to determine at the total energy of a given molecular species. The steps in G3B3 method are as follows:

1 An initial equilibrium structure is obtained at the B3LYP level with the 6-31G(*d*) basis set.

2 The B3LYP/6-31(G)d equilibrium structure is used to calculate harmonic frequencies, which are then scaled by a factor of 0.96 to take into account the known deficiencies at this level [79]. These frequencies give the zero-point energy, E(ZPE), used to obtain E_0 in step 7. This level of theory is adequate in most cases for the zero-point energies[84].

3 The equilibrium geometry is refined at the B3LYP/6-31(G)d level, using all electrons for the calculation of correlation energies. This is the final equilibrium geometry in the theory and is used for all single-point calculations at higher levels of theory in step 4. With the exception of the cases denoted by the symbol "(full)", the subsequent calculations include only valence electrons in the treatment of electron correlation.

4 A series of single-point energies calculations are carried out at higher levels of theory. The first higher level calculation is complete fourth-order Moller–Plesset perturbation theory[85] with the 6-31G(*d*) basis set, i.e. MP4(FC)/6-31G(*d*). This energy is then modified by a series of corrections from additional calculations:

- a correction for diffuse function[86], *ΔE(+)*

  $$\Delta E(+) = E[MP4(FC)/6\text{-}31+G(d)] - E[MP4(FC)/6\text{-}31G(d)]$$

- a correction for higher polarization functions on no-hydrogen atoms and *p*-function on hydrogen atoms [87], *ΔE(2df,p)*

  $$\Delta E(2df,p) = E[MP4(FC)/6\text{-}31G(2df,p)] - E[MP4(FC)/6\text{-}31G(d)]$$

  The 2*d* symbol implies two sets of uncontracted *d*-primitives with exponents twice and half the standard values[88]. The *p*-function exponent (1.1) for hydrogen is from ref.[88] while the *f*-function exponents are from ref [86].

- a correction for correlation effects beyond the fourth order perturbation theory using the method of quadratic configuration

interaction[89], *ΔE(QCI)*

$$\Delta E(QCI) = E[QCISD(T,FC)/6\text{-}31G(d)] - E[MP4(FC)/6\text{-}31G(d)]$$

- correction for the effect of larger basis set and for the non additivity caused by the assumption of the separate basis set extensions for the diffuse and higher polarization functions, *ΔE(G3large)*

$$\Delta E(G3large) = E[MP2(full)/G3large] - E[MP2/6\text{-}31G(2df,p)] - E[MP2/6\text{-}31+G(d)] + E[MP2/6\text{-}31G(d)]$$

The 6-31G basis set used here is derived for K, Ca, Ga–Kr by Rassolov *et al.* [reference therein 90] This basis set was constructed in a manner analogous to 6-31G* for the first and second rows and the 3*d* electrons are treated as part of the valence set. The polarization function is a *d* function with six second-order Cartesian Gaussians used for all atoms. It uses a spherical harmonic representation (seven functions) for the *f*-polarization function. The G3large basis set for the third-row atoms K, Ca, Ga–Kr is a contracted 8*s*7*p*3*d* Gaussian set with supplementary functions. The contracted set was derived by modification of the basis set referred to as "6-311G" that is used in the G2 theory for the third row. This modification involves a different contraction of the *p* and *d* core functions and a full reoptimization of the basis set at the Hartree–Fock level. The optimizations were done on the ground state atoms for Ga– Kr. For K and Ca the ground state optimization leads to *d* and *p* functions that are too diffuse. Therefore, K and Ca basis sets were obtained first by optimizing the 7*s*7*p* contracted set on the ground states. Next, an additional uncontracted *s* function was added to the set with the exponent equal to the geometric mean of the two outermost valence *s* functions. Then, the 7*p* functions were reoptimized on the excited 2*P* state of K and the 3*D* state of Ca. Finally, a set of *d* functions was obtained by rescaling those from Sc by the ratio of squares of nuclear charges. The resulting basis set is a

contraction of a 15*s*13*p*5*d* primitive set to 8*s*7*p*3*d*[90].

The largest basis set MP2 calculation in step 4 is carried out at the MP2(full) level. This is done to take some account of the core-related correlation contributions to the total energies. Such effects have been neglected in both G1 and G2 theories, but have been shown to be significant in several recent studies.

5 The MP4(FC)/6-31G(*d*) energy and the four corrections from step 4 are combined in an additive manner along with a spin–orbit correction, $\Delta E(SO)$, for atomic species only.

$$E(combined) = E[MP4(FC)/6\text{-}31G(d)] + \Delta E(+) + \Delta E(2df,p) + \Delta E(QCI) + \Delta E(G3large) + \Delta E(SO)$$

The spin–orbit correction is taken from experiment[91] whenever available and from accurate theoretical calculations in other cases.

6 A ‘‘higher level correction’’ (HLC) is added to take into account remaining deficiencies in the energy calculations:

$$E_e(G3B3) = E(combined) + E(HLC)$$

The HLC is $-An_\beta - B(n_\alpha - n_\beta)$ for molecules and $-Cn_\beta - D(n_\alpha - n_\beta)$ for atoms (including atomic ions). The n_β and n_α are the number of β and α valence electrons, respectively, with $n_\alpha > n_\beta$. The number of valence electron pairs corresponds to n_β. n_α is larger than n_β of a quantity equal to the number of unpaired electrons in the system. Thus, *A* is the correction for pairs of valence electrons in molecules, *B* is the correction for unpaired electrons in molecules, *C* is the correction for pairs of valence electrons in atoms, and *D* is the correction for unpaired electrons in atoms. The use of different corrections for atoms and molecules can be justified, in part, by noting that these extrapolations partially take into account the effects of basis functions with higher angular momentum, which are likely to be more important in molecules than in atoms. For G3B3 theory, *A* = 6.760 mhartrees, *B* = 3.233 mhartrees, *C* = 6.786 mhartrees, *D* = 1.269 mhartrees. The *A*, *B*, *C*, *D* values are chosen to give the

smallest average absolute deviation from experiment for the G2/97 test set of experimental energies[92]. The B3LYP density functional[93,94] used for the calculation of the geometries and zero-point energies is a linear combination of Hartree–Fock exchange, 1988 Becke[95] exchange, and Lee, Yang, Parr (LYP)[96] correlation.

7 Finally, the total energy at 0 K is obtained by adding the zero-point energy, obtained from the frequencies of step 2 to the total Energy:

$$E_0(G3B3) = E_e(G3B3) + E(ZPE)$$

The final total energy is effectively at the *QCISD(T,FULL)/G3large* level if the different additivity approximations worked well. The validity of such approximations has been previously investigated for G2 theory on the G2-1 subset of G2/97 and found to be satisfactory.
A summary output for a G3B3 calculation is the follow:

Temperature=	298.150000	Pressure=	1.000000
E(ZPE)=	0.064728	E(Thermal)=	0.070125
E(QCISD(T))=	-722.615825	E(Empiric)=	-0.121680
DE(Plus)=	-0.019091	DE(2DF)=	-0.236506
E(Delta-G3)=	-0.682544	E(G3-Empiric)=	-0.121680
G3(0 K)=	-723.610918	G3 Energy=	-723.605522
G3 Enthalpy=	-723.604577	G3 Free Energy=	-723.640039

Fig 3.2—1 Example of a summary output for a G3B3 calculation for 2Cl-pyrimidine molecule. All the energies are in Hartree.

The parameters in the red frame are the ones used for a ΔH and AE calculationand will be discussed in the next section.
The *G3(0K)* is exactly the same quantity $E_0(G3B3)$ that has been described above. Starting from this, it is possible to describe the other quantities.

G3(0K) = Zero-point-corrected electronic energy: $E_0(G3B3) = E_e(G3B3) + E(ZPE)$

G3 Energy = Thermal-corrected energy: $E = E_0(G3B3) + E_{trans} + E_{rot} + E_{vib}$

G3 Enthalpy = Enthalpy computed using the G3B3 predicted energy:

$H^{\circ}_{M,298}$ = E + RT

G3 Free Energy = Gibbs Free Energy computed using the G3B3 predicted energy: G = $H^{\circ}_{M,298}$ − TS

Using these quantities it is possible to calculate the ΔH values for all the species and subsequently the AE associated to each fragmentation channel according to eq.(3.1-25).

3.2.2 The Enthalpy of formation

The calculation of the enthalpy of formation follows two steps: 1) the calculation of the enthalpy of formation ΔH°_{f0} of the species involved in the reaction; 2) the calculation of the enthalpies of formation ΔH°_{f298} of the species at 298K. These calculations require the knowledge of:

- the atomization energy of the molecule, $\sum D_0\,(M)$;
- the heats of formation of the atoms at 0K, $\Delta H^{\circ}_{f0}(X)$;
- the enthalpy corrections of the atomic elements, $(H^{\circ}_{X,298} - H^{\circ}_{X,0})$;
- the enthalpy correction for the molecule, $(H^{\circ}_{M,298} - H^{\circ}_{M,0})$;

where *M* stands for the molecule/fragment, *X* represents each atom which makes up *M* and *x* will be the number of *X* atoms in *M*.
The atomization energy of *M* is calculated from the total energy $(\mathcal{E}_0(M))$, the zero-point energy $(\mathcal{E}_{ZPE}(M))$ and the energy of the constituent atoms [97]:

$$\sum D_0(M) = \sum_{atoms} x\,\mathcal{E}_0(X) - \mathcal{E}_0(M) - \mathcal{E}_{ZPE}(M) \tag{3.2-1}$$

In this equation, the $\mathcal{E}_0$ value corresponds to the E_e described before, so for the atomic species (X), where the E(ZPE) is equal to 0, the $\mathcal{E}_0$ value correspond to the G3(0K) value obtained in the output file, while for the molecules $\mathcal{E}_0(M) + \mathcal{E}_{ZPE}(M)$ correspond to E_e*(G3B3)* + *E(ZPE)*. So the last two terms match to E_0*(G3B3)* and it is possible to rewrite the equation (3.2-1) using the output values from the Gaussian code:

$$\sum D_0(M) = \sum_{atoms} x\,[G3(0K)](X) - [G3(0K)](M)$$

(3.2-2)

the enthalpy correction for all the species is:

$$H_T^\circ - H_0^\circ = \int_0^T C_P dT$$

(3.2-3)

The enthalpy of formation $\Delta H_{f0}^\circ(X)$ and the enthalpy correction $H_{X,298}^\circ - H_{X,0}^\circ$ are tabulated in ref [98]. The latter values, given for the elements in their standard states, are used to convert the atomic heats of formation at 0 K to those at 298 K. Experimental atomic enthalpies, which have the accuracy of ±0.84 kJ/mol [99] have been used. From this, it is possible to calculate $\Delta H_{f298}^\circ(M)$:

$$\Delta H_{f0}^\circ(M) = \sum_{atoms} x\Delta H_{f0}^\circ(X) - \sum D_0(M)$$

(3.2-4)

$$\Delta H_{f0}^\circ(M) = \sum_{atoms} x\Delta H_{f0}^\circ(X) - \left\{ \sum_{atoms} x\,[G3(0K)](X) - [G3(0K)](M) \right\}$$

(3.2-5)

$$\Delta H_{f298}^\circ(M) = \Delta H_{f0}^\circ(M) + (H_{M,298}^\circ - H_{M,0}^\circ) - \sum_{atoms} x(H_{X,298}^\circ - H_{X,0}^\circ)$$

(3.2-6)

Substituting the values obtained by the output of G3B3 calculation:

$H_{M,298}^\circ$ = G3 Enthalpy (for the molecule)
$H_{M,0}^\circ$ = G3 (0K) (for the molecule)

The eq.(3.2-6) can be rewritten:

$$\Delta H^{\circ}_{f298}(M) = \Delta H^{\circ}_{f0}(M) + [G3\ Enthalpy(M) - G3\ (0K)(M)] - \sum_{atoms} x(\ H^{\circ}_{X,298} - H^{\circ}_{X,0})$$

(3.2-7)

Substituting the eq.(3.2-5) in the eq.(3.1-24) for the calculation of the AE at 0K all the contributions associated to the atomic species are eliminated during subtraction. Then it possible to use the eq.(3.1-25) to calculate the AE at 298K. The value $H^{\circ}_{M,298} - H^{\circ}_{M,0}$ corresponds to the difference $G3\ Enthalpy(M) - G3\ (0K)(M)$ obtained from the output file of the G3B3 calculation performed for the specific fragment whose AE has been experimentally measured. All the theoretical and experimental values of AEs are compared in Table 4.2-1 of chapter 4 in order to associate a particular fragmentation pattern and geometry to the AE of each measured fragment of the 2Br-, 2Cl- and 5Br-pyrimidine molecules.

3.2.3 Calculation of enthalpies of formation of 2Cl-pyrimidine ionic fragments

The ab initio calculations of the enthalpy of the 2Cl-pyrimidine molecule and some of its ionic fragments have also been performed. The following study is defined as complementary to the previous one and more focused on getting information about the enthalpies of formation and the geometries of the ionic fragments rather than on their appearance energy values.

In a preliminary study the calculations of the gas phase enthalpy of formation of the 2Cl-pyrimidine, HCN and ClCN neutral molecules have been done with the G2, G3B3 and G4 methods. Comparing these results to the literature values it has been observed that the G2 and G3B3 calculations are in closer agreement to the experimental results than the G4 calculations (Table 4.2-2 in chapter 4). Although the mean absolute deviation between the computed and literature standard state enthalpies of formation for a set of benchmark organic molecules is about 3.89 kJ/mol for G3B3 [100] method, 6.15 kJ/mol for G2 [101] and 3.35 kJ/mol for G4 [102] calculations, in our set of molecules (2Cl-pyr, ClCN and HCN) the best agreement between calculated and measured values is achieved by G2 and G3B3 methods. Therefore, the enthalpy of formation of the ionic fragments

has been calculated only with the G3B3 and G2 methods. The geometries of all the fragments have been optimized at DFT-B3LYP 6-311G++(*2d,2p*) level of theory. The G2 theory requires only one additional calculation, MP2/6-311+G(3df,2p), with respect to G1 theory. The G2 energy is then obtained by:

$$E_0(G2) = E_0\,(Gl) + \Delta + 1.14\ npair \tag{3.2-8}$$

where

$$\Delta = \text{MP2/6-311+G(3df,2p)} - \text{MP2/6-311G(2df,p)} - \text{MP2/6-31+G(d,p)} + \text{MP2/6-311G(d,p)} \tag{3.2-9}$$

and *npair* is the number of valence pairs. The value of 1.14 was established by imposing a zero mean deviation between the calculated and experimental [103] atomization energies of 55 reference molecules.

In the second part of the study, the 2Cl-pyrimidine molecule has been considered. Combining the measured value of the AE and the gas phase enthalpies of formation $\Delta H^{\circ}_{f,gas}(m_i, M)$ of known species, the 'experimental' value of the enthalpy of formation $\Delta H^{\circ}_{f,gas}(m_1^+)$ of specific cationic fragments, not yet available in literature has been derived following eq.(3.2-10):

$$\Delta H^{\circ}_{f,gas}(m_1^+) = AE + \Delta H^{\circ}_{f,gas}(M) - \sum\left[\Delta H^{\circ}_{f,gas}(m_i)\right] \tag{3.2-10}$$

The experimental values used for the gas phase enthalpies of formation of the parent molecule ($\Delta H^{\circ}_{f,gas}(M)$) and of the neutral fragments ($\Delta H^{\circ}_{f,gas}(m_i)$) are found in the literature [104,105,99]. The $\Delta H^{\circ}_{f,gas}(m_1^+)$ values obtained for the charged fragments are then compared to the calculated thermochemical enthalpies of formation. In this way it is possible to assign to each fragment the proper geometry and fragmentation channel.

Summarising, our theoretical study can be divided in two parts. Following

eq.(3.1-25) in the first part the AE of a specific fragment has been derived by calculating the enthalpies of formation of all the species. The comparison of these values with the measured ones (for the three molecules under investigation 5Br-, 2Br- and 2Cl-pyrimiidne) is useful to define a particular fragmentation channel and a specific geometry associated to each fragment. In the second part the attention has been focused on 2Cl-pyrimidine. In this case it is possible to derive the 'experimental' enthalpy of formation of a specific ionic fragment (m^+) following eq.(3.2-10), by using the AE experimental value of that fragment and the experimental enthalpies of formation (present in literature) for the other species in eq.(3.2-10). Once this 'experimental' enthalpy of formation is derived it is possible to compare it with the theoretical ones calculated following the eq.(3.2-7) for that specific fragment (m^+). Also in this case different geometries associated to the same ionic fragment have been studied, but by the comparison of the enthalpies of formation values it is possible to choose the right one and see that the two approaches will lead to the same result for the case of 2Cl-pyrimidine molecule.

It has not been possible to perform this type of calculation for 2Br- and 5Br-pyrimidine molecules because in these cases the experimental enthalpy of formation has not been measured and there are no data available in literature.

The results of the G3B3 AEs, the G2 and G3B3 enthalpies of formation calculations and the optimized geometries are summarized for all the fragments in chapter 4.

3.3 Equations for $AE_{T(exp)}$ and ΔH°_{f298} calculation using the Gaussian outputs

It is possible to derive the exact equation to calculate the $AE_{T(exp)}$ and ΔH°_{f298} of a generic fragment using the quantity obtained in the outputs of a Gaussian calculation. Considering the following equation:

$$M + h\nu \rightarrow M^+ + e^- \rightarrow {m_1}^+ + m_i + e^- \tag{3.3-1}$$

the $AE_{T(exp)}$ is derived using the output values obtained performing a

G3B3 calculation as the ones in the red frame of Fig 4.1—1. Substituting eq.(3.2-5) in eq.(3.1-24) all the atomic contribution are deleted by the subtraction. The substitution of eq.(3.1-24) in eq.(3.1-25) considering the eq.(3.2-3) and the values obtained by the output of G3B3 calculation like the *G3 Enthalpy* equal to $H^{\circ}_{M,298}$ and the *G3 (0K)* equal to $H^{\circ}_{M,0}$ for a molecule, leads to the following equation for the $AE_{T(exp)}$ of the fragment m_1^+:

$$AE_{T(exp)}(m_1^+) = \{G3(0K)(m_1^+) + G3(0K)(m) - G3(0K)(M) - [G3Enthalpy(M) - G3(0K)(M)]\} * 27.2107 + 0.0642 \quad (3.3\text{-}2)$$

The value 27.2107 is the conversion factor from hartree to eV and 0.0642 eV equal to $\frac{5}{2}RT$ expressed in eV for a temperature of 298 K.

The final equation for the calculation of ΔH°_{f298} of a general molecule *M* or a general fragment m^+ is obtained by substituting the eq.(3.2-5) in eq.(3.2-7) using the values tabulated in [98] (expressed in kcal/mol) for the atomic $\Delta H^{\circ}_{f0}(X)$ and $H^{\circ}_{X,298} - H^{\circ}_{X,0}$ quantities:

$$\Delta H^{\circ}_{f298}(M) = \sum_{atoms} x\Delta H^{\circ}_{f0}(X) - \left\{\sum_{atoms} x\,[G3(0K)](X) - [G3(0K)](M)\right\} * 627.5095 + \{[G3\,Enthalpy(M) - G3\,(0K)(M)]\} * 627.5095 - \sum_{atoms} x(H^{\circ}_{X,298} - H^{\circ}_{X,0}) \quad (3.3\text{-}3)$$

The 627.5095 value is the conversion factor from hartree to kcal/mol. Another conversion has been done as it will be shown in the tables in chapter 4, in order to express the enthalpies of formation in kJ/mol which is the most common unit used. The eq.(3.3-3) can be used to calculate the enthalpy of formation of a general molecule *M* and its fragment m_i and substituting these values in eq.(3.2-10) together with the experimental values of AE for the unknown fragment m_1^+ it is possible to calculate the ΔH°_{f298} of m_1^+ as already described.

4 Photofragmentation of halogenated pyrimidine molecules in the VUV range

The pyrimidine molecule constitutes the building block of three important nucleobases of the DNA (C, T) and RNA (U). For this reason it is considered a prototype molecule for the study of the pyrimidinic bases. It is reasonable that the results obtained in the study of the pyrimidine molecules[38, 23, 24] could be transposed to all the bases with the same aromatic structure. Same considerations can be done for the pyrimidine molecule and its halogenated derivatives in order to understand the effect of the halogenations [32].

The halogenated pyrimidines constitute an important class of prototype radiosensitizing molecules. The study of their fragmentation dynamics is of interest to understand the fundamental mechanisms of the enhanced radiation damage when these molecules are selectively incorporated in the DNA of tumor cells. The study of these mechanisms represents the starting point to understand the fragmentation dynamics of the real radiosensitizers as the halogenated uracil molecules.

These target molecules have a very high vapour tension and it is possible to sublimate them without heating the sample; in this way the contamination of the experimental set-up is avoided. The ionization energy of the parent ion and some selected fragments of 2Cl-, 2Br and 5Br-pyrimidine molecules have been measured and calculated, the possible fragmentation pathways will be discussed and the role played by the halogen atom and/or site of halogenations will be unraveled.

The pyrimidine molecule has a 6-membered ring structure, with two N and four C atoms. In the present chapter the valence dissociation pathways of Br- and Cl- pyrimidine molecules, where the halogen atom is in positions 2 or 5 of the ring is discussed. The purpose is to study the effect of the different halogen substitutions (Cl or Br in the 2Cl- and 2Br-pyrimidine, respectively) and site of halogenation (2 or 5 for the 2Br and 5Br-pyrimidine, respectively) in the fragmentation dynamics of the pyrimidinic ring.

Fig 4.1—1b-d shows the mass spectra of the pyrimidine and of the three studied molecules measured at 17 and 14 eV photon energy, respectively.

For each molecule the experimental approach consisted in the measurement

of a) the mass spectrum at a fixed photon energy and b) the appearance energy of the selected fragments.
In the first type of experiment the QMS is scanned over the full m/z range in order to identify the charged species produced by the fragmentation process. In the second type of experiment, a specific m/z fragment is selected by the QMS, the photon energy is scanned, typically in the range 8-14 eV, and the photoionization efficiency curve (PEC) is measured. The analysis of this ion yield curve, provides the experimental measurement of the appearance energy (AE) of that particular fragment. The results obtained will be now discussed in the following sections.

4.1 The mass spectra

Several fragments/fragmentation channels common to all species are clearly observed in the spectra in Fig 4.1—1b-d. They are produced according to the photoreactions described by the following equations:

$$C_4H_3N_2X + hv \rightarrow \mathbf{C_4H_3N_2X^{+\bullet}} + e^- \quad (1)$$
$$C_4H_3N_2X + hv \rightarrow \mathbf{C_3H_2NX^{+\bullet}} + HCN + e^- \quad (2)$$
$$C_4H_3N_2X + hv \rightarrow \mathbf{C_2HX^{\bullet+}} + HCN + HCN + e^- \quad (3)$$
$$C_4H_3N_2X + hv \rightarrow \mathbf{C_3H_2N^{+}} + HCN + X^{\bullet} + e^- \quad (4)$$
$$C_4H_3N_2X + hv \rightarrow \mathbf{C_4H_3N_2^{+}} + X^{\bullet} + e^- \quad (5)$$
$$C_4H_3N_2X + hv \rightarrow \mathbf{C_3H_3N^{+\bullet}} + XCN + e^- \quad (6)$$
$$C_4H_3N_2X + hv \rightarrow \mathbf{C_3H_2N^{+}} + XCN + H^{\bullet} + e^- \quad (7)$$

which can be identified as the formation of the unfragmented parent ion, eq. (1), and the HCN eq. (2), 2(HCN) eq. (3), (HCN + X) eq. (4), (X) eq. (5) , (XCN) eq (6) and (XCN + H) eq.(7) losses. In these schemes *X = Cl, Br*, the detected charged fragment is reported in bold while the neutral, undetected, fragments are reported in italic. The photoionization efficiency curves of the most prominent fragments have been measured and will be discussed in sections 4.2, 4.3 and 4.4.
In the presentation and discussion of the results, it is important to remember the similarities and differences in the geometrical structure of the three samples among themselves and with respect to the pyrimidine molecule, which can be used as a reference. Indeed, as already mentioned

in the previous chapter and summarized in the eq. 1-7 there are fragmentation channels that can be considered equivalent in terms of bond breaking localization.

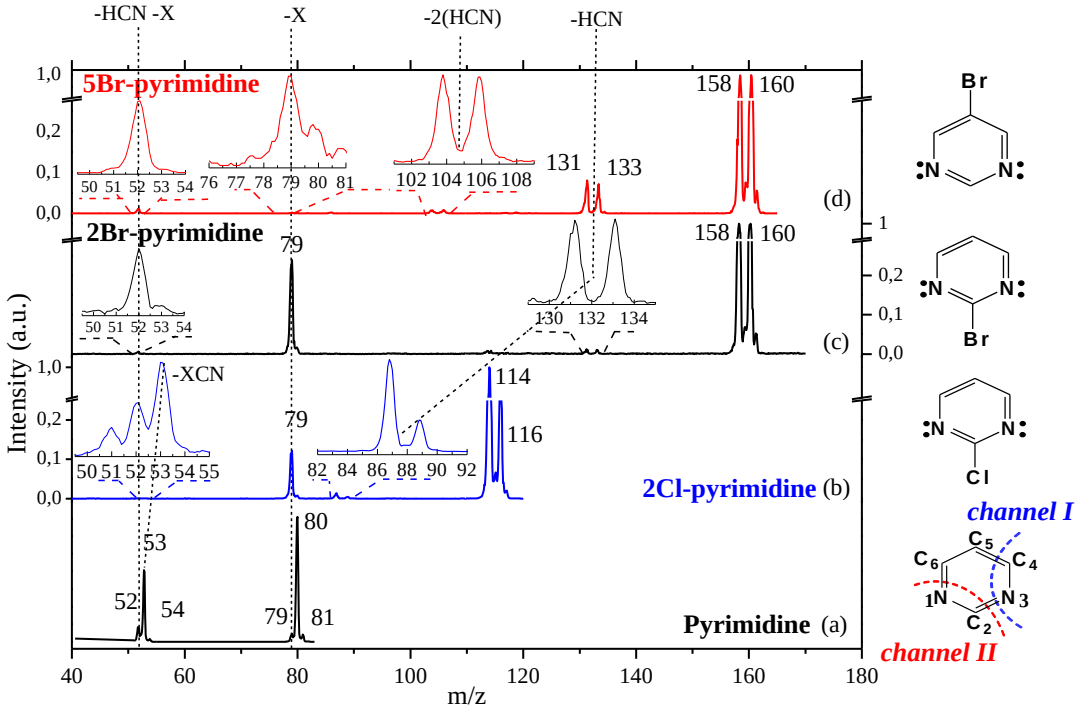

Fig 4.1—1 The photoionization mass spectra of (a) pyrimidine measured at 17eV photon energy, (b) 2Cl-pyrimidine, (c) 2Br-pyrimidine and (d) 5Br-pyrimidine recorded at 14 eV photon energy. The breaks in the y-axis are meant to emphasize low intensity features.

As it will be discussed later on, the comparison of these equivalent fragmentation channels, in the light of the theoretical results, provides essential information about the interplay of inductive and resonant effects induced by the halogenation on the pyrimidine ring, and their role in the dynamics of fragmentation. It is known from previous studies [109,106,107,108] that the leading fragmentation channels of the pyrimidine molecule in the VUV energy range are due to the loss of one or two neutral HCN fragments, and the loss of HCN + H leaving the residual $C_3H_3N^+$ (m/z=53), $C_2H_2^+$ (m/z=26) and $C_3H_2N^+$ (m/z=52) charged fragments, respectively (Fig 4.1—1a). Equivalent patterns can be identified in the halogenated pyrimidine molecules (eq. 2-7).

In Fig 4.1—1 the group of peaks at the highest m/z values correspond to the parent ions, with their respective isotopic distribution. At 14 eV they

always represent the dominant feature of the spectrum. In the Br-pyrimidine systems, the peaks at m/z=160 and 158 have almost the same intensity according to the relative abundances of the ^{79}Br and ^{81}Br isotopes (50.8 % and 49.2 % respectively), while in the 2Cl-pyrimidine case, the ratio of intensity of the peaks at m/z=114 and 116 is about a factor 3 due to ^{35}Cl and ^{37}Cl isotope ratio (75.77% and 24.23% respectively). The relative abundances of the Br and Cl isotopes are very useful fingerprints for the assignment of specific fragments in the mass spectra. The tiny features observed at 1 mass unit, above the parent ions, represent the contribution of the ^{13}C isotope, whose abundance with respect to ^{12}C is about 1%.

The mass spectrum of the pyrimidine molecule measured at 17 eV photon energy is shown in Fig 4.1—1a. The AE of the parent ion (m/z=80) and fragment at m/z=52 due to the loss of the HCN group has been measured. The values found (9.23 ± 0.03 and 13.48 ± 0.06 eV respectively) are consistent with the previous results by Schwell et al [109] (9.21 ± 0.05 and 13.75 ± 0.1).

The fragmentation channel due to the loss of a neutral HCN group in pyrimidine may occur via two different, but indistinguishable fragmentation pathways. In a case the process involves the rupture of the C2–N3 and C4–C5 bonds, resulting in an isonitrile form (R−NC see Fig 4.1—1). This type of fragmentation will be named *channel I* in the following. The other case, that will be named *channel II*, involves the rupture of the N1–C6 and C2–N3 bonds, resulting in a nitrile form (R−CN), i.e. acrylonitrile. The measurements of six different deuterium substituted pyrimidines by Milani-Nejad and Stidham [110] show that *channel I* is favored. The fragmentation channel due to the loss of a neutral HCN group can be observed also in the halogenated cases (eq. 2). In the 2Cl- and 2Br-pyrimidine molecules the position of the halogen atom in site 2 makes the two channels distinguishable. Indeed, *channel I* corresponds to the HCN loss with formation of different radical cations containing Br/Cl atom respectively (peaks at m/z=131/133 u. in the Br-pyrimidines, and 87/89 u. in the 2Cl-pyrimidine). On the other hand, *channel II* corresponds to XCN rather than HCN loss, leading to the formation of fragments of m/z =53 in both 2Cl- and 2Br-pyrimidine cases (eq. 6).

The channel corresponding to the loss of two HCN groups (eq. 3) is observed only in the 5Br-pyrimidine case at m/z=104/106 ($C_2HBr^{+\bullet}$ Fig

4.1—1d), while it is absent in the 2Br and 2Cl-pyrimidine cases. This can be explained by following the previous considerations on the interplay of *channel I* and *channel II* in the HCN loss. Indeed, in the 5Br-pyrimidine the loss of two HCN groups may occur following a combination of *channels I* and *II*, directly leaving a residual halogenated acetylene fragment. A similar mechanism is not available in the 2X-pyr molecules, where the loss of two HCN groups would imply a complicated molecular rearrangement.

In the pyrimidine mass spectrum the peak at m/z=79, due to the loss of the H atom, is barely visible [109]. In the halogenated pyrimidine cases, the same fragment can be attributed to the loss of the neutral halogen atom. In all cases, this will lead to a residual $C_4H_3N_2^+$ (eq. 5). In principle, in the Br-pyrimidines, the same m/z value could be also assigned to the $^{79}Br^+$ fragment, corresponding to the complementary process, where the breaking of the C-Br bond leaves the residual charge on the Br atom rather than on the ring. However, the absence of the twin peak due to the $^{81}Br^+$ isotope (Fig 4.1—1c and Fig 4.1—1d) clearly indicates that this second fragmentation channel, even though dominant in the higher photon energy range [111,112], can be excluded in the VUV range.

The peak at m/z=53, that in the pyrimidine molecule represents the HCN loss, has a correspondence in the halogenated cases in the loss of the CN group plus the halogen atom. It is observed only in the 2Cl-pyrimidine mass spectrum where it corresponds to the loss of the ClCN group (eq. 6). This may occur via fragmentation *channel II*, with the H atom replaced by Cl in position 2. In the 5Br-pyrimidine case, it is difficult to form this fragment as it would involve a complex rearrangement with a simultaneous/sequential loss of a CN group and the Br atom, thus it is unlikely. However, its absence in the case of the 2Br-pyrimidine molecule seems to suggest that the different halogen atoms affect the dynamics of this fragmentation channel. In contrast to the pyrimidine molecule, this seems to be a minor channel in the case of the halogenated molecules. In the works on pyrimidine by Schwell et al. [109], Vall-llosera et al. [113] and Plekan et al [114], where the incident photon energies are 20, 23 and 21.2 eV respectively, the intensity of the m/z=53 fragment is comparable to the intensity of the parent ion. The electron impact partial ionization cross section measurements performed in pyrimidine by Linert et al. [115] show similar trends, with the m/z =53 fragment among the most intense features

of the mass spectrum over the full electron energy range, apart from the near threshold region. One possible explanation of the different ratios observed here is that the low photon energy employed (14eV) corresponds to different relative cross section between the two channels. However another possibility is that *channel I* is favoured with respect to *channel II* for the breaking of the C-C and C-N bonds of the pyrimidinic ring in the case of 2Cl and 2Br-pyrimidine.

The peak at m/z=52, that in the pyrimidine case is due to the loss of the HCN + H fragments, is observed in all the spectra of the halogenated molecules and corresponds to the loss of the HCN group and the halogen atom (eq. 4) or the loss of XCN group and hydrogen atom (eq. 7).

In general, the observed branching ratios can be compared among the three spectra taken at the same photon energy and QMS setting (fig. Fig 4.1—1b-d), providing some hints on the more likely fragmentation patterns. By comparing, for example, the peaks at m/z=79 and 131/133 (87/89) in the Br- (Cl-) pyrimidine cases it follows that, at the same photon energy, the loss of the halogen atom appears to be more likely with respect to the HCN loss when the halogen atom is in position 2 of the ring, rather than in position 5.

4.2 Photoionization efficiency curves of 2Cl-pyrimidine

The photoionization efficiency curve of the parent ion and the three fragments m/z=52, 79 and 87 of 2Cl-pyrimidine are shown in figures Fig 4.2—1a-d respectively, while the principal fragmentation decay paths are shown in Scheme 4.2-1. The experimental AEs are collected in Table 4.2-1, where they are compared with the calculated values. A list of all the optimized geometries of the fragments is shown in appendix All the PECs are shown in Fig 4.2—1, Fig 4.3—1 and Fig 4.4—1 on a linear scale. The experimental AE values are determined from the semilog plots of the PEC by fitting straight lines to the background and to the ion signal in the threshold region, as shown for example in the inset of figure Fig 4.2—1a. The photon energy at the intersection of these two lines is the measured AE value at 298K ($AE_{T(exp)}$), the temperature of the experiment.

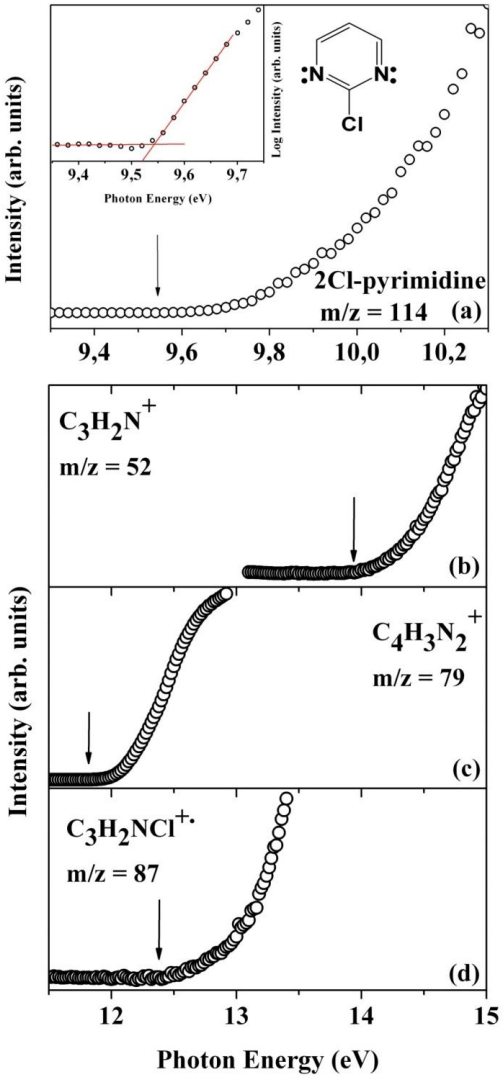

Fig 4.2—1 Photoionization efficiency curves of the parent ion (a) and three of the 2Cl-pyrimidine fragment ions (b), (c) and (d). In the parent ion case, (inset of figure a) the threshold region is expanded and reported in log scale. The measured AE values are indicated by an arrow and reported Table 4.2-1.

The uncertainty in the AE value is estimated to be about 0.05-0.10 eV and depends on the sharpness of the photoionization efficiency curve. Even though the use of the semilog rather than the linear scale has the advantage of increasing the sensitivity of the data analysis procedure, it is important to remember that the measured values of AE also depend on the sensitivity of the experimental set-up (time of acquisition, number of counts, statistics, efficiency and sensitivity of the instrumental set-up), so that the measured AE have to be considered as the upper limits of the effective AE.

channels			2Cl-pyrimidine				2Br-pyrimidine				5Br-pyrimidine			
m/z	*Possible fragment cation* m_1^+	*Neutral fragments*	AE_{exp} *(eV)*	AE_{G3B3} *(eV)*			AE_{exp} *(eV)*	AE_{G3B3} *(eV)*			AE_{exp} *(eV)*	AE_{G3B3} *(eV)*		
				Geom.	AE_{298K}	*Process*		*Geom.*	AE_{298K}	*Process*		*Geom.*	AE_{298K}	*Process*
(parent ion)			9.54 ± 0.05		9.61	(IE)	9.50 ± 0.05		10.00	(IE)	9.39 ± 0.08		9.91	(IE)
87 (2Cl-pyr) 131 (2Br-,5Br-pyr)	$C_3H_2NX^{+\bullet}$	HCN	12.40 ± 0.05	1. 2. 3. 4.	11.65 11.64 12.25 **12.35**	C C C C	12.52 ± 0.05	1. 2. 3. 4. 9.	11.45 11.48 12.06 12.20 **12.41**	C C C C C	12.08 ± 0.05	3. 2.	**11.96** 11.66	C.I C.II
104	$C_2HX^{+\bullet}$	2HCN	---	---	---	---		---	---	---	13.62 ± 0.05	1.	**13.42**	B
79	$C_4H_3N_2^+$	$X^\bullet$	11.84 ± 0.05		**11.92**	A	11.06 ± 0.05		**11.27**	A	12.35 ± 0.1		**12.33**	A
		HCN + $X^\bullet$		5. 6. 7.	14.79 14.33 12.65	A/B/C.3/C.4 C.1 C.2		5. 6. 7. 10.	14.15 **13.69** 12.01 14.34	A/B/C.3/C.4 C.1 C.2 C.5		4. 5. 6. 7.	**13.66** 15.08 14.70 11.97	A.II/C.IIa E.I/C.Ia/A.I E.II E.II’
52	$C_3H_2N^+$	$HCNX^\bullet$	13.92 ± 0.1	6. 7. 8.	14.04 12.36 14.71	D.1 D.2 D.3	13.60 ± 0.1	6. 7. 8.	13.92 12.23 14.59	D.1 D.2 D.3	13.17 ± 0.07	7.	12.20	D
		XCN + $H^\bullet$		7. 8.	**13.68** 16.03	E.2 E.3		7. 8.	**13.56** 15.91	E.2 E.3		--- ---	--- ---	--- ---

Table 4.2-1 Experimental and theoretical values of the halogenated pyrimidines appearance energy and fragmentation products. Theoretical AE corresponding to the proposed fragmentation paths are in bold.

For the **parent ion**, the measured IE value of 9.54 ± 0.05 eV is consistent with the calculated value of 9.61 eV, but lower than the experimental determination of 9.84 ± 0.02 of the $6b_2(n_{N-})$ ground electronic state of 2Cl-pyrimidine by photoelectron spectroscopy [116]. This difference can be explained considering that the photoelectron spectroscopy provides vertical ionization energies and depends on the Franck-Condon overlap between the involved states, while the experimental IE determined here corresponds to the onset of the ion signal. The theoretically predicted AE (11.92 eV) for the **m/z =79** fragment (process A) is also in good agreement with the experiment (11.84 ± 0.05 eV). In both cases, the final state of the reaction is relatively simple, with the unbroken molecule or the loss of the halogen atom, respectively. Further considerations will be needed in the case of the m/z =87 and 52 fragments, where several scenarios can, in principle, arise.
As discussed in the previous section, only *channel I* can contribute to the m/z =87 (AE = 12.40 ± 0.05 eV) fragment (process C) in the 2Cl-pyrimidine case. In the calculations several possible geometries for the residual $C_3H_2NCl^{+\bullet}$ fragment have been considered and their enthalpies of formation have been computed. The resulting four lowest geometries, labelled 1 to 4 in order of increasing energy, are reported in Scheme 4.2-1. The structure 4 is obtained in the DFT calculation by removing the C4, N3 atoms as well as the H atom bound to C4. In this way rearrangement or isomerization neither of the parent ion structure before the fragmentation nor of the residual charged fragments after the fragmentation are needed. The computed energy for structure 4 (12.35 eV) is consistent with the measured AE value within the experimental error. The other structures are obtained by isomerization. Structure 1 is the lowest in energy, therefore this geometry appears to be the most stable, as already proposed by Schwell et al. [109] for the HCN loss in pyrimidine. Indeed, the calculated AEs of structures 1, 2 and 3 are all lower than the experimental value, but transition from one to another requires a molecular rearrangement, i.e. the formation of transient species with barriers to overcome. In the present case the calculated barriers between the four configurations of the $C_3H_2NCl^{+\bullet}$ fragment, labelled 1-4 in Scheme 4.2-1, are all larger than 1 eV, as shown in Fig 4.2–2.

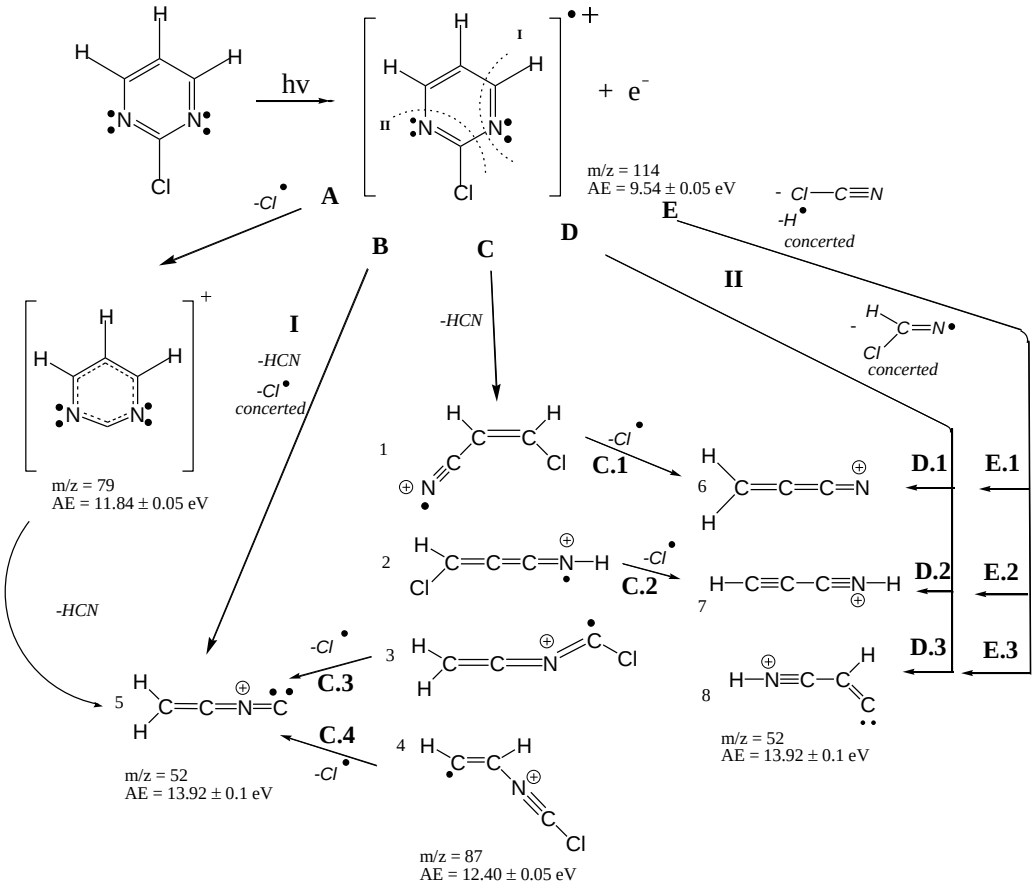

Scheme 4.2–1 Main fragmentation decay routes of the 2Cl-pyirimidine molecule. The measured values of the appearance energy are given for each fragment. The final geometries of the charged fragments have been labelled with numbers 1-8, while the possible fragmentation patterns are labelled with letters A-E. The E.n and D.n (n = 1,2,3) channels correspond to the loss of the H atom bound to C6, C5 or C4 atoms, respectively, after the loss of the ClCN group. The geometries have been optimized at DFT, B3LYP 6-311++G(2d,2p) level using the Gaussian09 suite of programs and the calculated energies are reported in Table 4.2-1.

The values of the calculated energy barriers are too high to explain the transition from the most likely structures 4 or 3 to the energetically more favorable structures 1 and 2 of the fragment. The proximity of the theoretical AE of fragment 4 to the experimentally measured AE may suggest that such stable geometry is formed in the threshold region and until there is not enough energy to overcome the barrier towards more stable geometries. In the light of these considerations the structure 4 has been assigned to the $C_3H_2NCl^{+\bullet}$ fragment (m/z=87).

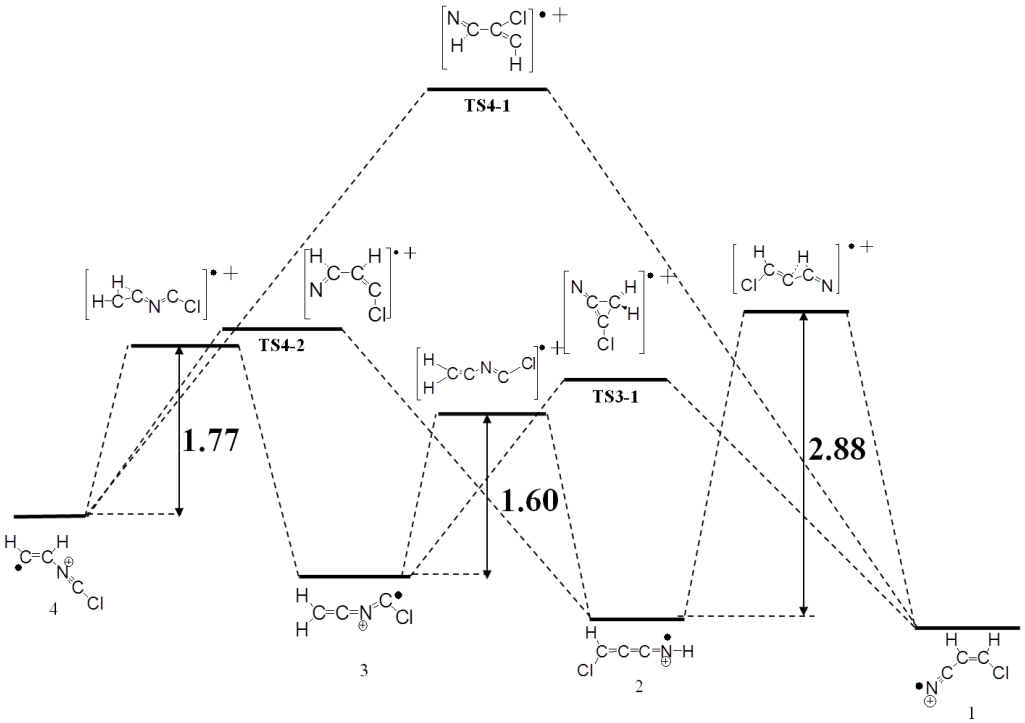

Fig 4.2—2 Potential energy barriers in eV between structures 4 to 1 of the H2C3NCl+• fragment of 2Cl-pyrimdine. In all the cases the geometries are optimized at the DFT-B3LYP level, the relative energies are calculated using B3LYP 6-31g(d) basis set and the transition states are obtained using a qst3 calculation. The energy barriers to reach TS4-2, TS4-1 and TS3-1 are respectively 1.83, 2.86 and 1.89 eV.

The **m/z=52** fragment is assigned to the residual $C_3H_2N^+$ ion after the HCN and Cl (or ClCN and H) loss. The experimental AE value is 13.92 ± 0.1 eV. This is a challenging case for the theoretical calculations. This fragment indeed may be obtained either by concerted (processes B, D and E) or sequential (processes A and C) reactions in the Scheme 4.2–1. Moreover different geometrical structures of the charged (structures 5-8) and neutral fragments can be involved (see Scheme 4.2–1). Firstly, the loss of HCN and Cl radical has been treated for first. This may happen in a simultaneous or a sequential way. From the theoretical point of view, in the first case (process B) the HCN group and the Cl atom are removed simultaneously from the neutral molecule, then the geometry of the fragment is re-optimized and its enthalpy of formation computed. The sum of the enthalpies of formation of the two separated neutral fragments HCN and $Cl^{\bullet}$, according to formula (22), gives the AE of 14.79 eV (Table 4.2-1), much higher than the experimental determination of 13.92 ± 0.1 eV. This

mechanism is related to the *channel I* of HCN loss. In the sequential process, the loss of the halogen atom may precede (process A) or follow (process C) the loss of the HCN group. In both cases the geometry of the intermediate fragment obtained removing the first species is re-optimized before removing the second one. In the latter case, process C, the first step coincides with the formation of the m/z=87 and has already been discussed in this section. The subsequent Cl loss from fragments in structures 1 to 4 leads to structures 5, 6 or 7 depending upon the intermediate state.
Another possible scenario implies the loss of the ClCN group and a hydrogen atom (processes D and E) in a concerted or sequential way proceeding through *channel II*. Several sequential cases (see Scheme 4.2–2 and Scheme 4.2–3) have been considered in the theoretical calculation, including the loss of each one of the three possible H atoms preceding/following the ClCN loss and the possibility of formation of both the $HCNCl^{\bullet}$ or $ClCN+H^{\bullet}$ neutral fragments.

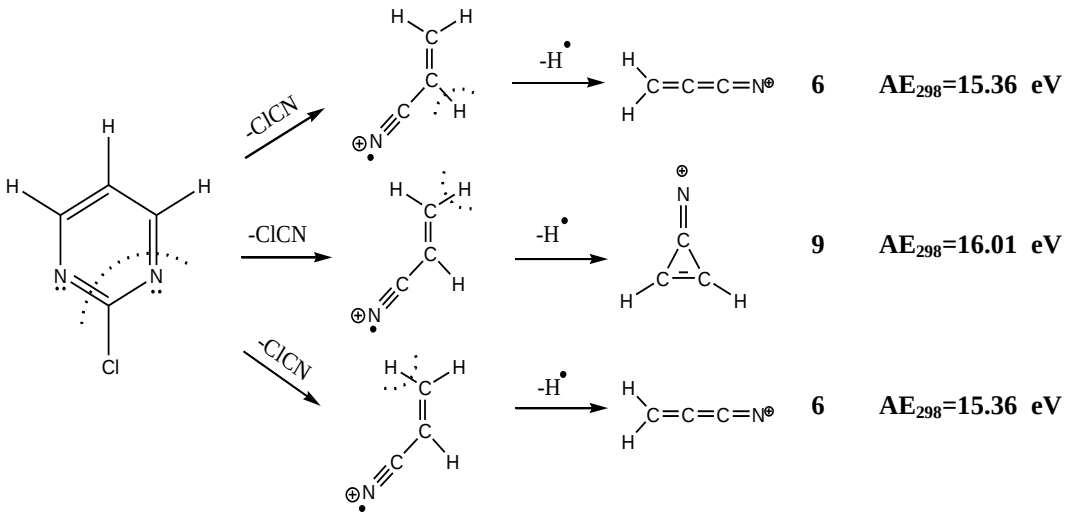

Scheme 4.2–2 Sequential fragmentation patterns of the ClCN loss followed by the H radical loss in the case of 2Cl-pyrimidine. The relative calculated AE_{298} are shown.

Most of these sequential patterns following *channel II* end up in similar final states as their equivalent concerted reactions, while others give three atom ring sterically hindered structures with correspondingly higher AE (structure 9 in Scheme 4.2–2 and structure 10 in Scheme 4.2–3).. For these reasons the sequential paths have been discarded and suggested that, from the energetic point of view, a concerted reaction is favoured. This leads to

the structures 6, 7 or 8 in Scheme 4.2–1, depending on which H atom is removed.

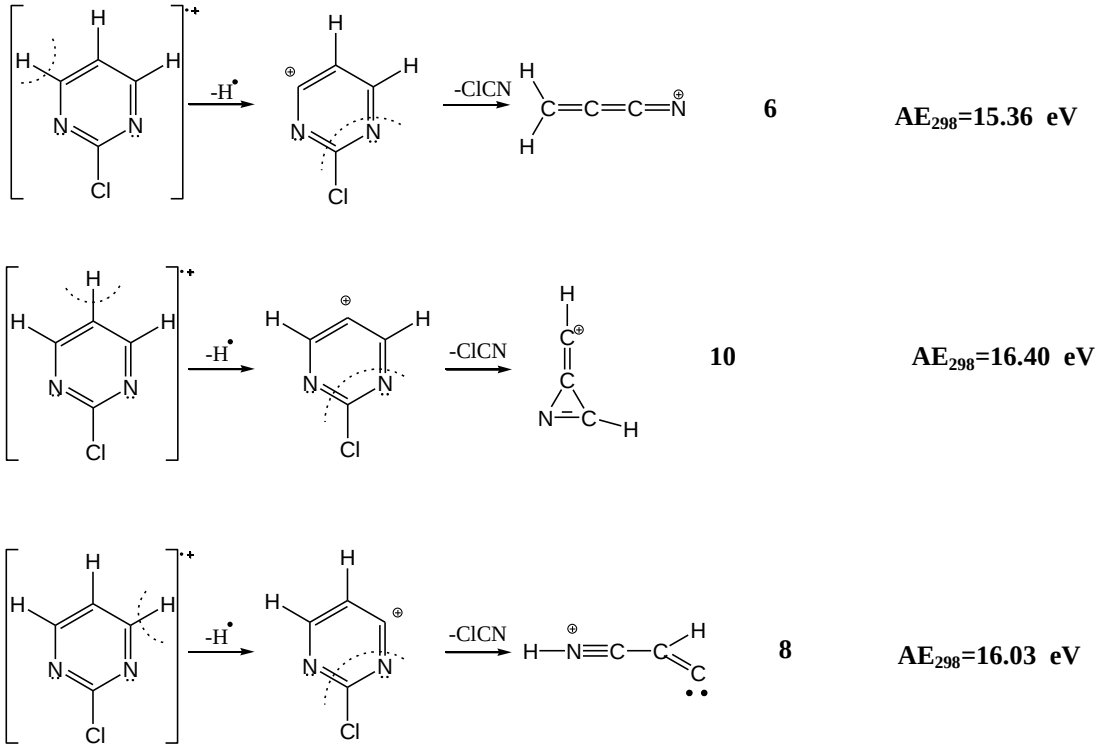

Scheme 4.2–3 Sequential fragmentation patterns of the H radical loss followed by the ClCN loss in the case of 2Cl-pyrimidine. The relative calculated AE_{298} are shown.

It is important to remember that in the present calculation the values of the AE depend not only on the geometry of the charged fragment but also on the structure of the neutral fragments and therefore, to some extent, on the fragmentation mechanism. So, for example, the appearance energies of processes C.1, D.1 and E.1 are all different although they end up with the same structure of the charged fragment, while the computed AEs of processes A, B, C.3 and C.4 are all the same and are therefore indistinguishable. This of course refers only to the adiabatic AE calculated according to eq.s (21-22), while most likely there will be energy barriers to overcome, not included in the present calculations. These results have been summarized in Table 4.2-1, where both the theoretical AE and the corresponding geometries and reaction mechanisms are reported.

The calculated AE for the charged fragment in geometry 5 (14.79 eV) is too high compared to the experimental value, so the fragmentation pathways A, B, C.3 and C.4 can be discarded. A similar conclusion applies to the pathways E.3, E.1, D.3 and C.1 with calculated AE of 16.03 eV, 15.36 eV, 14.71 eV and 14.33 eV, respectively. Mechanisms E.n and D.n (n = 1,2,3) of *channel II* type and leading to structures 6-8 differ only by the lost H atom. In these cases the linear structure 7 is obtained by forcing the input geometry to have the N1-C6-C5 angle larger or equal to 133°, which is greater than the equilibrium value of 122.48° for the neutral molecule. This would imply the existence of a reverse barrier for the formation of an activated complex with this larger angle preceding fragmentation. The overcoming of the barrier can explain the 0.24 eV difference between the measured and calculated AE values. As already mentioned, the calculations do not take into account the energy of the barrier, giving a theoretical AE lower than the experimental one. In the case where the linear structure 7 is formed in a sequential process from *channel I* via structure 2, (process C.2), no angle straining is needed. In such case an AE value lower than the experimental one is obtained. In principle this energy difference could be due to the need to overcome the potential barrier from structure 4 to 2 (see Fig 4.2—2). However, the value of the calculated barrier, 1.83 eV, is not consistent with the difference of 1.27 eV between the experimental and calculated AE for path C.2. The most probable path suggested is E.2, which gives the nearest AE value to the experimental one. Pattern E.2, corresponds to the concerted loss of ClCN + $H^{\bullet}$, involving the H atom bound to C5. The molecular rearrangement leading to the formation of the neutral $HClCN^{\bullet}$ radical with the migration of an H atom bound to the C4, C5 and C6 atoms, respectively, may occur, too, via processes D.1 to D.3. As already noted by Schwell et al. [109] in the pyrimidine case the loss of H_2CN or its isomer HCNH are less probable because these radicals involve more endothermic reactions and, moreover, their formation would require rearrangement of at least a H atom. So this pattern, although leading to more stable fragments, will probably require significant energy barriers to overcome.

4.2.1 Fragments enthalpies of formation: G2 and G3B3 calculations

In the previous section, the AE of selected fragments of the 2Cl-py molecule have been computed; and by comparing the theoretical and experimental AE values, a specific geometry and fragmentation pattern have been associated to each fragment.

In this section an alternative and complementary approach for the 2Cl-pyrimidine molecule has been considered. In this case combining the measured value of the AE and the gas phase enthalpies of formation $\Delta H^{\circ}_{f,gas}(m_i, M)$ of known species, the 'experimental' value of the enthalpy of formation $\Delta H^{\circ}_{f,gas}(m_1^+)$ of specific cationic fragments not yet available in the literature has been determined. The theoretical approach on which the procedure relies has been described in section 3.2.3 of chapter 3.

The combination of the measured AEs and the literature experimental $\Delta H^{\circ}_{f,gas}(M, 298K)$ of the neutral fragments found in literature [104, 99, 105] provides the experimental determination of the $\Delta H^{\circ}_{f,gas}(m_i^+, 298K)$ of the cation fragments, eq.(3.2-10). The comparison of these values with the theoretical ones, where the gas phase enthalpy of formation of the main fragments is directly calculated, allows to associate a particular geometry to each fragment and to suggest a specific fragmentation pattern.

The experimental value of ClCN $\Delta H^{\circ}_{f,gas}(M, 298K)$ used in eq.(3.2-10) is 132.38 kJ/mol (Table 4.2-2).

	$\Delta H^{\circ}_{f,gas}$ (kJ/mol)			
	G2	**G3B3**	**G4**	**exp**
2Cl-pyr	154.55	154.00	151.78	155.10 ± 1.6 [6]
HCN	130.38	128.08	128.15	135.14 ± 8.4 [7]
ClCN	131.80	131.82	130.87	132.38 [99]* 137.95 [105]*

*Table 4.2-2 Comparison of gas phase experimental enthalpies of formation with those calculated using G2, G3B3 and G4 methods. *these experimental values, are given in the litterature without uncertainty.*

The experimental values of the $\Delta H^{\circ}_{f,gas}(m_1^+)$ and those calculated using G2

and G3B3 methods are summarized in Table 4.2-3. In this table the structure 3 associated to the fragment at **m/z=87** has not been reported because the G2 energy calculation failed in the first step of the calculation (see section 3.2.3) involving the optimization of the geometry. Indeed G2 calculation optimizes the geometry at HF level and it is possible that starting from a geometry already optimized at DFT-B3LYP level of theory the computation does not recognize it as a minimum in the energy curve. For this reason the structure 3 has been discarded in the comparison of results in Table 4.2-3.

Among the three structures, the computed energies of 1245.04 kJ/mol and 1237.95 kJ/mol in the G2 and G3B3 methods, respectively, for structure 4 are the closest to the experimental value of 1216.40 ± 14.8 kJ/mol. The other structures are obtained by isomerization. The calculated $\Delta H^{\circ}_{f,gas}$ of structures 1 and 2 are lower than the experimental value (more than 30 kJ/mol) and transition from one to the other requires molecular rearrangement, i.e. the formation of transient species with barriers to overcome, as already discussed in the previous section, and shown in Fig 4.2—2. Consistently with the results obtained by the AE calculations the proximity of the theoretical $\Delta H^{\circ}_{f,gas}$ of fragment 4 to the experimental $\Delta H^{\circ}_{f,gas}$ one suggests that this stable geometry is the one formed, at least in the threshold region of ionisation.

The **m/z=79** fragment is assigned to the unbroken ring which has lost the halogen atom. The difference between the experimental and both calculated enthalpies of formation is about 20 kJ/mol, i.e. of the same order of magnitude found for the previous case. This suggests the presence of more stable structures of this fragment, like for example an open ring structure.

The **m/z=52** fragment ($C_3H_2N^+$) is considered as the product of the fragmentation channel involving the HCN and Cl loss that can preceed via sequential (process A and C in Scheme 4.2–1) or concerted (process B in Scheme 4.2–1) reactions or involving the ClCN and H loss in a sequential (Scheme 4.2–2 and Scheme 4.2–3) or concerted (process E in Scheme 4.2–1) manner. The possibility of the release of a HClCN moiety (process D in Scheme 4.2–1 has not been analysed because its experimental enthalpy of formation is not available in literature. Therefore there is no possibility to calculate the experimental $\Delta \boldsymbol{H^{\circ}_{f,gas}}(\boldsymbol{m_1^+})$ of $C_3H_2N^+$ obtained

by the releasing of HClCN.

Considering the HCN and Cl release, in the case of structure 5 the calculated energies using both the G2 and G3B3 theoretical methods are much higher than the experimental determination of 1241.75 ± 19.7 kJ/mol. Thus the fragmentation pathway B has been discarded. In the sequential process, the loss of the halogen atom may precede (process A) or follow (process C) the loss of the HCN group. This mechanism is related to the *channel I* of the HCN loss. In both cases the geometry of the intermediate fragment obtained removing the first species is re-optimized before removing the second one. In the latter case, process C, the first step coincides with the formation of the m/z=87 fragment as already discussed in this section. The subsequent Cl loss from the fragments represented by structures 1, 2 and 4 leads to structures 5, 6 and 7, respectively. Both the G3B3 and G2 calculated enthalpies of formation of these fragments differ by more than 70 kJ/mol with respect to the values experimentally derived. So the fragmentation pathways A and C can be discarded, too.

The m/z=52 fragment may also be formed by removing ClCN and H moieties. In this case eq.(3.3-3) gives a $\Delta H^{\circ}_{f,gas}$ value for the charged fragment of 1147.82 kJ/mol. The (ClCN + H) loss can be considered in a concerted (process D) or sequential (Scheme 4.2–2 and Scheme 4.2–3) process proceeding through channel II. Most of these sequential patterns end up in similar final states (structures 6 and 8) as their equivalent concerted reactions. Only two sequential process give a sterically hindered three atom ring structure and precisely structures 9 in Scheme 4.2–2 and 10 in Scheme 4.2–3. Their corresponding $\Delta H^{\circ}_{f,gas}$ are too high compared to the experimental value (see for example structure 10 in Table 4.2-3). No match is found between the theoretical and experimental enthalpies for structures 5, 8, 9 and 10 obtained after a sequential release of the two moieties.

In the concerted reaction case, by comparing structures 6, 7, and 8 it can be asserted that this fragment can be formed by a concerted reaction with the simultaneous release of ClCN and the H bound to carbon 5 (structure 7). In this case the deviation between experiment and theory is only 1.74 kJ/mol in the G3B3 calculation and 16.54 kJ/mol in the G2. Also for this fragment the conclusions reached are the same gained by the analysis of the AE of the fragments.

m/z	*Possible fragment cation m_1^+*	*Neutral fragments*	$\Delta H^\circ_{f,gas}$ *(kJ/mol)*			
			exp		**G2**	**G3B3**
				Geometry[a]	ΔH°_{298K}	ΔH°_{298K}
87	$C_3H_2NX^{+\bullet}$	HCN	1216.40 ± 14.8	**1.**	1173.58	1169.40
				2.	1183.72	1170.71
				4.	**1245.04**	**1237.95**
79	$C_4H_3N_2^+$	$Cl^\bullet$	1176.20 ± 6.4	1198.21		1196.51
52	$C_3H_2N^+$	HCN + $Cl^\bullet$	1241.76 ± 19.7	**5.**	1360.11	1356.40
				6.	1318.13	1311.78
				7.	1164.36	1149.56
		ClCN + $H^\bullet$	1147.82*	**6.**	1318.13	1311.78
				7.	**1164.36**	**1149.56**
				8.	1382.38	1376.27
				10.	1421.15	1411.97

*Table 4.2-3 Comparison between the experimental and calculated $\Delta H^\circ_{f,gas}(m_1^+)$. *No uncertainities are reported in literature for the ClCN enthalpy. [a]these geometries are the ones reported in Scheme 4.2–1 and Scheme 4.2–3.*

The mechanisms proposed in the present analysis are consistent with those already discussed by the study of the AEs and new information is provided in the calculation of the gas phase enthalpies of formation of some fragments. The results show that the presence of the Cl atom in position 2 favours the release of the halogen radical with respect to the fragmentation of the ring in the VUV fragmentation of 2Cl-pyrimidine. The comparison between theoretical and experimental results allows to gain a much deeper insight in the fragmentation pathway of each measured cation fragment. Indeed it is proposed that the formation of the $C_3H_2N^+$ fragment proceeds via the release of the $H^\bullet$ radical and ClCN group in a concerted breaking of the ring. The comparison between different computational methods suggests that the G2 method is the one providing the most consistent results as for as the gas phase enthalpies of formation for neutral molecules. The

best agreement with the experimental results in the case of cation molecules is achieved using G3B3 method (in particular for the m/z=52 fragment where the deviation from the experiment is only 1.74 kJ/mol). The deviation of about 20 kJ/mol for both methods in the case of the (m/z=79) $C_4H_3N_2^+$ cation and the (m/z=87) $C_3H_2N_X^{+\bullet}$ radical cation suggests the presence of more stable structures of these fragments, like for example an open ring structure in the case of $C_4H_3N_2^+$ ion.

4.3 Photoionization efficiency curves of 2Br-pyrimidine

The photoionization efficiency curves of the parent ion and of the three fragments, m/z=52, 79 and 131 of 2Br-pyrimidine are shown in figure Fig 4.3—1a-d, while the experimental and theoretical AEs are collected in Table 4.2-1. A schematic of the considered fragmentation pattern is sketched in Scheme 4.3-1. Apart from the replacement of the Cl with a Br atom, the 2Br-pyrimidine molecule presents many similarities with the 2Cl-pyrimidine, as for example the optimized geometrical structures of the different fragments and the possible fragmentation paths.

The experimental IE=9.50 ± 0.05 eV for the **parent ion** is lower than the vertical ionization potential of the $5b_2(n_{N-})$ ground state of the 2Br-pyrimidine ion, 9.93 ± 0.02 eV [116] measured in photoelectron spectroscopy. The calculated IE value of 10.00 eV is about 0.5 eV higher than the experimental IE and higher than the vertical ionization potential. Considering that the calculated IEs give the adiabatic thresholds, while the ground electronic state, measured by photoelectron spectroscopy, corresponds to a vertical transition, this larger value of the theoretical IE with respect to the experimental one is likely due to the basis set used in the G3B3 calculation, which doesn't include the *g*-type polarization functions into the G3large basis set for the elements beyond Al.

Indeed, also the vertical ionization potential calculated by O'Keeffe et al. [116] using the P3 calculation with the 6-311G(2df,2p) basis augmented by the SDD basis set gives a value that is higher than its corresponding experimental value.

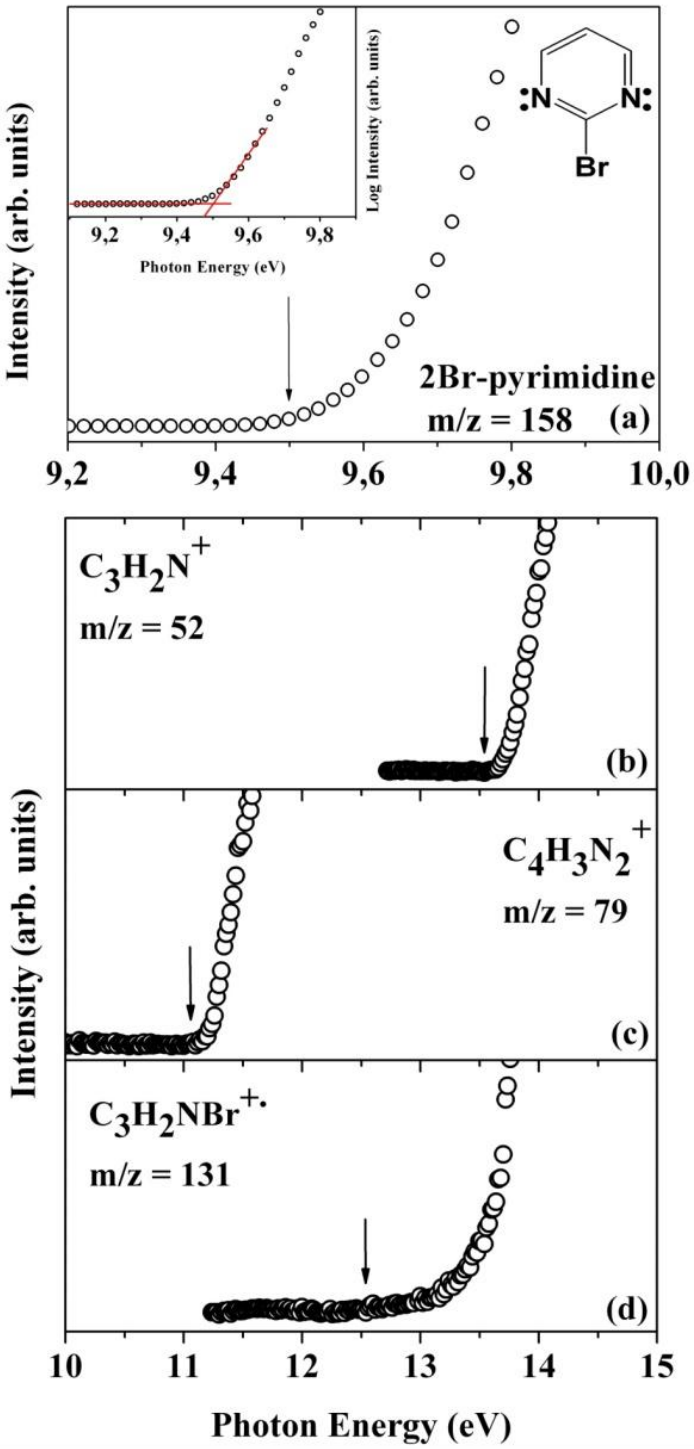

Fig 4.3—1 Photoionization energy curve of the parent ion (a) and three fragment ions of the 2Br-pyrimidine (b), (c) and (d). In the parent ion case, (inset of figure a) the threshold region is expanded and reported in log scale. The measured AE values are indicated by arrows and reported in Table 4.2-1.

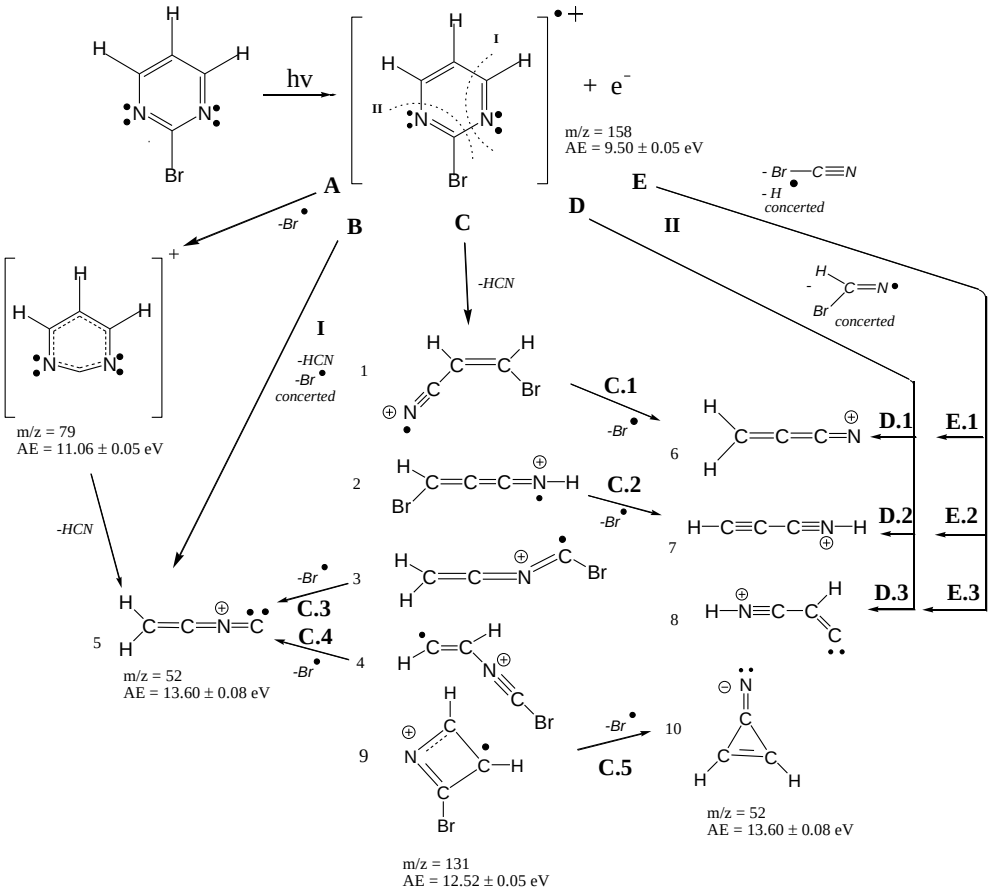

Scheme 4.3-1 Main fragmentation decay routes of 2Br-pyirimidine molecule. The measured values of the appearance energy are given for each fragmentation channel. The final geometries of the charged fragments have been labelled with numbers 1-9, while the possible fragmentation patterns are labeled with letters A-E. The D.n and E.n (n = 1,2,3) channels correspond to the loss of the H atom bound to C6, C5 or C4 atoms, respectively, after the loss of the BrCN group. The geometries have been optimized at DFT, B3LYP 6-311++G(2d,2p) level using the Gaussian09 suite of programs.

The difference between the calculated and measured AE values decreases to about 0.21 eV in the case of the **m/z=79** fragment (AE_{exp}=11.06 ± 0.05 eV), corresponding to the loss of the neutral Br atom. As for the parent ion case, a higher theoretical value can be similarly attributed to the lower level of accuracy of the present theoretical approach in the presence of the heavy Br atom in the molecule.

The HCN loss in 2Br-pyrimidine can proceed only through *channel I*,

producing the fragment at **m/z =131.** Its measured AE value is 12.52 ± 0.05 eV (process C in Scheme 4.3-1). According to the B3LYP predictions, the $C_3H_2NBr^{+\bullet}$ charged fragment may exist in several geometries that have been labelled 1 to 4 and 9 in Scheme 4.3-1 by increasing energy. Structures 1 to 4 are equivalent to the 2Cl-pyrimidine case (Scheme 4.3-1). Structure 9, the one with the highest enthalpy of formation among the five, is a four membered ring structure obtained in a DFT calculation by the rupture of the C2-N3 and C4-C5 bonds without any isomerization. Within the uncertainty of the present AE calculations this is the most similar to the experimental value and it is considered the most probable structure obtained during this fragmentation. Interestingly, the equivalent computational procedure in the 2Cl-pyrimidine case does not lead to a ring structure. The results are confirmed by performing a SDD B3LYP calculation employing the 6-311G(2df,2p) larger basis set for both cases of a Br or Cl halogen atom. Similarly to the case of 2Cl-pyrimidine, the values of the potential energy barriers between two structures in the series 1-4 and 9 are always larger than 1.3 eV (see Fig 4.3—2). Thus it does not seem to be possible to overcome such barriers to access the more stable structures 1 to 4.

The **m/z =52** peak is assigned to the $C_3H_2N^+$ fragment (AE = 13.60 ± 0.1 eV). This fragment may be formed either in a concerted (processes B, D and E) or in a sequential (processes A and C) reaction. Such fragmentation mechanisms have been described in detail in the case of the 2Cl-pyrimidine molecule, so they will be discussed very briefly here. In the concerted reaction the opening of the ring with the simultaneous release of the bromine atom and the HCN group via *channel I* leads to structure 5 (process B). The other channel, *channel II*, which involves the loss of the BrCN group and a H atom, leads to structures 6, 7 or 8 depending on the position of the H atom (processes D and E). The difference between processes D and E consists in the neutral complementary fragment, which can be formed by one or two separated moieties. Considering that the enthalpy of formation of $HCNBr^{\bullet}$ is smaller than $HCN+Br^{\bullet}$, the corresponding adiabatic AE for process D is smaller than for process E. Nevertheless, the D pattern will require molecular rearrangement, increasing the effective appearance energy of the ion formed via this particular path. In the sequential reaction, the loss of the $Br^{\bullet}$ radical may

precede (process A) or follow (process C) the loss of the HCN group. In the latter case the structure 5 is formed from the intermediate structures 3 and 4, while the loss of the halogen atom from fragments 1 and 2 leads to the structures 6 and 7.

As in 2Cl-pyrimidine also in 2Br-pyrimidine the structure 5 is characterized by a too high adiabatic AE value with respect to the experimental one and therefore paths A, B, C.3 and C.4 have been discarded. The absence of the peak corresponding to the m/z =53 fragment (due to the BrCN loss) in the mass spectrum makes unlikely that process E occurs sequentially. However this does not exclude that it could occur in a concerted manner with the simultaneous loss of the BrCN group and H atom (E.2 path with AE=13.56 eV). In contrast to 2Cl-pyrimidine, in the case of 2Br-pyrimidine the sequential loss of the HCN group and the $Br^{\bullet}$ radical has also been considered, i.e. path C.1 leading to structure 6 with AE=13.69 eV. Both these two paths are close in energy to the experimental value (AE=13.60 ± 0.1 eV). Therefore it concludes that in 2Br-pyrimidine the consecutive (-HCN, $-X^{\bullet}$) and concerted (-XCN, $-H^{\bullet}$) process are competitive, unlike the 2Cl-pyrimidine case where the concerted ClCN and $H^{\bullet}$ loss is dominant in the formation of the fragment at m/z=52. As it will be better discussed in section 4.5 this could be due to the different electronegativity of the Br atom with respect to Cl, which makes possible the rupture of Br−C bond at lower energy.

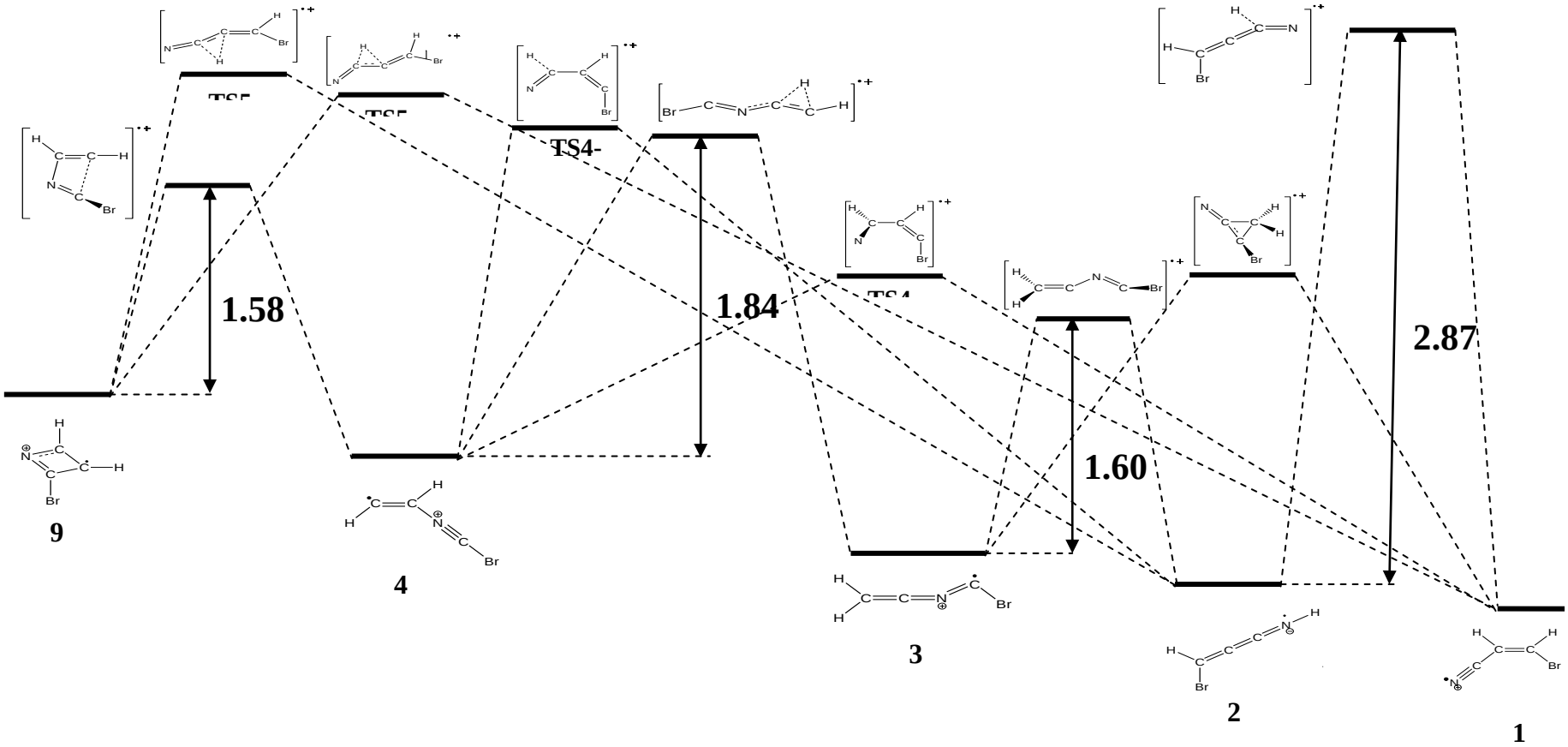

Fig 4.3—2 a) Potential energy barriers in eV between structures 9 and 4 to 1 of the H2C3NBr+• fragment of 2Br-pyr. In all cases the geometries are optimized at the DFT-B3LYP level, the relative energies are calculated using B3LYP 6-31g(d) basis set and the transition states are obtained using a qst3 calculation. The energy barriers to reach TS5-2, TS5-1, TS4-2 TS4-1 and TS3-1, are 1.90, 1.88, 1.88, 1.31, and 1.72 eV respectively.

4.4 Photoionization efficiency curves of 5Br-pyrimidine

In 5Br-pyrimidine the fragmentation patterns show significant differences with respect to the 2Cl- and 2Br-pyrimidine cases, because of the different halogen atom and its different location. The partial photoionization efficiency curve of the parent ion and the four ionic fragments m/z =52, 79, 104 and 131 are shown in Fig 4.4—1 while the experimental AEs, together with the calculated values are collected in Table 4.2-1. In Scheme 4.4-1 the investigated fragmentation paths of this molecule are sketched.

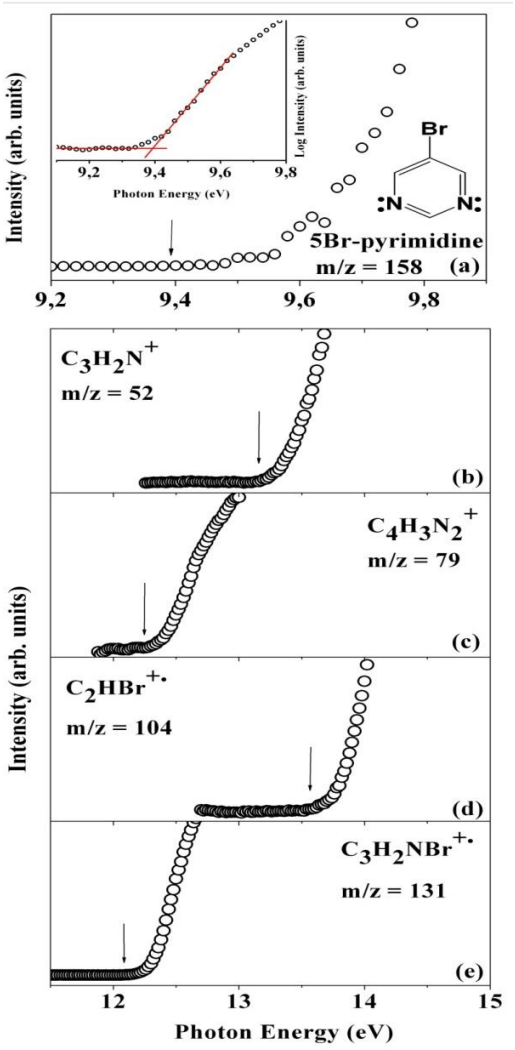

Fig 4.4—1 Photoionization energy curve of the parent ion (a) and four fragment ions of the 5Br-pyrimidine (b), (c), (d) and (e). In the parent ion case, (inset of figure a) the threshold region is expanded and reported in log scale. The measured AE values are indicated by arrow and reported in Table 4.2-1.

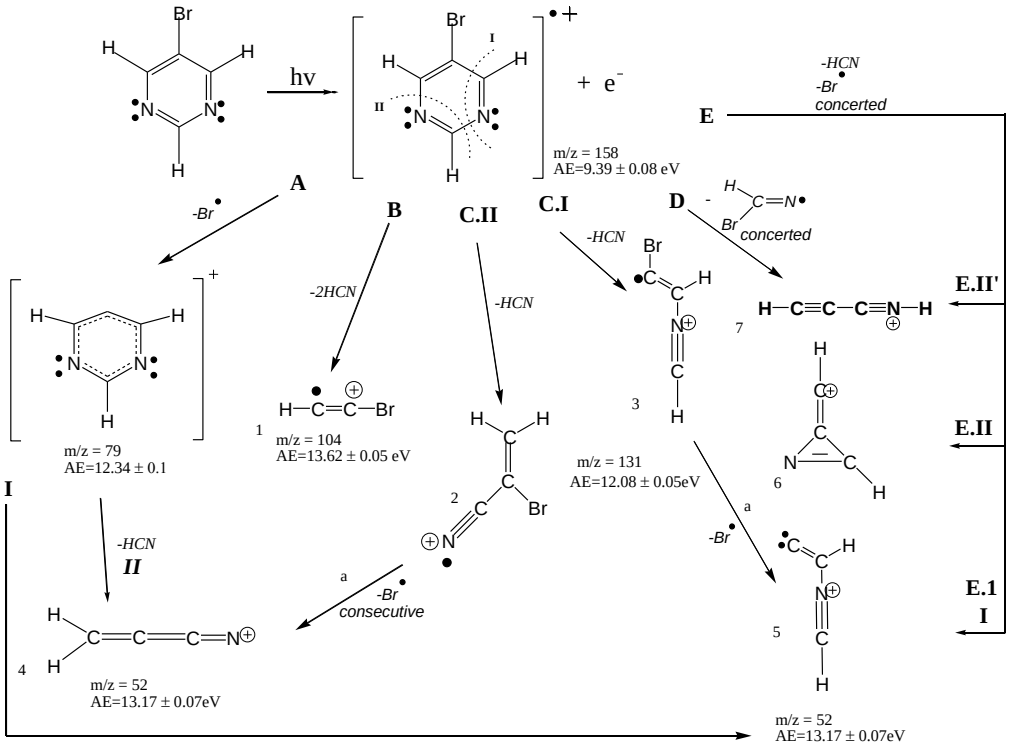

Scheme 4.4-1 Main fragmentation decay routes of the 5Br-pyrimidine molecule. The measured values of the appearance energy are given for each fragment. The final geometries of the charged fragments have been labelled with numbers 1-7, while the possible fragmentation patterns are labeled with letters A-E. For the concerted loss of HCN and Br•, channels I and II have been considered. In the latter case, where the final geometry 6 of the charged fragment has a 3-membered ring structure, the N1-C6-C5 angle of the ionized molecule has been forced to 'open', ending up in the linear structure 7. This latter process has been named II´. The difference between D and E processes is whether the neutral HCN and Br• fragments are bound or not. The geometries have been optimized at DFT, B3LYP 6-311++G(2d,2p) level using the Gaussian09 suite of programs.

For the **parent ion** the G3B3 method overestimates the experimental IE (9.39 ± 0.08 eV) by about 0.5 eV. As already discussed in the case of the 2Br-pyrimidine, this discrepancy can be attributed to the presence of the Br atom with a consequent reduced accuracy of the G3B3 calculation. Indeed, the experimental value, is significantly lower than the measured vertical

ionization potential of this molecule, at 9.93 ± 0.02 eV [116]. As for the 2Br-pyrimidine case, also the vertical ionization potential calculated by O'Keeffe et al. [116] using a similar computational analysis, the P3 calculation with the 6-311G(2df,2p) basis augmented by the SDD basis set, is higher than the correponding experimental one.

The loss of the radical halogen atom, $Br^{\bullet}$, leads to the **m/z =79** fragment (process A in Scheme 4.4-1). In this case, the theoretically predicted AE (12.33 eV) is in good agreement with the experiment (12.35 ± 0.1 eV). This seems to suggest that in the m/z =79 case, the computed enthalpy of formation of the charged fragment, which does not contain the Br atom, is more accurate.

The **m/z =104,** attributed to the halogenated acetylene cation, is due to the loss of two HCN groups (see process B in Scheme 4.4-1). The equivalent channel in pyrimidine is achieved by a combination of *channel I* and *II*, and is not observed in the 2Cl- and 2Br-pyrimidine cases, where the halogen atom in site 2 locks the loss of HCN via *channel II* and makes the formation of the halogenated acetylene very unlikely. This is instead a quite straightforward process when site 2 is occupied by a H atom, as in the pyrimidine or 5Br-pyrimidine cases. The calculated and measured AEs agree with each other supposing a reverse energy barrier. A process in which this cation is formed via the loss of N_2 and C_2H_2 from the parent cation has been also considered. As observed by Schwell et al. [109] in the case of pyrimidine this scheme is thermodynamically allowed, but it is kinetically less probable due to the required rearrangement to form N_2.

The previous considerations established that in 5Br-pyrimidine both *channel I* and *II* involving the loss of the HCN group are active. Each one of the two channels leads to the same **m/z =131** fragment, although with different final geometries (see structures 3, 2 for paths C.I and C.II respectively in Scheme 4.4-1) and therefore different computed AEs (see Table 4.2-1). The calculated AE for path C.II, corresponding to *channel II* and leading to structure 2, is lower than the one for path C.I., i.e. *channel I*, leading to structure 3. So, from the energetic point of view structure 3 is less stable than structure 2. However, structure 3 can be reached from the parent ion by removing directly the N1, C2 atoms and the H atom in position 2 and re-optimising the structure, while structure 2 requires isomerisation, i.e. the overtaking of an energy barrier. Furthermore, the

calculated AE of path C.I is in closer agreement with the experimental result. For these reasons, the fragmentation channel C.I appears to be more likely.

The situation is more complex for the **m/z =52** fragment (-HCN -Br), where both *channels I* and *II* as well as the concerted (processes D and E) and sequential reactions with Br loss following (C.IIa, C.Ia) or preceding (A) the HCN loss have been considered. All of these possibilities are summarized and sketched in Scheme 4.4-1, while the corresponding computed AEs are reported in *Table 4.2-1*. Structure 6 can be obtained by the concerted loss of the HCN group in *channel II* and the $Br^{\bullet}$ radical. However this geometry is quite unstable because of the high tension of the three atom ring. Structure 5, obtained either from a sequential or a concerted reaction with the loss of the HCN group in *channel I* and the $Br^{\bullet}$ radical is even more unstable than structure 6 so that their corresponding adiabatic AE values are higher than the experimental one. Therefore processes C.Ia, A.I, E.I and E.II can be discarded. The linear structure 7 for the $C_3H_2N^+$ fragment can be formed via the D and E.II' processes. This may occur via the concerted loss of the HCN group in *channel II* and the $Br^{\bullet}$ radical and then forcing the N1-C6-C5 angle to become larger than its equilibrium value of 121.31° to prevent the closing of the ring, that would lead to structure 6. The linear structure has been discarded because of the high reverse barrier of about 1.2 eV (difference between the experimental and theoretical value), which would lead to an activated complex very disadvantageous by the steric hindrance of the bromine atom, making the stretching of the angle difficult. The difference between the D and E processes is whether the neutral HCN and $Br^{\bullet}$ fragments are bound or separated. Their respective AEs are shifted by 0.23 eV, i.e. with the former (process D) having a higher AE than the latter (E process). Therefore the two separated neutral fragments are in a thermodynamically favorable condition. This is also reinforced by the fact that the production of the $HCNBr^{\bullet}$ radical (process D) requires the migration of the bromine atom, an endothermic reaction most likely involving some energy to overcome potential barriers. Finally let's consider structure 4. It can be reached in a sequential reaction via paths A.II and C.IIa with the $Br^{\bullet}$ loss respectively preceding or following the loss of the HCN group in *channel II*. The computed AE of 13.66 eV for m/z =52, not far from the experimental

measurements, suggests that this fragmentation channel proceeds via the sequential loss of the HCN and $Br^{\bullet}$ fragments.
These results suggest that in the case of 5Br-pyr, where the halogen atom is in position 5 on the ring, the fragmentation proceeds via the rupture of the ring instead of the release of the halogen atom. This behaviour will be better discussed in section 4.5.

4.5 The substituent effect

In the previous sections, the experimental and theoretical results of the study of the appearance energy of the most prominent fragments of three halogen substituted pyrimidine molecules have been presented and discussed. More information about the fragmentation dynamics of this class of molecules can be gathered by comparing the results obtained for equivalent fragmentation channels of the three selected targets and the unsubstituted pyrimidine molecule. The 2Cl-, 2Br- and 5Br-pyrimidine molecules allow the effects of the different halogen substitution (Cl or Br in the 2Cl- and 2Br-pyrimidine, respectively) and the site of halogenation (2 or 5 for the 2Br- and 5Br-pyrimidine, respectively) on the fragmentation dynamics of the pyrimidinic ring to be investigated. With this in mind, the AE of the main fragments and the corresponding proposed geometrical structure/fragmentation mechanisms will be discussed in this section.
In the case of the parent ion (eq. 1), the measured AE of the three molecules are very similar, to each other and to that of the unsubstituted pyrimidine molecule. The average value is about 9.48 ± 0.01 eV. As already observed by other authors for the cases of aminoacids and DNA/RNA bases [117 and references therein] this can be explained by the fact that the highest occupied molecular orbital (HOMO) in these molecules is often the nitrogen lone pair orbital. The simplicity of the photoreaction which leads to the parent ion, with just the singly ionized, unbroken, molecule in the final state offers the most straightforward way for a comparison of the experimental and theoretical values of the AE. There is a good agreement for the 2Cl-pyrimidine, but significant discrepancies have been observed in the brominated cases, with the theoretical values exceeding the experimental values by about 0.5 eV. Considering that the present computational approach gives the adiabatic threshold, i.e. the minimum

energy required for the selected process to happen, one should expect the experimental values to be larger than the calculated ones. However the observation that i) the measured AE values for the parent ions are consistently lower that the respective vertical ionization energy independently measured in photoelectron spectroscopy by O'Keeffe et al [116] while the calculated values are similar or even larger and ii) similar discrepancies have been observed by the same authors in the comparison between experimental and theoretical results obtained using the P3 calculation with the 6-311G(2df,2p) basis set for the vertical ionization potential of the 2Br- and 5Br-pyrimidine molecules seems to support the experimental findings of AE. The quality of the calculation in the case of the other fragments, where more than one structure is possible both for the neutral and charged fragments, is more difficult to assess and the possibility of systematic differences between experimental and theoretical results is something to be aware of in the comparison.

In the photon energy range investigated in the present work, the loss of the HCN group (eq. 2) seems to be more probable than the loss of the halogen atom (eq. 5) in the 5Br-pyrimidine, while the opposite occurs in the 2Cl- and 2Br-pyrimidine molecules. This can be observed in the mass spectra of Fig 4.1—1 as well as in the measured AE of the corresponding channels reported in Table 4.2-1. In Fig 4.1—1, the measured branching ratio of fragments with m/z 131 and 79 is greater than 1 in 5Br-pyrimidine and less than 1 in 2Br-pyrimidine (as well as in 2Cl-pyrimidine where m/z 87 and 79 is <<1). The charged fragment corresponding to the HCN loss channel has AE(5Br-pyrimidine)< AE(2Cl-pyrimidine)< AE(2Br-pyrimidine), showing that the HCN loss is thermodynamically favored in 5Br-pyrimidine, while the halogen loss becomes more likely in the other two cases. This suggests that a dominant role in this (-HCN) channel is played by the site of halogenation rather than the specific halogen atom. Indeed the halogen atom acts on the electronic structure of the pyrimidine derivatives, as well as in most aromatic compounds, via two main mechanisms, the inductive and the resonance effects [116, 118]. The former is due to the electronegativity of the halogen substituent which withdraws electron density from the ring while the latter is due to conjugation between the lone pair orbitals of the halogen atom and the π orbitals of the ring. In a resonance structure description of such an effect the halogen carries a

positive charge, while giving electronic charge to the aromatic system, thus forming a double bond with its C neighbor. The negative charge can be considered to be preferably localized on ortho and para positions with respect to the halogen. This suggests that the observation concerning the much favourable rupture of the ring in 5Br-pyrimidine, is probably due to the more relevant role played by the resonance compared to the inductive effect when the halogen atom is in position 5 rather than 2. In 5Br-pyrimidine, when the parent ion is formed one could imagine two possible scenarios, schematised in Scheme 4.5-1. When there is an activation of the ring in "ortho" position, the N3-C4 bond becomes stronger with respect to the N3-C2 and C4-C5 bonds thanks to the covalent and ionic nature of the bond. This makes more likely the rupture of the nearest bonds with a sequential release of the HCN group following *channel I*. On the other hand, when there is activation in "para" position, N1-C2 bond become stronger compared to the nearest ones. In this case the release of the HCN group will happen via *channel II*. These effects can explain the formation in 5Br-pyrimidine of the intense peaks at m/z =131 (due to HCN loss via either *channel I* or *II*) and 104 (due to the loss of two HCN groups via the joint action *channel I* and *II*). The situation is different when the halogen atom is bound to the C2 atom, where the same para-ortho activation leads to the HCN release via *channel I* (ortho activation) or C_2H_2 release (para activation). This simple picture only takes into account the site of halogenation of the pyrimidine ring to explain the experimental observation of efficient release of HCN in the case of halogenation in site 5. On the other hand, in 2Cl- and 2Br-pyrimidine the most likely fragmentation channel is the loss of the halogen atom, due to a more relevant inductive effect when the halogen atom is in position 2, surrounded at close range by two nitrogen atoms.

As already discussed, both *channels I* and *II* are available in the 5Br-pyrimidine case for the HCN loss, while only *channel I* is possible in the 2Cl- and 2Br-pyrimidine. Therefore the present experimental observations could be interpreted in the light of a preferred mechanism like *channel I* for the HCN loss and the breaking of the pyrimidinic ring. This explanation is consistent with the results of mass spectrometric studies of pyrimidine and a set of deuterated pyrimidines [110] which suggest that the loss of HCN involves mainly the C4 carbon atom rather than the C2 one.

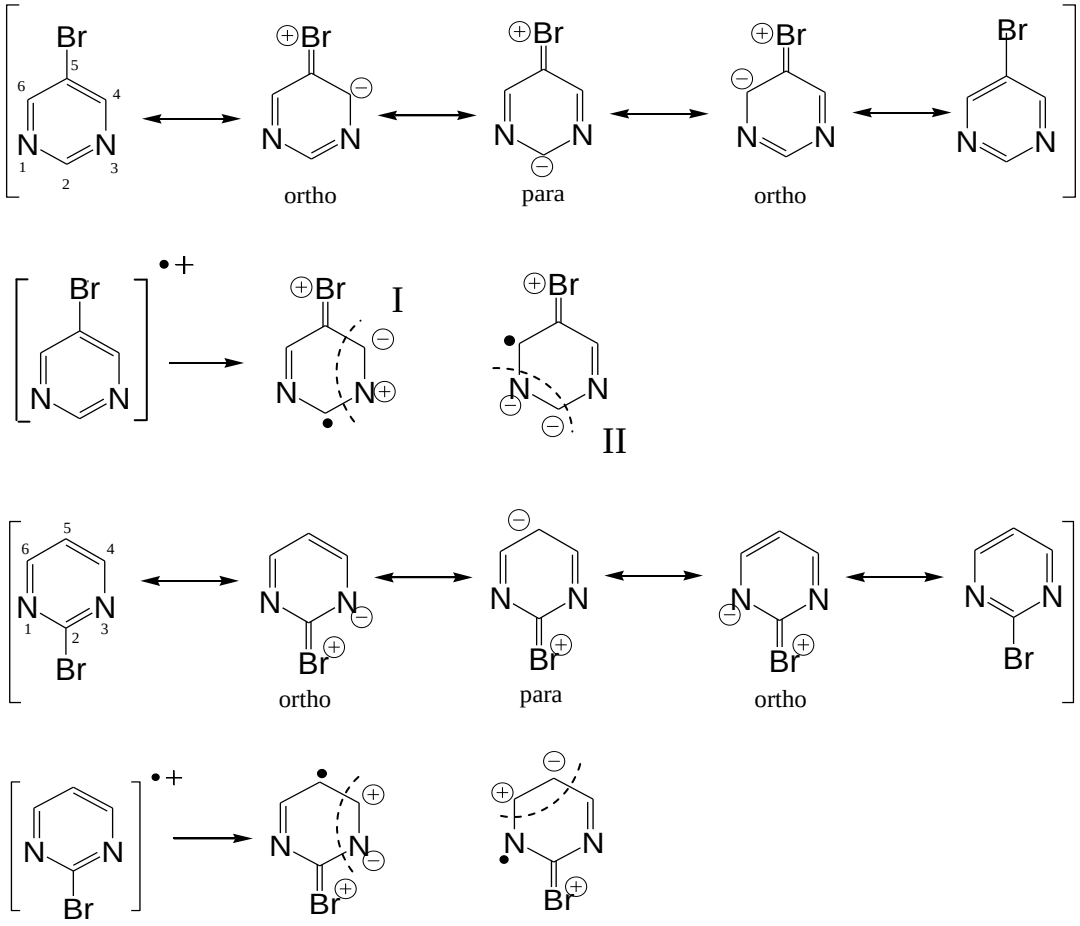

Scheme 4.5-1 Scheme of the resonance effect in 5Br-pyrimidine and 2Br-pyrimidine related to the ejection of the HCN group.

On the other hand this explanation would be in contrast with the suggestion of Schwell et al. [109] who associates the residual $C_3H_3N^{+\bullet}$ fragment of pyrimidine to the acrylo-nitrile form, which can be produced only by *channel II.* It should be noted that Schwell et al. [109] left the question open. In the present work the HCN loss proceeding via *channel II* in the 5Br-pyrimidine case leads to a more stable structure for the $C_3H_2NBr^+$ fragment, even though this requires a molecular rearrangement, while a better matching between theoretical and experimental AE values is observed considering the fragmentation via *channel I.* Thanks to the computational analysis performed it is possible to assign a specific geometry and fragmentation pathway to each cation fragment. In the case of 5Br-pyrimidine our results suggest that the most favorable path for the

HCN loss is through *channel I.* This is also consistent with the resonance schematic of Scheme 4.5-1, where the ortho limit structures have the major contribution to the hybrid structure (thanks to the symmetry of the molecule) favouring the corresponding fragmentation *channel I.*

Consistently with the arguments explained above, the -2(HCN) channel (eq. 3) has been observed only in the 5Br-pyrimidine molecule, where a combination of *channel I* and *II* can directly lead to the observed residual halogenated acetylene cation. This observation confirms that both channels are active.

It is important to clarify at this stage that *channel II* cannot exist as HCN loss channel when the halogen atom is in position 2, while it can still be considered as a mechanism of opening the ring via the breaking of the C2-N3 and N1-C6 bonds. In this case it leads to XCN loss (X = Cl, Br), therefore to a different m/z fragment (m/z=53) with respect to those due to HCN loss. The m/z =53 fragment is not observed in 5Br-pyrimidine, as this would imply a very significant molecular rearrangement with respect to the neutral molecule; it is observed in 2Cl-pyrimidine, but not in 2Br-pyrimidine. This is due to the fact that the chlorine atom is more electronegative than nitrogen, which is, in turn, more electronegative than bromine (Cl>N>Br>C). This different atom's electronegativity is the key to explain the relative contribution of eq. 5 (-X) and 6 (-XCN) in 2X-pyrimidines when X=Cl or Br. The values of difference of electronegativity (Δx) of the involved bonds have been calculated and are shown in Fig 4.5—1 and Fig 4.5—2.

The Cl atom can weaken the C-N bond more efficiently than the Br atom making the ClCN loss possible and competing with the loss of Cl radical. On the other hand the Br atom (which is less electronegative than the two nearest N atoms) can weaken the X-C bond favouring the release of the Br radical more than the BrCN group. As in the HCN loss channel the dominant role was played by the site of halogenation, in the case of the XCN channel the most relevant role is played by the particular halogen atom (see Fig 4.5—1).

This simple explanation based on the atom's electronegativity is supported by the observation that the halogen loss channel, which is more intense when the halogen atom is in position 2 rather than 5, is enhanced in the case of the 2Br-pyrimidine more than 2Cl-Pyrimidine.

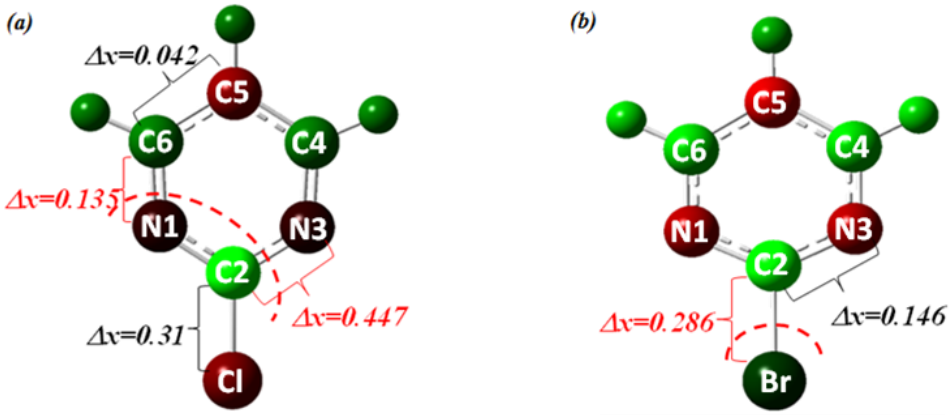

Fig 4.5—1 Difference of electronegativity (Δx) of the bonds involved in the ejection of the ClCN group in 2Cl-pyrimidine (a) and Br• in 2Br-pyrimidine (b). In red are the highest values with respect to the neighboring bonds.

The effect of weakening of the C2-X bond, due to the presence of the nearby N atoms in position 1 and 3, is more pronounced in 2Br-pyrimidine because of the higher electronegativity of the bromine atom.
On the other hand in the case of 5Br-pyrimidine the difference of electronegativity of the C5-Br bond is comparable with the nearest bonds therefore the release of the halogen atom is in competition with the breaking of the ring resulting in a less intense peak at m/z=79 (see Fig 4.5—2).

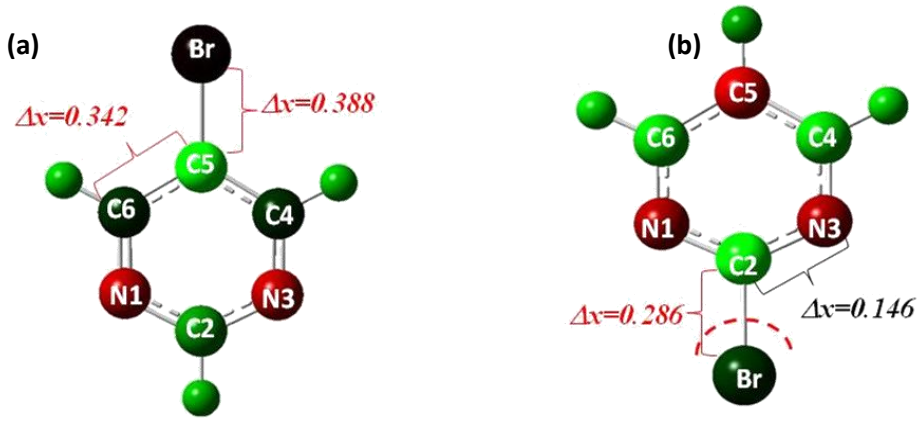

Fig 4.5—2 Difference of electronegativity (Δx) of the bonds involving in ejection of Br atom in 5Br-pyrimidine (a) and 2Br-pyrimidine (b). In red are the highest values with respect to the neighboring bonds.

The cation fragment in photoreaction 4 and 7 corresponds to m/z =52. As

reported in Table 4.2-1 and in Scheme 4.2–1, Scheme 4.3-1 and Scheme 4.4-1 the description of this channel is quite complex and several scenarios can arise.

Summarizing the results of the present work, the formation of the $HCNX^{\bullet}$ fragment, in all cases, is unfavored according to energy considerations, while two separated fragments have a more stable configurations. These neutral fragments could be HCN and $X^{\bullet}$ (eq. 4) or XCN and $H^{\bullet}$ (eq. 7). From a theoretical point of view, while in the 2Cl-pyrimidine the proposed fragmentation mechanism is a concerted reaction leading to the release of the ClCN neutral fragment and a $H^{\bullet}$ radical, in the 2Br-pyrimidine both process may happen even though in different ways: concerted BrCN and $H^{\bullet}$ loss or sequential HCN and $Br^{\bullet}$ loss. Considering the larger uncertainty of the theoretical calculation in the brominated cases both options can be leaved open considering the two channels in competition. In the case of 5Br-pyrimidine the proposed mechanism is a sequential process with the release of a $Br^{\bullet}$ radical and a neutral HCN group proceeding via *channels II*. This implies that in the chlorinated case, the free radical is $H^{\bullet}$ while in the brominated cases, particularly 5Br-pyrimidine, the free radical is $Br^{\bullet}$.

The present results suggest that the presence of the Br atom in position 5 favors the breaking of the ring while the presence in position 2 favors the release of the halogen radical in a more efficient way for 2Br-pyrimidine compared to 2Cl-pyrimidine. These observations have also been rationalized in terms of i) the interplay between the resonance and inductive effects as well as ii) the electronegativity of the halogen atoms.

The present findings suggest that the effect of these molecules employed as radiosensitizers could be different if embedded in a real cellular environment. The choice of the most suitable radiosensitizer should be dictated by the goal of the therapy. The choice of the halogen in position two can lead to the release of the small $H^{\bullet}$ radical or the more reactive $Br^{\bullet}$ radical and it could be useful if the purpose of the radiotherapy is focussed on destroying of the environment surrounding the cell nucleus. On the other hand, if the aim of the therapy is the direct damage of the DNA chain then the 5Br-pyrimidine could be the most appropriate choice because it induces more significant breaking of the ring.

5 Halogenated nucleobases

In the first part of this chapter the results obtained by the thermal decomposition analysis through FT-IR spectroscopy (described in chapter 2.4) of four different halogenated uracil molecules will be discussed. The particular target molecules under investigation in this part of the work are the halogenated nucleobases described in the chapter 1 section 1.3.2, that are 5F-, 5Cl-, 5Br- and 5I-Uracil.
The second part of this chapter will be focused on the XPS and NEXAFS characterization of these molecule. The experiments have been performed at the GasPhase beamline of the Elettra Synchrotron radiation source in Trieste and the characteristics of the beamline are described in section 2.2.3.
The last part is dedicated to the ion beam fragmentation studies of 5BrU and its homogeneous and hydrated cluster compounds. The experiments were performed at the ARIBE beamline of Ganil in Caen, France. The set up of the beamline has already been described in section 2.3.2.

5.1 FT-IR characterization

With the 5-substitution on the uracil ring, several key and inter-related effects, that produce the marked differences in the biological and pharmacological activities of these nucleobases, can be underlined.

- The first effect refers to the structural change mainly caused by the longer C-X bond (X = F, Cl, Br, I) with respect to the C-H one of the uracil molecule.
- The second and the most important effect, is the drastic change of the intermolecular interactions. This effect is specially pronounced with the 5-halo derivatives where the higher electronegativity of the halogen atom compared to hydrogen produces a perturbation in the electronic environment of the heterocyclic ring, and therefore new possibilities for intermolecular H-bonds through the halogen atom. The halogen substitution also increases the polarizability of the nucleobases.

As described in chapter 2.4 the FT-IR analysis has been performed in order to find the proper sublimation temperature, avoiding the thermal

decomposition of the molecule passing from the solid to the gas phase. Table 5.1-1 summarises, for all the molecules, the maximum temperature, as read at the top (T_T) and at the bottom (T_B) of the oven, usable to sublimate the powders without having any change in the molecular structure of the sample.
Following the experimental procedure described in chapter 2.4.4 the condensed powder of each sample has been collected (after the heating process) on the aluminium plate and has been analysed through FT-IR spectroscopy. Comparing the FT-IR spectra of these molecules with those of the respective samples not subjected to heating, no differences have been found up to the temperature describe in the Table 5.1-1.

	T_T (C°)	**T_B (C°)**
5FU	323	272
5ClU	349	315
5BrU	369	323
5IU	224	181

Table 5.1-1 The maximum temperature reached to sublimate the sample without generating any change in the molecular structure of the samples with a background pressure of $2x10^{-6}$ mbar.

Some differences have been observed in the spectra of the 5FU and 5IU molecules heated at 346° (T_T) – 317° (T_B) and 301° (T_T) – 254° (T_B), respectively.
As shown in the Fig 5.1—1 and Fig 5.1—3 for 5IU and 5FU, respectively, the difference in the bending and stretching of some bonds in the molecule suggest the presence of a different tautomeric form. The most common tautomeric form for these molecules, stable at room temperature and standard pressure, is the ketonic form depicted on the left-hand side of Fig 1.3—2. However in Fig 5.1—1, where the spectra of the heated 5IU (in red) and the same molecule at standard temperature and pressure (in black) are compared, the presence of "new" absorption band can be observed, in the red spectrum, at 3436 cm^{-1}. This band is attribuited to the stretching of O–H bond [119].

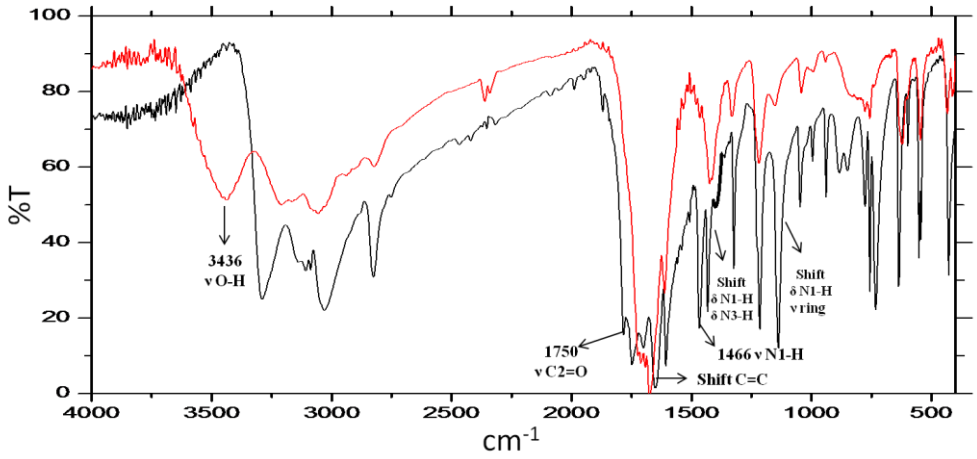

Fig 5.1—1 Comparison between the FT-IR spectra of two samples of 5IU. The red one is the spectrum of 5IU that has been heated setting the oven at the temperature values of 301°C at the top and 254°C at bottom with a base pressure in the vacuum chamber of $5 \cdot 10^{-6}$ mbar. The black one is the spectrum of 5IU at standard temperature and pressure. The most important different absorption bands and their assignment [119] are indicated.

Other differences in the FT-IR spectrum of the heated sample can be observed in the region of low frequency with the disappearance of the band at 1750 cm^{-1} associated to the stretching of C2=O double bond and the one at 1466 cm^{-1}, associated to the stretching of N1–H bond [119].
These evidences, together with the shift of some characteristic modes, as for example the (νC=C), the (δN1-H + δN3-H) and the (νring + δN1-H), suggest that a transition from the ketonic to an enolic form might have happened, with the H atom moving from N1 to the O8 (see. right-hand side of Fig 5.1—2).

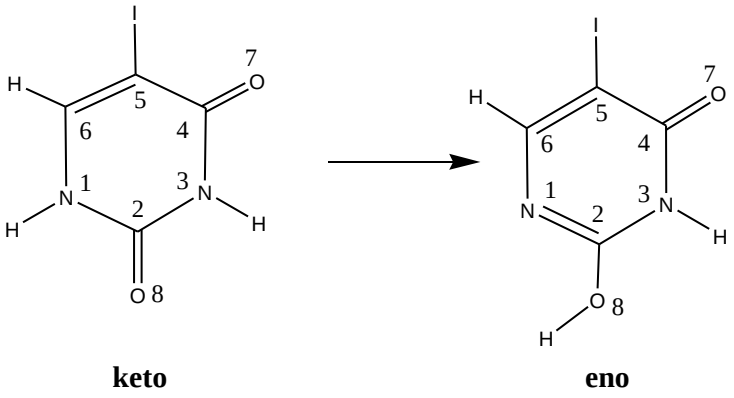

Fig 5.1—2 The 5IU keto-eno hypothesized transition.

Also in the case of 5FU a similar behaviour has been observed. The spectra in Fig 5.1—3 show the presence of a new band at 3418 cm^{-1} (red spectrum) due to the stretching of the O–H group and a decreasing of the band at 3136 cm^{-1} due to the bending of N1–H bond. Moving towards the lower frequencies region it is evident the decrease in the relative intensity of the band at 1429 cm^{-1} associated to the collective vibration (vring + δN1–H) as well as of the band at 1183 cm^{-1} associated to the bending of N–H bond. Also in this case the hypothesized tautomeric transition involves the migration of the hydrogen from the N1 to the O8 atom.

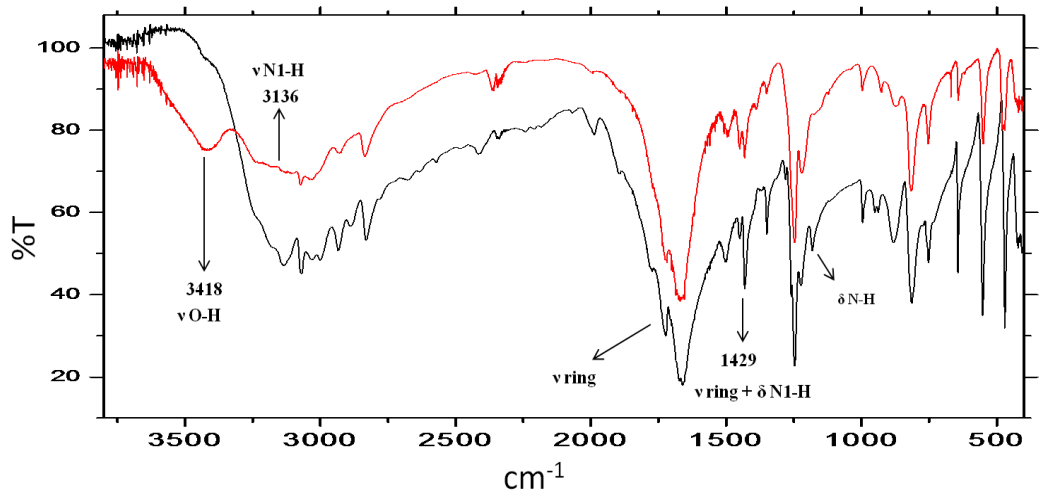

Fig 5.1—3 Comparison between the FT-IR spectra of two samples of 5FU. The red one is the spectrum of 5FU heated setting the oven at the temperature values of 346°C at the top and 317°C at bottom, with a base pressure in the vacuum chamber of $5 \cdot 10^{-6}$ mbar. The black one is the spectrum of 5FU at standard temperature and pressure. The most important different absorption bands and their assignments [120] are indicated.

Studies of tautomeric phenomena have been valuable in many areas of chemistry as demonstrated by several reviews of experimental and theoretical studies in chemistry and biochemistry. The Fig 5.1—4, extracted from ref [120], shows the tautomerism in 5FU (the energies were calculated at MP2/6-31G** level) suggesting that tautomer T3 is the least stable while tautomer T2 (the one proposed above) is the most stable excluding the keto form.

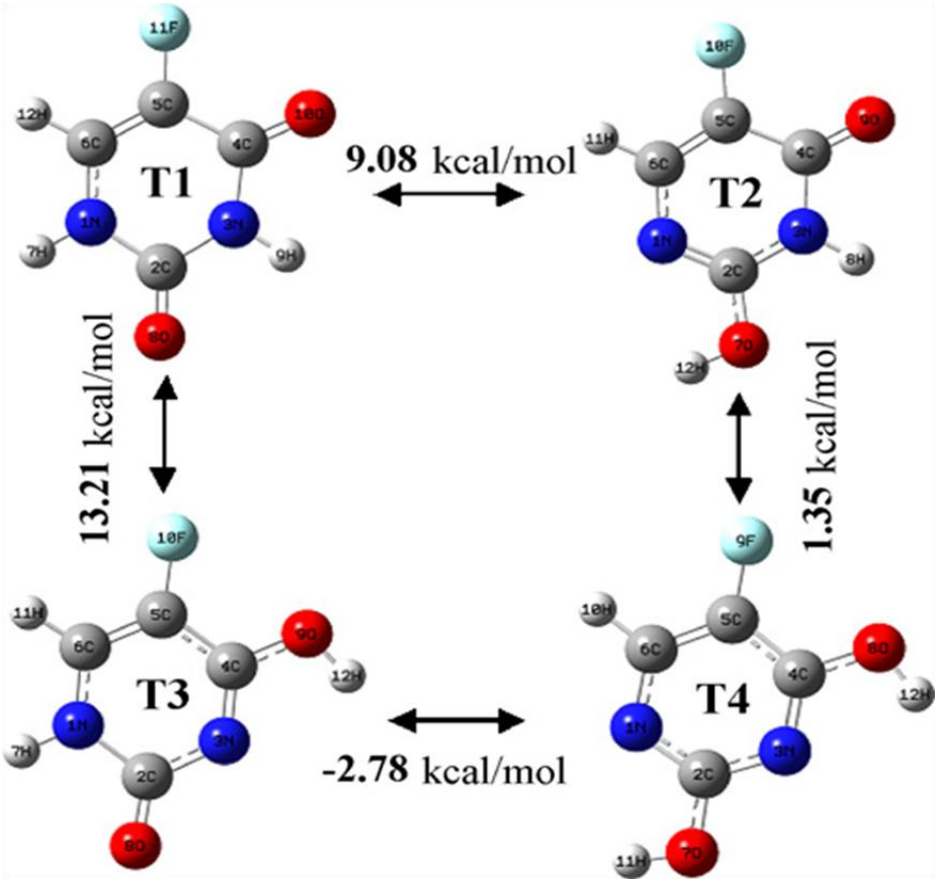

*Fig 5.1—4 Tautomerism in 5FU [120]. The energies were calculate at MP2/6-31G** level. The stability order is : T1 > T2 > T4 > T3. The molecular modeling of a single structure does not include any intermolecular interactions and thus it is equivalent to predicting the monomeric structure in the vapor phase.*

The absence of a (O–H) band in the 3500-3700 cm^{-1} range and the appearance of (C=O) modes as strong bands in the black spectra of Fig 5.1—1 and Fig 5.1—3 indicate that in the solid state these compounds exist in the keto form. The results obtained by this first FT-IR analysis suggest that 5FU and 5IU are subject to tautomerization induced by the high temperature. However, several doubts also arised concerning this interpretation, indeed it could be possible that the tautomerization occurs during the condensation phase, maybe catalysed by the surface of the aluminium plate on which the molecules have been recondensed. Therefore, a more detailed characterization through XPS spectroscopy has been performed to confirm/disproof the proposed mechanism of tautomerisation and possibly give more information about which kind of

tautomer is formed. Indeed the XPS spectroscopy is sensible to the environment surrounding the single atom and it can give information about which nitrogen and oxygen atom is involved in the transition. Moreover the XPS experiments have been performed in gas phase giving the possibility to understand if the tautomerism occurs in gas phase or during the condensation phase. For these reasons and in order to obtain a complete characterisation of the inner shell excitation/ionisation of these molecules in gas phase, a series of XPS and NEXAFS measurements have been performed. The results will be presented and discussed in the next section.

5.2 XPS and NEXAFS characterization of halogenated uracils

In this section a detailed investigation of the inner shell photoabsorption and photoionization of the four halogenated uracils has been undertaken. Here the results of the XPS and NEXAFS measurements in the region of the C, N and O K edges are reported together with the results of the uracil molecule already studied by Feyer et al. [121, 122]. The complex nature of the targets and the highly selective information provided by spectroscopic techniques such as photoelectron and NEXAFS spectroscopies, strongly require theoretical support for the interpretation of the results. Therefore, the XPS experimental results are compared to the theoretical predictions for both the keto and eno forms of a DFT-B3LYP calculation [123], which has been previously used to successfully describe the binding energies of core electrons in gas phase halogenated pyrimidine molecules [118] and nitrotoluene isomers [124]. These theoretical results have been obtained using a pseudopotential DFT method [125] that is, an ab initio approach where core electrons are not explicitly included in a self-consistent field (SCF) calculation. A core hole is induced when the pseudopotential is generated and this “excited state” pseudopotential is then used to evaluate the relative binding energy. This approach has been used here together with a hybrid HF-DFT approach to evaluate the interelectronic interactions, namely, the B3LYP exchange-correlation functional [126] as implemented in the Quantum-ESPRESSO suite [127]. The results are summarized in Fig 5.2—1.

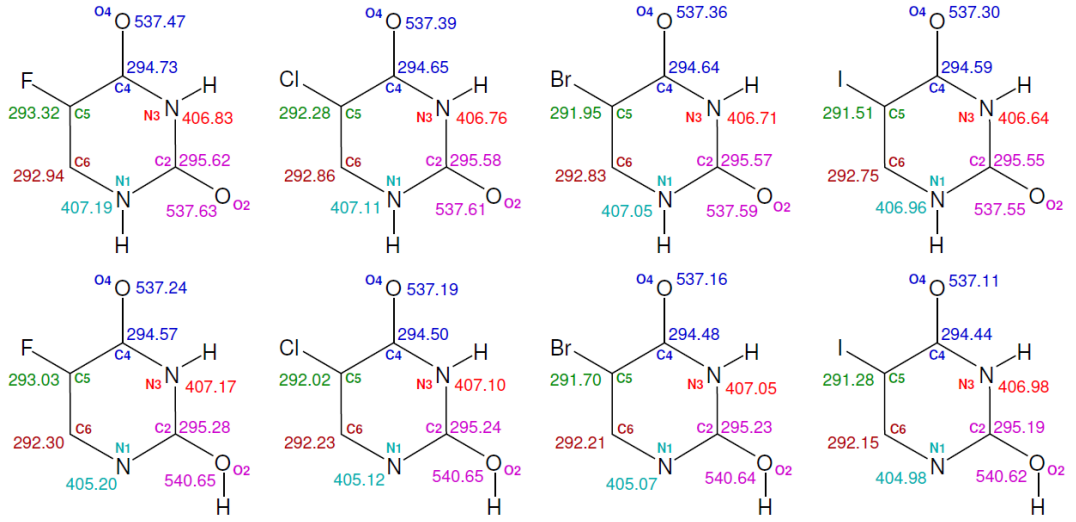

Fig 5.2—1 DFT-B3LYP theoretical prediction of C, N and O 1s BE for the keto and eno form of the four different halogenated uracil molecules [123].

5.2.1 The XPS spectra

For each molecule, the spectra have been measured at temperatures well below their respective ‘critical’ temperatures, where no sign of thermal decomposition or possible tautomersation transitions could be observed in the IR analysis. Therefore the experimental results reported in Fig 5.2—2, Fig 5.2—4 and Fig 5.2—6 for the C, N and O XPS spectra respectively, are compared directly to the theoretical predictions for the keto form. The C(1s) XPS spectra of uracil and its halogenated derivatives is composed of four main peaks, corresponding to the ionization of the four non-equivalent carbon atomic sites in the molecule, the C5, C6, C4 and C2. Each one of these XPS peaks is most likely the convolution of an undefined number of overlapping and unresolved vibrational progressions. The resulting lineshape of each peak has been approximated in the fitting procedure by a Gaussian function with the position of the centroid and the full width at half maximum (FWHM) used as free parameters and constraining the values of the areas of the four peaks to be equal to each other, with a tolerance of 20%. This procedure provides a good description of the spectra. The centroid of each peak has been assumed as the binding energy of the state and is reported in Table 5.2-1 together with the BE of the reference molecule used for the calibration of the spectrum. The calibration has been made using a mixture of the molecule under investigation with the

calibrant and, measuring the BE of the two molecules at the same time, in the same spectrum. In the case of 5FU the calibration has been made with CH_4. In this case it was possible to resolve the vibrational structure of CH_4, assigning the value of 290.689 eV to the first of the three peaks, associated to the adiabatic transition between the ground state and the v=0 state of the ion [66].

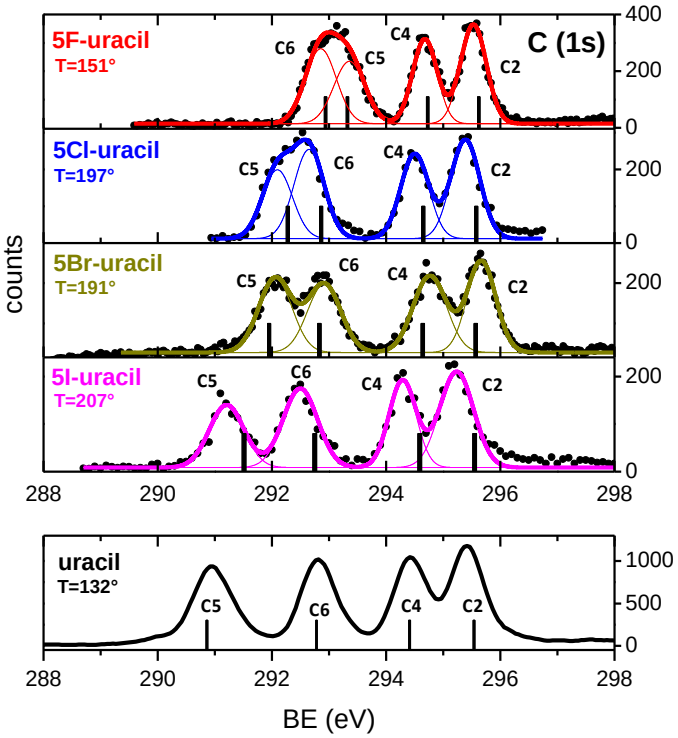

Fig 5.2—2 XPS spectra of C (1s) ionization of the four halogenated uracil molecules. The uracil spectrum is extracted from [121]. The theoretical values of BE for the four non equivalent C atoms in the keto form are shown as black bars. The experimental temperatures used to evaporate the samples are also reported in °C.

For the other 5XU molecules, X=Cl, Br, I, the spectra were calibrated with respect to CO_2. In this case the vibrational structure is not resolved and the peak associated to C (1s) ionization of CO_2 has been fitted with a single Gaussian function to which the value of 297.69 eV has been assigned [66]. This value corresponds to the vertical ionization energy identified as the sum on the vibrational profiles of the single adiabatic transitions. In the same Table 5.2-1 the results of the DFT-B3LYP calculations [123] are reported. The different binding energies of the non-equivalent C atoms of

the uracil molecule are due to the different chemical environment 'experienced' by the 1s electrons in the four different C sites (see Fig 5.2—3). In the halogenated case, the presence of the halogen atom has the overall effect of shifting the binding energies of all core electrons towards higher values with respect to the uracil case.

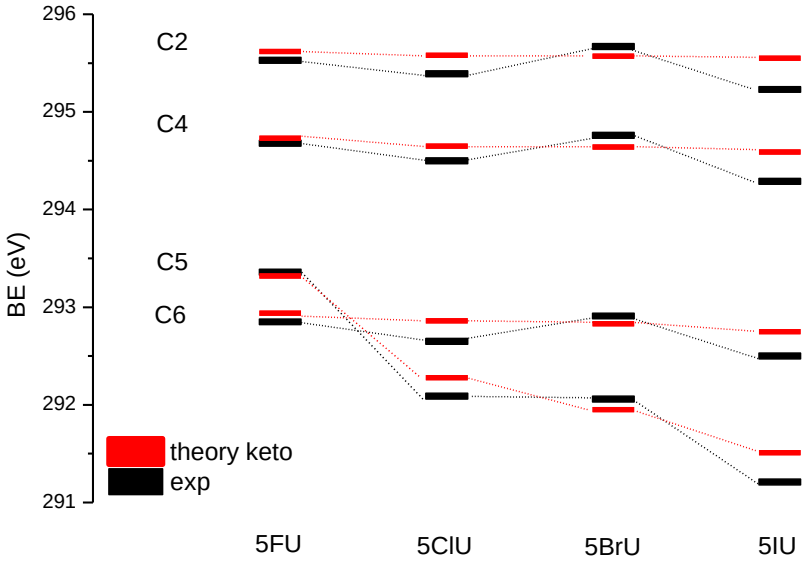

Fig 5.2—3 Correlation diagram for the C (1s) halogenated uracils from the experimental measurements (in black) and DFT calculations (in red).

It can be easily understood that the carbon atom that is most affected by the halogenation process is C5, which is directly bound to the halogen atom and sees its BE energy shifted of an amount that increases with the increasing electronegativity of the halogen atom. This is due to the inductive effect. In the inductive model an electron attractive substituent removes charge density from the neighbouring sites, decreasing the shielding effect of the farthest electrons. In this way the 1s electron on the less electronegative atom will be more affected by the nuclear attraction, increasing its BE.

The keto theoretical values differ from the experimental ones of about 0.2 eV, not uncommon in theoretical calculations involving core electrons. As it is shown in Fig 5.2—3 the computational analysis overestimates the BE values for the C 1s in the 5ClU and 5IU and understimates it in the case of 5BrU. There is a very good agreement for 5FU.

.Molecule		BE (eV) calibrant	Exp (eV)		Theory (eV) (DFT-B3LYP)			
			FIT	ΔE	keto	ΔE_{keto}	eno	ΔE_{eno}
5FU	C5	CH_4 290.689 (adiabatic)	293.36 ± 0.01	0.51± 0.02	293.32	0.38	293.03	0.73
	C6		292.85 ± 0.01		292.94		292.30	
	C4		294.68 ± 0.01	0.85± 0.02	294.73	0.89	294.57	0.71
	C2		295.53 ± 0.01		295.62		295.28	
5ClU	C5	CO_2 297.69 (vertical)	292.09 ± 0.02	0.56± 0.04	292.28	0.58	292.02	0.21
	C6		292.65 ± 0.02		292.86		293.23	
	C4		294.50 ± 0.01	0.89± 0.02	294.65	0.93	294.50	0.74
	C2		295.39 ± 0.01		295.58		295.24	
5BrU	C5	CO_2 297.69 (vertical)	292.06 ± 0.02	0.85± 0.04	291.95	0.88	291.70	0.51
	C6		292.91 ± 0.02		292.83		292.21	
	C4		294.76 ± 0.01	0.91± 0.02	294.64	0.93	294.48	0.75
	C2		295.67 ± 0.01		295.57		295.23	
5IU	C5	CO_2 297.69 (vertical)	291.21 ± 0.02	1.29± 0.04	291.51	1.24	291.28	0.87
	C6		292.50 ± 0.02		292.75		292.15	
	C4		294.29 ± 0.02	0.94± 0.04	294.59	0.96	294.44	0.75
	C2		295.23 ± 0.02		295.55		295.19	

Table 5.2-1 Comparison between the theoretical and experimental values of C (1s) BE for the four halogenated uracil molecules.

The XPS spectra of nitrogen and oxygen are reported in Fig 5.2—4 and Fig 5.2—6, respectively. In both cases, the measured spectra are composed of one peak, corresponding to the ionization of the two non-equivalent, but experimentally unresolved, nitrogen and oxygen atomic sites, respectively. The resulting lineshape of each peak has been approximated in the fitting procedure by two Gaussian functions with the position of the centroid as free parameter and setting the values of the areas and the FWHM of the two peaks to be equal to each other. In all cases this procedure provides a

good description of the spectra.

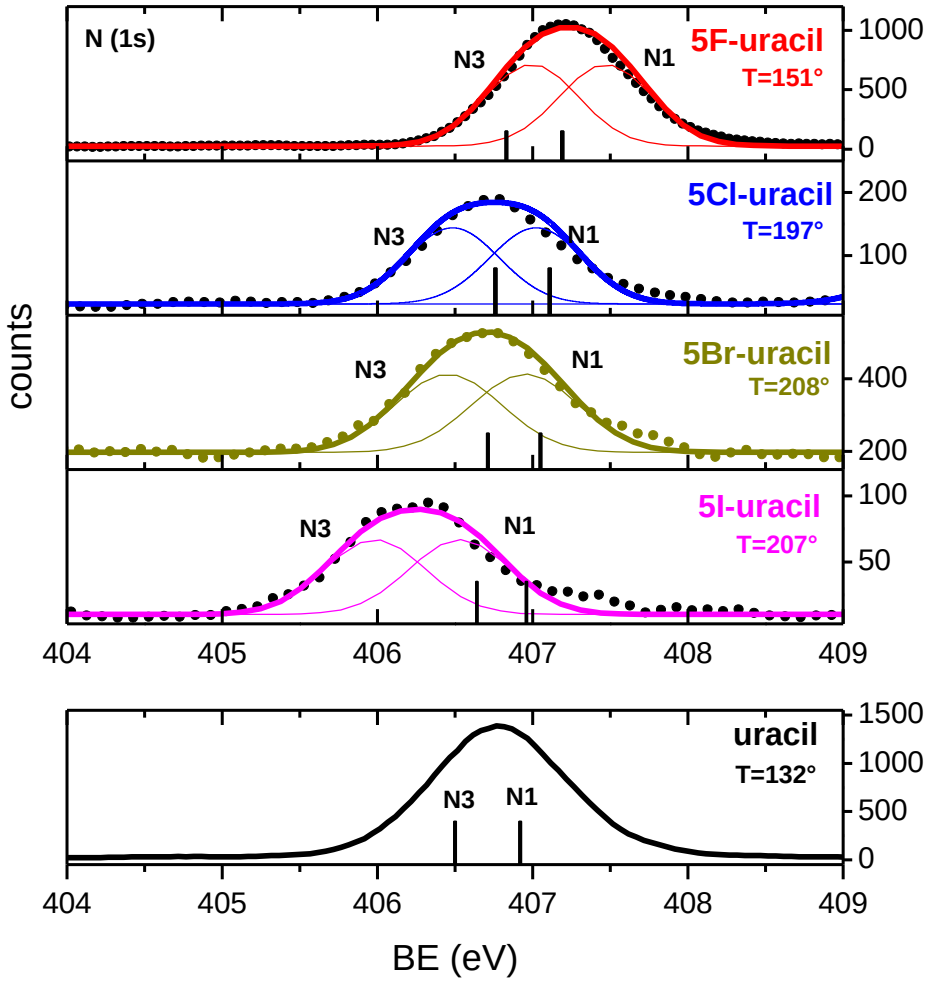

Fig 5.2—4 XPS spectra of N (1s) ionization of the four halogenated uracil molecules. The uracil spectrum is extracted from [121]. The theoretical values of BE for the two non equivalent N atoms in the keto form are shown as black bars. The experimental temperatures used to evaporate the samples are shown in °C.

Similar to C case, also in the N and O XPS spectra it can be observed that the keto theoretical results present an overall shift with respect to the experimental ones, systematically underestimating the BE in the case of 5FU (0.22 eV) (both N and O) and overestimating them in the case of 5IU (0.54 eV), 5ClU (0.18 eV) and 5BrU (0.18 eV) as described in Table 5.2-2 and easily observed by the correlation diagram in Fig 5.2—5.

Molecule		BE (eV) calibrant	Exp (eV)		Theory (eV) (DFT-B3LYP)			
			FIT	ΔE	keto	ΔE_{keto}	eno	ΔE_{eno}
5FU	N3	N_2	406.99 ± 0.01	0.48 ± 0.02	406.83	0.36	407.17	1.97
	N1	409.9	407.47 ± 0.01		407.19		405.20	
5ClU	N3	N_2	406.48 ± 0.02	0.54 ± 0.04	406.76	0.35	407.10	1.98
	N1	409.9	407.02 ± 0.02		407.11		405.12	
5BrU	N3	N_2	406.45 ± 0.12	0.50 ± 0.30	406.71	0.34	407.05	1.98
	N1	409.9	406.95 ± 0.18		407.05		405.07	
5IU	N3	N_2	405.98 ± 0.07	0.55 ± 0.17	406.64	0.32	406.98	2
	N1	409.9	406.53 ± 0.10		406.96		404.98	

Table 5.2-2 Comparison between the theoretical and experimental values of N (1s) BE for the four halogenated uracil molecules.

In general, the trend towards increasing BE values of the N (1s) peaks with the increasing of the electronegativity of the halogen substituent appears to be qualitatively well reproduced by the theoretical calculations. Consistently with the experimental results, these calculated chemical shifts also show a very weak dependency of on the specific halogen atom. However, the distance, ΔE, between the two non-equivalent sites, N1, N3 and O7, O8 is always larger in the experiment than in the theory. Even though it cannot be excluded that this is due to a limitation of the fitting procedure, taking into account two completely unresolved peaks, a more substantial explanation, due to the limits in the accuracy of the theoretical calculations has been considered, and will be discussed later in this section.
Another oddity lying in the theoretical results is that the BE of N1 (1s) is higher than N3 (1s) peak. A qualitative analysis of the chemical environment of the N3 and N1 atoms that takes into account the inductive effect would suggest the opposite conclusion, the N1 atom being surrounded by a H atom, a C=O group and a C-H group unlike N3 surrounded by two C=O groups and a H atom. Similar considerations are

valid in the analysis of the O (1s) spectra (Fig 5.2—6). In this case the discrepancies between theory and experiment are observed not only between the different halogenated molecules but also between the different oxygen atoms in the same molecule. For example, the Table 5.2-3 shows that in the case of 5ClU the theoretical calculations overestimate the BE of the O7(1s) (0.11 eV) and undestimate the BE of the O8 (1s) (0.18 eV). The same considerations are valid for 5BrU, while the theory overestimate the BE in the case of 5IU and underestimate it in the case of 5FU, as it is clearly shown by the correlation diagrams in Fig 5.2—7.

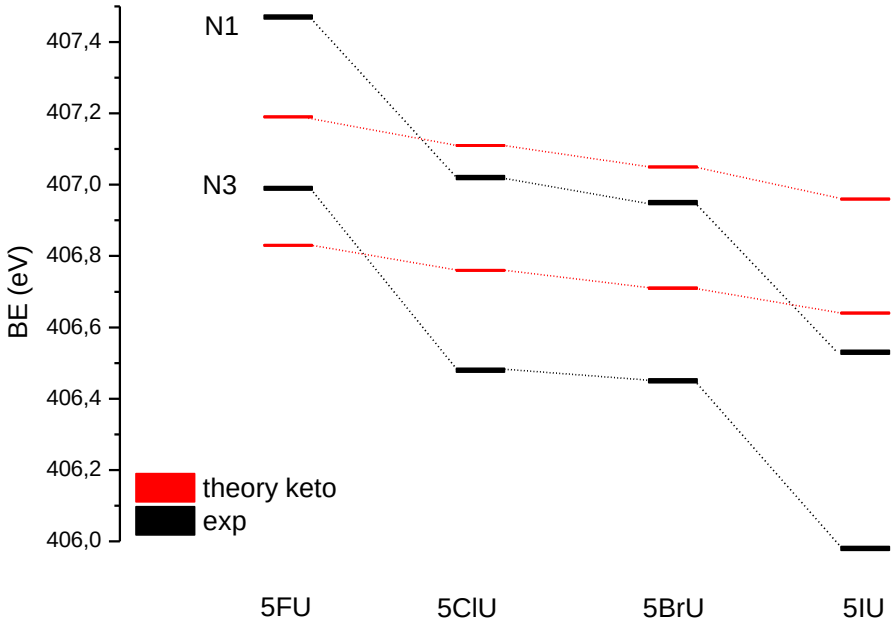

Fig 5.2—5 Correlation diagram for the N(1s) halogenated uracils from the experimental measurements (in black) and DFT calculations (in red).

Even though there is a good qualitative agreement between the experimental observations and the theoretical predictions of the C, N and O XPS spectra of the halogenated uracil molecules, some significant discrepancies are observed, particularly in the O and N cases. This disagreement could be explained considering the possibility that the treatment of the ionized state with a single determinant approach as in the case of the DFT calculation is not enough.

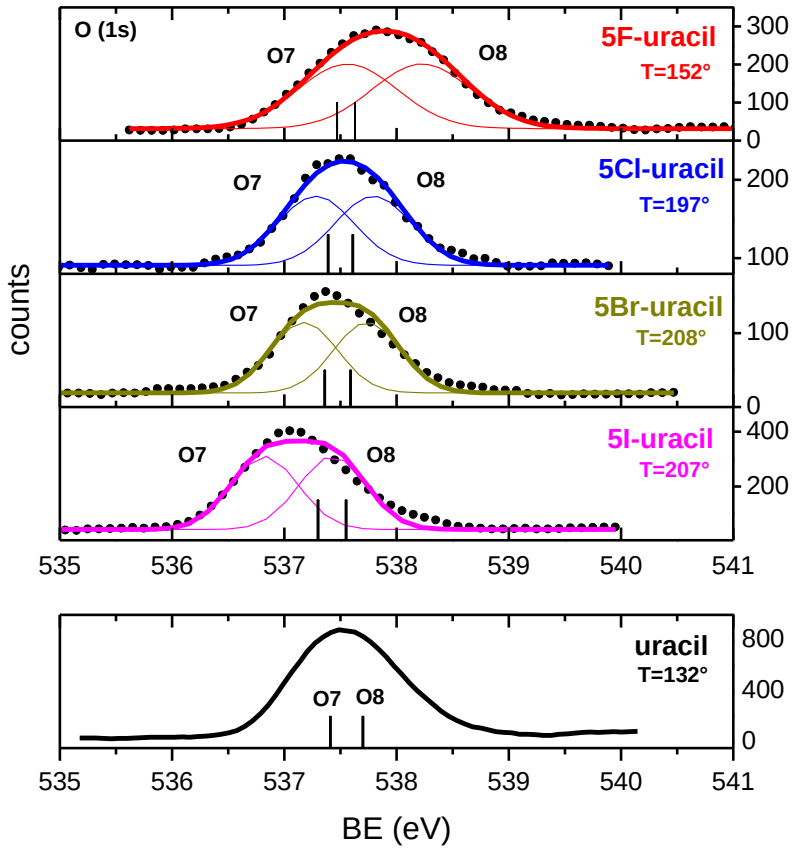

Fig 5.2—6 XPS spectra of O (1s) ionization of the four halogenated uracil molecules. The uracil spectrum is extracted from [121]. The theoretical values of BE for the two non equivalent O atoms in the keto form are shown as black bars.. The experimental temperatures used to evaporate the samples are shown in °C.

The problem, that seems to be more evident in the O and N cases, was already observed in the case of the isolated NO_2 molecule, where there is a huge vibronic coupling (the Born-Oppenhaimer approximation is no longer valid) and an inherently multireference ground state.

All this indicates that it may be difficult to obtain accurate XPS lines in some of these cases, and further theoretical investigation is underway in order to overtake what seems to be a real limit in the present theoretical approach.

Indeed, one of the DFT limitations is that it does not solve effectively the exchange and correlation integral that takes into account the interaction of an electron with all the other electrons and their relative positions.

In order to include the electron correlation, a wavefunction that is a linear

combination of more determinants has to be constructed. The Multi-Configuration Self Consistent Field (MCSCF) is a self-consistent method in which the wavefunction is defined as a linear combination of single Slater determinant Ψ:

$$\Phi_{MCSCF} = c_0\Psi_{HF} + c_1\Psi_1 + c_2\Psi_2 \ldots$$

The obtained wave function Φ is called configuration state function (CSF). A critical point is the choice of a good active space for a MCSCF calculation, which means choosing the right orbitals and configuration to ensure a good flexibility to Φ for a good description of the systems. In the present case the system under investigation is very complex. The halogenated uracil is an aromatic system with several resonant structures, each of which has to be taken into account and correctly described in the calculations.

Molecule		**BE (eV)** calibrant	**Exp (eV)**		**Theory (eV) (DFT-B3LYP)**			
			FIT	ΔE	keto	ΔE_{keto}	eno	ΔE_{eno}
5FU	O7	CO_2 541.254	537.56 ± 0.26	0.66± 0.52	537.47	0.16	537.24	3.41
	O8		538.22 ± 0.26		537.63		540.65	
5ClU	O7	CO_2 541.254	537.28 ± 0.07	0.51± 0.12	537.39	0.22	537.19	3.46
	O8		537.79 ± 0.05		537.61		540.65	
5BrU	O7	CO_2 541.254	537.17 ± 0.05	0.57± 0.09	537.36	0.23	537.16	3.48
	O8		537.74 ± 0.04		537.59		540.64	
5IU	O7	CO_2 541.254	536.82 ± 0.03	0.61± 0.07	537.30	0.25	537.11	3.51
	O8		537.43 ± 0.04		537.55		540.62	

Table 5.2-3 Comparison between the theoretical and experimental values of O (1s) BE for the four halogenated uracil molecules.

For example the overlap of the π orbitals of the ring with the *p* orbitals of the halogen and nitrogen atoms could have significant resonant effects, affecting the BE of these electrons.

Among the possible types of calculation that are being considered to properly describe the present results there is the Complete Active Space method (CASSCF). On one hand, this method allows for a more complete description of the system, considering all possible arrangements of the electrons in the active space.

On the other hand, it could become computationally much heavier and prohibitively time consuming. Another possibility is the Restricted Active Space method (RASSCF) in which a limited number of excitations outside the active space are allowed. The excitations are usually limited to 1 or 2 electrons. Also, a modified Gaussian pseudopotential could introduce a gap in the core (not correlated with the valence electrons) using a normal basis set for the valence electrons. There are, indeed, several ways to be explored in order to improve the present theoretical results and the work is in progress.

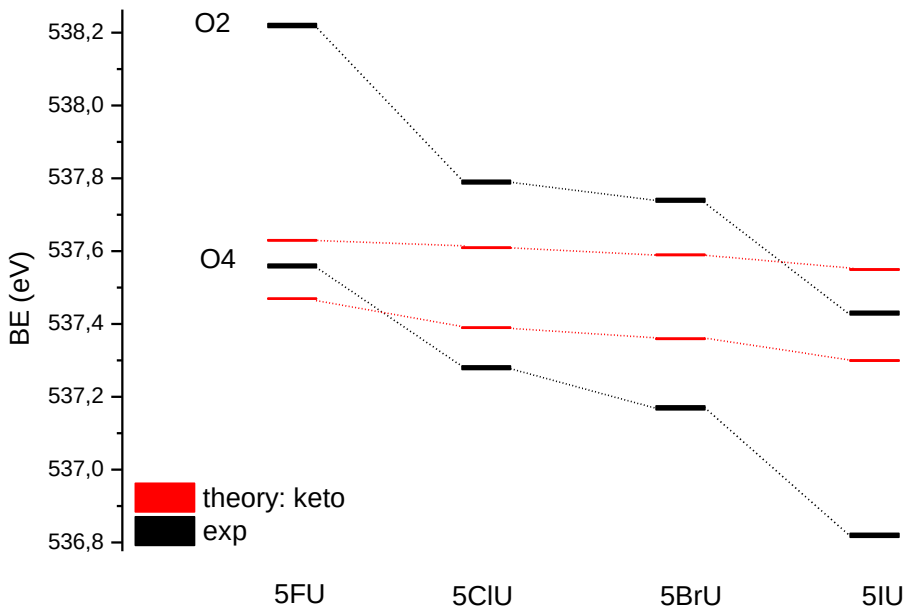

Fig 5.2—7 Correlation diagram for the O (1s) halogenated uracils from the experimental measurements (in black) and DFT calculations (in red).

5.2.2 The NEXAFS spectra

In Fig 5.2—8, Fig 5.2—9 and Fig 5.2—10 the NEXAFS spectra for the excitation of 1s electrons from C, N and O atomic sites of the four molecules are shown. Similarly to the XPS spectra, also in the NEXAFS experiments the photon energy scale was calibrated using a mixture of the molecule under study and a calibration gas with well known absorption peaks in the same energy range, i.e. 525-550 eV for the oxygen atom.

The limitations faced by the present single determinant DFT theoretical method applied to the study of the XPS of halouracil molecules suggest that similar or even worst results would be achieved in the calculation of the NEXAFS spectra, due to the involvement of intermediate excited states, which are expected to make the correlation terms even more important.

Therefore, considering the analogies between the molecules, some hints in the interpretation of the present spectra can be derived by the NEXAFS spectra of uracil [122], pyrimidine and halogenated pyrimidines [31]. As already mentioned in the work of Feyer et al. [122] the strongest features of a NEXAFS spectrum can normally be explained by one or more core-to-valence transitions, many of which are to vacant π^* orbitals. In the uracil case, indeed, the three lowest vacant molecular orbitals are of π^* type, and they contribute to the NEXAFS spectra with configurations that will be labelled LUMO, LUMO+1 and LUMO+2 in the following. The rest of the excitations can be considered to various members of Rydberg series.

The C (1s) NEXAFS spectra of uracil and its halogenated compounds, Fig 5.2—8, show a few common aspects, but are well characterized by different energy positions of the peaks that result in a specific fingerprint of each molecule. In all cases, the spectra are dominated by strong, discrete, features in the low energy region. Similarly to the pyrimidine and uracil cases these features can be assigned to the so called 'π^* resonance', representing the transition of the 1s electron to the antibonding lowest unoccupied molecular orbital (LUMO).

Less intense transitions to other final states, LUMO+1, LUMO+2 and Rydberg states as well as possible overlapping vibrational progressions will most likely produce the shoulders and additional minor features observed in the spectra. In the region above threshold, two broad features, labelled E and F in the uracil case, are observed in all cases.

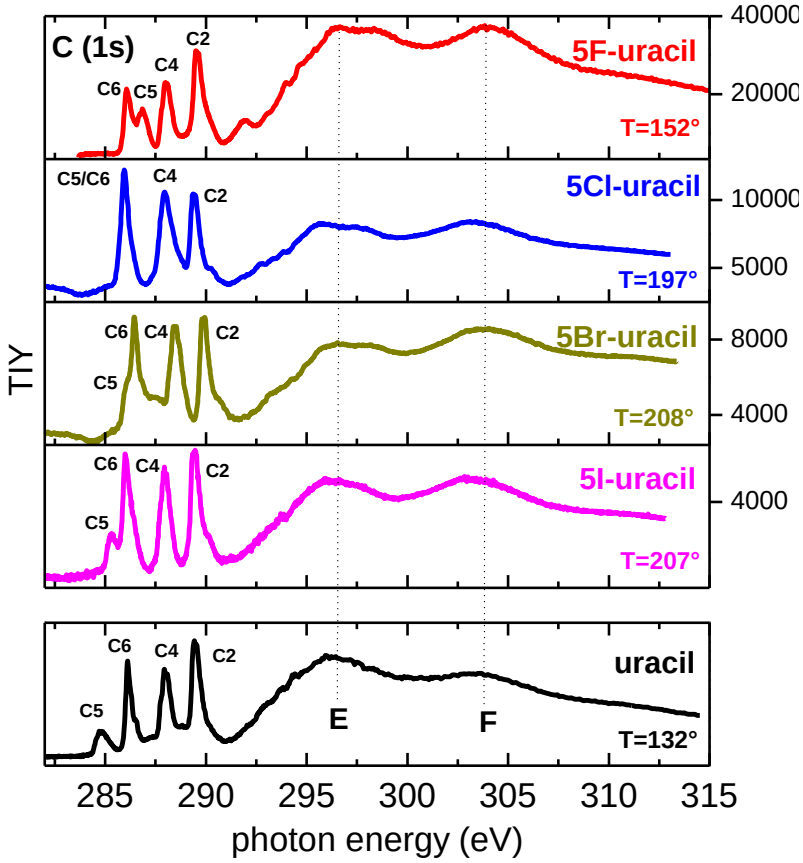

Fig 5.2—8 NEXAFS spectra of C (1s) excitation of the four halogenated uracil molecules. The uracil spectrum is extracted from [122].

Similarly to the Uracil case [122] these can be tentatively attributed to σ* shape resonances, i.e. metastable states in which an electron even though in the continuum, is still temporarily trapped in the vicinity of the molecule due the shape of a potential barrier.

The N (1s) NEXAFS spectra, Fig 5.2—9, are less structured than the C ones, because there are only two non-equivalent N atoms rather than the 4 carbon atoms. The N (1s) NEXAFS spectra present several features that, according to the uracil case discussed in the literature [122] have been labelled with letters A-E. According to the ADC(2)s/6-311+G* calculations [122], features A and B arise mainly from a group of transitions from the 1s orbitals of N1/N3 to the LUMO (A) and LUMO+1 (B) orbitals, respectively, including Rydberg excitations. Features C and D, are dominated by higher Rydberg transitions and transitions to the LUMO+3. Only very tiny differences are observed among the five spectra, i.e. between the uracil and its halogenated compounds, suggesting little effects

of the halogenation process to the N atoms, which are indeed quite far away from the halogenation site in position 5. A similar behaviour was already observed in NEXAFS spectra of the halogenated pyrimidine molecules [31]. The small, discrete structures, clearly visible at about 401eV, on top of feature A of the 5IU, 5BrU and 5ClU molecules, are due to the π* transition of the N_2 molecule present as contamination from the residual gas in the vacuum chamber.

The O(1s) NEXAFS spectra, Fig 5.2—10, are composed of three main features, labelled A-C. According to the uracil case, the intense peaks A and B are assigned to the transitions from the O7 and O8 (1s) to the LUMO orbital, respectively, while feature C comprises various excitations to Rydberg states. Similarly to the N case, very little influence of the halogenation process can be seen on the O (1s) NEXAFS spectra.

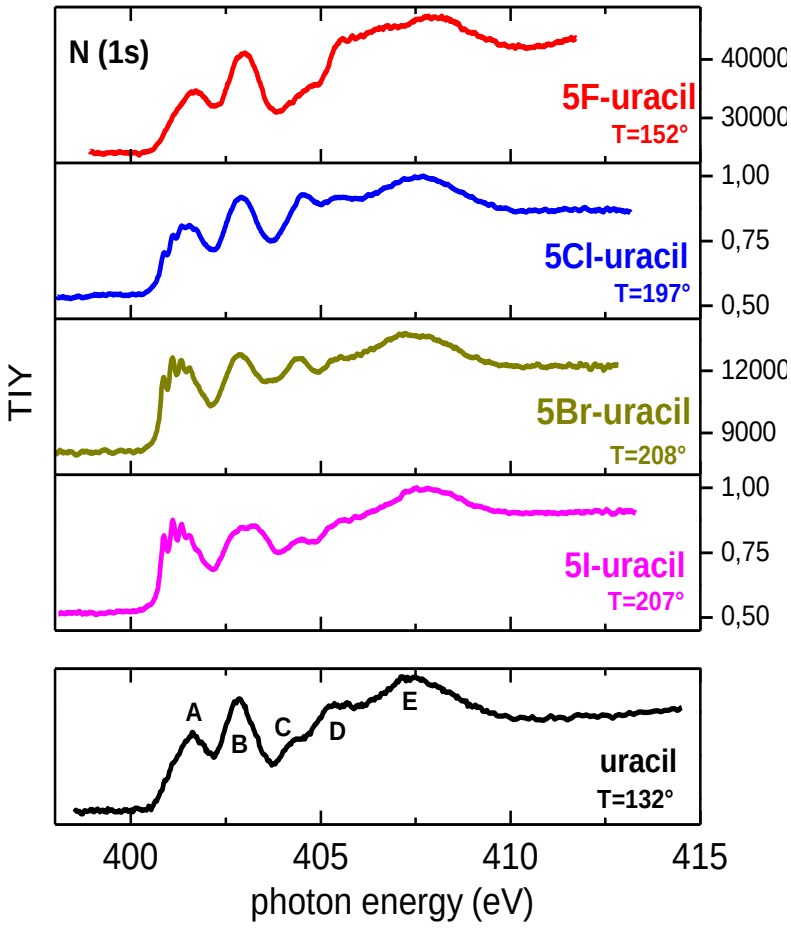

Fig 5.2—9 NEXAFS spectra of N (1s) excitation of the four halogenated uracil molecules. The uracil spectrum is extracted from [122].

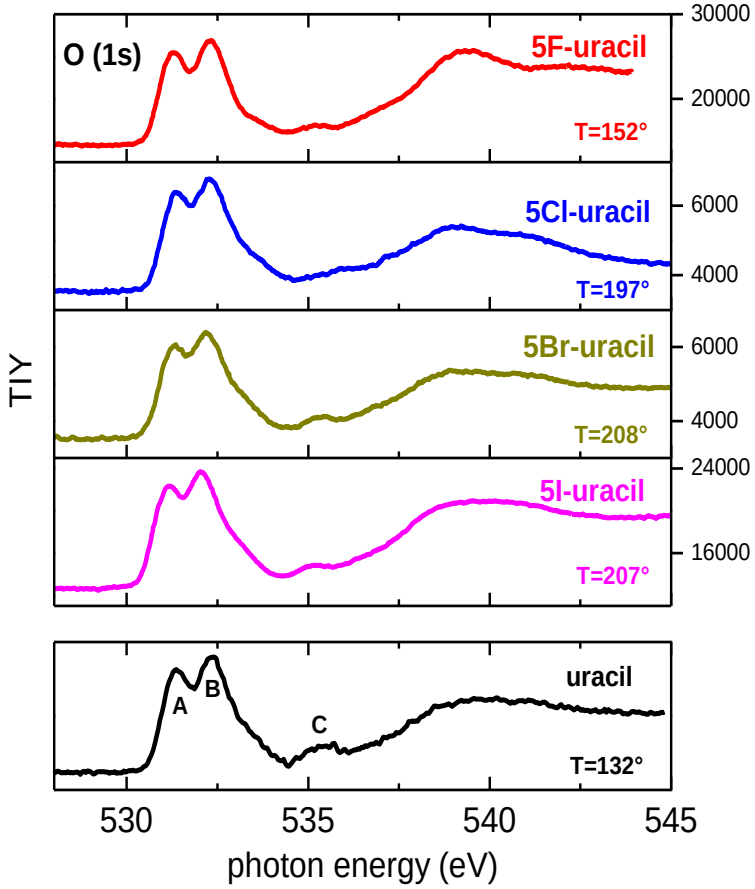

Fig 5.2—10 NEXAFS spectra of O (1s) excitation of the four halogenated uracil molecules. The uracil spectrum is extracted from [122].

The investigation of the keto-enol tautomerism in gas phase through XPS analysis has not been completed because of technical problems encountered during the experimental procedure at the GasPhase beamline of the ELETRRA synchrotron radiation source. The temperatures suggested from the FT-IR tests to produce a tautomerisation in the 5FU (~330°C) and 5IU (~270°C) molecules, produced such an intense vapour beam to evaporate the target molecules more than 20 times faster than the normal operation (typical evaporation rate is 4 mg/hour). As a consequence, the fast contamination of the set-up produced a tick coating of the analysers. Being these molecules insulators the contamination produced a charging-up of the electrodes and large unstable kinetic shifts in the XPS spectra. An attempt has been performed in the case of 5FU, but already at 250°C the measurement could not be handled anymore. Therefore the XPS could not be used to confirm/disproof the possible tautomerisation in gas phase.

5.3 Ion-impact ionization/fragmentation of 5BrU

This section presents the results of the fragmentation studies of the 5BrU molecule induced by the impact with low energy ions of $^{12}C^{4+}$ at 36 keV. These multiply charged ions with intermediate charge state resemble the condition of carbon ions used in hadrontherapy, below the Bragg peak energy. In the second and third part of the chapter the same projectile has been used to study the fragmentation of homogeneous clusters and hydrated clusters of 5BrU molecules respectively. The increasing size and complexity of the target from isolated molecule to clusters and hydrated clusters, is meant to mimic the presence of an environment surrounding the single molecule in order to simulate a more realistic biological system.
The purpose of this part of the work is to understand how the environment can affect the fragmentation properties of the single molecule which is a key step in building a basic model that can be applied to a more realistic context, as the cellular environment.
The motivation to study 5BrU is given by the important role that this molecule has in radiobiology and astrochemistry: while 5BrU is not naturally found in DNA, it can be substituted for thymine and incorporated in the DNA of fast replicating tumor cells, making them more sensitive to the lethal effects of UV, x-ray, and γ-ray radiation [128, 46]. Moreover recent theoretical studies about the canonical (keto) and rare (enol) tautomers of U and 5BrU in clusters comprising 50 and 100 water molecules (nanodroplets) have been performed at DFT-B3LYP level of theory [129]. The results show that the gas phase tautomerization energies of uracil and 5BrU are very similar, favoring the keto tautomer. However, in the hydrated phase, the tautomeric preference of 5BrU is reversed. This result indicates that the bromine atom in the 5-position considerably increases the proportion of the hydroxyl group present in uracil.
All these considerations have been taken into account in the analysis of the spectra.

5.3.1 Single molecule

As well as in 5Br-pyr the fragmentation mass spectra of 5BrU present a series of double peaks due to the isotopic effect of the ^{79}Br and ^{81}Br and their relative abundance. The double peak at m/z=190/192 is due to the

parent ion, called M^+ in the following study, while there is no evidence of the double charged parent ion (see Fig 5.3—1).
The most important dissociation reactions are described below:

$$C_4H_3BrN_2O_2^{+}{}_{(m/z=190/192)} \rightarrow C_3H_2BrNO^{+}{}_{(m/z=147/149)} + HCNO_{(m/z=43)} \quad (5.3\text{-}1)$$

$$C_4H_3BrN_2O_2^{+}{}_{(m/z=190/192)} \rightarrow C_2HBr^{+}{}_{(m/z=104/106)} + 2HCNO_{(m/z=86)} \quad (5.3\text{-}2)$$

$$C_4H_3BrN_2O_2^{+}{}_{(m/z=190/192)} \rightarrow C_2BrOH^{+}{}_{(m/z=120/122)} + HCNO_{(m/z=43)} + HCN_{(m/z=27)} \quad (5.3\text{-}3)$$

$$C_4H_3BrN_2O_2^{+}{}_{(m/z=190/192)} \rightarrow C_2BrNH_3^{+}{}_{(m/z=120/122)} + C_2O_2N_{(m/z=70)} \quad (5.3\text{-}4)$$

$$C_4H_3BrN_2O_2^{+}{}_{(m/z=190/192)} \rightarrow C_2HBrN^{+}{}_{(m/z=118/120)} + HCNO_{(m/z=43)} + COH_{(m/z=29)} \quad (5.3\text{-}5)$$

$$C_4H_3BrN_2O_2^{+}{}_{(m/z=190/192)} \rightarrow BrC^{+}{}_{(m/z=91/93)} + C_3H_3N_2O_2\ (m/z=99) \quad (5.3\text{-}6)$$

$$C_4H_3BrN_2O_2^{+}{}_{(m/z=190/192)} \rightarrow Br^{+}{}_{(m/z=79/81)} + C_4H_3N_2O_2\ (m/z=111) \quad (5.3\text{-}7)$$

The charged fragments obtained after the dissociation are indicated with an arrow in the mass spectrum in Fig 5.3—1.

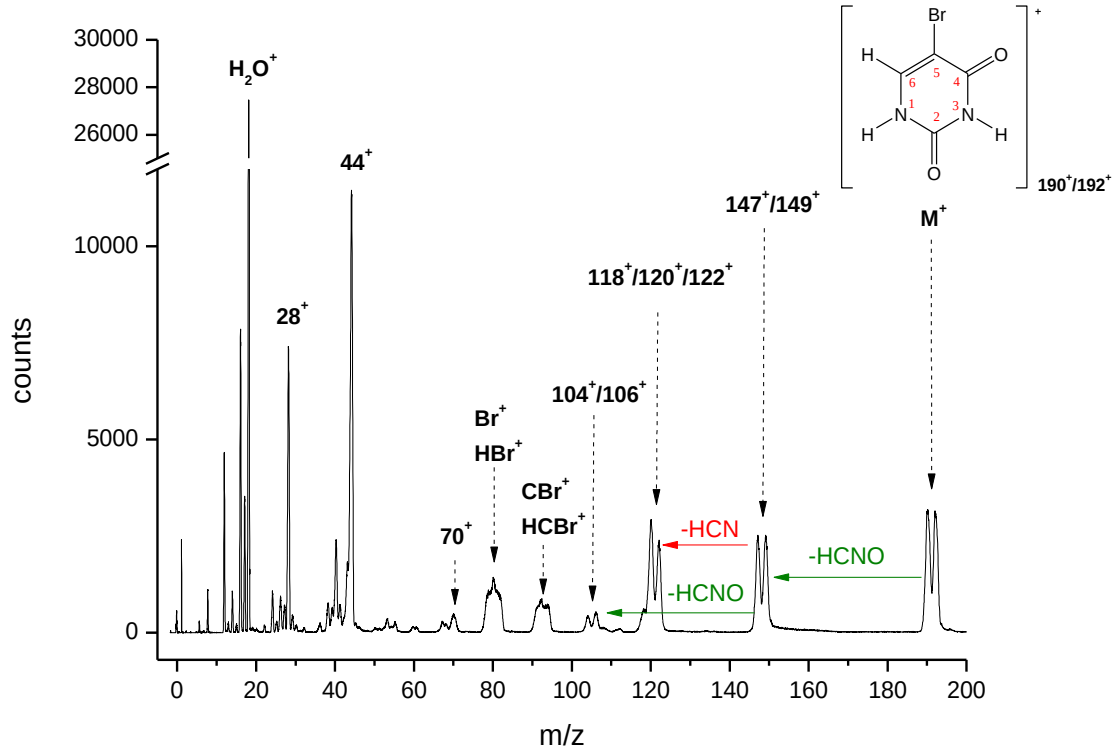

Fig 5.3—1 The mass spectrum of 5BrU after the collision with $^{12}C^{4+}$ projectile at 36 keV.

Starting from the higher values of m/z, fragment at m/z=147/149 could be obtained by three different fragmentation processes and, depending on the location of the bond breaking, a second loss of HNCO is possible. Indeed as it is observed in Fig 5.3—2 the process ***a*** involves the breaking of the C4–C5 and C2–N3 bonds and in this case the release of another HCNO group is possible following the process ***c*** (with the breaking of the C2–N3 and N1–C6 bonds) with a remaining fragment at m/z=104/106 associated to C_2HBr^+ as described by eq.(5.3-2). In the case of process ***b*** a further release of a HCN group is not possible. This observation will turn out to be important in the discussion of the m/z=118/120/122.

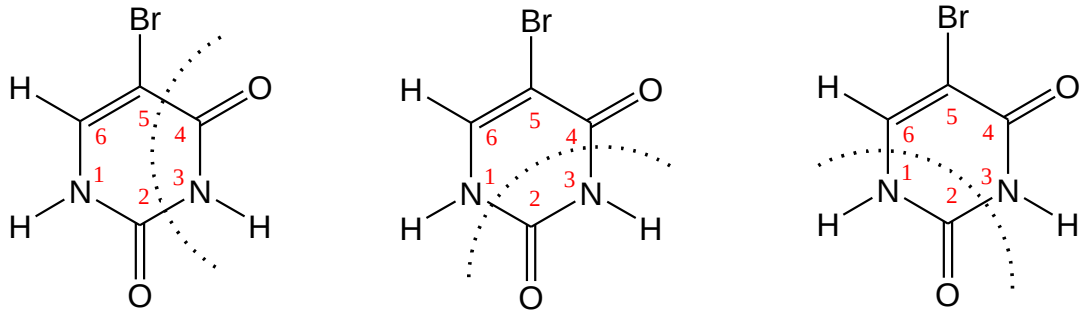

Fig 5.3—2 The different fragmentation processes associated to the formation of a fragment at m/z=147/149.

The m/z=120/122 has to be attributed to a fragment containing the Br atom so that an equal intensity distribution between the two peaks should be measured. However this is not the case, and the presence of an additional fragmentation channel at m/z=118/120 can be suggested to explain the non-isotopic proportionality of these peaks. In Fig 5.3—3 two possible scenarios, due to two different kind of hydrogen migration leading to 118/120 and 120/122 features are described. In the first case the H bound to C6 migrates towards the O7 forming an OH group. This “new” structure can subsequently break giving a fragment at m/z=118/120 following the ***d*** pattern or a fragment at m/z=120/122 following the ***e*** pattern. The relative probability of processes ***d*** and ***e*** can explain the different intensity ratio between the peaks 120/122 and 118/120.

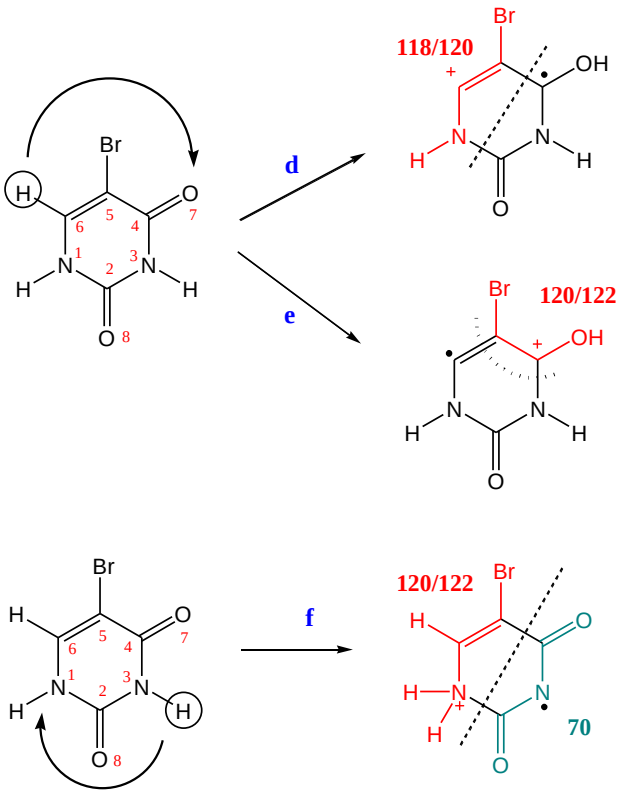

*Fig 5.3—3 Different fragmentation processes responsible of the fragment at m/z=118/120 (process **d**) and 120/122 (processes **e** and **f**)*

Another possible way of fragmentation responsible of the peak at m/z=120/122. The fragmentation pattern ***f*** in Fig 5.3—3 describes the migration of the H bound to N3 towards the N1 atom. In this way the fragment at m/z=120/122 (in red) and a fragment at m/z=70 (in green) that is also present in the mass spectrum can be formed.

The absence of the protonated parent ion seems to suggest that the H transfer is an intramolecular migration, probably induced by the excitation, ionization process, providing the necessary energy. Also the fragment HBr^+ has already been described by previous photoelectron-photoion coincidence studies (PEPICO) as an hydrogen migration from N3 towards the Br atom. In that case the fragment HBr^+ has been collected in coincidence with HN1C6H, confirming that the H that migrates is the one joined to N3 on the ring [130].

Another interesting feature of the single-molecule system is the presence of doubly charged fragments. In this molecule the double peak at m/z=59.5/60.5 is due to the formation of the fragment $119^{2+}/121^{2+}$ (Fig 5.3—4). It seems that this fragment does not exist singly charged. The

uniqueness of this doubly charged fragment suggests that the presence of the bromine atom somehow stabilizes the doube charge long enough for this fragment to be detected.

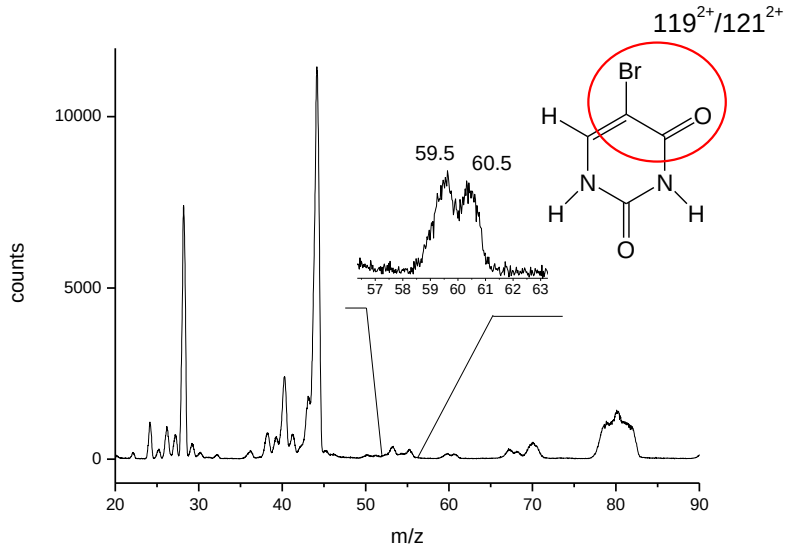

Fig 5.3—4 Double charged fragment at m/z=59.5/60.5 due to the presence of $(119/121)^{2+}$.

The two intense peaks at m/z = 18 and m/z = 44 in the mass spectrum assigned to H_2O^+ and CO_2^+ respectively are mostly due to impurities rather than fragmentation of the molecule. Data processing makes it possible to track selected fragments over the time of acquisition. The cold "trap" surrounding the interaction region is cooled down to the liquid nitrogen temperature, recondensing the molecular and also the residual gas in the vacuum chamber, and producing an overall improvement of the background pressure in the chamber. The H_2O peak is due to the presence of water in the residual gas and in the powder of the molecule. Its decomposition into OH^+ and O^+ contributes to the peaks m/z = 17 and 16. The evolution in time of the intensity of the water molecule peak shows that its partial pressure tends to decrease in time, as the background vacuum improves. The 5BrU molecule can not break into a fragment of m/z=44 so that the high intensity of the CO_2^+ fragment could not be explained as due to residual gas only. Another possible source is the degassing from Thermocoax wire for heating the furnace.

5.3.2 Cluster

The purpose of the study of the molecular aggregation of 5BrU is the understanding of the effects of the environment on the fragmentation dynamic of the single molecule. It is important to remember that the cluster source employed in this experiment does not ensure a full control of the kind of clusters created. This information is not known 'a priory' but, as it will be discussed later on in this chapter, some models can be proposed based on the fragmentation studies performed in this work. One of the questions that usually rises is about the nature of the cluster and which kind of forces are responsible of the aggregation. It is possible to divide these typologies in *planar*, where the molecules are kept together by hydrogen bonds, or *stacked* where the forces responsible of the aggregation are the London dispersion forces (see Fig 5.3—5).

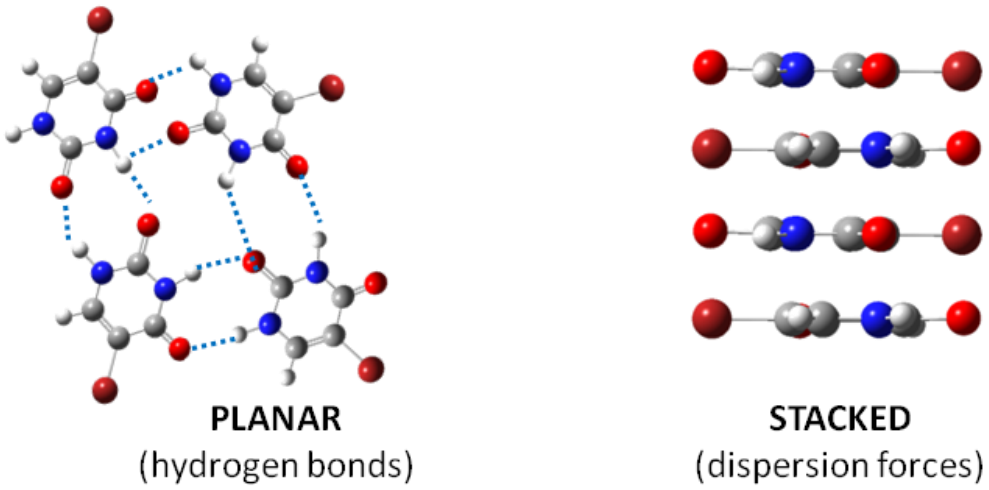

Fig 5.3—5 Different kind of cluster.

The presentation and discussion of the mass spectrum will be divided in two region: the region of m/z ≤ 200 (Fig 5.3—6), which contains the fragmentation of the monomer, and the region m/z > 180 (Fig 5.3—7), which refers to the cluster region.

In Fig 5.3—6 and Fig 5.3—7 the fragmentation spectra of the isolated molecule and clusters of 5BrU are compared. The region of the spectrum up to the mass of the monomer (Fig 5.3—6) shows some substantial differences. A general feature in the case of the clusters is the very broad shape of the peaks due to the latge amount of kinetic energy involved in the

rupture of the cluster. Furthermore in the cluster spectrum it is possible to observe the protonation of the monomer. Therefore the peaks at m/z = 190/192 are no longer distinguishable and the non-isotopic proportionality is explained by the presence of protonated species. The fit procedure confirms this theory, as this broad peak can be fitted with four Gaussian functions; two of them are fixed at 190 and 192 for the monomer and the other two at 191 and 193 for the protonated monomer. These couples of Gaussian functions are forced to have the same shape. The isotopic contribution of ^{13}C has been taken into account. The fit procedure shows that there is a larger quantity of protonated monomer with respect to the unprotonated one.

It is possible that the H^+ is gained from the fragmentation of larger clusters. Apparently the finite environment of a cluster is sufficient to allow "characteristic" fragmentation channels, which are normally only present in the condensed phase, as for example the OH-loss peak at m/z=174. OH loss is the only channel observed that can exclusively be due to exocyclic bond cleavage. This peak is centered at m/z = 174 and it is in principle due to a double peak at m/z = 173/175, but the high kinetic energy of these fragments dominate over the resolution. The fragmentation process responsible of this fragment is described in Fig 5.3—6.

The lost of the OH group suggests that the geometry of the cluster created in the source is planar rather than stacked because only the formation of a hydrogen bond between the monomers can explain this fragmentation patterns visible only in the case of the cluster. Other previous studies have already proven this theory [131].

Another interesting peak in the cluster spectrum, which is completely absent in the case of the isolated single molecule, is the one at m/z=84. This is associated to a fragmentation pattern that involves the same species that produce the fragment at m/z=174 and in particular the rest of the dimer that does not survive and quickly fragments giving rise to the m/z = 84.

As shown in Fig 5.3—6 the monomer that has retained the OH group will fragment loosing the Br, HCNH and O atoms, giving rise to the peak at m/z = 84. The hydrogen bonds that kept together the two monomers are no longer such after the breaking of the dimer, but the H and O atoms will be covalently bound to the other O and H, respectively.

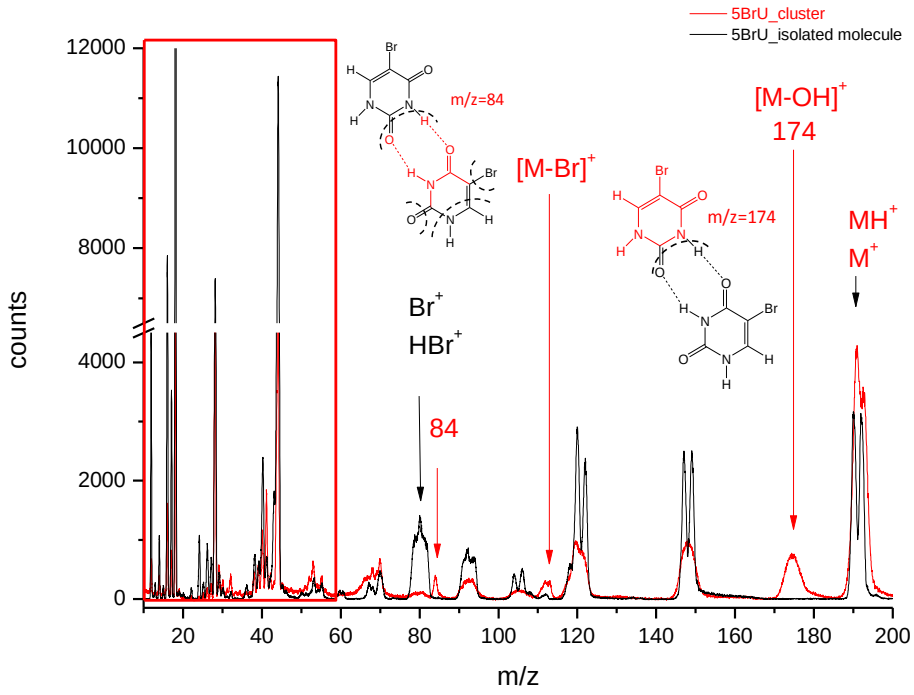

Fig 5.3—6. Comparison between the spectrum of 5BrU isolated molecule (in black) and clusters (in red). The rectangle highlights the region at low masses. The most important fragmentation channel for both targets are shown. The fragmentation involving the loss of OH group (m/z=174) and the formation of the fragment at m/z=84 are described. These spectra are obtained after the collision with $^{12}C^{4+}$ ions at 36 keV and have been normalised to their respective total areas up to m/z = 200.

In the region of low masses, highlighted with a rectangle in Fig 5.3—6 where the two spectra have been normalised to their respective areas up to the monomer, the relative intensities of the peaks in the cluster spectrum are smaller compared to the isolated molecule. This suggests a "protective effect" of the environment on the single molecule, reducing its fragmentation.

This "protective effect" has already been observed studying the ion-beam fragmentation of aminoacids [132] and can be explained considering that in the cluster system the energy absorbed by the collision with the ion-beam can be dissipated by breaking the cluster in addition to the monomers that form it. While in the single molecule, the only way to dissipate the energy is the fragmentation of the monomer.

Moreover the absence of doubly charged fragments suggests that the

cluster, probably due to its larger size, helps stabilizing the two charges far away from each other, before the breaking, creating only singly charged fragments.

It is important to notice that in the cluster case, the peak at m/z=111, associated to the charged ring $[M\text{-}Br]^+$ is more intense with respect to the isolated molecule while the opposite happens for the peak associated to the lost of the Br^+ (and HBr^+). This seems to confirm that for the single molecule the energy transferred to the system is completely spent in breaking the molecule into small fragments while in the cluster the charged ring survives, because most of the energy is spent in breaking the cluster and the rest is employed in relaxing processes. On the other hand the isolated molecule releases a larger quantity of Br^+ and HBr^+ with respect to the cluster.

Looking at the region of the high masses (m/z > 180) in Fig 5.3—7, a series of interesting feature can be observed regarding the formation of clusters of different size. In Fig 5.3—7 the highest peak is the monomer of 5BrU and this is followed by a distribution of monocharged aggregates up to size n = 8. Between the peaks of the clusters, the formation of less intense peaks corresponding to the loss of a bromine atom by the aggregates is observed. The very small peak at m/z=79/81 in Fig 5.3—6 suggests that the bromine loss is less probable in the clusters than in the isolated molecule where this atom is embedded in a more complex structure that does not exclude its participation in hydrogen bond bridge between monomers. The broad tails that follow the cluster peaks in Fig 5.3—7 can be explained by a process of delayed fragmentation of excited metastable states that take place in the region of ionization-acceleration of the TOF spectrometer. If the ionic state of the intact target molecule/cluster lives long enough, it can be extracted from the ionisation region as a still unfragmented object. When the fragmentation takes place a sudden change of m/z will happen. If this occurs still in the TOF acceleration region, then the fragment is accelerated in turn but for less time than that of the same fragment formed at former times, before the extraction. It therefore appears on the spectrum between the mass of the fragment and the one of the intact molecule. This is the reason of the long tail of the peak.

Another possibility is the emission of a fragment in the area of free flight. Cations are subject to acceleration field and respond according to their m/z

ratio. However, the free flight zone has a constant field, meant to "give time" to the different m/z particles to spread according to their time of flight. Therefore, a fragment "born" in the free flight zone, has the same speed as the larger molecule that it is derived from. The fragment is coincident with the intact molecule in the spectrum and it is not possible to determine this contribution.

This phenomenon of delayed fragmentation gives information about the kinetics of fragmentation of the molecule. But in this specific work the study of the kinetic aspects has not been taken into account.

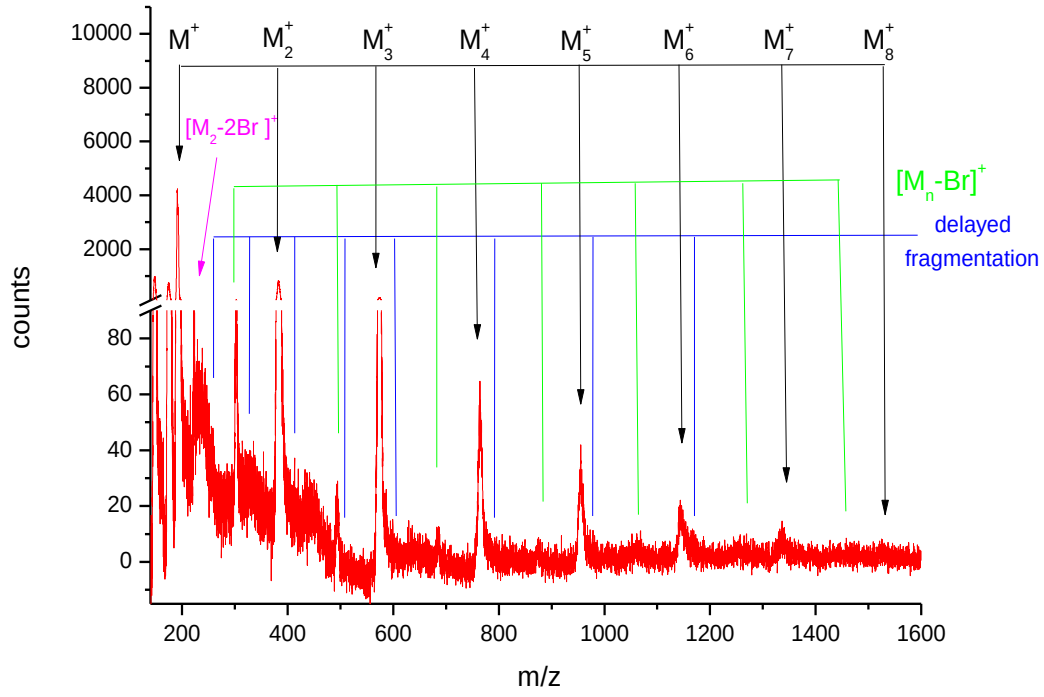

Fig 5.3—7 Magnification of the cluster spectrum in the region of high masses. The maximum number of 5BrU molecules bound together into a cluster is 8 at m/z=1528.

5.3.3 Hydrated cluster

The study of hydrated clusters of 5BrU molecules has the purpose to investigate the role of the environment on the fragmentation dynamic at the single molecule level. In this case the environment contains also water molecules to mimic a more realistic environment of a cell nucleus.

The first question which arises is about the type of hydrated cluster that could be formed. The water molecules could be scattered between the monomers or set all around the cluster in form of water clusters (see for example Fig 5.3—8).

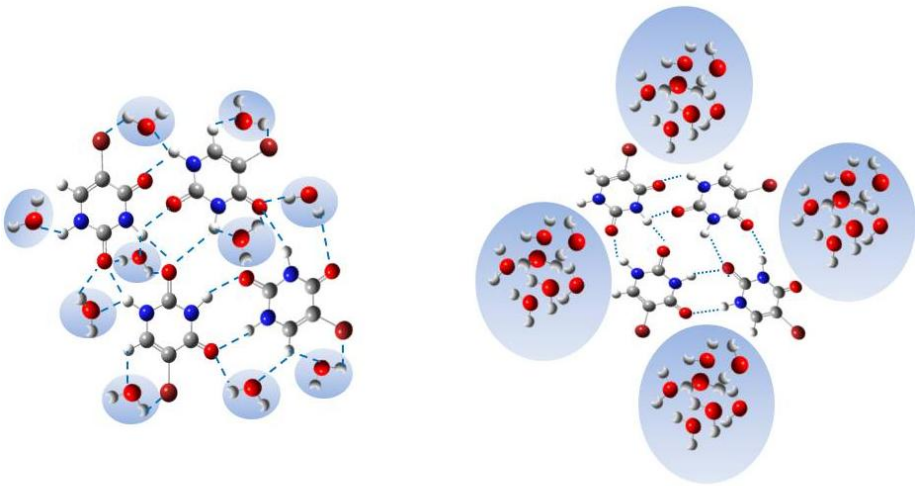

*Fig 5.3—8 Different type of hydrated clusters of 5BrU molecules. The water molecules could be scattered among the 5BrU molecules (configuration **a**) or they could create clusters and surround the cluster of 5BrU molecules (configuration **b**).*

The analysis of m/z spectra can help answering this question. The mass spectra of the hydrated and homogeneous clusters are shown and compared in Fig 5.3—9 for the m/z region up to the monomer, M^+. This figure shows a series of new fragments in the 5BrU and its hydrated clusters, indicated by arrows, which will be now discussed.
In this low m/z region a series of peaks associated to the formation of water clusters of increasing size can be observed. The peaks at m/z= 37, 55, 73, 91 and 109 are due to the H_3O^+ molecule (m/z=19) to which a series of water molecules (m/z=18) has been added (see list a).

list a:

H_3O^+	m/z = 19
$(H_2O)(H_3O)^+$	m/z = 37
$(H_2O)_2(H_3O)^+$	m/z = 55
$(H_2O)_3(H_3O)^+$	m/z = 73
$(H_2O)_4(H_3O)^+$	m/z = 91
$(H_2O)_4(H_3O)^+$	m/z = 109

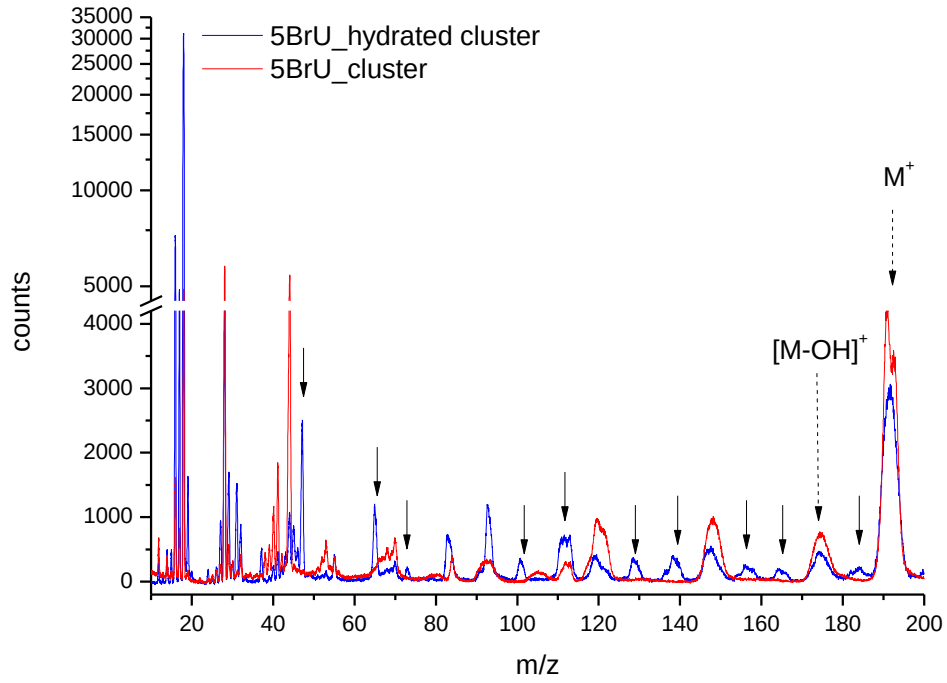

Fig 5.3—9 Comparison of the m/z spectra of the homogeneous cluster (in red) and the hydrated cluster (in blue) of 5BrU molecules. The two spectra are normalised to the total area. A series of new fragments in the region up to the monomer is indicated by the arrows in the blue spectrum.

The series is shown in Fig 5.3—10. The peaks are completely resolved and they can be fitted by a single Gaussian function up to the m/z=73. After that, the shape of the peaks is very broad. Several reasons contribute to this broad lineshape, from the degrading m/z resolution of the TOF spectrometer, to the large kinetic energy release involved in the cluster fragmentation and, most important, the complexity of the target system that can give rise to several possible fragmentation channels, that in principle have to be considered in the assignment of each feature in the spectrum. To make the situation even more complex, the protonated species have also to be taken into account. Fortunately, some 'constraints' can help to disentangle all these contributions, through a fitting procedure.

The analysis program that has been used for the fitting is Fityk. The procedure that has been adopted consists of: i) identify all the possible fragments that contribute to a m/z peak; ii) for each fragment consider the

possible presence of the protonated species; iii) for all the fragments that contain a Br atom, constrain two Gaussian functions to have the same shape and area, with two unit of atomic mass shift; iv) set the same FWHM for the Gaussian functions associated to a fragment and its respective protonated one. In the latter case it has been assumed that the kinetic energy of a fragment and its protonated species is the same. Once the procedure to fit the peak is concluded it is possible to move to the next member of the series, obtained adding a H_3O^+ or a H_2O molecule to the mass of interest depending on the cases, as will be described below. Interestingly, even though both the water (m/z = 18) and protonated water molecule (m/z = 19) are observed, while there is a clear evidence of a strong predominance and even exclusive formation of protonated water clusters rather than water clusters.

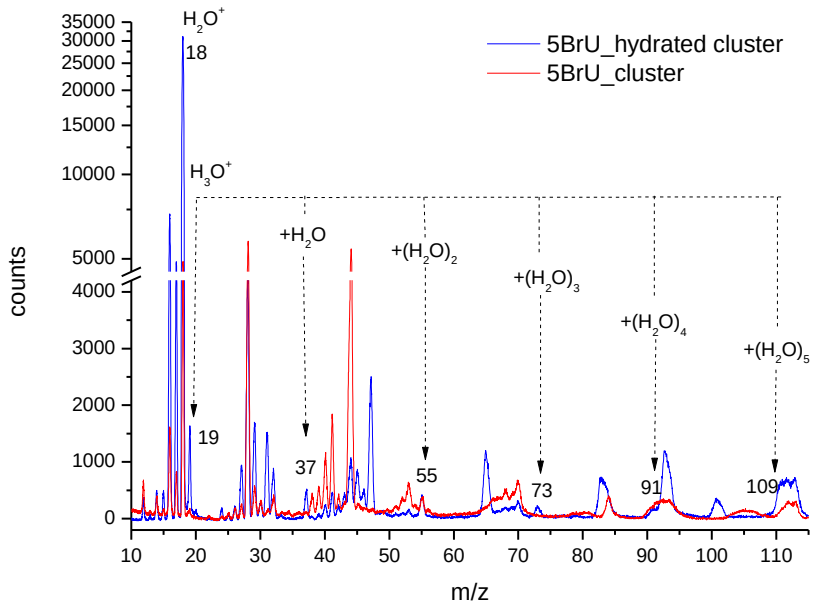

Fig 5.3—10 Comparison between the 5BrU hydrated clusters (blue) and 5BrU homogeneous clusters (red) spectra in the m/z region of the water clusters. The peaks due to the formation of water clusters in the blue spectrum are indicated by arrows (see also list a).

In the same region of low m/z there is evidence of another series. It is the fragment HCNH (m/z = 28) with the addition of an increasing number of water molecules (see list b). Similarly to the water cluster case, it is interesting to note that this hydrated fragment is protonated since the first

term at m/z = 47 corresponding to the acquisition of a protonated water molecule.

list b:

$HCNH^+$	m/z = 28
$(HCNH)(H_3O)^+$	m/z = 47
$(HCNH)(H_2O)(H_3O)^+$	m/z = 65
$(HCNH)(H_2O)_2(H_3O)^+$	m/z = 83
$(HCNH)(H_2O)_3(H_3O)^+$	m/z = 101
$(HCNH)(H_2O)_4(H_3O)^+$	m/z = 119

Also in this case the peaks are completely resolved up to m/z=65 while starting from m/z = 83 we have to add new Gaussian functions in the fitting procedure due to the presence of different fragments. For example the peak indicated as m/z = 83 in Fig 5.3—11 has a broad shape due to two contributions: one at m/z = 83 due to $(HCNH)(H_2O)_2(H_3O)^+$ and another one at m/z = 84 due to $(C_3O_2NH_2)^+$ from a cluster fragmentation that has already been described in section 5.3.2.

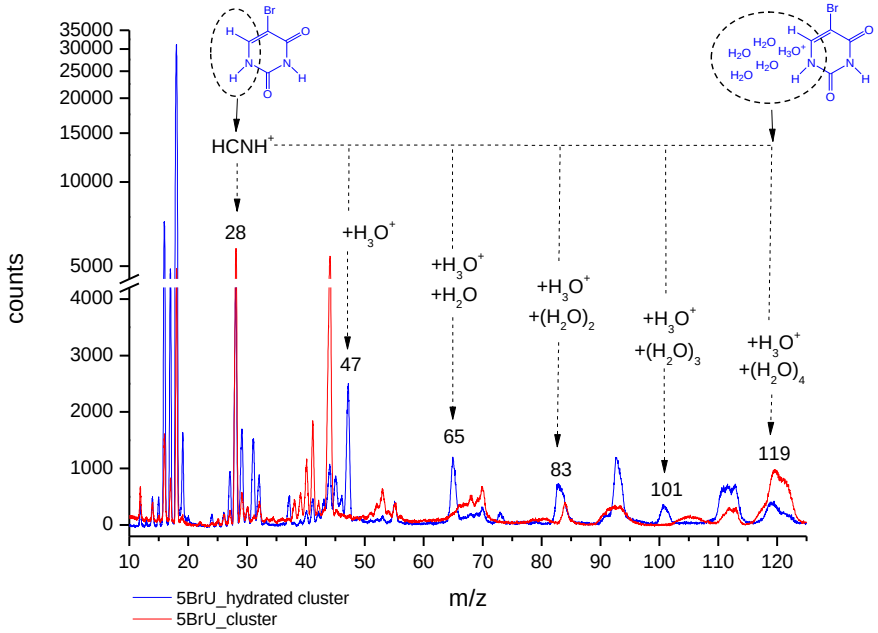

Fig 5.3—11 Comparison between the 5BrU hydrated cluster (blue) and 5BrU homogeneous cluster (red) spectra in the low m/z region. The peaks due to the $HCNH^+$ fragment and its hydrated series in the blue spectrum are indicated by the arrows (see also list b).

The observation of hydrated fragments is quite surprising and somehow in contrast with the previous observation of a "protective effect" of the environment on the single molecule.

Fig 5.3—12 shows the areas of the Gaussian functions associated to these peaks as a function of the number of water molecules, in both the cases of water clusters and the HCNH hydrated series described above. The exponential decay of the intensity of these series confirms the validity of the present assignment that homogeneous, protonated, water clusters as well as $HCNH^+$ hydrated series are formed in the fragmentation of 5BrU hydrated clusters [133, 134]. The term n=3 of the series, associated to the formation of a cluster of water molecules composed by $(H_2O)_2(H_3O)^+$ and the same water cluster joined to the HCNH fragment clearly show a different behaviour with respect the other members of the series. Their relative intensities are too large and do not follow the exponential decrease. This could be due to a "magic number" in the formation of water clusters where the molecules prefer joining together as described in Fig 5.3—13. and one could image that this cluster keeps the same configuration also when it is joined to the HCNH fragment. The situation changes moving towards fragments at highest values of m/z surrounded by three water molecules. Therefore these two points, even though they are reported in Fig 5.3—12, have been excluded from the fitting procedure.

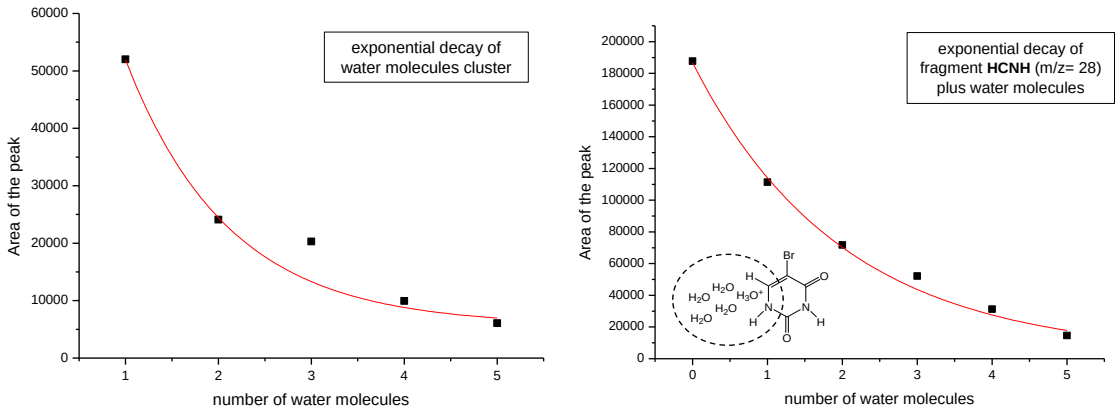

Fig 5.3—12 The exponential decay of the peaks areas in the case of water clusters and HCNH hydrated series.

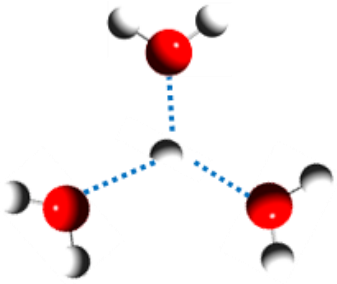

Fig 5.3—13 Proposed configuaration of water cluster with 3(H_2O)+H^+.

Moving in the region of the spectrum around the parent ion, another series corresponding to a hydrated fragment can be identified. As depicted in Fig 5.3—14 the fragment at m/z= 147/149 (centred in the figure at 148) can be found joined to an increasing number of water molecules up to 4 (list c).

list c:

$BrC_3H_2NO^+$ m/z = 147/149 described as $[M\text{-}HCNO]^+$

$(BrC_3H_2NO)(H_3O)^+$ m/z = 166/168 described as $[M\text{-}HCNO](H_3O)^+$

$(BrC_3H_2NO)(H_2O)(H_3O)^+$ m/z = 184/186 described as $[M\text{-}HCNO](H_2O)(H_3O)^+$

$(BrC_3H_2NO)(H_2O)_2(H_3O)^+$ m/z = 202/204 described as $[M\text{-}HCNO](H_2O)_2(H_3O)^+$

$(BrC_3H_2NO)(H_2O)_3(H_3O)^+$ m/z = 220/222 described as $[M\text{-}HCNO](H_2O)_3(H_3O)^+$

The broad shape of these peaks, presenting several shoulders, shows a clear hint of the presence of other possible fragments most likely belonging to series of hydrated fragments whose intensity decrease exponentially as function of the number of water molecules (see Fig 5.3—16). These series have been considered in the fitting procedure even though they will not be discussed here. The contributions to the peak at m/z = 148, for example, are reported below:

list d:

$CBr(H_2O)_2(H_3O)^+$ m/z = 146/148

$BrC_3H_2NO^+$ m/z = 147/149 described as $[M\text{-}HCNO]^+$

$C_4H_2N_2O_2(H_2O)(H_3O)^+$ m/z = 147 described as $[M\text{-}Br\text{-}H](H_2O)(H_3O)^+$

$C_4HN_2O_2(H_2O)(H_3O)^+$ m/z = 146 described as $[M\text{-}Br\text{-}2H](H_2O)(H_3O)^+$

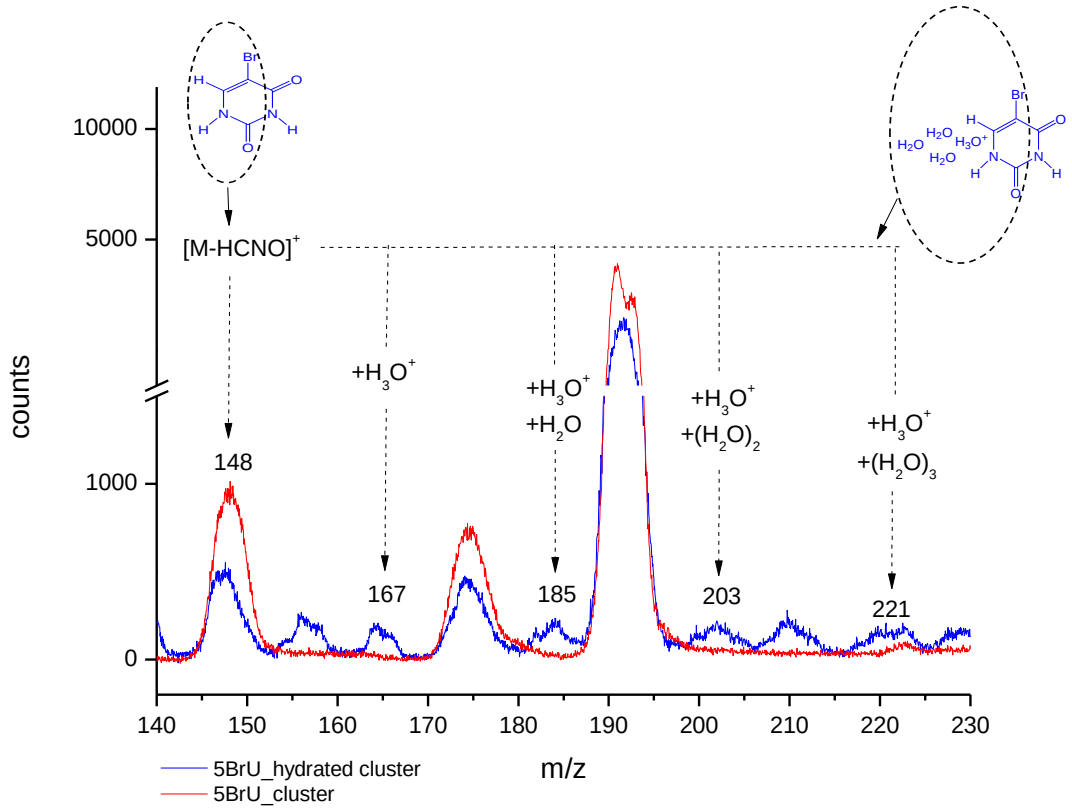

Fig 5.3—14 Comparison between the 5BrU hydrated cluster (blue) and 5BrU homogeneous cluster (red) spectra. The peaks due to the fragment [M-HCNO]$^+$ and its hydrated series in the blue spectrum are indicated by the arrows (see also list c).

Once the fitting procedure for the first peak of a series, corresponding just to the molecular fragment, is completed, as in this case the m/z=147/149, then the next peak obtained adding a H_3O^+ to this first fragment is analysed. It must be noted that the second fragment of a series is always obtained adding a m/z equal to 19. This means that when the first water molecule joins the fragment, the cluster is already protonated, otherwise, if the cluster is not protonated the water molecule that joins the uncharged fragment corresponds to H_3O^+. From the n=2 term, the rest of the peaks in the series are obtained adding water molecules (m/z = 18) to the previous fragment. It is not known how these water molecules are bound together thanks to hydrogen bridge bonds. It is possible that the configuration described in Fig 5.3—13 is no more valid for three water molecules when they are bound to a larger fragment as in the case of [M-HCNO]. In this case the number three does not seems to be a “magic number” and the

contribution at n = 3 has been taken into account in the fitting procedure of the exponential decrease (Fig 5.3—16).

During the fitting procedure, each fragment and its protonated species have been taken into account but the fitting procedure failed considering the hydration of the protonated and non-protonated species. The proper optimization of the fitting procedure was achieved by considering only the hydration of the no-protonated species. This is reasonable considering that a H_3O^+ molecule bound to a protonated species, as for example a protonated monomer $[M+H]^+$, would be linked to the opposite side of the molecule with respect to the place of H^+, because it is very unlikely that two positive charge are localized on the same site. As a consequence the fragmentation of the short living doubly charged species will most likely give rise to a non-protonated hydrated fragment (bound to H_3O^+) and the a protonated fragment.

The next relevant peak centered at m/z = 167 could be due to several fragments reported in:

list e:

$CBr(H_2O)_3(H_3O)^+$	m/z = 164/166	
$BrC_3H_2NO(H_3O)^+$	m/z = 166/168	described as $[M\text{-}HCNO](H_3O)^+$
$C_4H_2N_2O_2(H_2O)_2(H_3O)^+$	m/z = 165	described as $[M\text{-}Br\text{-}H](H_2O)_2(H_3O)^+$
$C_4HN_2O_2(H_2O)_2(H_3O)^+$	m/z = 164	described as $[M\text{-}Br\text{-}2H](H_2O)_2(H_3O)^+$
$BrC_3HNO_2^+$	m/z = 162/164	described as $[M\text{-}HCNH]^+$
$BrC_3H_2NO_2^+$	m/z = 163/165	described as $[M\text{-}HCN]^+$

As can be noticed, the fragments considered for the broad peak at m/z = 167 are the same as already considered for m/z = 148 (see list d), to which one water molecule has been added. In addition two new fragments have been considered. The $BrC_3HNO_2^+$ fragment represents the counterpart of the previous HCNH fragment discussed above (see list b). The $BrC_3H_2NO_2^+$ fragment is its protonated species. By this point the series built on the $[M\text{-}HCNH]^+$ fragment, i.e. $[M\text{-}HCNH](H_3O)^+$ and $[M\text{-}HCNH](H_3O)(H_2O)_n^+$ starts.

Moving towards higher values of m/z, another series of hydrated fragments, which starts from m/z = 174, appears. This fragment is due to the loss of the OH group during the fragmentation of the cluster and it has already been treated in 5.3.2. As depicted in Fig 5.3—15, a series extending

up to n = 4 is clearly observed (list f).

list f:

$BrC_4H_2N_2O^+$ m/z = 173/175 described as $[M\text{-}OH]^+$

$(BrC_4H_2N_2O)(H_3O)^+$ m/z = 192/194 described as $[M\text{-}OH](H_3O)^+$

$(BrC_4H_2N_2O)(H_2O)(H_3O)^+$ m/z = 210/212 described as $[M\text{-}OH](H_2O)(H_3O)^+$

$(BrC_4H_2N_2O)(H_2O)_2(H_3O)^+$ m/z = 228/230 described as $[M\text{-}OH](H_2O)_2(H_3O)^+$

$(BrC_4H_2N_2O)(H_2O)_3(H_3O)^+$ m/z = 246/248 described as $[M\text{-}OH](H_2O)_3(H_3O)^+$

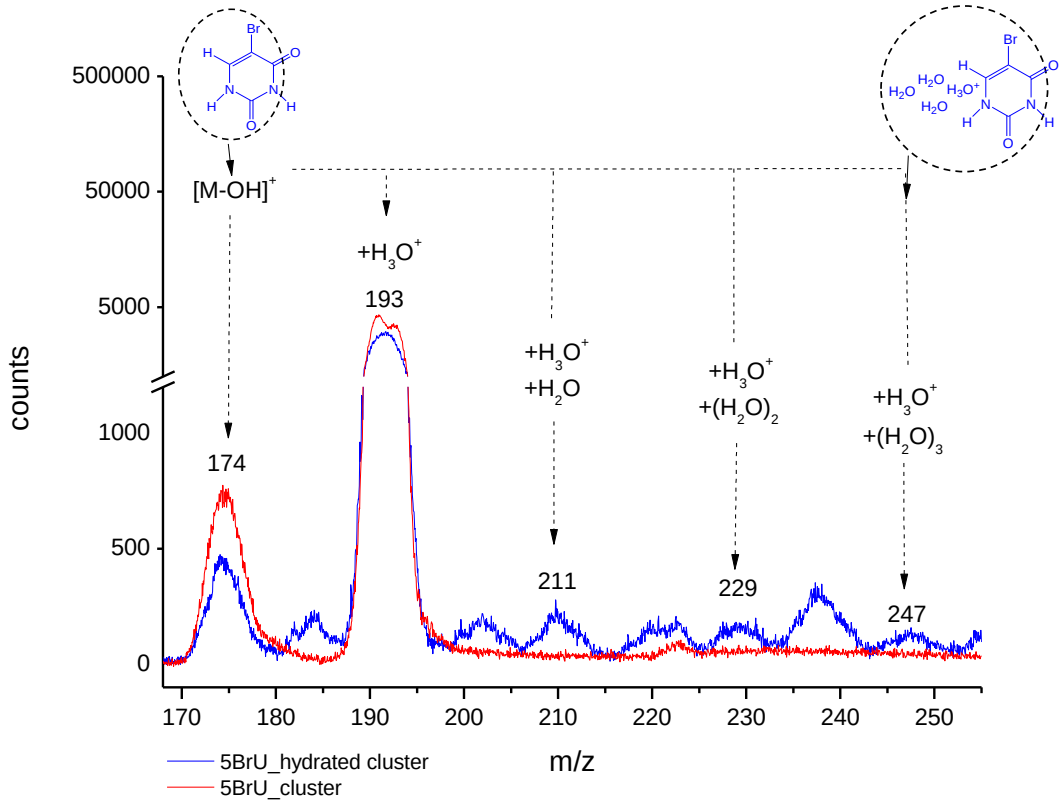

Fig 5.3—15 Comparison between the 5BrU hydrated cluster (blue) and 5BrU homogeneous cluster (red) spectra. The peaks due to the fragment $[M\text{-}OH]^+$ and its hydrated series in the blue spectrum are indicated by the arrows (see list f).

The trend of the areas for the peaks concerning the series of the hydrated $[M\text{-}HCNO]^+$ and $[M\text{-}OH]^+$ fragments are shown in Fig 5.3—16.

The previous observation and assignment, supported by the fitting data analysis, consistently suggest that the presence of the water molecules induce a fragmentation of the pyrimidinic ring that affects the bonds N1-C2 and C6-C5 in the formation of hydrated $HCNH^+$ fragment and C2-N3 and

C4-C5 in the formation of hydrated $[M\text{-}HCNO]^+$ fragment.

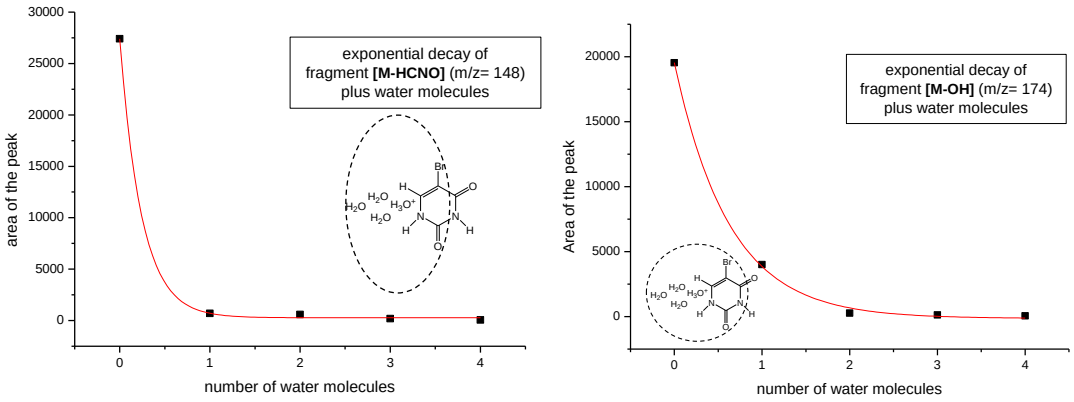

Fig 5.3—16 The exponential decay of the peaks area associated to the series of hydrated $[M\text{-}HCNO]^+$ fragment and hydrated $[M\text{-}OH]^+$ fragment.

A particularly interesting trend was observed during the fitting of the series of hydrated $[M\text{-}HCNO]^+$ fragment (list c). The Fig 5.3—17 shows the lineshape of the peak around the m/z =203. This feature is quite complex to describe, because several fragments can in principle contribute to its lineshape. Among them, a member of the hydrated series of the $[M\text{-}HCNO]^+$ fragment is present. All the Gaussian functions in blue in Fig 5.3—17 describe the fragments that are listed in list e, to which two water molecules have been added. It is evident from the figure that there is a large region at higher masses that is not covered by the blue Gaussian functions and it is not possible in this way to obtain a good description of the data. In order to cover the entire region and obtain a better fit it is necessary to introduce two Gaussian functions. The centers of these function correspond to the fragment at m/z:

list g

m/z = 203/205 $[M\text{-}HCNO](H_2O)_2(H_3O)^+ + \mathbf{H}$

The new features could be explained with a tautomerism involving the migration of the H atom from N3 to O8 atom. This model suggests the presence of three water molecules situated between C2 and N3 atom in order to catalyse a hydrogen migration between the N3 and O8 as depicted in Fig 5.3—18.

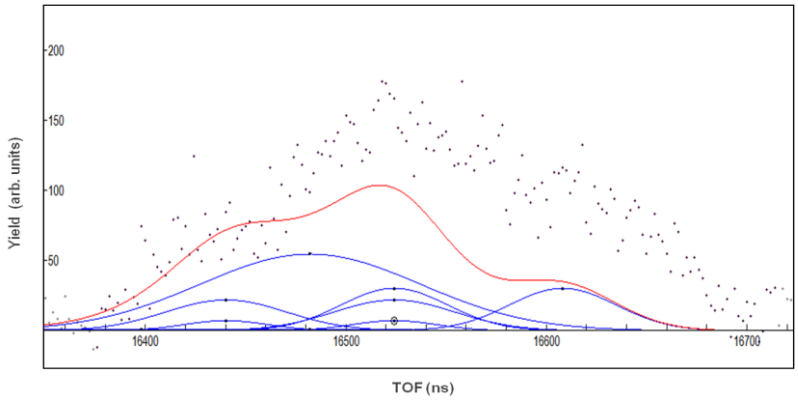

Fig 5.3—17 Screenshot during the fit procedure concerning the peak around the m/z = 203 in the [M-HCNO]$^+$ series. There is a large region at higher masses that is not covered by the fragments considered in list e. The data have been reported and fitted as function of time of flight (ns).

This tautomerism is responsible of the increase of one unit of atomic mass for the fragment [M-HCNO]$(H_2O)_2(H_3O)^+$.

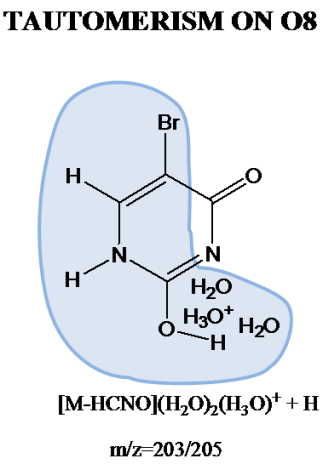

Fig 5.3—18 Tautomerism on O8 responsible of the new gaussian functions introduced in the fitting procedure around the m/z = 203. The water molecules could be situated between C2 and N3 inducing the increase of one unit of atomic mass for the fragment [M-HCNO]$(H_2O)_2(H_3O)^+$.

This arrangement is supported by the observation of the series of the hydrated BrC_2O^+ fragment, starting at m/z = 119/121 as described in Fig 5.3—19. The same treatment already discussed for the other series of hydrated fragments has been applied to the series of hydrated BrC_2O^+ fragment, which is observed to be bound up to a maximum of 7 water

molecules as described in Fig 5.3—19.

Also in this case, arriving to fit the peak at m/z around 229, the introduction of new Gaussian functions is needed for a proper description of the peak lineshape.

list h reports all the fragments considered for the peak around m/z = 229. These fragments, that have been used to fit the peak, are the continuation of the series at m/z = 229 (Fig 5.3—19). It is evident in Fig 5.3—20 that new fragments have to be introduced in the case of this broad peak at m/z around 229.

list h

$(C_4H_3BrN_2O_2)(H_2O)(H_3O)^+$ m/z = 227/229 described as $[M](H_2O)(H_3O)^+$

$(BrC_2NH)(H_2O)_5(H_3O)^+$ m/z = 227/229

$(BrC_2O)(H_2O)_5(H_3O)^+$; m/z = 228/230

$(BrC_4H_2N_2O)(H_2O)_2(H_3O)^+$ m/z = 228/230 described as $[M\text{-}OH](H_2O)_2(H_3O)^+$

$(BrC_4H_1N_2O)(H_2O)_2(H_3O)^+$ m/z = 229/231 described as $[M\text{-}O](H_2O)_2(H_3O)^+$

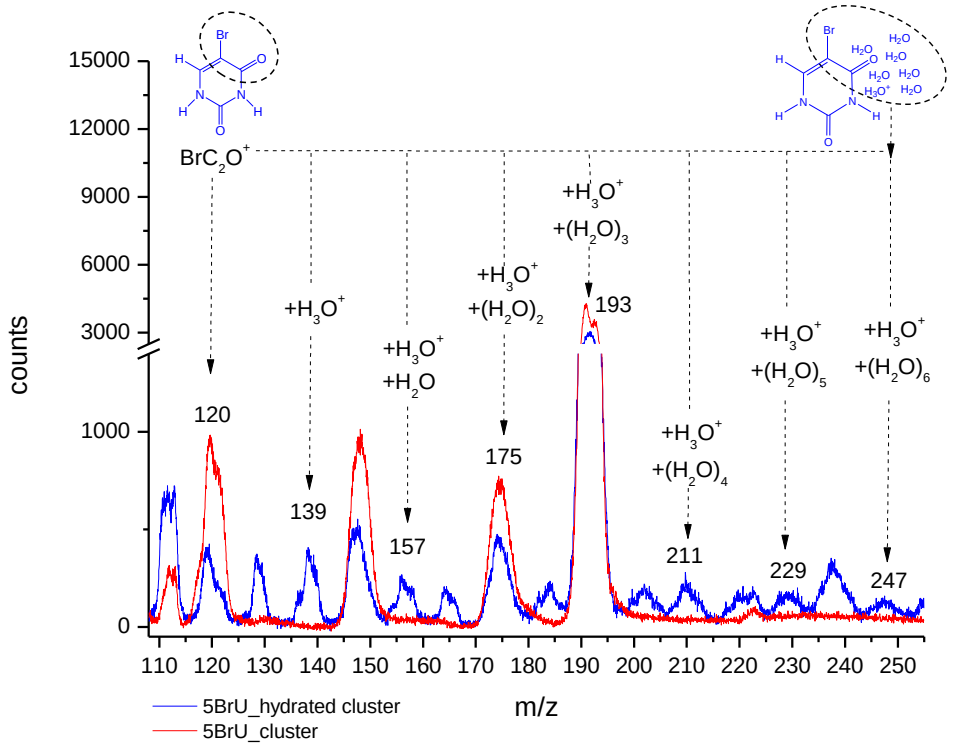

Fig 5.3—19 Comparison between the 5BrU hydrated cluster (blue) and 5BrU homogeneous cluster (red) spectra. The peaks due to the fragment $[BrC_2O]^+$ and its hydrated series in the blue spectrum are indicated by the arrows.

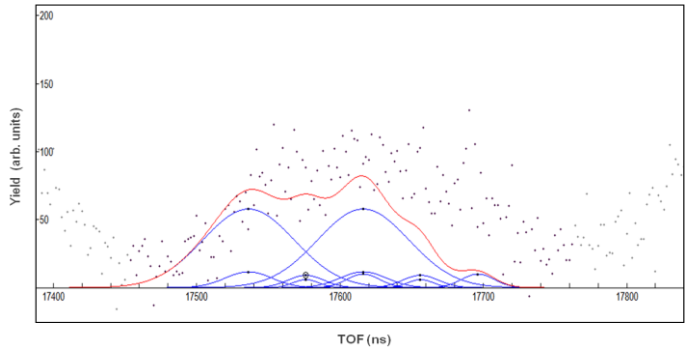

Fig 5.3—20 Screenshot during the fit procedure concerning the peak around the m/z = 229 in the BrC_2O^+ hydrated series. There is a large region at highest masses that is not covered by the fragments considered in list h. The data have been reported and fitted in function of time of flight (ns).

The two couple of new Gaussian functions added to list h correspond to the fragments at m/z:

list i

m/z = 229/231 $(BrC_2O)(H_2O)_5(H_3O)^+$ + **H**;
m/z = 229/231 $[M\text{-}OH](H_2O)_2(H_3O)^+$ + **H**;

The arrangement of water molecules proposed for these fragments is described in Fig 5.3—21 (b-c).

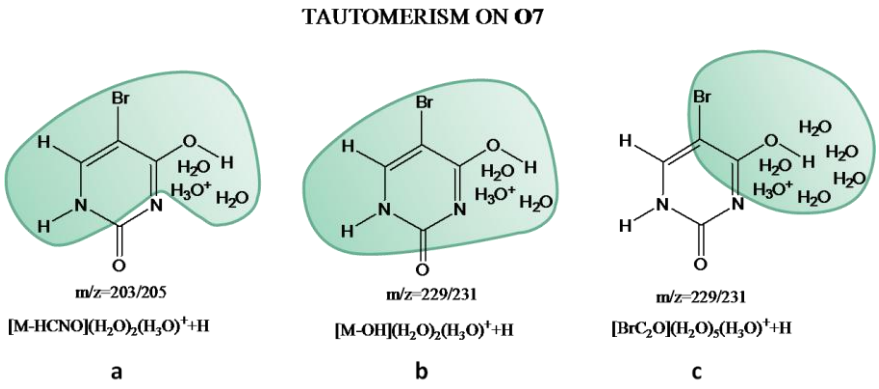

*Fig 5.3—21 Tautomerism on O7 responsible for the new Gaussian functions introduced in the fitting procedure around the m/z = 203 and m/z = 229. The water molecules could be situated between N3 and C4 sites inducing the tautomerisation process and the increase of one unit of atomic mass for the fragments (**a**) $[M\text{-}HCNO](H_2O)_2(H_3O)^+$, (**b**) $[M\text{-}O](H_2O)_2(H_3O)^+$ and (**c**) $BrC_2O(H_2O)_5(H3O)^+$.*

The fits obtained after the addition of new fragments are shown in Fig 5.3—22.

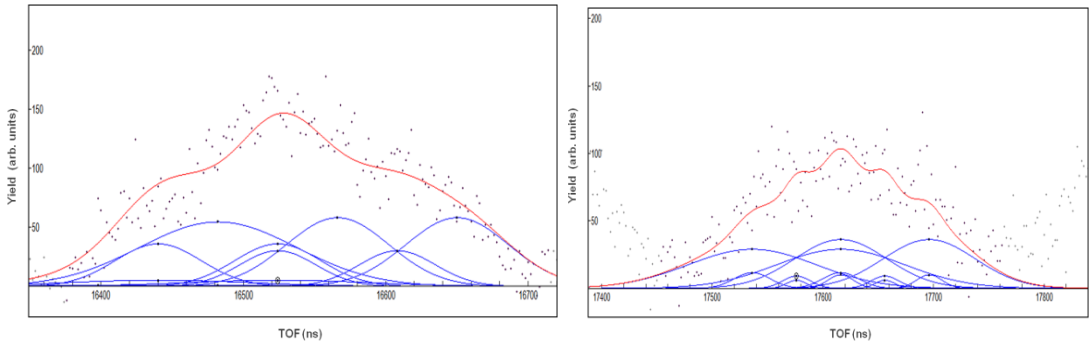

Fig 5.3—22 The fit obtained after the introduction of new Gaussian functions for the peak around m/z = 203 on the left and m/z = 229 on the right. The data have been reported and fitted in function of time of flight (ns).

Another difference that is observed in the mass spectrum of the hydrated 5BrU clusters with respect to the homogeneous cluster is the absence of the peak at m/z = 105 due to the BrC_2H fragment.
This fragment is obtained during the fragmentation process of the single molecule (see eq 5.3.1-2) and of the homogeneous clusters (see Fig 5.3—23). The reason of the inhibition of this fragmentation channel in the hydrated cluster must be strictly connected to the presence of the water.
As proposed in the previous discussion, the water molecules are probably located near the 5BrU molecules in the regions described in Fig 5.3—24, promoting the fragmentation dynamics described in this chapter.
As already described by van Mourik et al. [129] the water molecules do not enter in the region between the Br and O7 atoms because of the steric hindrance of the halogen atom.
At this point of discussion it is possible to add that also the region between the Br and the H atom bound to C6 most likely can not be occupied by the water molecules because of the same reason and this is demonstrated by the absence of the fragment BrC_2H in hydrated form.

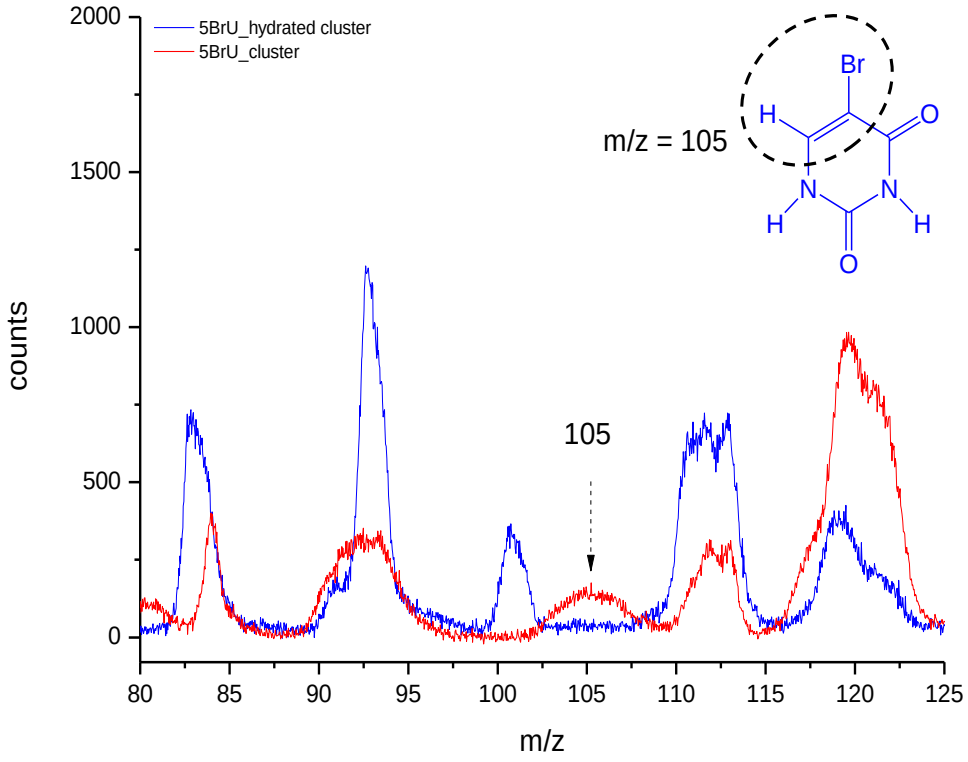

Fig 5.3—23 Evidence of the absence of the m/z = 105 fragment in the 5BrU hydrated cluster (blue spectrum). This fragmentation channel could be inhibited by the presence of water molecules between the N1 and C6 atoms.

Furthermore it is possible that when these molecules bound together to form a cluster, the Br atom is directly involved in a hydrogen bridge bond, as already described in chapter 5.3.2, and in all these cases the regions near the Br atom are not affected by hydration. Indeed also in the case of hydrated clusters, peaks corresponding to clusters $(5BrU)_n$ with n up to 8, that have lost one Br atom can be observed, indicating that the quantity of Br cation released is very low. These Br atoms can be radical or can be embedded in hydrogen bond. In any case large clusters which have lost more than one Br atom are not observed suggesting that the Br atoms are directly interested in the bounds that keep together the single monomers inside the cluster. We don't have evidence of hydrated clusters (Fig 5.3—25).

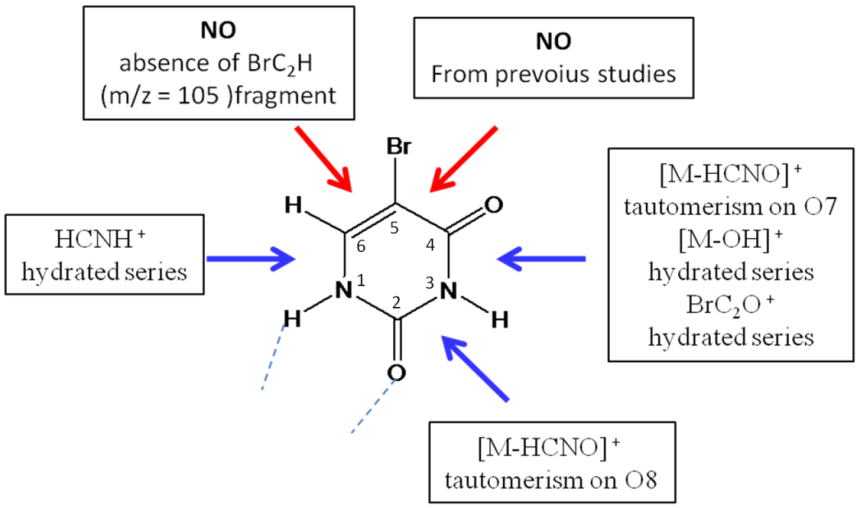

Fig 5.3—24 Summary of the preferential (blue) and neglected (red) positions of water attachment proposed in this work. The dot lines represent the hydrogen bonds that bound the monomers to form the cluster. In the rectangles the fragmentation channels that support the interpretation of the fragmentation dynamic are indicated. The previous study is referred to [129].

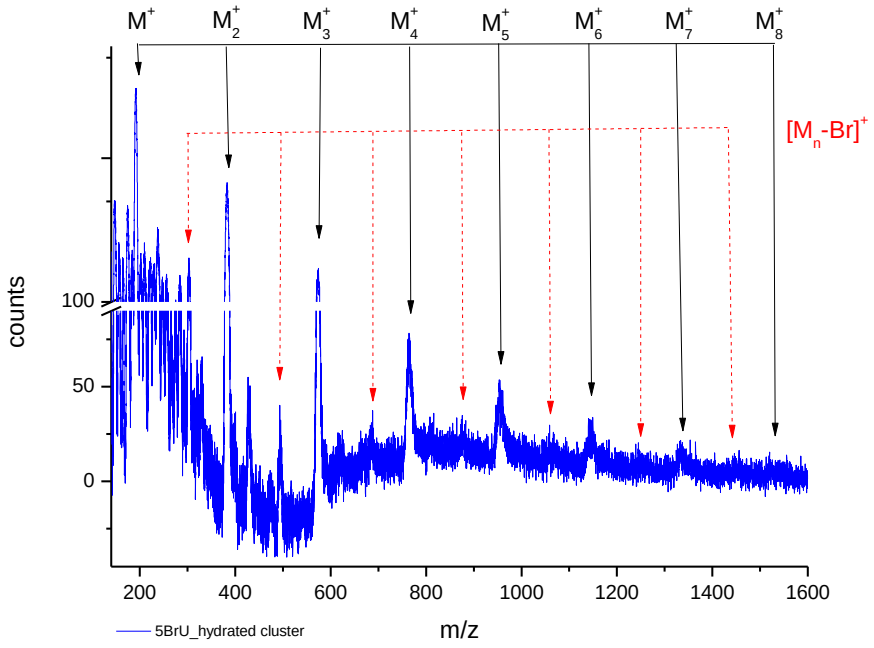

Fig 5.3—25 Magnification of the hydrated cluster spectrum in the region of high masses. The maximum observed size of 5BrU clusters is 8 at m/z=1528. There is no evidence of hydrated clusters.

The evidence of a tautomerism open up for very important discussions about the consequences of this process in biological systems such as cell nucleus.

The existence of such tautomers is supported by experimental results which show that a bromine atom in position 5 considerably increases the acidity of the uracil and the proportion of the enol tautomer present in 1-methyluracil [135]. Hu et al. [136] have used the presumed existence of 5BrU enol tautomers to hypothesize a mechanism for the mutagenic activity of 5BrU, which mutates G–C to A–T and A–T to G–C (see Fig 5.3—26).

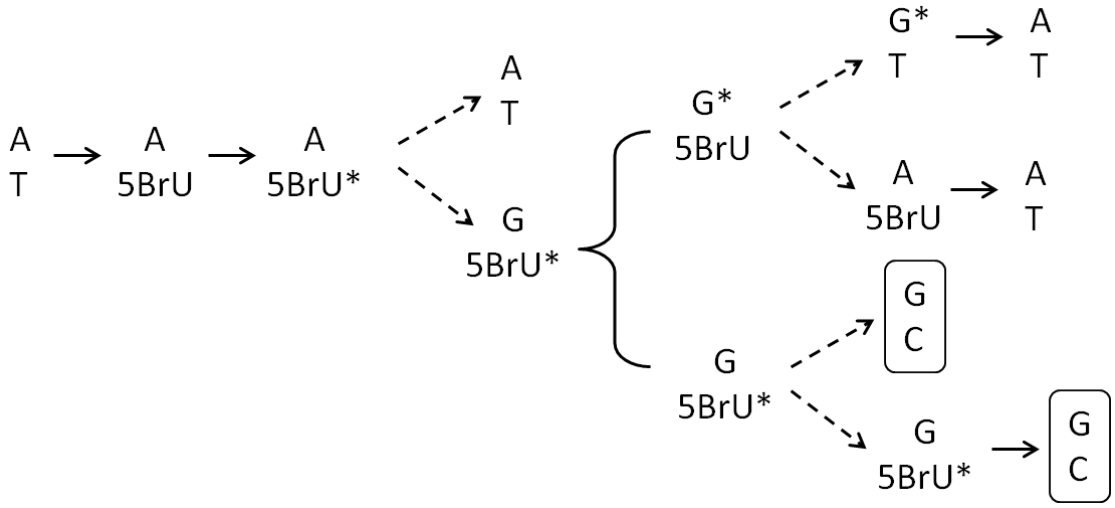

Fig 5.3—26 The keto→enol tautomerization mechanism of 5BrU mutagenicity proposed by Hu et al. [136]. The asterisk indicates the enol tautomeric form. The dashed lines represent DNA replication. The boxed base pairs indicate mutation.

According to this mechanism, the substitution of T by 5BrU in an A–T base pair is followed by keto → enol tautomerization of 5BrU leading to an A-5BrU(enol) base pair. As 5BrU(enol) prefers to pair with G [137], replication produces an A–T and G-5BrU(enol) base pair. In the next replication cycle the G-5BrU(enol) base pair replicates into G–C and G-5BrU(enol) base pairs, completing the mutation from A–T to G–C. Tautomerization of G-5BrU(enol) to G(enol)-5BrU yields G(enol)-T and A-5BrU base pairs, which are repaired to A–T by DNA repair mechanisms, and this route therefore does not lead to mutation.

If the tautomerism induced by water molecules proposed in this work would happen also in real systems at the cellular level, the 5BrU molecule should be considered a mutagenic agent. However being selectively introduced in cancerous cells for the tumor treatment, the mutagenic effect would not have relevant importance, because that cells are destined to die through the absorption of radiation.

This section has shed light on the mechanisms of fragmentation induced by the impact of low energy ions (C^{4+}) with single molecule of 5BrU and its homogeneous and hydrated clusters. The theory of "protective effect" which appears to be valid in the case of homogeneous clusters is no longer valid for the hydrated ones. In this case a several hydrated fragments have been observed, highlighting how the water molecules are found preferentially bound to some specific sites in the 5BrU molecule, thereby inhibiting some channels of fragmentation. This inhibitory effect must be added to the promoting effect of the keto-enol tautomerization which could involve the O8 or O7 atoms starting from n = 3 water molecules bound. This effect is considered of relevant importance because of the mutagenic consequences it may have within the cellular environment.

6 Conclusions and future perspectives

This work has been focused on the study of the different fragmentation dynamics of molecules of biological interest in gas phase. The results obtained using different radiation sources and different type of target molecules, from halogenated pyrimidines to halogenated uracils, have highlighted the relevant importance of the inductive, resonant and steric hindrance effects of the halogen atom used in the substitution of the aromatic ring.

The halogenated pyrimidines constitute an important class of prototype radiosensitizing molecules, and therefore the study of their fragmentation dynamics is of interest to understand the fundamental mechanisms of the enhanced radiation damage when these molecules are selectively incorporated in the DNA of tumor cells. The ionization energy of the parent ion and the appearance energy of some selected fragments of 2Cl-, 2Br and 5Br-pyrimidine molecules have been measured and calculated, the possible fragmentation pathways have been discussed and the role played by the halogen atom and/or site of halogenation have been unraveled. For the parent ion case, the experimental ionization energy values are all very similar to that of pyrimidine because in all these molecules the highest occupied molecular orbital is the nitrogen lone pair. The HCN loss channel is found to be favoured with respect to the halogen radical loss channel in the 5Br-pyrimidine case, while the opposite occurs in the case of the 2Cl- and 2Br-pyrimidine molecules. The 2(HCN) loss is only observed in the 5Br-pyrimidine. Therefore, the present results suggest that the presence of the Br atom in position 5 favours the breaking of the ring while the presence in position 2 favours the release of the halogen radical in a more efficient way for 2Br-pyrimidine compared to 2Cl-pyrimidine. The comparison between theoretical and experimental results makes it possible to suggest the correct fragmentation pathway to each measured cation fragment proposing the release of the $Br^{\bullet}$ radical in the brominated cases and of the $H^{\bullet}$ radical in the chlorinated case. These observations have also been rationalized in terms of i) the interplay between the resonance and inductive effects induced on the pyrimidinic ring by the presence of the different halogen atom/site of halogenation as well as ii) the electronegativity of the halogen atoms.

The present findings suggest that the choice of the most suitable radiosensitizer should be dictated by the goal of the therapy. If the main purpose is to target the environment surrounding the cell nucleus then the choice of the halogen in position 2 can lead to the release of the small $H^{\bullet}$ radical or the more reactive $Br^{\bullet}$ radical, if on the other hand, the purpose is the direct damage of the DNA chain then the 5Br-pyrimidine, which induces more significant breaking of the ring, is the most powerful choice.

The subsequent study has been focused on the 5Br-Uracil molecule which is the basic component of the 5Br-deoxyuridine used as radiosensitizer in tumor radiotherapy. The inductive and resonant effects already observed in the case of halogenated pyrimidine molecules have been investigated through XPS and NEXAFS measurements. The lack of ad-hoc theoretical results limits the conclusions in the analysis of the XPS spectra which display a relevant shift in the C (1s) spectra. In particular the binding energy of the C5, which is directly bound to the halogen atom, is the most affected by the shift to higher values of BE. This behaviour is explained by the inductive effect, in which an electron attractive substituent removes charge density from the neighbouring sites decreasing the shielding effect of the farthest electrons. In this way the 1s electron will be more affected by the nuclear attraction, increasing its BE. The disagreement between the theoretical (DFT -B3LYP study) and experimental values in the case of N (1s) and O (1s) energies are probably due to a resonance effect induced by the halogen substituent. In order to understand this effect a more sophisticated calculation, that more properly includes the electron correlations is needed.

Another really important aspect in the biological systems is the keto-enol tautomerism. These molecules can be severely affected by this process, in particular in acqeous environment. Previous theoretical studies [129] suggested that the energy necessary to obtain a keto-enol tautomerism for the uracil molecule in gas phase is too high to be achieve by thermal condition. The same theoretical study underlines that this energy is low in the case of 5BrU surrounded by water molecules. The presence of the bromine atom in position 5 prevents water from “approaching” the regions near the bromine atom because of its steric hindrance. For this reason the water molecules are preferentially located in the regions near the NH and OH bonds, favouring the H migration from the

N to the O atom, i.e. tautomerism. The evidence of a keto- enol tautomerism for of 5IU and 5FU observed in the FT-IR spectra, was not confirmed by the XPS analysis. It could be possible that the energy necessary for this transition in gas phase is too high while the powder analysed by FT-IR spectroscopy may reveal tautomerism catalised by the metallic surface of the plate during the condensation phase. These results are concerned with the study of isolated molecules, and therefore refer to intrinsic molecular properties.

The fragmentation experiments performed at the ARIBE beamline in Ganil (France), were meant to investigate the effect of the environment in the dynamics of the fragmentation and in the induced tautomerism of 5Br-uracil, a halo-substituted RNA base of pyrimidinic type.

The radiation source used in this case was a low energy beam of $^{12}C^{4+}$/ions at 36 keV. We have studied 5BrU because of its important role in radiobiology. 5BrU is not naturally found in DNA but it can be substituted for thymine and incorporated in DNA during replication. The study of the fragmentation spectrum of the single isolated molecule represents the first step to understand the dynamics of the fragmentation before moving towards more realistic targets as the homogeneous and hydrated clusters of the same molecule. The differences observed in the mass spectra provided evidence of the "protective role" played by the environment in the case of homogeneous clusters with respect to the single molecule. Indeed in the clusters there is less amount of small fragments released with respect to the large ones and no evidence of doubly charged fragments is present, suggesting that the cluster stabilize the two charges away of each other before fragmentation occurs. In the cluster spectrum also, less quantity of Br cations is observed. This may be due to the release of the Br atom, which could be radical, or to the bounding of the monomers inside the cluster via a hydrogen bridge involving the Br atom. The present experiments do not provide conclusive explanation, except for the clear observation that the clusters are arranged in a planar configuration, as demonstrated by the observation of the fragment $[M\text{-}OH]^+$.

Interestingly, the situation of hydrated clusters of 5BrU molecules provides new insights about the "protective effect" that is usually associated to the presence of an environment with respect to the isolated molecule, as was the case of the homogeneous clusters of 5BrU. The present work shows a

clear evidence of several series of 5BrU fragments bound up to 5 or 6 water molecules. The regions around the single molecule, in which the water is supposed to be, are in agreement with previous theoretical models [129]. As already mentioned, the “protective effect” of the environment, observed in some aminoacids [132] consists in a reduced molecular fragmentation of the monomer when embedded in the cluster, and is based on the idea that the easiest way to release the absorbed energy in a cluster is by breaking the cluster rather than the monomer.

Finally the most relevant result of this part of the work is the observation of tautomerism induced by the water molecules on the N3-O7 and N3-O8 pairs of atoms. The fitting procedure of the series of hydrated fragments provides evidence that this effect “opens” when a sufficient number of water molecules is present. The keto-enol tautomerism can have very important consequences. Indeed if the effect occurs in the cell nucleus, where 5BrU is surrounded by water molecules, the replication phase of the DNA chain can induce mutagenesis (see Fig 5.3—26), with all its consequences.

In conclusion, the results obtained in this thesis show how spectroscopic and mass spectrometer studies of the basic components of biological molecules in a controlled environment can provide detailed insights on the dynamics at molecular level of the radiation damage and how the same effects can be exploited in radiotherapy.

The present work will be continued by further studies on the fragmentation of hydrated uracil clusters by ion impact. If, at variance with 5BrU, the results will display a protective effect of the water molecules, then we could conclude that the present results have allowed to explain clearly why 5BrU is considered the most suitable radiosensitizer in radiotherapy.

7 Appendix

2Cl:

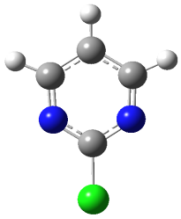

Zero-point correction= 0.067425 (Hartree/Particle)
Thermal correction to Energy= 0.072664
Thermal correction to Enthalpy= 0.073608
Thermal correction to Gibbs Free Energy= 0.038406
Sum of electronic and zero-point Energies= -723.852505
Sum of electronic and thermal Energies= -723.847266
Sum of electronic and thermal Enthalpies= -723.846322
Sum of electronic and thermal Free Energies= -723.881524

Temperature=	298.150000	Pressure=	1.000000
E(ZPE)=	0.064728	E(Thermal)=	0.070125
E(QCISD(T))=	-722.615825	E(Empiric)=	-0.121680
DE(Plus)=	-0.019091	DE(2DF)=	-0.236506
E(Delta-G3)=	-0.682544	E(G3-Empiric)=	-0.121680
G3(0 K)=	-723.610918	G3 Energy=	-723.605522
G3 Enthalpy=	-723.604577	G3 Free Energy=	-723.640039

2Cl radical ion:

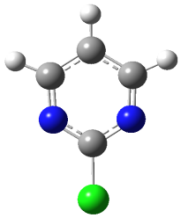

Zero-point correction= 0.066185 (Hartree/Particle)
Thermal correction to Energy= 0.071535
Thermal correction to Enthalpy= 0.072479
Thermal correction to Gibbs Free Energy= 0.036513
Sum of electronic and zero-point Energies= -723.514544
Sum of electronic and thermal Energies= -723.509195
Sum of electronic and thermal Enthalpies= -723.508250
Sum of electronic and thermal Free Energies= -723.544216

Temperature=	298.150000	Pressure=	1.000000
E(ZPE)=	0.063538	E(Thermal)=	0.069054
E(QCISD(T))=	-722.278755	E(Empiric)=	-0.118153
DE(Plus)=	-0.011742	DE(2DF)=	-0.231301
E(Delta-G3)=	-0.681169	E(G3-Empiric)=	-0.118153
G3(0 K)=	-723.257581	G3 Energy=	-723.252065
G3 Enthalpy=	-723.251121	G3 Free Energy=	-723.287360

HCN:

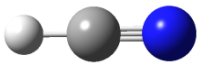

Zero-point correction= 0.016466 (Hartree/Particle)
Thermal correction to Energy= 0.019004
Thermal correction to Enthalpy= 0.019948
Thermal correction to Gibbs Free Energy= -0.002908
Sum of electronic and zero-point Energies= -93.406151
Sum of electronic and thermal Energies= -93.403613
Sum of electronic and thermal Enthalpies= -93.402669
Sum of electronic and thermal Free Energies= -93.425525

Temperature=	298.150000	Pressure=	1.000000
E(ZPE)=	0.015807	E(Thermal)=	0.018366
E(QCISD(T))=	-93.178444	E(Empiric)=	-0.033800
DE(Plus)=	-0.005883	DE(2DF)=	-0.058153
E(Delta-G3)=	-0.117775	E(G3-Empiric)=	-0.033800
G3(0 K)=	-93.378248	G3 Energy=	-93.375689
G3 Enthalpy=	-93.374744	G3 Free Energy=	-93.397629

Cl:

Zero-point correction= 0.000000 (Hartree/Particle)
Thermal correction to Energy= 0.001416
Thermal correction to Enthalpy= 0.002360
Thermal correction to Gibbs Free Energy= -0.015677
Sum of electronic and zero-point Energies= -460.136242
Sum of electronic and thermal Energies= -460.134826
Sum of electronic and thermal Enthalpies= -460.133882
Sum of electronic and thermal Free Energies= -460.151919

Temperature=	298.150000	Pressure=	1.000000
E(ZPE)=	0.000000	E(Thermal)=	0.001416
E(QCISD(T))=	-459.570499	E(Empiric)=	-0.022967
DE(Plus)=	-0.001782	DE(2DF)=	-0.053045
E(Delta-G3)=	-0.344451	E(G3-Empiric)=	-0.022967
G3(0 K)=	-459.992744	G3 Energy=	-459.991327
G3 Enthalpy=	-459.990383	G3 Free Energy=	-460.008421

HClCN:

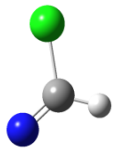

Zero-point correction= 0.018041 (Hartree/Particle)
Thermal correction to Energy= 0.021409
Thermal correction to Enthalpy= 0.022353
Thermal correction to Gibbs Free Energy= -0.007821
Sum of electronic and zero-point Energies= -553.560780
Sum of electronic and thermal Energies= -553.557412
Sum of electronic and thermal Enthalpies= -553.556468
Sum of electronic and thermal Free Energies= -553.586642

Temperature=	298.150000	Pressure=	1.000000
E(ZPE)=	0.017319	E(Thermal)=	0.020729
E(QCISD(T))=	-552.755495	E(Empiric)=	-0.057313
DE(Plus)=	-0.008590	DE(2DF)=	-0.116536
E(Delta-G3)=	-0.461133	E(G3-Empiric)=	-0.057313
G3(0 K)=	-553.381747	G3 Energy=	-553.378337
G3 Enthalpy=	-553.377393	G3 Free Energy=	-553.407632

ClCN:

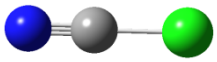

Zero-point correction= 0.008777 (Hartree/Particle)
Thermal correction to Energy= 0.011869
Thermal correction to Enthalpy= 0.012813
Thermal correction to Gibbs Free Energy= -0.013940
Sum of electronic and zero-point Energies= -552.999519
Sum of electronic and thermal Energies= -552.996427
Sum of electronic and thermal Enthalpies= -552.995483
Sum of electronic and thermal Free Energies= -553.022237

Temperature=	298.150000	Pressure=	1.000000
E(ZPE)=	0.008426	E(Thermal)=	0.011561
E(QCISD(T))=	-552.206691	E(Empiric)=	-0.054080
DE(Plus)=	-0.006901	DE(2DF)=	-0.110403
E(Delta-G3)=	-0.462548	E(G3-Empiric)=	-0.054080
G3(0 K)=	-552.832196	G3 Energy=	-552.829061
G3 Enthalpy=	-552.828117	G3 Free Energy=	-552.854944

H

Zero-point correction= 0.000000 (Hartree/Particle)
Thermal correction to Energy= 0.001416
Thermal correction to Enthalpy= 0.002360
Thermal correction to Gibbs Free Energy= -0.010654
Sum of electronic and zero-point Energies= -0.500273
Sum of electronic and thermal Energies= -0.498857
Sum of electronic and thermal Enthalpies= -0.497912
Sum of electronic and thermal Free Energies= -0.510927

Temperature=	298.150000	Pressure=	1.000000
E(ZPE)=	0.000000	E(Thermal)=	0.001416
E(QCISD(T))=	-0.498233	E(Empiric)=	-0.001269
DE(Plus)=	0.000000	DE(2DF)=	0.000000
E(Delta-G3)=	-0.001585	E(G3-Empiric)=	-0.001269
G3(0 K)=	-0.501087	G3 Energy=	-0.499671
G3 Enthalpy=	-0.498726	G3 Free Energy=	-0.511741

79:

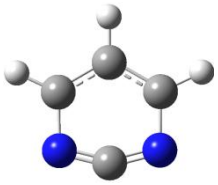

Zero-point correction= 0.064259 (Hartree/Particle)
Thermal correction to Energy= 0.068472
Thermal correction to Enthalpy= 0.069417
Thermal correction to Gibbs Free Energy= 0.037676
Sum of electronic and zero-point Energies= -263.287659
Sum of electronic and thermal Energies= -263.283446
Sum of electronic and thermal Enthalpies= -263.282501
Sum of electronic and thermal Free Energies= -263.314243

Temperature=	298.150000	Pressure=	1.000000
E(ZPE)=	0.061688	E(Thermal)=	0.066030
E(QCISD(T))=	-262.624731	E(Empiric)=	-0.094640
DE(Plus)=	-0.009330	DE(2DF)=	-0.173103
E(Delta-G3)=	-0.336125	E(G3-Empiric)=	-0.094640
G3(0 K)=	-263.176240	G3 Energy=	-263.171899
G3 Enthalpy=	-263.170954	G3 Free Energy=	-263.202882

1:

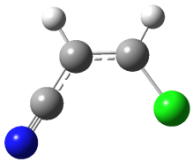

Zero-point correction= 0.041241 (Hartree/Particle)
Thermal correction to Energy= 0.046332
Thermal correction to Enthalpy= 0.047277
Thermal correction to Gibbs Free Energy= 0.011629
Sum of electronic and zero-point Energies= -630.018743
Sum of electronic and thermal Energies= -630.013652
Sum of electronic and thermal Enthalpies= -630.012708
Sum of electronic and thermal Free Energies= -630.048355

Temperature=	298.150000	Pressure=	1.000000
E(ZPE)=	0.039592	E(Thermal)=	0.044788
E(QCISD(T))=	-629.020127	E(Empiric)=	-0.084353
DE(Plus)=	-0.007135	DE(2DF)=	-0.161921
E(Delta-G3)=	-0.566502	E(G3-Empiric)=	-0.084353
G3(0 K)=	-629.800445	G3 Energy=	-629.795249
G3 Enthalpy=	-629.794305	G3 Free Energy=	-629.830152

2:

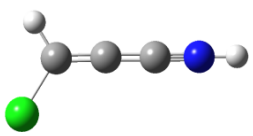

Zero-point correction= 0.038584 (Hartree/Particle)
Thermal correction to Energy= 0.044733
Thermal correction to Enthalpy= 0.045677

Thermal correction to Gibbs Free Energy= 0.008030
Sum of electronic and zero-point Energies= -630.020027
Sum of electronic and thermal Energies= -630.013878
Sum of electronic and thermal Enthalpies= -630.012933
Sum of electronic and thermal Free Energies= -630.050581

Temperature=	298.150000	Pressure=	1.000000
E(ZPE)=	0.037040	E(Thermal)=	0.043312
E(QCISD(T))=	-629.009853	E(Empiric)=	-0.084353
DE(Plus)=	-0.006598	DE(2DF)=	-0.169671
E(Delta-G3)=	-0.567587	E(G3-Empiric)=	-0.084353
G3(0 K)=	-629.801022	G3 Energy=	-629.794751
G3 Enthalpy=	-629.793806	G3 Free Energy=	-629.831714

3:

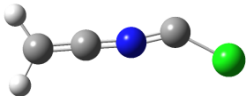

Zero-point correction= 0.039264 (Hartree/Particle)
Thermal correction to Energy= 0.044887
Thermal correction to Enthalpy= 0.045831
Thermal correction to Gibbs Free Energy= 0.009864
Sum of electronic and zero-point Energies= -630.003477
Sum of electronic and thermal Energies= -629.997854
Sum of electronic and thermal Enthalpies= -629.996909
Sum of electronic and thermal Free Energies= -630.032877

Temperature=	298.150000	Pressure=	1.000000
E(ZPE)=	0.037693	E(Thermal)=	0.043434
E(QCISD(T))=	-628.990120	E(Empiric)=	-0.084353
DE(Plus)=	-0.006944	DE(2DF)=	-0.168120
E(Delta-G3)=	-0.566518	E(G3-Empiric)=	-0.084353
G3(0 K)=	-629.778361	G3 Energy=	-629.772620
G3 Enthalpy=	-629.771676	G3 Free Energy=	-629.807878

4:

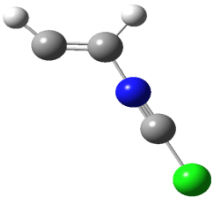

Zero-point correction= 0.039697 (Hartree/Particle)
Thermal correction to Energy= 0.045150
Thermal correction to Enthalpy= 0.046094
Thermal correction to Gibbs Free Energy= 0.010233
Sum of electronic and zero-point Energies= -629.984430
Sum of electronic and thermal Energies= -629.978977
Sum of electronic and thermal Enthalpies= -629.978033
Sum of electronic and thermal Free Energies= -630.013895

Temperature=	298.150000	Pressure=	1.000000
E(ZPE)=	0.038109	E(Thermal)=	0.043683
E(QCISD(T))=	-628.986908	E(Empiric)=	-0.084353
DE(Plus)=	-0.007431	DE(2DF)=	-0.166300
E(Delta-G3)=	-0.567828	E(G3-Empiric)=	-0.084353

G3(0 K)=	-629.774711	G3 Energy=	-629.769137
G3 Enthalpy=	-629.768193	G3 Free Energy=	-629.804285

5:

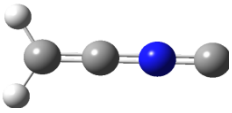

Zero-point correction= 0.035401 (Hartree/Particle)
Thermal correction to Energy= 0.040108
Thermal correction to Enthalpy= 0.041052
Thermal correction to Gibbs Free Energy= 0.009788
Sum of electronic and zero-point Energies= -169.771502
Sum of electronic and thermal Energies= -169.766794
Sum of electronic and thermal Enthalpies= -169.765850
Sum of electronic and thermal Free Energies= -169.797115

Temperature=	298.150000	Pressure=	1.000000
E(ZPE)=	0.033985	E(Thermal)=	0.038775
E(QCISD(T))=	-169.335790	E(Empiric)=	-0.060840
DE(Plus)=	-0.005208	DE(2DF)=	-0.105294
E(Delta-G3)=	-0.219113	E(G3-Empiric)=	-0.060840
G3(0 K)=	-169.692260	G3 Energy=	-169.687470
G3 Enthalpy=	-169.686526	G3 Free Energy=	-169.717952

6:

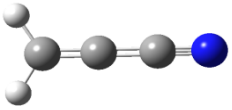

Zero-point correction= 0.035678 (Hartree/Particle)
Thermal correction to Energy= 0.040266
Thermal correction to Enthalpy= 0.041210
Thermal correction to Gibbs Free Energy= 0.010127
Sum of electronic and zero-point Energies= -169.785650
Sum of electronic and thermal Energies= -169.781063
Sum of electronic and thermal Enthalpies= -169.780119
Sum of electronic and thermal Free Energies= -169.811201

Temperature=	298.150000	Pressure=	1.000000
E(ZPE)=	0.034251	E(Thermal)=	0.038922
E(QCISD(T))=	-169.352063	E(Empiric)=	-0.060840
DE(Plus)=	-0.004233	DE(2DF)=	-0.104175
E(Delta-G3)=	-0.222077	E(G3-Empiric)=	-0.060840
G3(0 K)=	-169.709137	G3 Energy=	-169.704466
G3 Enthalpy=	-169.703522	G3 Free Energy=	-169.734762

7:

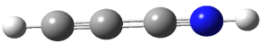

Zero-point correction= 0.037324 (Hartree/Particle)
Thermal correction to Energy= 0.041904
Thermal correction to Enthalpy= 0.042848
Thermal correction to Gibbs Free Energy= 0.017930
Sum of electronic and zero-point Energies= -169.835711

Sum of electronic and thermal Energies= -169.831131
Sum of electronic and thermal Enthalpies= -169.830187
Sum of electronic and thermal Free Energies= -169.855105

Temperature=	298.150000	Pressure=	1.000000
E(ZPE)=	0.035831	E(Thermal)=	0.040511
E(QCISD(T))=	-169.407969	E(Empiric)=	-0.060840
DE(Plus)=	-0.004007	DE(2DF)=	-0.110815
E(Delta-G3)=	-0.223130	E(G3-Empiric)=	-0.060840
G3(0 K)=	-169.770931	G3 Energy=	-169.766250
G3 Enthalpy=	-169.765306	G3 Free Energy=	-169.790398

8:

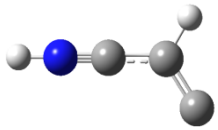

Zero-point correction= 0.035572 (Hartree/Particle)
Thermal correction to Energy= 0.040156
Thermal correction to Enthalpy= 0.041100
Thermal correction to Gibbs Free Energy= 0.009626
Sum of electronic and zero-point Energies= -169.751000
Sum of electronic and thermal Energies= -169.746416
Sum of electronic and thermal Enthalpies= -169.745472
Sum of electronic and thermal Free Energies= -169.776945

Temperature=	298.150000	Pressure=	1.000000
E(ZPE)=	0.034149	E(Thermal)=	0.038832
E(QCISD(T))=	-169.325478	E(Empiric)=	-0.060840
DE(Plus)=	-0.005845	DE(2DF)=	-0.106154
E(Delta-G3)=	-0.220416	E(G3-Empiric)=	-0.060840
G3(0 K)=	-169.684584	G3 Energy=	-169.679901
G3 Enthalpy=	-169.678957	G3 Free Energy=	-169.710603

C:

Zero-point correction= 0.000000 (Hartree/Particle)
Thermal correction to Energy= 0.001416
Thermal correction to Enthalpy= 0.002360
Thermal correction to Gibbs Free Energy= -0.013508
Sum of electronic and zero-point Energies= -37.776009
Sum of electronic and thermal Energies= -37.774593
Sum of electronic and thermal Enthalpies= -37.773649
Sum of electronic and thermal Free Energies= -37.789517

Temperature=	298.150000	Pressure=	1.000000
E(ZPE)=	0.000000	E(Thermal)=	0.001416
E(QCISD(T))=	-37.692647	E(Empiric)=	-0.013712
DE(Plus)=	-0.007148	DE(2DF)=	-0.017516
E(Delta-G3)=	-0.049131	E(G3-Empiric)=	-0.013712
G3(0 K)=	-37.780154	G3 Energy=	-37.778738
G3 Enthalpy=	-37.777794	G3 Free Energy=	-37.793662

N:

Zero-point correction= 0.000000 (Hartree/Particle)
Thermal correction to Energy= 0.001416
Thermal correction to Enthalpy= 0.002360
Thermal correction to Gibbs Free Energy= -0.014381
Sum of electronic and zero-point Energies= -54.478999
Sum of electronic and thermal Energies= -54.477582
Sum of electronic and thermal Enthalpies= -54.476638
Sum of electronic and thermal Free Energies= -54.493380

Temperature=	298.150000	Pressure=	1.000000
E(ZPE)=	0.000000	E(Thermal)=	0.001416
E(QCISD(T))=	-54.367490	E(Empiric)=	-0.014841
DE(Plus)=	-0.005263	DE(2DF)=	-0.023374
E(Delta-G3)=	-0.060766	E(G3-Empiric)=	-0.014841
G3(0 K)=	-54.471734	G3 Energy=	-54.470317
G3 Enthalpy=	-54.469373	G3 Free Energy=	-54.486115

2Br:

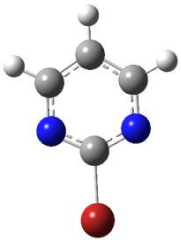

Zero-point correction= 0.066726 (Hartree/Particle)
Thermal correction to Energy= 0.072214
Thermal correction to Enthalpy= 0.073158
Thermal correction to Gibbs Free Energy= 0.036577
Sum of electronic and zero-point Energies= -2835.359643
Sum of electronic and thermal Energies= -2835.354155
Sum of electronic and thermal Enthalpies= -2835.353211
Sum of electronic and thermal Free Energies= -2835.389792

Temperature=	298.150000	Pressure=	1.000000
E(ZPE)=	0.064057	E(Thermal)=	0.069702
E(QCISD(T))=	-2835.356518	E(Empiric)=	-0.121680
DE(Plus)=	-0.018836	DE(2DF)=	-0.222840
E(Delta-G3)=	-1.458167	E(G3-Empiric)=	-0.121680
G3(0 K)=	-2837.113983	G3 Energy=	-2837.108338
G3 Enthalpy=	-2837.107394	G3 Free Energy=	-2837.144244

2Br radical ion:

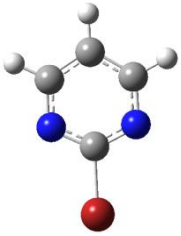

Zero-point correction= 0.066267 (Hartree/Particle)
Thermal correction to Energy= 0.071939
Thermal correction to Enthalpy= 0.072883
Thermal correction to Gibbs Free Energy= 0.035182
Sum of electronic and zero-point Energies= -2835.010716
Sum of electronic and thermal Energies= -2835.005044
Sum of electronic and thermal Enthalpies= -2835.004100
Sum of electronic and thermal Free Energies= -2835.041801

Temperature=	298.150000	Pressure=	1.000000
E(ZPE)=	0.063616	E(Thermal)=	0.069446
E(QCISD(T))=	-2835.006888	E(Empiric)=	-0.118153
DE(Plus)=	-0.013525	DE(2DF)=	-0.216505
E(Delta-G3)=	-1.454885	E(G3-Empiric)=	-0.118153
G3(0 K)=	-2836.746339	G3 Energy=	-2836.740510
G3 Enthalpy=	-2836.739565	G3 Free Energy=	-2836.777544

HCN:

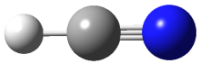

Zero-point correction= 0.016466 (Hartree/Particle)
Thermal correction to Energy= 0.019004
Thermal correction to Enthalpy= 0.019948
Thermal correction to Gibbs Free Energy= -0.002908
Sum of electronic and zero-point Energies= -93.406151
Sum of electronic and thermal Energies= -93.403613
Sum of electronic and thermal Enthalpies= -93.402669
Sum of electronic and thermal Free Energies= -93.425525

Temperature=	298.150000	Pressure=	1.000000
E(ZPE)=	0.015807	E(Thermal)=	0.018366
E(QCISD(T))=	-93.178444	E(Empiric)=	-0.033800
DE(Plus)=	-0.005883	DE(2DF)=	-0.058153
E(Delta-G3)=	-0.117775	E(G3-Empiric)=	-0.033800
G3(0 K)=	-93.378248	G3 Energy=	-93.375689
G3 Enthalpy=	-93.374744	G3 Free Energy=	-93.397629

Br:

Zero-point correction= 0.000000 (Hartree/Particle)
Thermal correction to Energy= 0.001416
Thermal correction to Enthalpy= 0.002360
Thermal correction to Gibbs Free Energy= -0.016830
Sum of electronic and zero-point Energies= -2571.656918
Sum of electronic and thermal Energies= -2571.655502

Sum of electronic and thermal Enthalpies= -2571.654558
Sum of electronic and thermal Free Energies= -2571.673748

Temperature=	298.150000	Pressure=	1.000000
E(ZPE)=	0.000000	E(Thermal)=	0.001416
E(QCISD(T))=	-2572.331872	E(Empiric)=	-0.027227
DE(Plus)=	-0.001603	DE(2DF)=	-0.035837
E(Delta-G3)=	-1.122712	E(G3-Empiric)=	-0.027227
G3(0 K)=	-2573.519251	G3 Energy=	-2573.517835
G3 Enthalpy=	-2573.516891	G3 Free Energy=	-2573.536081

HBrCN:

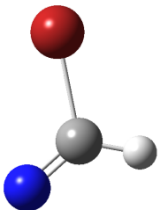

Zero-point correction= 0.017234 (Hartree/Particle)
Thermal correction to Energy= 0.020814
Thermal correction to Enthalpy= 0.021758
Thermal correction to Gibbs Free Energy= -0.009930
Sum of electronic and zero-point Energies= -2665.071712
Sum of electronic and thermal Energies= -2665.068132
Sum of electronic and thermal Enthalpies= -2665.067188
Sum of electronic and thermal Free Energies= -2665.098876

Temperature=	298.150000	Pressure=	1.000000
E(ZPE)=	0.016545	E(Thermal)=	0.020171
E(QCISD(T))=	-2665.501105	E(Empiric)=	-0.057313
DE(Plus)=	-0.008368	DE(2DF)=	-0.101234
E(Delta-G3)=	-1.237677	E(G3-Empiric)=	-0.057313
G3(0 K)=	-2666.889152	G3 Energy=	-2666.885526
G3 Enthalpy=	-2666.884582	G3 Free Energy=	-2666.916348

BrCN:

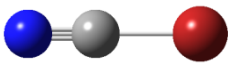

Zero-point correction= 0.007462 (Hartree/Particle)
Thermal correction to Energy= 0.010779
Thermal correction to Enthalpy= 0.011723
Thermal correction to Gibbs Free Energy= -0.011373
Sum of electronic and zero-point Energies= -2664.511705
Sum of electronic and thermal Energies= -2664.508388
Sum of electronic and thermal Enthalpies= -2664.507443
Sum of electronic and thermal Free Energies= -2664.530540

Temperature=	298.150000	Pressure=	1.000000
E(ZPE)=	0.007163	E(Thermal)=	0.010511
E(QCISD(T))=	-2664.951024	E(Empiric)=	-0.054080
DE(Plus)=	-0.007416	DE(2DF)=	-0.096152
E(Delta-G3)=	-1.237692	E(G3-Empiric)=	-0.054080
G3(0 K)=	-2666.339201	G3 Energy=	-2666.335853
G3 Enthalpy=	-2666.334909	G3 Free Energy=	-2666.358056

1:

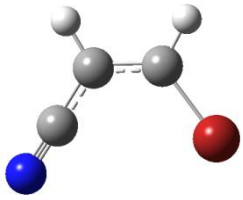

Zero-point correction= 0.040637 (Hartree/Particle)
Thermal correction to Energy= 0.045839
Thermal correction to Enthalpy= 0.046783
Thermal correction to Gibbs Free Energy= 0.009935
Sum of electronic and zero-point Energies= -2741.534847
Sum of electronic and thermal Energies= -2741.529645
Sum of electronic and thermal Enthalpies= -2741.528701
Sum of electronic and thermal Free Energies= -2741.565548

Temperature=	298.150000	Pressure=	1.000000
E(ZPE)=	0.039011	E(Thermal)=	0.044322
E(QCISD(T))=	-2741.767431	E(Empiric)=	-0.084353
DE(Plus)=	-0.007350	DE(2DF)=	-0.148542
E(Delta-G3)=	-1.341902	E(G3-Empiric)=	-0.084353
G3(0 K)=	-2743.310567	G3 Energy=	-2743.305257
G3 Enthalpy=	-2743.304312	G3 Free Energy=	-2743.341367

2:

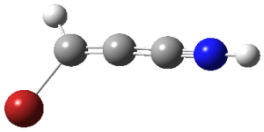

Zero-point correction= 0.037762 (Hartree/Particle)
Thermal correction to Energy= 0.044140
Thermal correction to Enthalpy= 0.045084
Thermal correction to Gibbs Free Energy= 0.005881
Sum of electronic and zero-point Energies= -2741.533377
Sum of electronic and thermal Energies= -2741.526999
Sum of electronic and thermal Enthalpies= -2741.526055
Sum of electronic and thermal Free Energies= -2741.565258

Temperature=	298.150000	Pressure=	1.000000
E(ZPE)=	0.036251	E(Thermal)=	0.042754
E(QCISD(T))=	-2741.755203	E(Empiric)=	-0.084353
DE(Plus)=	-0.006833	DE(2DF)=	-0.155824
E(Delta-G3)=	-1.343452	E(G3-Empiric)=	-0.084353
G3(0 K)=	-2743.309414	G3 Energy=	-2743.302912
G3 Enthalpy=	-2743.301967	G3 Free Energy=	-2743.341442

3:

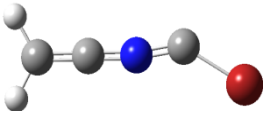

Zero-point correction= 0.038575 (Hartree/Particle)
Thermal correction to Energy= 0.044389
Thermal correction to Enthalpy= 0.045333
Thermal correction to Gibbs Free Energy= 0.007995

Sum of electronic and zero-point Energies= -2741.519233
Sum of electronic and thermal Energies= -2741.513419
Sum of electronic and thermal Enthalpies= -2741.512475
Sum of electronic and thermal Free Energies= -2741.549813

Temperature=	298.150000	Pressure=	1.000000
E(ZPE)=	0.037032	E(Thermal)=	0.042966
E(QCISD(T))=	-2741.737637	E(Empiric)=	-0.084353
DE(Plus)=	-0.007247	DE(2DF)=	-0.154704
E(Delta-G3)=	-1.341384	E(G3-Empiric)=	-0.084353
G3(0 K)=	-2743.288293	G3 Energy=	-2743.282359
G3 Enthalpy=	-2743.281415	G3 Free Energy=	-2743.318997

4:

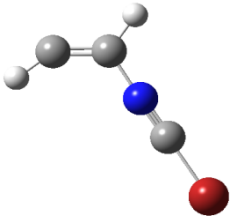

Zero-point correction= 0.039376 (Hartree/Particle)
Thermal correction to Energy= 0.044895
Thermal correction to Enthalpy= 0.045840
Thermal correction to Gibbs Free Energy= 0.008795
Sum of electronic and zero-point Energies= -2741.500327
Sum of electronic and thermal Energies= -2741.494808
Sum of electronic and thermal Enthalpies= -2741.493864
Sum of electronic and thermal Free Energies= -2741.530909

Temperature=	298.150000	Pressure=	1.000000
E(ZPE)=	0.037801	E(Thermal)=	0.043442
E(QCISD(T))=	-2741.733412	E(Empiric)=	-0.084353
DE(Plus)=	-0.007501	DE(2DF)=	-0.153424
E(Delta-G3)=	-1.342206	E(G3-Empiric)=	-0.084353
G3(0 K)=	-2743.283094	G3 Energy=	-2743.277454
G3 Enthalpy=	-2743.276509	G3 Free Energy=	-2743.313788

5:

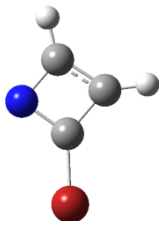

Zero-point correction= 0.039003 (Hartree/Particle)
Thermal correction to Energy= 0.044072
Thermal correction to Enthalpy= 0.045016
Thermal correction to Gibbs Free Energy= 0.007864
Sum of electronic and zero-point Energies= -2741.496797
Sum of electronic and thermal Energies= -2741.491728
Sum of electronic and thermal Enthalpies= -2741.490784
Sum of electronic and thermal Free Energies= -2741.527936

Temperature=	298.150000	Pressure=	1.000000

E(ZPE)=	0.037442	E(Thermal)=	0.042617
E(QCISD(T))=	-2741.728292	E(Empiric)=	-0.084353
DE(Plus)=	-0.008030	DE(2DF)=	-0.153846
E(Delta-G3)=	-1.338241	E(G3-Empiric)=	-0.084353
G3(0 K)=	-2743.275320	G3 Energy=	-2743.270146
G3 Enthalpy=	-2743.269202	G3 Free Energy=	-2743.306552

6:

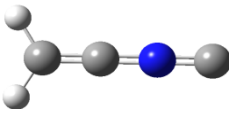

Zero-point correction= 0.035401 (Hartree/Particle)
Thermal correction to Energy= 0.040108
Thermal correction to Enthalpy= 0.041052
Thermal correction to Gibbs Free Energy= 0.009788
Sum of electronic and zero-point Energies= -169.771502
Sum of electronic and thermal Energies= -169.766794
Sum of electronic and thermal Enthalpies= -169.765850
Sum of electronic and thermal Free Energies= -169.797115

Temperature=	298.150000	Pressure=	1.000000
E(ZPE)=	0.033985	E(Thermal)=	0.038775
E(QCISD(T))=	-169.335790	E(Empiric)=	-0.060840
DE(Plus)=	-0.005208	DE(2DF)=	-0.105294
E(Delta-G3)=	-0.219113	E(G3-Empiric)=	-0.060840
G3(0 K)=	-169.692260	G3 Energy=	-169.687470
G3 Enthalpy=	-169.686526	G3 Free Energy=	-169.717952

7:

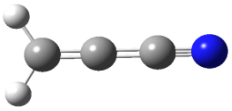

Zero-point correction= 0.035678 (Hartree/Particle)
Thermal correction to Energy= 0.040266
Thermal correction to Enthalpy= 0.041210
Thermal correction to Gibbs Free Energy= 0.010127
Sum of electronic and zero-point Energies= -169.785650
Sum of electronic and thermal Energies= -169.781063
Sum of electronic and thermal Enthalpies= -169.780119
Sum of electronic and thermal Free Energies= -169.811201

Temperature=	298.150000	Pressure=	1.000000
E(ZPE)=	0.034251	E(Thermal)=	0.038922
E(QCISD(T))=	-169.352063	E(Empiric)=	-0.060840
DE(Plus)=	-0.004233	DE(2DF)=	-0.104175
E(Delta-G3)=	-0.222077	E(G3-Empiric)=	-0.060840
G3(0 K)=	-169.709137	G3 Energy=	-169.704466
G3 Enthalpy=	-169.703522	G3 Free Energy=	-169.734762

8:

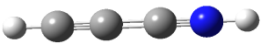

Zero-point correction= 0.037324 (Hartree/Particle)
Thermal correction to Energy= 0.041904

Thermal correction to Enthalpy= 0.042848
Thermal correction to Gibbs Free Energy= 0.017930
Sum of electronic and zero-point Energies= -169.835711
Sum of electronic and thermal Energies= -169.831131
Sum of electronic and thermal Enthalpies= -169.830187
Sum of electronic and thermal Free Energies= -169.855105

Temperature=	298.150000	Pressure=	1.000000
E(ZPE)=	0.035831	E(Thermal)=	0.040511
E(QCISD(T))=	-169.407969	E(Empiric)=	-0.060840
DE(Plus)=	-0.004007	DE(2DF)=	-0.110815
E(Delta-G3)=	-0.223130	E(G3-Empiric)=	-0.060840
G3(0 K)=	-169.770931	G3 Energy=	-169.766250
G3 Enthalpy=	-169.765306	G3 Free Energy=	-169.790398

9:

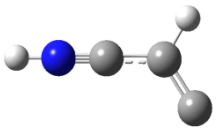

Zero-point correction= 0.035572 (Hartree/Particle)
Thermal correction to Energy= 0.040156
Thermal correction to Enthalpy= 0.041100
Thermal correction to Gibbs Free Energy= 0.009626
Sum of electronic and zero-point Energies= -169.751000
Sum of electronic and thermal Energies= -169.746416
Sum of electronic and thermal Enthalpies= -169.745472
Sum of electronic and thermal Free Energies= -169.776945

Temperature=	298.150000	Pressure=	1.000000
E(ZPE)=	0.034149	E(Thermal)=	0.038832
E(QCISD(T))=	-169.325478	E(Empiric)=	-0.060840
DE(Plus)=	-0.005845	DE(2DF)=	-0.106154
E(Delta-G3)=	-0.220416	E(G3-Empiric)=	-0.060840
G3(0 K)=	-169.684584	G3 Energy=	-169.679901
G3 Enthalpy=	-169.678957	G3 Free Energy=	-169.710603

10:

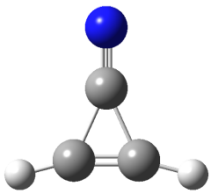

Zero-point correction= 0.035062 (Hartree/Particle)
Thermal correction to Energy= 0.039664
Thermal correction to Enthalpy= 0.040608
Thermal correction to Gibbs Free Energy= 0.008526
Sum of electronic and zero-point Energies= -169.755978
Sum of electronic and thermal Energies= -169.751377
Sum of electronic and thermal Enthalpies= -169.750433
Sum of electronic and thermal Free Energies= -169.782514

Temperature=	298.150000	Pressure=	1.000000
E(ZPE)=	0.033660	E(Thermal)=	0.038348
E(QCISD(T))=	-169.328340	E(Empiric)=	-0.060840

DE(Plus)=	-0.004406	DE(2DF)=	-0.105232
E(Delta-G3)=	-0.220066	E(G3-Empiric)=	-0.060840
G3(0 K)=	-169.685223	G3 Energy=	-169.680535
G3 Enthalpy=	-169.679591	G3 Free Energy=	-169.711834

5Br:

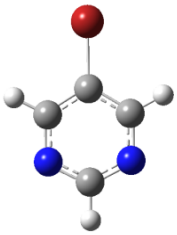

Zero-point correction= 0.067166 (Hartree/Particle)
Thermal correction to Energy= 0.072660
Thermal correction to Enthalpy= 0.073604
Thermal correction to Gibbs Free Energy= 0.036351
Sum of electronic and zero-point Energies= -2835.358730
Sum of electronic and thermal Energies= -2835.353236
Sum of electronic and thermal Enthalpies= -2835.352292
Sum of electronic and thermal Free Energies= -2835.389545

Temperature=	298.150000	Pressure=	1.000000
E(ZPE)=	0.064479	E(Thermal)=	0.070129
E(QCISD(T))=	-2835.356249	E(Empiric)=	-0.121680
DE(Plus)=	-0.018564	DE(2DF)=	-0.222186
E(Delta-G3)=	-1.458546	E(G3-Empiric)=	-0.121680
G3(0 K)=	-2837.112745	G3 Energy=	-2837.107096
G3 Enthalpy=	-2837.106151	G3 Free Energy=	-2837.143672

5Br radical ion:

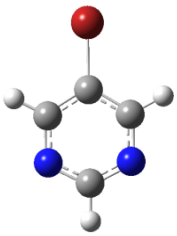

Zero-point correction= 0.066236 (Hartree/Particle)
Thermal correction to Energy= 0.072288
Thermal correction to Enthalpy= 0.073232
Thermal correction to Gibbs Free Energy= 0.033843
Sum of electronic and zero-point Energies= -2835.010270
Sum of electronic and thermal Energies= -2835.004218
Sum of electronic and thermal Enthalpies= -2835.003274
Sum of electronic and thermal Free Energies= -2835.042663

Temperature=	298.150000	Pressure=	1.000000
E(ZPE)=	0.063586	E(Thermal)=	0.069787
E(QCISD(T))=	-2835.008382	E(Empiric)=	-0.118153
DE(Plus)=	-0.013303	DE(2DF)=	-0.216727
E(Delta-G3)=	-1.455460	E(G3-Empiric)=	-0.118153
G3(0 K)=	-2836.748440	G3 Energy=	-2836.742239
G3 Enthalpy=	-2836.741295	G3 Free Energy=	-2836.780967

HCN:

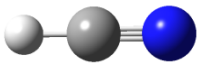

Zero-point correction= 0.016466 (Hartree/Particle)
Thermal correction to Energy= 0.019004
Thermal correction to Enthalpy= 0.019948
Thermal correction to Gibbs Free Energy= -0.002908
Sum of electronic and zero-point Energies= -93.406151
Sum of electronic and thermal Energies= -93.403613
Sum of electronic and thermal Enthalpies= -93.402669
Sum of electronic and thermal Free Energies= -93.425525

Temperature=	298.150000	Pressure=	1.000000
E(ZPE)=	0.015807	E(Thermal)=	0.018366
E(QCISD(T))=	-93.178444	E(Empiric)=	-0.033800
DE(Plus)=	-0.005883	DE(2DF)=	-0.058153
E(Delta-G3)=	-0.117775	E(G3-Empiric)=	-0.033800
G3(0 K)=	-93.378248	G3 Energy=	-93.375689
G3 Enthalpy=	-93.374744	G3 Free Energy=	-93.397629

HBrCN:

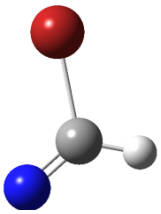

Zero-point correction= 0.017234 (Hartree/Particle)
Thermal correction to Energy= 0.020814
Thermal correction to Enthalpy= 0.021758
Thermal correction to Gibbs Free Energy= -0.009930
Sum of electronic and zero-point Energies= -2665.071712
Sum of electronic and thermal Energies= -2665.068132
Sum of electronic and thermal Enthalpies= -2665.067188
Sum of electronic and thermal Free Energies= -2665.098876

Temperature=	298.150000	Pressure=	1.000000
E(ZPE)=	0.016545	E(Thermal)=	0.020171
E(QCISD(T))=	-2665.501105	E(Empiric)=	-0.057313
DE(Plus)=	-0.008368	DE(2DF)=	-0.101234
E(Delta-G3)=	-1.237677	E(G3-Empiric)=	-0.057313
G3(0 K)=	-2666.889152	G3 Energy=	-2666.885526
G3 Enthalpy=	-2666.884582	G3 Free Energy=	-2666.916348

1:

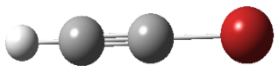

Zero-point correction= 0.018100 (Hartree/Particle)
Thermal correction to Energy= 0.021592
Thermal correction to Enthalpy= 0.022537
Thermal correction to Gibbs Free Energy= -0.003586
Sum of electronic and zero-point Energies= -2648.042317
Sum of electronic and thermal Energies= -2648.038824
Sum of electronic and thermal Enthalpies= -2648.037880

Sum of electronic and thermal Free Energies= -2648.064003

Temperature=	298.150000	Pressure=	1.000000
E(ZPE)=	0.017376	E(Thermal)=	0.020919
E(QCISD(T))=	-2648.506300	E(Empiric)=	-0.050553
DE(Plus)=	-0.003264	DE(2DF)=	-0.090763
E(Delta-G3)=	-1.225144	E(G3-Empiric)=	-0.050553
G3(0 K)=	-2649.858648	G3 Energy=	-2649.855105
G3 Enthalpy=	-2649.854161	G3 Free Energy=	-2649.880362

2:

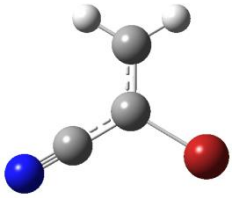

Zero-point correction= 0.040135 (Hartree/Particle)
Thermal correction to Energy= 0.045445
Thermal correction to Enthalpy= 0.046389
Thermal correction to Gibbs Free Energy= 0.009591
Sum of electronic and zero-point Energies= -2741.525935
Sum of electronic and thermal Energies= -2741.520625
Sum of electronic and thermal Enthalpies= -2741.519681
Sum of electronic and thermal Free Energies= -2741.556478

Temperature=	298.150000	Pressure=	1.000000
E(ZPE)=	0.038530	E(Thermal)=	0.043959
E(QCISD(T))=	-2741.757626	E(Empiric)=	-0.084353
DE(Plus)=	-0.007741	DE(2DF)=	-0.148579
E(Delta-G3)=	-1.341880	E(G3-Empiric)=	-0.084353
G3(0 K)=	-2743.301648	G3 Energy=	-2743.296219
G3 Enthalpy=	-2743.295275	G3 Free Energy=	-2743.332295

3:

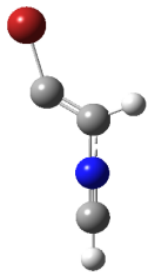

Zero-point correction= 0.039270 (Hartree/Particle)
Thermal correction to Energy= 0.044807
Thermal correction to Enthalpy= 0.045751
Thermal correction to Gibbs Free Energy= 0.008870
Sum of electronic and zero-point Energies= -2741.509771
Sum of electronic and thermal Energies= -2741.504235
Sum of electronic and thermal Enthalpies= -2741.503291
Sum of electronic and thermal Free Energies= -2741.540172

Temperature=	298.150000	Pressure=	1.000000
E(ZPE)=	0.037700	E(Thermal)=	0.043358
E(QCISD(T))=	-2741.743499	E(Empiric)=	-0.084353
DE(Plus)=	-0.007555	DE(2DF)=	-0.151636

E(Delta-G3)=	-1.341328	E(G3-Empiric)=	-0.084353
G3(0 K)=	-2743.290672	G3 Energy=	-2743.285013
G3 Enthalpy=	-2743.284069	G3 Free Energy=	-2743.321185

4:

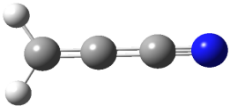

Zero-point correction= 0.035678 (Hartree/Particle)
Thermal correction to Energy= 0.040266
Thermal correction to Enthalpy= 0.041210
Thermal correction to Gibbs Free Energy= 0.010127
Sum of electronic and zero-point Energies= -169.785650
Sum of electronic and thermal Energies= -169.781063
Sum of electronic and thermal Enthalpies= -169.780119
Sum of electronic and thermal Free Energies= -169.811201

Temperature=	298.150000	Pressure=	1.000000
E(ZPE)=	0.034251	E(Thermal)=	0.038922
E(QCISD(T))=	-169.352063	E(Empiric)=	-0.060840
DE(Plus)=	-0.004233	DE(2DF)=	-0.104175
E(Delta-G3)=	-0.222077	E(G3-Empiric)=	-0.060840
G3(0 K)=	-169.709137	G3 Energy=	-169.704466
G3 Enthalpy=	-169.703522	G3 Free Energy=	-169.734762

5:

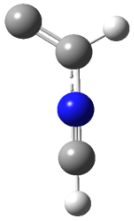

Zero-point correction= 0.035796 (Hartree/Particle)
Thermal correction to Energy= 0.040188
Thermal correction to Enthalpy= 0.041132
Thermal correction to Gibbs Free Energy= 0.010015
Sum of electronic and zero-point Energies= -169.725832
Sum of electronic and thermal Energies= -169.721440
Sum of electronic and thermal Enthalpies= -169.720496
Sum of electronic and thermal Free Energies= -169.751613

Temperature=	298.150000	Pressure=	1.000000
E(ZPE)=	0.034364	E(Thermal)=	0.038848
E(QCISD(T))=	-169.301041	E(Empiric)=	-0.060840
DE(Plus)=	-0.006475	DE(2DF)=	-0.103647
E(Delta-G3)=	-0.218963	E(G3-Empiric)=	-0.060840
G3(0 K)=	-169.656602	G3 Energy=	-169.652118
G3 Enthalpy=	-169.651174	G3 Free Energy=	-169.682448

6:

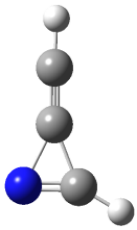

Zero-point correction= 0.035665 (Hartree/Particle)
Thermal correction to Energy= 0.039940
Thermal correction to Enthalpy= 0.040884
Thermal correction to Gibbs Free Energy= 0.010022
Sum of electronic and zero-point Energies= -169.742482
Sum of electronic and thermal Energies= -169.738207
Sum of electronic and thermal Enthalpies= -169.737262
Sum of electronic and thermal Free Energies= -169.768124

Temperature=	298.150000	Pressure=	1.000000
E(ZPE)=	0.034238	E(Thermal)=	0.038605
E(QCISD(T))=	-169.312668	E(Empiric)=	-0.060840
DE(Plus)=	-0.005198	DE(2DF)=	-0.106333
E(Delta-G3)=	-0.219866	E(G3-Empiric)=	-0.060840
G3(0 K)=	-169.670666	G3 Energy=	-169.666299
G3 Enthalpy=	-169.665355	G3 Free Energy=	-169.696369

7:

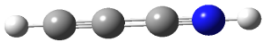

Zero-point correction= 0.037324 (Hartree/Particle)
Thermal correction to Energy= 0.041904
Thermal correction to Enthalpy= 0.042848
Thermal correction to Gibbs Free Energy= 0.017930
Sum of electronic and zero-point Energies= -169.835711
Sum of electronic and thermal Energies= -169.831131
Sum of electronic and thermal Enthalpies= -169.830187
Sum of electronic and thermal Free Energies= -169.855105

Temperature=	298.150000	Pressure=	1.000000
E(ZPE)=	0.035831	E(Thermal)=	0.040511
E(QCISD(T))=	-169.407969	E(Empiric)=	-0.060840
DE(Plus)=	-0.004007	DE(2DF)=	-0.110815
E(Delta-G3)=	-0.223130	E(G3-Empiric)=	-0.060840
G3(0 K)=	-169.770931	G3 Energy=	-169.766250
G3 Enthalpy=	-169.765306	G3 Free Energy=	-169.790398

8 ACKNOWLEDGEMENTS

Questo lavoro è stato parzialmente finanziato da:

Consiglio Nazionale delle Ricerche, Istituto CNR-IMIP.
Progetti MIUR PRIN 2009W2W4YF e 2009SLKFEX, MIUR FIRB RBFR10SQZI.
Progetto di grande rilevanza del MAE Italia-Slovenia, 'Dynamics at nanoscale'.
Progetto Galileo 2012 n. G12-44 'New ligth on radiosensitisers', Fondato da Ministero dell'Istruzione, dell'Università e della Ricerca e Università Italo Francese .
European COST Action MP1002 Nano-Ion Beam Cancer Theraphy (Nano-IBCT).
Programma 'Supporto agli utenti italiani di Elettra', Elettra-Sincrotrone Trieste S.C.p.A. di interesse nazionale.

Al termine di questi tre anni desidero ringraziare,
il dott. Lorenzo Avaldi, la dott.ssa Paola Bolognesi e il prof. Walther Caminati per avermi dato la possibilità di lavorare a questo progetto. I miei amici e colleghi tutti, in particolare Adriana, Patrizia e Antonella per il supporto chimico, Annarita e Giuseppe per quello teorico, Daniele, Robert, Patrick e Sandro per l'aiuto tecnico presso le beamlines. Un grazie anche ai colleghi di Caen, Alicia, Patrick e Sylvain.
E infine un grazie affettuosissimo ad Alessandra, Alessio, Annarita e Francesco per gli 'intermezzi gossip' e tutti i momenti passati insieme, indimenticabili, e a Pina per le piacevoli 'pause' caffè e preziosi consigli materni.
Grazie anche a Violetta, Roberta, Andrea, Alessandro e Carlo, miei cari amici.

[1] H. Kamminga, Protoplasm and the Gene. In *Clay Minerals and The Origin of Life*, edited by
[2] A. Oparin, *Genesis and Evolutionary Development of Life.* New York: Academic P, 1968.
[3] J. Watson and F. Crick, A Structure for Deoxyribose Nucleic Acid. *Nature* 171:737-38, 1953.
[4] J. Watson and F. Crick, Genetical Implications of the Structure of Deoxyribose Nucleic Acid. *Nature* 171:964-67, esp. 964, 1953.
[5] T.D. Schneider, Information Content of Individual Genetic Sequences. *Journal of Theoretical Biology* 189:427-41, 1997.
[6] W.R. Loewenstein, *The Touchstone of Life: Molecular Information, Cell Communication, and the Foundations of Life.* New York: Oxford UP, 1999.
[7] B. Kuppers, *Information and the Origin of Life.* Cambridge, MA: MIT P, 1990.
[8] A.I. Oparin, *The Origin of Life,* translated by S. Morgulis. New York: Macmillan, 1938.
[9] S.C. Meyer, *Of Clues and Causes: A Methodological Interpretation of Origin of Life Studies.* Ph.D. thesis, Dept. of History and Philosophy of Science, Cambridge University, 1991.
[10] H. Judson, *Eighth Day of Creation.* New York: Simon and Schuster, 1979.
[11] R. Watanabe, H. Nikjoo, *Int. J. Radiat. Biol*. 78, 953–966 (2002)
[12] G. Vall-llosera, M.A. Huels, M. Coreno, A. Kivimaki, K. Jakubowska, . Stankiewicz and E. Rachlew, *Chem. Phys. Chem.*, 9, 1020-1029 (2008).
[13] B. BoudaRffa, P. Cloutier, D. Hunting, M. A. Huels, L. Sanche, *Science*, 287, 1658–1660 (2002).
[14] H. Abdoul-Carime, L. Sanche, *Int. J. Radiat. Biol*., 78, 89–99 (2002).
[15] A. Yokoya, R. Watanabe, T. Hara, *J. Radiat. Res*., 40, 145–158 (1999).
[16] K. Hieda, T. Hirono, A. Azami, M. Suzuki, Y. Furusawa, H. Maesawa, N. Usami, A. Yokoya, K. Kobayashi, *Int. J. Radiat. Biol*., 70, 437–445 (1996).
[17] L. Sanche, *Eur. Phys. J. D., 35*, 367-390 (2005).
[18] H. Abdoul-Carime, M.A. Huels, E. Illenberger, L. Sanche, *J. Am.Chem. Soc*., 123, 5354-5355 (2001).
[19] D. Radisic, Y. Jae Ko, J.M. Nilles, S.T. Stokes, M.D Sevilla, J. Rak, K.H. Bowen, *J. Chem Phys*., 134, 015101 (2011).
[20] H. Abdoul-Carime, P.C. Dugal, L. Sanche, *Radiation Research,* 153, 23-28 (2000).
[21] J.A. O'Donoghue, T.E. Wheldon, *Physics in Medicine and Biology.*, 41, 1973-1991 (1996).
[22] F. Buchegger, F. Perillo-Adamer, Y.M. Dupertuis, A. B. Delaloye, *Eur J Nucl Med Mol Imaging.*, 33, 1352-1363 (2006).
[23] P. Bolognesi, P. O'Keeffe, L. Avaldi, *Soft X-ray Interaction with Organic Molecules of Biological Interest. In Radiation Damage in Biomolecular Systems*, Gomez-Tejedor, G.G.; Fuss M.C., Eds.; Springer Science+Business Media B.V, 2012; p. 165
[24] P. Bolognesi, P. O'Keeffe, V. Feyer, O. Plekan, K. Prince, M. Coreno, G. Mattioli, A. Amore Bonapasta, W. Zhang, V. Carravetta, Y. Ovcharenko, L. Avaldi, *Journal of Physics: Conference Series*, 212, 012002 (2010).
[25] M. Schwell, H-W. Joachims, H. Baumagärtel, S. Leach, *Chem. Phys*., 353, 145-162 (2008).
[26] G. Vall-llosera, M. Coreno, P. Erman, M.A. Huels, K. Jakubowska, A. Kivimäki, E. Rachlew, M. Stankiewicz,. *Int. J. Mass. Spectrometry*, 275, 55-63 (2008).
[27] I. Linert, M. Dampc, B. Mielewska, M. Zubek, *Eur. Phys. J. D*, 66, 20 (2012).
[28] P. O'Keeffe, P. Bolognesi, A.R. Casavola, D. Catone, N. Zema, S. Turchini, L. Avaldi, *Mol. Phys*., 107, 2025 (2009).
[29] M. Stener, P. Decleva, D. M. P. Holland, D. A. Shaw, *J. Phys. B: At. Mol. Opt. Phys.*, 44, 075203 (2011).
[30] A.W. Potts, D.M. P Holland, A.B. Trofimov, J. Schirmer, L. Karlsson, K. Siegbahn, *J. Phys. B: At. Mol. Opt. Phys.*, 36, 3129-3146 (2003).
[31] P. Bolognesi, P. O'Keeffe, E. Ovcharenko, M. Coreno, L. Avaldi, V. Feyer, O. Plekan, K.C. Prince, W. Zhang, V. Carravetta, *J. Chem. Phys.*, 133, 034302 (2010).
[32] P. Bolognesi, G. Mattioli, P. O'Keeffe, V. Feyer, O. Plekan, Y. Ovcharenko, K.C Prince, M. Coreno, A. Amore Bonapasta, L. Avaldi, *J. Phys. Chem. A.*, 113, 13593-13600 (2009).
[33] G. Vall-llosera, B. Gao, A. Kivimäki, M. Coreno, J. Alvarez Ruiz, M. De Simone, H. Ågren, E. Rachel, *J. Chem. Phys.*, 128, 044316 (2008).
[34] L. Storchi, F. Tarantelli, S. Veronesi, P. Bolognesi, E. Fainelli, L. Avaldi, *J. Chem. Phys.*, 129, 154309 (2008).
[35] K. Tanaka, E.O. Sako, E. Ikenaga, K. Isari, S.A. Sardar, S. Wada, T. Sekitani, K. Mase, N. Ueno, *J. Electron Spectrosc. Relat. Phenom.*, 119, 255-266 (2001).

[36] K. Tanaka, H. Kizaki, R. Sumii, Y. Matsumoto, S. Wada, *Radiation Physics and Chemistry*., 75, 2076-2079 (2006).
[37] S. Nagaoka, H. Fukuzawa, G. Prumper, M. Takemoto, O. Takahashi, K. Yamaguchi, T. Kakiuchi, K. Tabayashi, I.H. Suzuki, J.R. Harries, Y. Tamenori, K. Ueda, *J. Phys. Chem A.*, 115, 8822-8831 (2011).
[38] O. Plekan, M. Coreno, V. Feyer, A. Moise, R. Richter, M. de Simone, E. Sankari, K.C. Prince, *Phys. Scr.*, 78, 058105 (2008).
[39] M.A. Palafox, J. Talaya, A. Guerrero-Martinez, G. Tardajos, H. Kumar, J.K. Vats, V.K. Rastogi, *Spectroscopy Letts*. 43, 51 (2010).
[40] C.A. Presant, W. Wolf, V. Waluch, C. Wiseman, P. Kennedy, D. Blaney, R.R. Brechner, *Lancet*, 343, 1184 (1994).
[41] U.P Singh, B.N. Singh, A.K. Ghosh, R.K Singh, A. Sodhi, *J. Inorg. Biochem* 44, 277 (1991).
[42] D.W. Adair, K.A. Smiles, D. King, *Eur Path Appl EP* 565412 A1, 51, (1993).
[43] M.C. Bacchus-Montabonel et al, *Phys Rev A* 79, 012710 (2009).
[44] M.C. Bacchus-Montabonel et al, *Phys Rev A* 74, 054702 (2006).
[45] M.C. Bacchus-Montabonel et al, *Phys Rev A* 72, 052706 (2005).
[46] T. van Mourik, V.I. Danilov, V.V. Dailidonis, N. Kurita, H. Wakabayashi, T. Tsukamoto *Theor. Chem. Acc.*, 125, 233–244 (2010).
[47] F. R. Elder, A. M. Gurewitsch, R. V. Langmuir, H. C. Pollock, *Phys. Rev.*, 71, 829 (1947).
[48] E.E. Koch, D.E. Eastman and Y. Farges in *Handbook of Synchrotron Radiation*, Vol. 1a, Chapter 1, Ed. by E.E. Koch (North-Holland Publishing Company, Amsterdam), (1983).
[49] J. Schwinger, *Phys. Rev*. 75, 1912 (1949).
[50] S. Mobilio and A. Balerna in *Synchrotron Radiation: Fundamental, Methodologies and Applications* Conference Proceeding Vol. 82, Ed. S. Mobilio and G. Vlaic, SIF, Bologna, 1- 23 (2003).
[51] G. Materlik, in *Uses of Synchrotron Radiation in Biology*, Ed. by H.B. Stuhrmann (Academic Press Inc.-London), (1982).
[52] A. Derossi, F. Lama, M. Piacentini, T. Prosperi, N. Zema, *Rev. Sci. Instrum*., 66, 1718-1720 (1995).
[53] http://www.chemspider.com/
[54] G.V. Marr, J.B. West, *Atomic data and Nuclear Tables*, 18, 497-508 (1976).
[55] J.C. Traeger, R. G. McLoughlin, *J. Am. Chem. Soc.*, 103, 3647-3652 (1981).
[56] S. Leach, H. Joachims, H. Baumgartel, *J. Phys. Chem. A.*, 114, 4847-4856 (2010).
[57] R.R. Blyth, R. Delaunay, M. Zitnik, J. Krempasky, R. Krempaska, J. Slezak, K.C. Prince, R. Richter, M. Vondracek, R. Camilloni, L. Avaldi, M. Coreno, G. Stefani, C. Furlani, M. de Simone, S. Stranges, M.-Y. Adam, *Electron Spectrosc. Relat. Phenom* 101–103, 959–964 (1999).
[58] O. Plekan, M. Coreno, V. Feyer, A. Moise, R. Richter, M. de Simone, R. Sankari, K.C. Prince, *Phys. Scr.*, 78 058105 (2008).
[59] www.thermocoax.com
[60] B.K. Agarwl, X-ray spectroscopy, Springer, Berlin (1991).
[61] D.C. Konigsberg and R. Prins eds., *X-ray absorption: principles and application techniques of EXAFS, SEXAFS and XANES*, J. Wiley, New York, (1988).
[62] J: Stohr, NEXAFS Spectroscopy, Springer, Berlin, (1996).
[63] M. Tronc, G. C. King, F. H. Read, *J. Phys. B* 12, 137 (1979).
[64] C.T. Chen, Y. Ma, F. Sette, *Phys. Rev. A*, 40, 11 (1984).
[65] G.R. Wight, C.E. Brion, *J. Electron Spectrosc. Relat. Phenom*. 3, 191 (1974).
[66] V. Myrseth, J.D. Bozek, E. Kukk, L.J. Saethre and T.D. Thomas, *J. Electron Spectrosc. Relat. Phenom*, 122, 57-63, (2002).
[67] P. van der Straten, R. Mongerstern and A.Z. Niehaus, *Phys. D*, 8, 35 (1988).
[68] T. Darrah Thomas, W. Robert, Jr. J. Shaw,. *J. Electron Spectrosc. Relat. Phenom.*, 5, 1081 (1974).
[69] K.C. Prince, L. Avaldi, M. Coreno, R. Camilloni and M. de Simone, *J. Phys. B: At. Mol. Opt. Phys.*, 32, 2551–2567 (1999).
[70] C. Prigent, E. Lamour, J. Mérot, B. Pascal, J.-P. Rozet, M. Trassinelli, D. Vernhet, J.-Y. Pacquet, L. Maunoury, F. Noury, J.-M. Ramillon, *Journal of Physics: Conference Series*, 163, 012111 (2009).

[71] T. Bergen, X. Biquard, A. Brenac, F. Chandezon, B. A. Huber, D. Jalabert, H. Lebius, M. Maurel, E. Monnand, J. Opitz, A. Pesnelle, B. Pras, C. Ristori, J. C. Rocco, *Rev. of Scient. Instr.*, 70, 8 (1999).
[72] A. Bárány, G. Astner, H. Cederquist, H. Danared, S. Huldt, P. Hvelplund, A. Johnson, H. Knudsen, L. Liljeby, and K.-R. Rensfelt, *Nucl. Instr. Meth. Phys. Res. B*, 9, 397 (1985).
[73] W.C Wiley and I.H. Mclaren. Time. *Review of Scientific Instruments*, 26, 1150 (1955).
[74] Gaussian 09, Revision A.1, M. J. Frisch et all., Gaussian, Inc., Wallingford CT, (2009).
[75] S.G. Lias, P. Ausloos, *J. Am. Chem. Soc.*, 100, 6027-6034 (1978).
[76] J.C. Traeger, R.G. McLoughlin, *J. Am. Chem. Soc.*, 103, 3647-3652 (1981).
[77] W.A. Chupka, *J. Chem. Phys.*, 54, 1936-1947 (1971).
[78] K.E. McCulloh, *Int. J. Mass Spectrom. Ion Phys*., 21, 333-342 (1976).
[79] A.G. Baboul, L.A. Curtiss, P.C. Redfem, K. Raghavachari, *J. Chem Phys*, 110, 7650-7657 (1999).
[80] D. Bond, *J. Org. Chem*, 72, 5555-5566 (2007).
[81] C.Peng, P.Y. Ayala, H.B. Schlegel, M.J. Frisch, *J. Comp. Chem*., 17, 49-56 (1996).
[82] C. Peng, H.B. Schlegel, *Israel J. Chem.*, 33, 449-454 (1993).
[83] L.A. Curtiss, K. Raghavachari, P.C. Redfern and J.A. Pople, *J. Chem. Phys*., 106, 1063 (1997).
[84] L.A. Curtiss, K. Raghavachari, J.A. Pople, *J. Chem. Phys*. 103, 4192 (1995).
[85] R. Krishnan, M.J. Frisch, J.A. Pople, *J. Chem. Phys*. 72, 4244 (1980).
[86] M.J. Frisch, J.A. Pople, J.S. Binkley, *J. Chem. Phys*. 80, 3265 (1984).
[87] T. Clark, J. Chandrasekhar, G.W. Spitznagel, P. v R. Schleyer, *J. Comput. Chem*. 4, 294 (1983).
[88] P.C. Hariharan, J.A. Pople, *Theor. Chim. Acta* 28, 213 (1973).
[89] J.A. Pople, N. Head-Gordon, K. Raghavachari, *J. Chem. Phys*. 87, 5968 (1987).
[90] L.A. Curtiss, P.C. Redfern, V. Rassolov, G. Kedziora, J.A. Pople, *J. Chem. Phys*. 114, 9287 (2001).
[91] C. Moore, *Natl. Bur. Stand. (U.S.) Circ* 467 (1952).
[92] L.A. Curtiss, J.E. Carpenter, K. Raghavachari, J.A. Pople, *J. Chem.Phys*. 96, 9030 (1992).
[93] A.D. Becke, *J. Chem. Phys*. 98, 5648 (1993).
[94] P.J. Stephens, F.J. Devlin, C.F. Chabalowski, M.J. Frisch, *J. Phys. Chem*. 98, 11623 (1994).
[95] A.D. Becke, *Phys. Rev. A*, 38, 3098 (1988).
[96] C. Lee, W. Yang, R.G. Parr, *Phys. Rev. B*, 37, 785 (1988).
[97] J.W. Ochterski, Gaussian Inc., (2000).
[98] L.A. Curtiss, K. Raghavachari, P.C. Redfern, J. A. Pople, *J.Chem.Phys*., 106, 1063 (1997).
[99] B.J. McBride, S. Heimel, J.G. Ehlers, S. Gordon, *NASA-SP-3001*, 17, 303 (1963).
[100] A.G. Baboul, L.A. Curtiss, P.C. Redfern, K. Raghavachari, *J. Chem. Phys*., 110, 7650 (1999).
[101] L.A. Curtiss, K. Raghavachari, P.C. Redfern, J.A. Pople, *J. Chem. Phys*., 106, 1063 (1997).
[102] L.A. Curtiss, P.C. Redfern, K. Raghavachari, *J. Chem. Phys*., 126, 084108 (2007).
[103] L.A. Curtiss, K. Raghavachari, G.W. Trucks, J.A. Pople, *J. Chem. Phys*., 94, 7221 (1991).
[104] M.A. V. Ribeiro da Silva, L. M. P. F. Amaral, J. R. B. Gomes, *J. Phys. Chem. B* 111, 792 (2007).
[105] M.W. Chase, Jr., C.A. Davies, J.R. Downey, Jr., D.J. Frurip, R.A. McDonald, A.N. Syverud, *J. Phys. Chem. Ref. Data*, 14, Suppl.1, (1985).
[106] G. Vall-llosera, M. Coreno, P. Erman, M.A. Huels, K. Jakubowska, A. Kivimäki, E. Rachlew, M. Stankiewicz, *Int. J. Mass. Spectrometry*, 275, 55-63 (2008).
[107] I. Linert, M. Dampc, B. Mielewska, M. Zubek, *Eur. Phys. J. D*, 66, 20 (2012).
[108] O. Plekan, M. Coreno, V. Feyer, A. Moise, R. Ricther, M. de Simone, E. Sankari, K. Prince, *Phys. Scr.*, 78, 058105 (2008).
[109] M. Schwell, H-W. Joachims, H. Baumagärtel, S. Leach, *Chem. Phys*., 353, 145-162 (2008).
[110] F. Milani-Nejad, H.D. Stidham, *Spectrochimica Acta*, 31A, 1433-1453 (1975).
[111] P. Bolognesi, P. O'Keeffe, L. Avaldi, Soft X-ray Interaction with Organic Molecules of Biological Interest. In Radiation Damage in Biomolecular Systems, Gomez-Tejedor, G.G.; Fuss M.C., Eds.; Springer Science+Business Media B.V, 2012; p. 165
[112] P. Bolognesi, P. O'Keeffe, V. Feyer, O. Plekan, K. Prince, M. Coreno, G. Mattioli, A. Amore Bonapasta, W. Zhang, *Journal of Physics: Conference Series*, *212*, 012002 (2010).
[113] G. Vall-llosera, B. Gao, A. Kivimäki, M. Coreno, J. Alvarez Ruiz, M. De Simone, H. Ågren, E. Rachel, *J. Chem. Phys.*, 128, 044316 (2008).
[114] O. Plekan, M. Coreno, V. Feyer, A. Moise, R. Ricther, M. de Simone, E. Sankari, K. Prince, *Phys. Scr.*, *78*, 058105 (2008).

[115] I. Linert, M. Dampc, B. Mielewska, M. Zubek, *Eur. Phys. J. D*, 66, 20 (2012).
[116] P. O'Keeffe, P. Bolognesi, A.R. Casavola, D. Catone, N. Zema, S. Turchini, L. Avaldi, *Mol. Phys*., 107, 2025 (2009).
[117] O. Plekan, V. Feyer, R. Ricther, M. Coreno, M. de Simone, K:C. Prince, *Chem. Phys*., 334, 53-63 (2007).
[118] P. Bolognesi, G. Mattioli, P. O'Keeffe, V. Feyer, O. Plekan, Y. Ovcharenko, K.C. Prince, M. Coreno, A. Amore Bonapasta, L. Avaldi, *J. Phys. Chem. A.*, 113, 13593-13600 (2009).
[119] V.K. Rastogi,, M. Alcolea Palafox, A. Guerrero-Martínez, G. Tardajos, J.K. Vats, I. Kostova, S. Schlucker, W. Kiefer , *Journal of Molecular Structure: THEOCHEM* 940, 29–44 (2010).
[120] V.K. Rastogi, M. Alcolea Palafox, *Spectrochimica Acta Part A* 79, 970– 977 (2011).
[121] V. Feyer, O. Plekan, R. Richter, M. Coreno, G. Vall-llosera, K.C. Prince, A.B. Trofimov, I.L. Zaytseva, T.E. Moskovskaya, E.V. Gromov, J. Schirmer, *J. Phys. Chem. A.*, 113, 5736-5742 (2009).
[122] V. Feyer, O. Plekan, R. Richter, M. Coreno, M. de Simone, K.C. Prince, A.B. Trofimov, I. L. Zaytseva, J. Schirmer, *J. Phys. Chem. A, 114*, 10270–10276 (2010).
[123] G. Mattioli (2013) private Communications.
[124] F. Rondino, D. Catone, G. Mattioli, A.A. Bonapasta, P. Bolognesi, A.R. Casavola, M. Coreno, P. O'Keeffe, L. Avaldi, *RSC Adv*.,4,5272 (2014).
[125] M.C. Payne, M.P. Teter, D.C. Allan, T.A. Arias, J.D. Joannopulos, *ReV. Mod. Phys.*, 64, 1045 (1992).
[126] A. D. Becke, *J. Chem. Phys*., 98, 5648 (1993).
[127] P. Giannozzi, et al. *J. Phys.: Condens. Matter*, 21, 395502 (2009).
[128] T. J. Kinsella, P. P. Dobson, J. B. Mitchell, A. J. Fornace, *Jr., Int. J. Radiat. Oncol., Biol., Phys*. 13, 733 (1987).
[129] T. van Mourik, V.I. Danilov, V.V. Dailidonis, N. Kurita, H. Wakabayashi, T. Tsukamoto *Theor Chem Acc.* 125, 233–244 (2010).
[130] E. Itälä, D. T. Ha, K. Kooser, E. Rachlew, M. A. Huels, E. Kukk. *J. Chem. Phys.* 133, 154316 (2010).
[131] T. Schlathölter et al. *ChemPhysChem.*, 7, 2339-2345 (2006).
[132] S. Maclot, M. Capron, R. Maisonny, A. Ławicki, A. Méry, J. Rangama, J.Y. Chesnel, S. Bari, R. Hoekstra, T. Schlathclter, B. Manil, L. Adoui, P. Rousseau, B. A. Huber, *ChemPhysChem*, 12, 930–936 (2011).
[133] S. Legendre, *Etude de l'ionisation et de la dissociation d'H2O induites par collision avec des ions multichargés rapides*. PhD thesis, Université de Caen Basse-Normandie, (2002).
[134] R. Maisonny, *Étude expérimentale de la fragmentation d'agrégats d'eau induite par impact d'ions Multichargés*, PhD thesis, Université de Caen Basse-Normandie, (2006).
[135] A.R. Katritzky, A.J. Waring, *J. Chem. Soc.*, 1540 (1962).
[136] X. Hu, H. Li, J. Ding, S. Han, *Biochemistry* 43, 6361–6369 (2004).
[137] H. Yu, R. Eritja, J.B. Bloom, M.F. Goodman, *J Biol Chem* 268, 15935–15943 (1993).